

Modelling of Dynamic Edge Loading in Total Hip  
Replacements with ceramic on polyethylene  
Bearings

By  
Faezeh Jahani

Submitted in accordance with the requirements for the degree  
of Doctor of Philosophy

The University of Leeds School of Mechanical Engineering  
September, 2017

The candidate confirms that the work submitted is her own, except where work which has formed part of jointly-authored publications has been included. The contribution of the candidate and the other authors to this work has been explicitly indicated below. The candidate confirms that appropriate credit has been given within the thesis where reference has been made to the work of others.

This copy has been supplied on the understanding that it is copyright material and that no quotation from the thesis may be published without proper acknowledgement.

© 2017 The University of Leeds and Faezeh Jahani

The right of Faezeh Jahani to be identified as Author of this work has been asserted by her in accordance with the Copyright, Designs and Patents Act 1988.

## **Acknowledgement**

My first appreciation goes to the brilliant supervision team that I had the pleasure to work with. Prof. Ruth Wilcox, Dr Alison Jones, Prof. David Barton and Prof John Fisher, thank you for such an amazing opportunity and believing in me. This piece of work is the mirror of the amazing effort of my supervisor Dr Alison Jones who guided and supported me throughout my PhD not only professionally but also emotionally. She wisely provided the emotional support in the times that I needed understanding. I also like to thank Mr James Brooks who was a great help to my project.

My appreciation goes to EPSRC and DePuy Synthes for providing funding for me to be able to finish this PhD.

My family gave me the motivation to go for the biggest achievement of my life. I am genuinely indebted to my father, Sadegh Jahani, my mother, Fatemeh Sharei and my sister, Razieh Jahani for the hardships I caused them to peruse my dream. I hope this thesis could make them proud. My other sister, Massoumeh Jahani not only has been a family to me throughout this journey, she also has been a mentor. Simply thank you for everything you have done for me. I also like to thank my niece and my nephew, Arina Saeid and Radin Ahmadi, for understanding all those weekends of work instead of playing time with them.

I am blessed not only because of having a supportive supervisors and family, but also, for the amazing friends who listened to my complaints and reminded me of my goal. Behnaz Bazmi and Bahare Mousaei, especially thank you for your timeless kindness. My special thanks goes to my rock, Matthew Smith, who is the biggest blessing of my life. I am humbly grateful firstly for understanding my frustrations

every time I didn't get the result I wanted and secondly, for every little effort you made to make me feel I can do this.

I worked in a very supportive environment the support of experimental studies experts, Mazen Al-Hajjar and Murat Ali, can't be forgotten. Also special thanks to everyone in room X301 for kind and enjoyable atmosphere to work in.

I believe in the greatest power who brought all these people to my life and showed me the path I am taking. Thank you God.

## **Abstract**

The performance of total hip replacement (THR) devices can be affected by various factors such as quality of the tissues surrounding the joint, mismatch of the component centres or the cup positioning during hip replacement surgery. Experimental studies have shown that these factors can cause the separation of the two components during the walking cycle (dynamic separation) and the contact of the femoral head with the rim of the acetabular liner (edge loading), which can lead to increased wear and shortened implant lifespan.

There is a need for flexible pre-clinical testing tools which allow THR devices to be assessed under these adverse conditions. In this work, a novel dynamic finite element model was developed that is able to generate dynamic separation as it occurs during the gait cycle. In addition, the ability to interrogate contact mechanics and material strain under separation conditions provides a unique means of assessing the severity of edge loading. This study demonstrates these model capabilities for a range of simulated surgical translational mismatch values, cup inclination angles and swing phase loads for ceramic-on-polyethylene implants.

The computational model was developed to replicate one station of the Leeds II hip simulator that mimic *in vitro* adverse conditions. Firstly, a computational sensitivity model was developed under standard conditions for a stable computational contact. The mechanism of separation was also added. The finite element model was able to predict medial-lateral separation as it occurred dynamically in the gait cycle, including cases where the femoral head was in contact with the rim of the cup. The increase in medial-lateral separation with increased translational mismatch, cup inclination angle and decreased swing phase load were in broad agreement with existing experimental data.

The factors that increased the separation level, also increased the permanent deformation on the cup. However, steep cup inclination angle resulted in a higher number of conditions with permanent deformation than the standard cup inclination angle. Moreover, despite the low axial load during swing phase, under some separation conditions, reduced contact area created stress value higher than those at the peak axial load.

The developed computational tool can be used to understand the effect of various factors on the separation and contact mechanics simultaneously. As separation is a multi-factorial phenomenon, this model can assist to focus on the selected factors that affect the separation experimentally. Moreover, the effect of components specifications such as materials, geometry, and the cup thickness can be investigated with this model.

## Table of contents

|   |           |
|---|-----------|
| Acknowledgement.....                              | III       |
| Abstract .....                                    | V         |
| Table of Figures.....                             | XIII      |
| Chapter 1 Introduction and Literature review..... | 1         |
| <b>1.1 Introduction.....</b>                      | <b>1</b>  |
| <b>1.2 THR design and performance.....</b>        | <b>2</b>  |
| 1.2.1 Gait Cycle.....                             | 4         |
| 1.2.2 Hip disorders .....                         | 4         |
| 1.2.3 Total hip replacement (THR).....            | 5         |
| 1.2.4 Types of hip replacements .....             | 7         |
| 1.2.5 Gait cycle of THRs .....                    | 10        |
| 1.2.6 Failure of hip replacements.....            | 12        |
| 1.2.7 Dynamic separation.....                     | 14        |
| 1.2.8 Positioning of THR.....                     | 17        |
| <b>1.3 Tribology of artificial hip joint.....</b> | <b>20</b> |
| 1.3.1 Wear .....                                  | 20        |
| 1.3.3 Friction and Lubrication .....              | 27        |
| 1.3.3 Contact mechanics.....                      | 29        |
| <b>1.4 Computational studies .....</b>            | <b>32</b> |
| 1.4.1 Finite element modelling of THRs .....      | 34        |
| 1.4.2 Two-Dimensional hip models.....             | 35        |
| 1.4.3 Axisymmetric hip models.....                | 36        |

|   |           |
|---|-----------|
| 1.4.4 Three-Dimensional hip models under idealised condition.....                         | 38        |
| 1.4.5 Three dimensional hip models under microseparation condition .....                  | 41        |
| 1.4.6 Coupling of dynamic and contact mechanic analysis.....                              | 47        |
| 1.4.7 THR dynamic modelling.....  | 50        |
| 1.4.8 Wear modelling .....  | 53        |
| <b>1.5 Summary .....</b>  | <b>53</b> |
| <b>1.6 Aims and objective.....</b>  | <b>55</b> |
| <br>Chapter 2 Development of the explicit model under concentric loading<br>conditions 59 |           |
| <b>2.1 Introduction.....</b>  | <b>59</b> |
| <b>2.2 Experimental setup of Leeds II hip simulator .....</b>                             | <b>60</b> |
| <b>2.3 Design of numerical study .....</b>  | <b>62</b> |
| <b>2.4 Methods of Numerical Analysis.....</b>   | <b>64</b> |
| 2.4.1 Dynamic solving processors.....   | 64        |
| 2.4.2 Contact algorithms .....  | 66        |
| <b>2.5 Development of the Numerical Model.....</b>  | <b>70</b> |
| 2.5.1 Materials.....  | 70        |
| 2.5.2 Study I: mesh sensitivity analysis.....   | 74        |
| 2.5.3 Study II: Contact methods .....   | 76        |
| 2.5.4 Study III: Loading.....   | 76        |
| <b>2.6 Results of concentric loading condition .....</b>                                  | <b>78</b> |
| 2.6.1 Study I: Mesh sensitivity analysis.....   | 78        |
| 2.6.2 Study II: Contact methods .....   | 86        |

|            |  |            |
|------------|--|------------|
| 2.6.3      | Study III: Loading condition .....                 | 89         |
| <b>2.7</b> | <b>Discussion</b> .....                            | <b>93</b>  |
| <b>2.8</b> | <b>Key points</b> .....                            | <b>95</b>  |
| Chapter 3  | Model development under adverse conditions.....    | 97         |
| <b>3.1</b> | <b>Introduction</b> .....                          | <b>97</b>  |
| <b>3.2</b> | <b>Technical Background</b> .....                  | <b>100</b> |
| 3.2.1      | Stability and time incrementation .....            | 101        |
| 3.2.2      | An oscillatory system .....                        | 104        |
| <b>3.3</b> | <b>Materials and methods</b> .....                 | <b>107</b> |
| 3.3.1      | Geometry and alignment.....                        | 107        |
| 3.3.2      | Assembly.....                                      | 107        |
| 3.3.3      | Material properties .....                          | 108        |
| 3.3.4      | Finite element mesh.....                           | 110        |
| 3.3.5      | Methods.....                                       | 111        |
| 3.3.6      | Spring representation .....                        | 113        |
| 3.3.7      | Boundary conditions, loads and analysis steps..... | 114        |
| 3.3.8      | <b>Inclusion of damping</b> .....                  | <b>117</b> |
| 3.3.9      | Mass effect.....                                   | 118        |
| 3.3.10     | Model input sensitivity .....                      | 119        |
| 3.3.11     | Model output measures.....                         | 120        |
| <b>3.4</b> | <b>Results</b> .....                               | <b>121</b> |
| 3.4.1      | Spring representation .....                        | 121        |
| 3.4.2      | Inclusion of damping.....                          | 123        |

|            |   |            |
|------------|---|------------|
| 3.4.3      | Mass effect.....  | 128        |
| 3.4.4      | Model input sensitivity .....                             | 130        |
| <b>3.5</b> | <b>Discussion.....</b>                                    | <b>132</b> |
| <b>3.6</b> | <b>Key findings.....</b>                                  | <b>136</b> |
| Chapter 4  | Parametric sweep, validation and sensitivity testing..... | 137        |
| <b>4.1</b> | <b>Introduction.....</b>                                  | <b>137</b> |
| <b>4.2</b> | <b>Methodology .....</b>                                  | <b>139</b> |
| 4.2.1      | Input parameters .....                                    | 141        |
| 4.2.2      | Outputs and experimental comparison.....                  | 145        |
| 4.2.3      | Friction sensitivity test.....                            | 147        |
| <b>4.3</b> | <b>Results.....</b>                                       | <b>148</b> |
| 4.3.1      | <i>In silico</i> parameter sweep.....                     | 148        |
| 4.3.2      | Comparison of <i>in vitro</i> and <i>in silico</i> .....  | 152        |
| 4.3.3      | Friction sensitivity test.....                            | 156        |
| 4.3.4      | Maximum load at the rim.....                              | 157        |
| <b>4.4</b> | <b>Discussion.....</b>                                    | <b>165</b> |
| 4.4.1      | Computational results.....                                | 166        |
| 4.4.2      | Validation .....  | 168        |
| 4.4.3      | Friction sensitivity analysis .....                       | 173        |
| 4.4.4      | Summary of the key findings.....                          | 173        |
| Chapter 5  | Parametric sweep contact mechanics analyses .....         | 175        |
| <b>5.1</b> | <b>Introduction.....</b>                                  | <b>175</b> |
| <b>5.2</b> | <b>Methodology .....</b>                                  | <b>176</b> |

|   |            |
|---|------------|
| <b>5.3 Results</b> .....  | <b>181</b> |
| 5.3.1 Input parameters study.....                                   | 181        |
| 5.3.2 Material failure risk.....                                    | 188        |
| 5.3.3 Separation study.....   | 200        |
| 5.3.4 Friction .....  | 203        |
| <b>5.4 Discussion</b> .....   | <b>209</b> |
| 5.4.1 Contact behaviour due to the input parameters.....            | 209        |
| 5.4.2 Discussion of stress behaviour throughout gait cycle.....     | 210        |
| 5.4.3 Failure Prediction .....                                      | 213        |
| 5.4.4 The correlation between separation and contact mechanics..... | 215        |
| 5.4.5 Friction effect .....   | 215        |
| 5.4.6 Model improvements .....                                      | 216        |
| <b>5.5 Key points</b> .....   | <b>217</b> |
| Chapter 6 Final discussion and future work .....                    | 219        |
| <b>6.1 Model development</b> .....                                  | <b>219</b> |
| <b>6.2 Discussion of findings</b> .....                             | <b>221</b> |
| <b>6.3 Limitations</b> .....  | <b>223</b> |
| <b>6.4 Possible applications and future work</b> .....              | <b>224</b> |
| <b>6.5 Conclusion</b> .....   | <b>227</b> |
| Chapter 7 Bibliography.....   | 229        |
| Chapter 8 Appendix .....  | 249        |
| <b>8.1 Experimental studies</b> .....                               | <b>249</b> |
| 8.1.1 Dynamic separation .....                                      | 250        |

|            |   |            |
|------------|---|------------|
| 8.1.2      | Load at the rim.....                            | 251        |
| <b>8.2</b> | <b>Python script for output processing.....</b> | <b>252</b> |

## Table of Figures

|   |    |
|---|----|
| Figure 1.1 Hip joint: the bones associated with hip joint and the surrounding ligaments and cartilages (Tank and Gest, 2008).....   | 3  |
| Figure 1.2 Rotational motions of the hip (Buechel and Pappas, 2012) .....   | 3  |
| Figure 1.3 Gait cycle (Iosa <i>et al.</i> , 2013) .....   | 4  |
| Figure 1.4 The McKee-Farrar Total Hip Replacement (Buechel and Pappas, 2012).....   | 6  |
| Figure 1.5 Hard-on-soft THR bearings, The Charnley Total Hip Replacement (Buechel and Pappas, 2012)   | 8  |
| Figure 1.6 Ceramic-on-ceramic THR implanted in the body .....   | 10 |
| Figure 1.7 Kinematic analysis of hip joint during a gait cycle, FE denotes flexion-extension; AA, adduction-abduction; IER, internal-external rotation (Johnston and Smidt, 1969) .....   | 11 |
| Figure 1.8 Kinetic analysis of gait cycle (Bergmann <i>et al.</i> , 2001) .....   | 12 |
| Figure 1.9 Schematic of separation and sliding during the swing phase .....   | 15 |
| Figure 1.10 The wear stripes on the ball in in vitro and retrieval components (Manaka <i>et al.</i> , 2004) .....   | 16 |
| Figure 1.11 Schematic of translational and rotational variation. Concentric bearings (A), a mismatch between the centres of the head and the cup (B), the schematic of standard (C), steep and low inclination angle (D).....                           | 19 |
| Figure 1.12: 2D model of THR with A) 1 mm PMMA and B) with metal backing (Carter, Vasu and Harris, 1982).....   | 36 |
| Figure 1.13 The axisymmetric models of THR A) The axisymmetric finite element model of Jin <i>et al</i> (1999) B) Axisymmetric THR model of Mak and Jin (Mak and Jin, 2002) C) FE model of metal backed plastic cup in Bartel <i>et al</i> (1985) ..... | 37 |
| Figure 1.14 Clinically tested IP and Labinus (Korhonen <i>et al.</i> , 2005) .....  | 39 |
| Figure 1.15 Contact area of the Labinus and IP cup under loading cycle in a) experimentally tested and b) numerical models (Korhonen <i>et al.</i> , 2005) .....  | 40 |
| Figure 1.16 Maximum stress of FE models (Plank <i>et al.</i> , 2005).....   | 41 |
| Figure 1.17 THR modelled by Mak <i>et al</i> with 45° cup inclination angle (Mak and Jin, 2002) .....   | 42 |
| Figure 1.18 Contact pressure analysis of the CoC THR model under 0-500 µm lateral microseparation and 65° to 90° condition (Sariali <i>et al.</i> , 2012) .....   | 43 |
| Figure 1.19 Contact mechanics analysis of MoP THR in different penetration rate (Hua <i>et al.</i> , 2012) .....  | 44 |

|   |    |
|---|----|
| Figure 1.20 Three different geometry of cup rim in Mak et al study (Mak <i>et al.</i> , 2011).....  | 45 |
| Figure 1.21 Contact pressure contour comparison during the gait cycle for both deformable (left) and rigid<br>body (with softened contact) (right) analyses (Halloran, Petrella and Rullkoetter, 2005)..... | 50 |
| Figure 1.22 The pendulum model used in Liu et al study (Liu <i>et al.</i> , 2010).....  | 52 |
| Figure 1.23 a) CAD and b) FE models of an artificial hip joint in Gao et al study (Gao <i>et al.</i> , 2015) .....  | 53 |
| Figure 1.24 The flowchart and order of the chapters with a brief description of the chapters focus .....  | 58 |
| Figure 2.1 Schematic of the experimental set up of Leeds II hip simulator with rotation and loading<br>locations indications.....   | 61 |
| Figure 2.2 Example of Paul cycle loading in Leeds II hip simulator (Paul, 1976; Al-Hajjar et al., 2013) .....   | 62 |
| Figure 2.3 The difference in explicit and implicit approaches of output calculation .....   | 65 |
| Figure 2.4 Master-slave surfaces contact constraint in ABAQUS that represent the penetration and gap<br>between the master and slave surface .....  | 68 |
| Figure 2.5 Assembly of the simplified model. The crosses locate the boundary conditions on the head and<br>the cup holder. ....   | 71 |
| Figure 2.6 Loading condition of the study I versus time .....   | 74 |
| Figure 2.7 The implementation of the variable versus time using smooth step amplitude in ABAQUS<br>(ABAQUS 6.12 Documentation, 2012).....   | 75 |
| Figure 2.8 Paul cycle loading. The graph represents the twin peak load that is applied to the Leeds II hip<br>simulator axially.....  | 78 |
| Figure 2.9 Contact area on the head, for different mesh resolution combinations. Each plot represents<br>each meshing ratio condition that was carried out.....   | 79 |
| Figure 2.10 Contact area on the cup inner surface for different mesh resolution combinations under<br>standard condition .....  | 80 |
| Figure 2.11 Comparison of contact area generated on the contact surfaces using 0.75:0.75 and 0.75:1.5<br>cases under standard condition. ....   | 81 |
| Figure 2.12 Contact area values versus number of elements, across all mesh cases with both static and<br>dynamic loading under standard condition.....  | 81 |
| Figure 2.13 Position of the selected nodes which their nodal pressure was recorded to compare the<br>contact pressure distribution of different meshing ratios .....  | 85 |

|   |     |
|---|-----|
| Figure 2.14 The nodal Pressure distribution along the line aligned with z axis for meshing ratio of 0.75:0.75 and 1.5:0.75 under standard condition.....  | 86  |
| Figure 2.15 Predicted contact area on the head and cup inner surface using different contact constraint enforcement methods namely penalty and kinematic contact constraint enforcement under standard condition .....            | 87  |
| Figure 2.16 Contact pressure distribution on the cup surface using A) Kinematic and B) Penalty contact constraint method under standard condition .....   | 88  |
| Figure 2.17 Contact pressure distribution on the head surface using A) Kinematic and B) Penalty contact constraint method under standard condition .....  | 88  |
| Figure 2.18 Contact area using preloading of the model on the head and the cup inner surface using tabular and smooth step loading amplitude under standard condition .....   | 89  |
| Figure 2.19 Contact area during preloading step on the head and the cup inner surface based on tabular and smooth step loading amplitude under standard condition.....  | 90  |
| Figure 2.20 Reaction force in preloading step using different load amplitude under standard condition   | 91  |
| Figure 2.21 Input loading and predicted reaction force (RF) of the analysis using Paul cycle loading under standard condition .....   | 92  |
| Figure 3.1 The effect of meshing and material properties on the stability limit of the computational analysis .....   | 102 |
| Figure 3.2 Simplified cup holder, Pinnacle® 100 series shell, outer diameter 56mm, Pinnacle® neutral polyethylene liner, bearing diameter 36mm, BioloX Delta® femoral head, bearing diameter 36mm (DePuy Synthes, Leeds, UK)..... | 107 |
| Figure 3.3 The assembly in the computational model (A) and schematic of the experimental set up (B) .....   | 108 |
| Figure 3.4 Nonlinear Stress-strain behaviour for UHMWPE (1050 GUR).....   | 109 |
| Figure 3.5 Meshing of each component A) Metal shell, B) Polyethylene cup, c) cup unit and D) head ..  | 111 |
| Figure 3.6 Flowchart of the chapter 3 studies.....  | 112 |
| Figure 3.7 Illustration of precontact step: vertical movement of the head.....  | 115 |
| Figure 3.8 Spring compression step illustration: Compression of the spring medial/laterally .....   | 115 |
| Figure 3.9 Spring stabilisation step illustration: Cup moves away from the head and the spring extends .....  | 116 |

|   |     |
|---|-----|
| Figure 3.10 Medial/lateral displacement of the cup using a truss element as the spring with 3mm translational mismatch level and 300N swing phase load .....  | 121 |
| Figure 3.11 Medial-lateral behaviour of the model with ABAQUS spring element as the spring with 3mm translational mismatch level and 300N swing phase load .....  | 123 |
| Figure 3.12 The effect of damping on the M/L displacement of the model with specific dashpot coefficient, 3mm translational mismatch level and 300N swing phase load. Each plot represents the value of dashpot coefficient (Ns/mm). .....    | 125 |
| Figure 3.13 contact area versus time for the model with 3mm mismatch level, 300N swing phase load, 45° inclination angle and 70 Ns/mm .....   | 127 |
| Figure 3.14 M/L displacement behaviour for various dashpot coefficient with true mass values, 3mm translational mismatch level and 300N swing phase load .....  | 128 |
| Figure 3.15 Critically damped model of artificial and true mass on M/L displacement behaviour with sampling frequency of 20 with 300N swing phase load and 3mm translational mismatch level ...   | 129 |
| Figure 3.16 Contact area comparison using true and artificial mass values for the analyses with 3mm translational mismatch level and 300N swing phase load .....  | 130 |
| Figure 3.17 The M/L displacement of the cases that represent the analyses with 1mm and 4mm translational mismatch level, 45° inclination angle and 300N swing phase load .....  | 131 |
| Figure 3.18 Contact area derived from analyses versus time with 300N swing phase load, 45° inclination angle and translational mismatch variation of 1mm and 4mm .....  | 131 |
| Figure 4.1 The assembly of the components in the computational model for the parametric testing purposes .....  | 139 |
| Figure 4.2 The difference in assembly of fully concentric (A) where the head and the cup have the same centre and THR bearing with translational mismatch level (B) where there is a translational distance between the bearing centres ..... | 142 |
| Figure 4.3 Rotational mismatch configuration. A) 45° inclination angle clinically B) 65° inclination angle clinically .....   | 143 |
| Figure 4.4 The input gait cycle loading versus time for each swing phase load of 70N, 100N, 200N and 300N .....   | 143 |

|   |     |
|---|-----|
| Figure 4.5 The schematic of dynamic separation measurement <i>in vitro</i> . A) The point where the separation is measured from (concentric cup and head and no spring compression), B) Minimum dynamic separation and C) Maximum dynamic separation (edge loading).....  | 145 |
| Figure 4.6 The intersection of the load and the separation for maximum load at the rim calculations. The corresponding load to the dynamic separation of 0.5mm is recorded as the maximum load at the rim .....   | 146 |
| Figure 4.7 Maximum dynamic separation versus the variation of translational mismatch levels (1mm to 4mm) and swing phase loads (70N to 300N) and 45° inclination angle.....   | 149 |
| Figure 4.8 Maximum dynamic separation versus the variation of translational mismatch levels (1mm to 4mm) and swing phase loads (70N to 300N) and 65° inclination angle.....   | 150 |
| Figure 4.9 The effect of standard and steep cup inclination and translational mismatch of 1mm to 4mm on the maximum computational dynamic separation with 70N swing phase load .....  | 151 |
| Figure 4.10 The effect of cup inclination and translational mismatch on the maximum computational dynamic separation with 300N swing phase load .....   | 152 |
| Figure 4.11 Comparison of computational dynamic separation and experimental dynamic separation. The legend represents the swing phase load and the cup inclination angle. Standard is referred to 45° inclination angle and steep is referred to 65° inclination angle .....  | 153 |
| Figure 4.12 The effect of translational mismatch and swing phase load on the maximum dynamic separation of the THR <i>in vitro</i> and in silica under 45° inclination angle. The letters E and C in the legend section represents experimental and computational data, respectively (in vitro testing was carried out by Murat Ali, Appendix) .....  | 155 |
| Figure 4.13 The effect of translational mismatch and swing phase load on the maximum dynamic separation of the THR <i>in vitro</i> and in silica under 65° inclination angle. The letters E and C in the legend section represents experimental and computational data, respectively (in vitro testing was carried out by Murat Ali, Appendix) .....  | 156 |
| Figure 4.14 Comparison of computational and experimental maximum dynamic separation under steep inclination angle (friction coefficient of 0.1). Experimental bars represents the dynamic separation <i>in vitro</i> , Computational bars represent the maximum dynamic separation with friction coefficient of 0.1 between the contact surfaces and computational frictionless bars represents the maximum dynamic separation with no friction between the contact surfaces..... | 157 |

|  |     |
|--|-----|
| Figure 4.15 Computational maximum force on the rim with different translational mismatch level and swing phase loads under 45° inclination angle .....   | 158 |
| Figure 4.16 Computational maximum force on the rim versus translational mismatch level of 1mm to 4mm and swing phase loads under 65° inclination angle .....   | 159 |
| Figure 4.17 Comparison of the load the rim when the head is moving to concentric condition and when the head is moving to the edge under standard cup inclination angle. At the legend of this graph, the word 'in' represents the maximum load at the rim when the head was relocating into the cup and the word 'out' represents the maximum load at the rim when the head was separating out of the concentric point..... | 160 |
| Figure 4.18 Comparison of the load the rim when the head is moving to concentric condition and when the head is moving to the edge under steep cup inclination angle. At the legend of this graph, the word 'in' represents the maximum load at the rim when the head was relocating into the cup and the word 'out' represents the maximum load at the rim when the head was separating out of the concentric point.....    | 161 |
| Figure 4.19 Experimental and computational maximum force on the rim under 70N swing phase load, standard (45°) and steep (65°) cup inclination angle, and 3mm and 4mm translational mismatch level (Appendix) .....  | 162 |
| Figure 4.20 Experimental and computational maximum force on the rim under 100N swing phase load, standard (45°) and steep (65°) cup inclination angle, and 3mm and 4mm translational mismatch level (Appendix) .....   | 163 |
| Figure 4.21 Experimental and computational maximum force on the rim under 200N swing phase load, standard (45°) and steep (65°) cup inclination angle, and 3mm and 4mm translational mismatch level (Appendix) .....   | 163 |
| Figure 4.22 The cup positioning with respect to the resultant force. A) Resultant force caused from high swing phase load and low spring force B) Edge contact due to low swing phase load and high spring force .....   | 166 |
| Figure 4.23 Horizontal travelling distance by the cup with different cup inclination angle. A) Steep cup inclination angle and B) standard cup inclination angle.....  | 167 |
| Figure 5.1 The studies and outputs measurements of the chapter 5 .....   | 177 |

|   |     |
|---|-----|
| Figure 5.2 The nodes on the symmetry line of the contact pressure with respect to the angle from the centre of the line to the lateral edge.....  | 178 |
| Figure 5.3 Nodal contact pressure along the line of the symmetry recorded at the end of the swing phase load. Each graph represent the nodal pressure for each swing phase load under standard and steep cup inclination angle. The description of the plots, which is the same for all graphs, represents the cup inclination angle and the translational mismatch level. .... | 183 |
| Figure 5.4 Contact pressure contours and the maximum contact pressure on the liner inner surface throughout the gait cycle under 45° inclination angle, 70N swing phase load, translational mismatch level of 0 and 4mm .....   | 185 |
| Figure 5.5 Contact pressure contours and the maximum contact pressure on the liner inner surface throughout the gait cycle under 65° inclination angle, 70N swing phase load and translational mismatch level of 0 and 4mm. ....  | 186 |
| Figure 5.6 The contact area at the end of the swing phase load for various translational mismatch level and swing phase loads. The contact area of the analyses under standard and steep cup inclination angle are plotted as 'standard' and 'steep', respectively .....  | 188 |
| Figure 5.7 Stress distribution of the analysis with 0 mismatch level under 45° inclination angle (solid lines) and 65° inclination angle (dotted lines) with swing phase load of 70N to 300N .....  | 189 |
| Figure 5.8 The maximum von Mises stress throughout the gait cycle for all of the conditions. The dashed line plots represent steep cup inclination angle and the solid line plots represent standard cup inclination angle at different mismatch level .....  | 191 |
| Figure 5.9 The cross sectional contour of von Mises stress at the end of swing phase load under standard cup inclination angle for the analyses with swing phase load of 70N to 300N and translational mismatch level of 0mm to 4mm.....  | 193 |
| Figure 5.10 The cross sectional contour of von Mises stress at the end of swing phase load under steep cup inclination angle for the analyses with swing phase load of 70N to 300N and translational mismatch level of 0mm to 4mm.....  | 194 |
| Figure 5.11 Comparison of the maximum compressive stress and von Mises stress under standard cup inclination angle translational mismatch levels of 0mm to 4mm .....  | 195 |
| Figure 5.12 Comparison of maximum compressive stress and von Mises stress under steep cup inclination angle and translational mismatch levels of 0mm to 4mm .....   | 196 |

|  |     |
|--|-----|
| Figure 5.13 Maximum plastic strain in the cases with various translational mismatch level and swing phase loads under 45° inclination angle.....   | 197 |
| Figure 5.14 Maximum plastic strain in the cases with 65° inclination angle and all of the swing phase loads and translational mismatch levels.....   | 198 |
| Figure 5.15 Contact area and von Mises stress versus time in the analyses with 4mm translational mismatch level, various swing phase loads and standard cup inclination angle.....   | 199 |
| Figure 5.16 Contact area and von Mises stress versus time in the analyses with 4mm translational mismatch level, various swing phase loads and steep cup inclination angle.....  | 200 |
| Figure 5.17 Contact area at the maximum separation during the gait cycle under standard and steep cup inclination angle with all translational mismatch levels and swing phase loads.....  | 201 |
| Figure 5.18 The comparison of separation with von Mises stress, compressive stress and contact pressure. The analyses under standard cup inclination angle are presented as Plot A and the analyses under steep cup inclination angle is presented as Plot B ..... | 202 |
| Figure 5.19 The comparison of separation with plastic strain for both standard and steep cup inclination angles with all translational mismatch levels and swing phase loads.....  | 203 |
| Figure 5.20 Effect of friction on the contact pressure along symmetrical line under standard cup inclination angle, 300N and 70N swing phase load and 4mm translational mismatch level.....  | 204 |
| Figure 5.21 Effect of friction on contact pressure along the symmetrical line under steep cup inclination angle, 300N and 70N swing phase load and 4mm translational mismatch level.....   | 205 |
| Figure 5.22 Effect of friction on the analyses under standard cup inclination angle with the lowest (70N) and highest (300N) swing phase load. The figure represents the effect of friction on the von mises stress during a gait cycle.....                       | 206 |
| Figure 5.23 Effect of friction on the analyses under steep cup inclination angle with the lowest (70N) and highest (300N) swing phase load. The figure represents the effect of friction on the von mises stress during a gait cycle.....                          | 206 |
| Figure 5.24 The effect of friction on the compressive stress of the analyses. The friction coefficient of 0.1 was applied on the lowest (70N) and highest (300N) swing phase load and on the standard and steep cup inclination angle.....                         | 207 |

Figure 5.25 The comparison of the contact area in the frictional and frictionless analyses. The friction coefficient of 0.1 was applied on the lowest (70N) and highest (300N) swing phase load and on the standard and steep cup inclination angle..... 208

Figure 5.26 The effect of friction on the plastic strain on the lowest (70N) and the highest (300N) swing phase load with 4mm translational mismatch level and on the standard and steep cup inclination angle. .... 208

Figure 5.27 The correlation between the input parameters and edge loading, adverse stress behaviour and plastic strain occurrence. The green, yellow and orange cells represent the edge loading, adverse stress and plastic strain occurrence for various swing phase loads, respectively ..... 210

Figure 5.28 The worn and deformed area of the UHMWPE cup under 0mm, 2mm and 4mm translational mismatch level, standard and steep cup inclination angle and 70N swing phase load. The worn area indicates the worn and deformation on the inner surface of the liner (Appendix) ..... 214

Figure 8.1 Experimental maximum separation versus swing phase load and translational mismatch level under 45° inclination angle. .... 250

Figure 8.2 Experimental maximum separation versus swing phase load and translational mismatch level under 65° inclination angle. .... 250

Figure 8.3 The load at the rim with various translational mismatch level and swing phase loads under 45° cup inclination angle..... 251

Figure 8.4 The load at the rim with various translational mismatch level and swing phase loads under 65° cup inclination angle..... 251

Figure 8.5 The location of the in vitro wear and deformation under concentric conditions, 2mm and 4mm translational mismatch level, standard and steep cup inclination angle and 70N swing phase load carried out by Murat Ali (partially shown in Ali *et al*, 2016)..... 252

## Table of Tables

TABLE 1.1 OVERVIEW OF AVAILABLE HIP SIMULATORS THE POSITIVE VALUE IN THE F/E, I/E ROTATION AND A/A REPRESENTS FLEXION, INTERNAL ROTATION AND ABDUCTION AND THE NEGATIVE VALUE REPRESENTS EXTENSION, EXTERNAL ROTATION AND ADDUCTION, RESPECTIVELY (MODIFIED FROM AFFATATTO, LEARDINI AND ZAVALLONI, 2006) ..... 23

|  |     |
|--|-----|
| TABLE 1.2 WEAR RATE OF DIFFERENT BEARING MATERIALS IN STANDARD AND MICROSEPARATION<br>CONDITION .....  | 25  |
| TABLE 1.3 FRICTION FACTOR OF TYPICAL BEARINGS FOR ARTIFICIAL HIP IMPLANTS IN THE PRESENCE OF<br>BOVINE SERUM SIMULATOR (JIN <i>ET AL.</i> , 2006) .....  | 28  |
| TABLE 1.4 CONTACT STRESS OF DIFFERENT BEARING COUPLES.....   | 32  |
| TABLE 1.5 PREVIOUS COMPUTATIONAL STUDIES ON CONTACT MECHANICS OF THRS .....  | 35  |
| TABLE 1.6 PREVIOUS STUDIES ON COUPLING OF KINEMATIC AND FE METHODS.....  | 47  |
| TABLE 1.7 SUMMARY OF THE ADVANTAGES AND LIMITATIONS OF DIFFERENT FE MODELLING TYPES ...  | 54  |
| TABLE 2.1 COMPARISON OF ADVANTAGES AND DISADVANTAGES OF IMPLICIT AND EXPLICIT APPROACHES<br>IN ABAQUS.....   | 66  |
| TABLE 2.2 GEOMETRIC AND MATERIAL PROPERTIES OF SIMPLIFIED COMPUTATIONAL MODEL<br>COMPONENTS .....  | 72  |
| TABLE 2.3 FULL LIST OF MODELLING CASES OF STAGE 1 OF DEVELOPMENT NAMELY, MESHING RATIO<br>BETWEEN THE HEAD AND THE CUP INNER SURFACE, LOADING AMPLITUDE AND CONTACT<br>CONSTRAINT ALGORITHM.....   | 73  |
| TABLE 2.4 THE LOADING CONDITIONS OF THE PRELOADING STUDY AT THE SPECIFIC TIME POINTS (STUDY<br>III).....   | 77  |
| TABLE 2.5 PRESSURE DISTRIBUTIONS FOR DIFFERENT MESH CONFIGURATIONS UNDER STANDARD<br>CONDITION. THE ANALYSES THAT WERE CARRIED OUT WITH THE SAME ELEMENT SIZE ON THE<br>BEARING SURFACES ARE HIGHLIGHTED. ....   | 84  |
| TABLE 3.1 THE SUMMARY OF THE TRUSS AND SPRING ELEMENT FEATURES TO USE AS THE EXPERIMENTAL<br>SPRING.....   | 103 |
| TABLE 3.2 SUMMARY OF THE DAMPING METHODS AVAILABLE IN ABAQUS AND THE ADVANTAGES AND<br>DISADVANTAGES OF EACH METHOD .....  | 106 |
| TABLE 3.3 MATERIAL AND GEOMETRIC PROPERTIES OF THE COMPONENTS.....   | 109 |
| TABLE 3.4 THE DETAILS OF THE COMPONENTS ELEMENTS .....   | 110 |
| TABLE 3.5 THE VARIATION AND DETAILS OF THE STUDIES THAT WERE CARRIED OUT IN CHAPTER 3 BASED<br>ON THE MAIN VARIABLES NAMELY, SPRING REPRESENTATION METHOD, MISMATCH LEVEL,<br>STABILISATION TIME, DASHPOT COEFFICIENT AND COMPONENT MASS CONDITION ..... | 113 |
| TABLE 3.6 TRUSS AND SPRING ELEMENT PROPERTIES TO REPRESENT THE EXPERIMENTAL SPRING .....   | 114 |

|  |     |
|--|-----|
| TABLE 3.7 STEPS, LOADING CONDITIONS AND BOUNDARY CONDITIONS OF THE ANALYSES .....  | 117 |
| TABLE 3.8 DASHPOT COEFFICIENT ASSIGNED FOR EACH CASE WITH SPRING ELEMENT AS THE SPRING   | 118 |
| TABLE 3.9 TRUE MASS VALUES OF THE COMPONENTS AND THE MATERIAL USED FOR EACH COMPONENT<br>.....   | 119 |
| TABLE 3.10 DESCRIPTION OF THE VARIABLES NAMELY MISMATCH LEVEL, CUP INCLINATION ANGLE,<br>SWING PHASE LOAD, STABILISATION LOAD AND DASHPOT COEFFICIENT ON BOTH CASES .....                          | 119 |
| TABLE 4.1 MATERIAL PROPERTIES OF THE COMPONENTS THE COMPUTATIONAL ANALYSES IN THE<br>PARAMETRIC SWEEP OF CHAPTER 4 .....   | 139 |
| TABLE 4.2 THE MESHING CONFIGURATIONS AND THE ELEMENT SIZE OF THE COMPONENTS IN THE<br>COMPUTATIONAL ANALYSES IN THE PARAMETRIC SWEEP OF CHAPTER 4 .....  | 140 |
| TABLE 4.3 THE BOUNDARY AND LOADING CONDITIONS ON EACH STEP OF THE COMPUTATIONAL<br>ANALYSES IN THE PARAMETRIC SWEEP OF CHAPTER 4 .....   | 140 |
| TABLE 4.4 THE FULL SET OF TEST CASES IN THE PARAMETER SWEEP BASED ON VARIOUS TRANSLATIONAL<br>MISMATCH LEVEL, SWING PHASE LOAD AND CUP INCLINATION ANGLE .....                                     | 141 |
| TABLE 4.5 DASHPOT COEFFICIENT OF ANALYSIS WITH 45° INCLINATION ANGLE, TRANSLATIONAL<br>MISMATCH LEVEL OF 1MM TO 4MM AND SWING PHASE LOAD OF 70N TO 300N .....                                      | 144 |
| TABLE 4.6 DASHPOT COEFFICIENT OF ANALYSIS WITH 65° INCLINATION ANGLE, TRANSLATIONAL<br>MISMATCH LEVEL OF 1MM TO 4MM AND SWING PHASE LOAD OF 70N TO 300N .....                                      | 144 |
| TABLE 5.1 THE COMPARISON OF CONTACT AREA IN THE ALL ANALYSES THAT WERE CARRIED OUT AT THE<br>PEAK (3KN) AND MINIMUM LOAD (SWING PHASE LOAD) UNDER STANDARD AND STEEP CUP<br>INCLINATION ANGLE..... | 187 |

# Chapter 1 Introduction and Literature review

## 1.1 Introduction

Total hip replacement (THR) is considered to be the most successful treatment for hip diseases such as osteoarthritis. Over 101,000 THRs were implanted in England and Wales in 2015 (*National Joint Registry, 2016*). Artificial hip joints have developed significantly over time and their developments were mostly due to the initial inappropriate design and/or material used in the prosthesis (Buechel and Pappas, 2012). The increasing demand of younger patients for artificial hip joints has resulted in the need for increased longevity and functionality of THRs, especially for hard-on-soft THR bearings due to their high popularity (*National Joint Registry, 2016*). One of the reasons for the failure of THR is the wear of the bearings. There have been a great number of studies of the performance of artificial hip joint *in vitro* (e.g. Nevelos *et al.*, 2000; Williams *et al.*, 2008; Al-Hajjar *et al.*, 2010).

*In vitro* testing has been accomplished by the development of computational models to predict the performance of implanted hip joint (e.g. Gao *et al.* 2015; Hua *et al.* 2012; Liu *et al.* 2013; Mak and Jin 2002). Such studies have predicted the wear of the bearings under idealised implantation conditions (Al-Hajjar *et al.*, 2010; Gao *et al.*, 2015), and also under adverse conditions when the wear of the THR is affected significantly (Al-Hajjar *et al.*, 2010; Sariali *et al.*, 2012; Ali *et al.*, 2016). The conventional method of testing the THR has been under idealised conditions and it is only recently that adverse conditions have been introduced (Williams *et al.*, 2007; Al-Hajjar *et al.*, 2010). In this chapter, previous studies on the effects of factors such as surgical procedure, biotribological parameters, and implant designs are reviewed. This chapter is organised into three main sections:

- THR design and performance: this section includes the performance of natural and artificial hip joints. Also, the factors that affect the performance of the hip are described.
- Tribological aspects: this section covers the effects of biotribological factors such as wear, friction, lubrication, and contact mechanics of the bearings on the performance of artificial hip joints under different conditions.
- Computational aspects: this section covers previous studies of the contact mechanics and dynamic analyses of artificial hip joints using computational modelling.

## **1.2 THR design and performance**

The hip joint (Figure 1.1) is a ball and socket joint which is surrounded by articular capsule containing synovial fluid. The synovial fluid allows the presence of synovial cavity between two articulating bones of the hip (femur and acetabulum) which allows the free movement of the joint. The articulating bone surfaces are covered by a layer of articular cartilage (hyaline cartilage) to produce a smooth and slippery surface, reducing friction, and aiding shock absorption during articulating bones movement (Tortora and Derrickson, 2009).

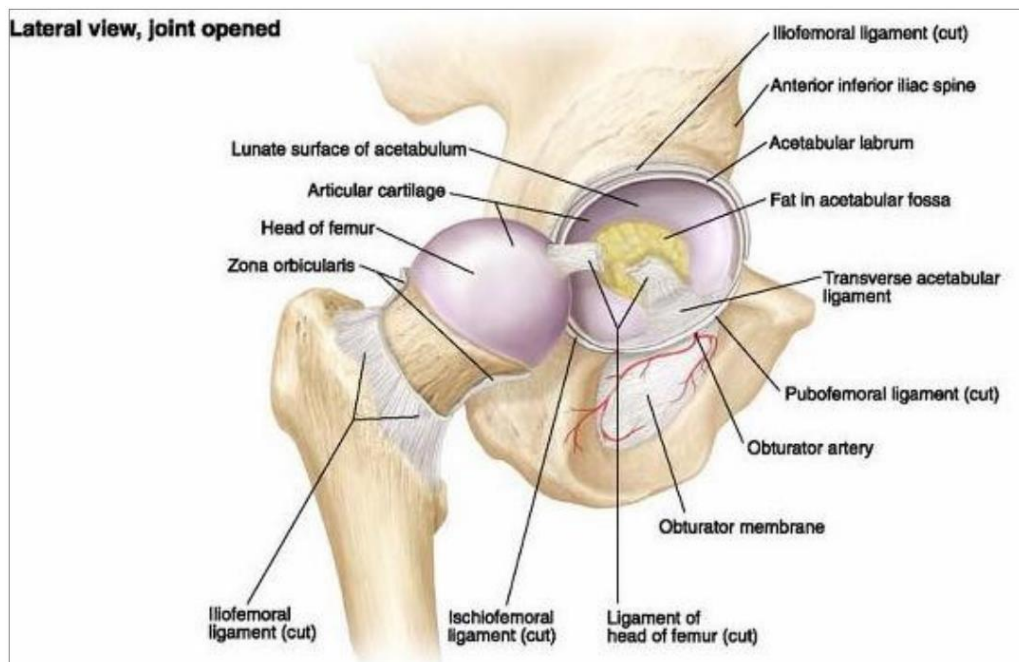


**Figure 1.1 Hip joint: the bones associated with hip joint and the surrounding ligaments and cartilages (Tank and Gest, 2008)**

The head of the femur and acetabulum are attached to each other by iliofemoral, pubofemoral, and ischiofemoral ligaments and they are surrounded by rectus femoris muscles for better stability (Tortora and Derrickson, 2009). The hip joint movements (Figure 1.2) is flexion/extension (F/E), abduction/ adduction (A/A), and medial/lateral rotation of thigh (internal/external rotation) and the degree of the movement depends on the activity.

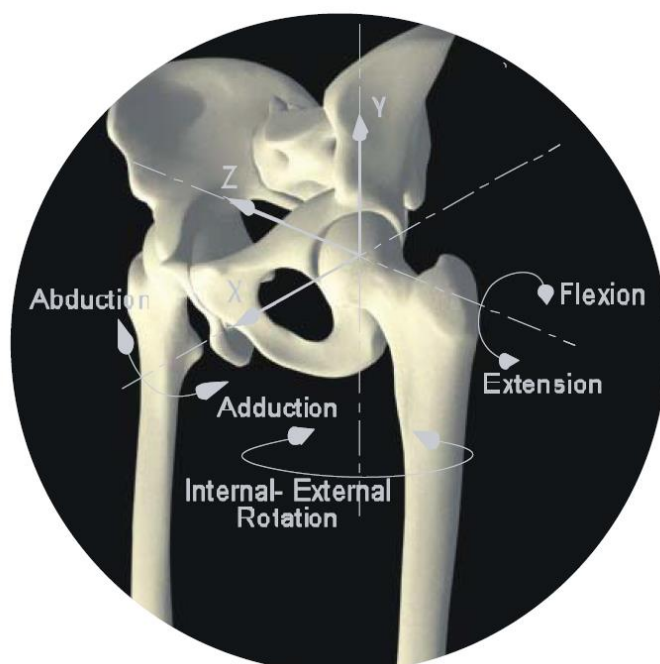


**Figure 1.2 Rotational motions of the hip (Buechel and Pappas, 2012)**

### 1.2.1 Gait Cycle

The gait cycle is a series of hip movements that occur during walking and is based on two major phases: 1) the stance phase and 2) the swing phase (Baker, 2013). As Figure 1.3 shows, the stance phase starts when the (right) leg heel contacts the ground and finishes with toe off of the same leg. There are two main tasks during stance phase to be accomplished: 1) weight acceptance and 2) single limb support. When the right leg heel strikes the ground (initial contact), both limbs are in contact with the ground (double support). Then, when the right leg foot is flattened, the double support finishes and all the weight is shifted to the supporting leg (left leg) until heel strike of the left foot. The swing phase is the period from when the right foot leaves the ground to the next heel contact of the same leg. The stance phase is about 60% of one gait cycle and swing phase 40%.

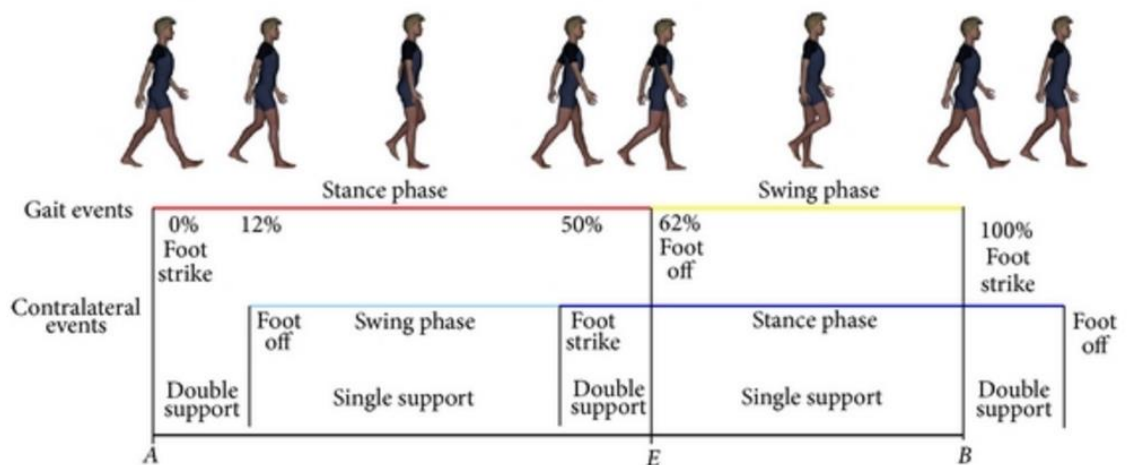


Figure 1.3 Gait cycle (Iosa *et al.*, 2013)

### 1.2.2 Hip disorders

There are several disorders that could have a major effect on the natural hip (Kennon, 2008):

- Osteoarthritis: the layer of cartilage between femur and acetabulum bone is worn away.

- Rheumatoid arthritis: the body's immune system attacks the joint and leads to painful and swollen joints and finally the destruction of the cartilage in the joint.
- Avascular necrosis (Osteonecrosis) : the death of femoral head if the femoral head of the joint does not receive enough blood supply in cases such as trauma and clotting diseases.
- Septic arthritis: infection of the joint is the main cause of septic arthritis.
- Fracture and trauma: Fracture of hip and pelvis usually require surgery to fix and stabilise the bone by utilising different methods such as pinning, plates and screws.
- Tumours: there are two different cancers that can affect hip function: 1) bone tumour which is very rare and 2) metastatic cancer which spreads to the hip from other locations.

### **1.2.3 Total hip replacement (THR)**

Treatment of hip disorders depends on the severity of the injury or damage to the hip. If the medical and physiological treatments on the hip joint are not successful, then hip replacement is recommended to the patient. Hip replacement is a surgical procedure in which the natural hip joint is replaced by a synthetic hip joint with an artificial load bearing material. The predominant diagnosis for hip replacement, accounting for 92% of cases was reported to be osteoarthritis in England and Wales in 2016 (*National Joint Registry, 2016*).

There are two types of hip replacement:

1. Hemi replacement: in this surgery the femoral head of the hip is removed and an artificial one is implanted.
2. Total replacement (total hip arthroplasty): in which both the acetabular cup and the femoral head are replaced. It usually consists of stem and femoral

head that are placed in the femur and a liner and acetabular shell that are placed in the pelvis.

THRs have been developed and gradually have become more reliable over time due to better understanding of the appropriate design, materials, biomechanics, and fixation to the natural bone. For example, THRs have had extensive development based on the material combinations and their biocompatibility with the human body. The earliest attempts at hip joint replacement started in the 1860s with materials such as wood (Carnochan, 1860), ivory (Gluck, 1890), and rubber (Delbert, 1919) which failed due to the inappropriate biocompatibility and durability of materials used. Up to the 1950s, Vitallium was the most successful material used in hip replacements because of its inert property within the human body. However, vitallium was not universally accepted (Coombs *et al.* 1990). Later on, the use of stainless steel and then improving to a cobalt-chromium-molybdenum (CoCrMo) alloy in hip replacement was introduced by McKee (McKee and Watson-Farrar, 1966) as the bearing surfaces by the exact fit of the two components (Figure 1.4).



**Figure 1.4 The McKee-Farrar Total Hip Replacement (Buechel and Pappas, 2012)**

John Charnley initiated a successful development of the hip replacement. He coordinated with engineers to achieve wear resistant components combined with

the application of a biocompatible grouting agent of adequate strength (Buechel and Pappas, 2012). Charnley introduced metallic femoral head with high molecular weight polyethylene acetabular cup. In the early 1970s, the use of ceramics in hip replacements was introduced by Boutin (Boutin, 1972). Ceramic surfaces have better hardness and better wear resistance than metals or polyethylene. However, the main reason for using ceramics in hip replacements was the lower toxicity of the wear products than other bearing materials (Granchi *et al.*, 2003).

### **1.2.4 Types of hip replacements**

During total hip arthroplasty, the femoral head is usually replaced with ceramic or metallic components and the acetabular cup can be replaced with ceramic, metallic, or polymeric components. If one of the bearing surfaces is polymer, the bearing is called 'hard-on-soft' and if both the components are made of metal or ceramic, it is called 'hard-on-hard'.

#### **1.2.4.1 Hard-on-soft bearings**

Hard-on-soft bearings (Figure 1.5) namely Metal-on-polyethylene (MoP) and ceramic-on-polyethylene (CoP) acetabular cups are the most popular bearings in England and Wales (*National Joint Registry*, 2016). Acetabular bearings are made of ultra-high molecular weight polyethylene (UHMWPE) or modified UHMWPE and the femoral head composed of metal alloys, stainless steel, cobalt-chromium, and titanium alloy as well as ceramic materials, aluminium oxide, and zirconia oxide. In ceramic-on-polyethylene bearing surfaces, alumina and zirconia are the main ceramics which are used (Buechel and Pappas, 2012).



**Figure 1.5 Hard-on-soft THR bearings, The Charnley Total Hip Replacement (Buechel and Pappas, 2012)**

Despite all the success of total hip arthroplasty, polyethylene wear is considered to be the primary cause of failure of THR (Bono *et al.*, 1994). The wear characteristics of UHMWPE reduce its longevity, and has been the major issue limiting its use in prostheses. Clinical studies have shown that the wear debris associated with the component results in osteolysis and aseptic loosening over the long term, and consequently a revision surgery may be required (Dattani, 2007; Kurtz and Patel, 2016). Polyethylene bearings are favoured among surgeons due to their tolerance to malalignment and the ability of the material to act as a shock absorber. Due to this popularity, there is a drive to improve the UHMWPE wear performance (García-Rey and García-Cimbrelo, 2010). Therefore, it is a major concern to decrease the wear of the polyethylene bearings for a longer durability.

Various methods have been used to improve polyethylene wear properties by cross linking, heat treatments and sterilisation methods. However, it is a challenging task to decrease the wear rate of polyethylene and retain the similar fatigue resistance simultaneously (Bracco *et al.*, 2017). The initial step in the modification of

polyethylene was a sterilisation step by gamma irradiation. During this irradiation, the molecular cross linking of the polyethylene occurs. Cross linking that has been shown to reduce the occurrence of osteolysis and revision surgery (Ries and Link, 2012; Hanna *et al.*, 2016). However, oxidation of the polyethylene can also take place which can result in degradation and higher brittleness. The modern cross-linking procedure was improved to eliminate the contact of free radicals with air (McKellop *et al.*, 1999; García-Rey and García-Cimbreló, 2010). One of the methods that reduces the free radicals is heat treatment (melting or annealing) after the irradiation that produces highly crosslinked UHMWPE. However, this method affects the fatigue strength and fracture of the malpositioned liner due to the lower crystallinity of the polyethylene (Halley *et al.*, 2004; Oral *et al.*, 2006). Therefore, it is important to use a crosslinking balance that maintain optimum long term physical and wear properties (McKellop *et al.*, 1999).

#### **1.2.4.2 Hard-on-hard bearing**

Hard-on-hard surface bearings consist of ceramic-on-ceramic, metal-on-metal or ceramic-on-metal. Although the first generation of metal on metal THR failed, the long-term survivorship of these bearings has been comparable to Charnley's metal polyethylene coupled bearing design which could make them a suitable choice for young patients. The low steady wear rate of metal-on-metal bearings is the best feature of this type of bearing. However, high metal ion level or high particle concentration of metallic bearings can cause cell death and tissue necrosis (Germain *et al.*, 2003). The higher coefficient of friction of metallic coupled bearings compare to other types is another disadvantage of them (Brockett *et al.*, 2006). Ceramic-on-ceramic bearings (Figure 1.6) represent the lowest friction in articulating surfaces of all, they also have the lowest wear rate under standard walking conditions (Nevelos *et al.*, 2000). Furthermore, the toxicity of ceramic materials has been

reported to be less than metallic bearings (Germain *et al.*, 2003). Recently, a ceramic matrix composite bearing (Biolox Delta) has been introduced with increased toughness and decreased risk of fracture properties (Al-Hajjar *et al.*, 2010).



**Figure 1.6 Ceramic-on-ceramic THR implanted in the body**

Ceramic-on-metal bearings with different hardness values have been utilised to be able to decrease the wear rate and friction of metal-on-metal bearings and to eliminate ceramic insert chipping (Williams *et al.*, 2007). Since there is a size limitation of ceramics bearing due to modular insert of them, ceramic against metal bearing also provided design flexibility to be able to use metal insert acetabular cup with different ceramic femoral head size. It is reported that ceramic-on-metal coupled bearings have less metal ion release than metal-on-metal bearings and same wear rates as ceramic-on-ceramic bearings (Isaac *et al.*, 2009).

### **1.2.5 Gait cycle of THRs**

The range of motion during a gait cycle has been studied previously (Johnston and Smidt, 1969). It was demonstrated that the degree of flexion/extension varies

between  $-25^{\circ}$  and  $15^{\circ}$ , abduction/adduction between  $-3.75^{\circ}$  and  $4.6^{\circ}$  and external, internal rotation between  $-7.5^{\circ}$  and  $6^{\circ}$  (Figure 1.7). However, the motion of a hip joint is patient specific and it differs between patients.

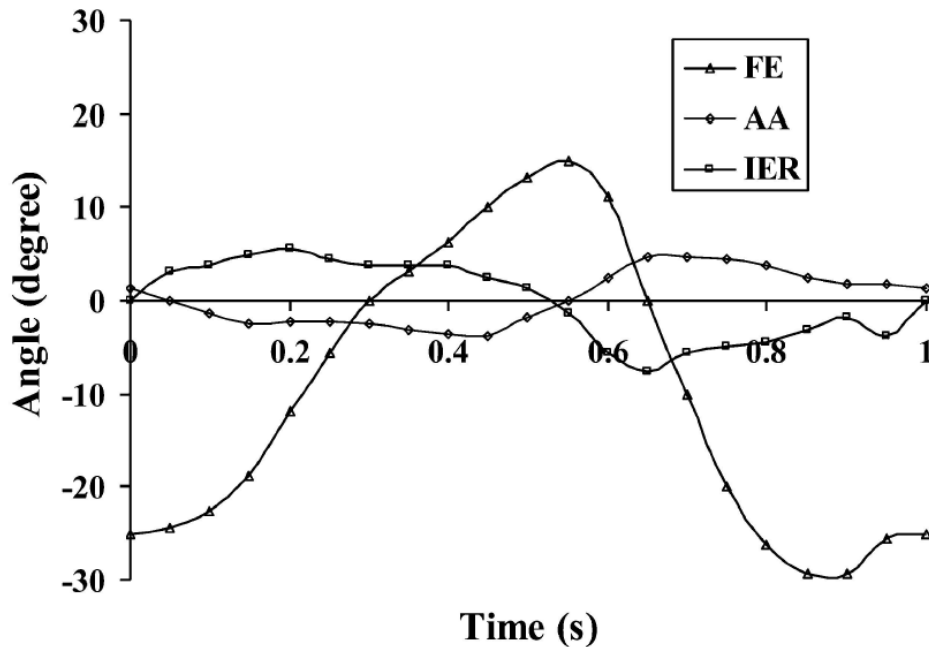


**Figure 1.7 Kinematic analysis of hip joint during a gait cycle, FE denotes flexion-extension; AA, adduction-abduction; IER, internal-external rotation (Johnston and Smidt, 1969)**

The load on the hip joint during a gait cycle can be up to two and a half times of the person's body weight (Bergmann *et al.*, 2001) at the maximum ( $F_p$ ). A contact force curve with a double peak during walking is usually regarded as 'normal'. The resultant force on a hip joint in a normal walking cycle is shown in Figure 1.8 which demonstrates that the load largely occurs from the heel strike in the stance phase up to the toe off. In a single leg stance, the abductors muscles are closer to hip joint rather than centre of patient's gravity. In consequence, forces of three times body weight could be supported by the abductors (Dandy and Edwards, 2009).

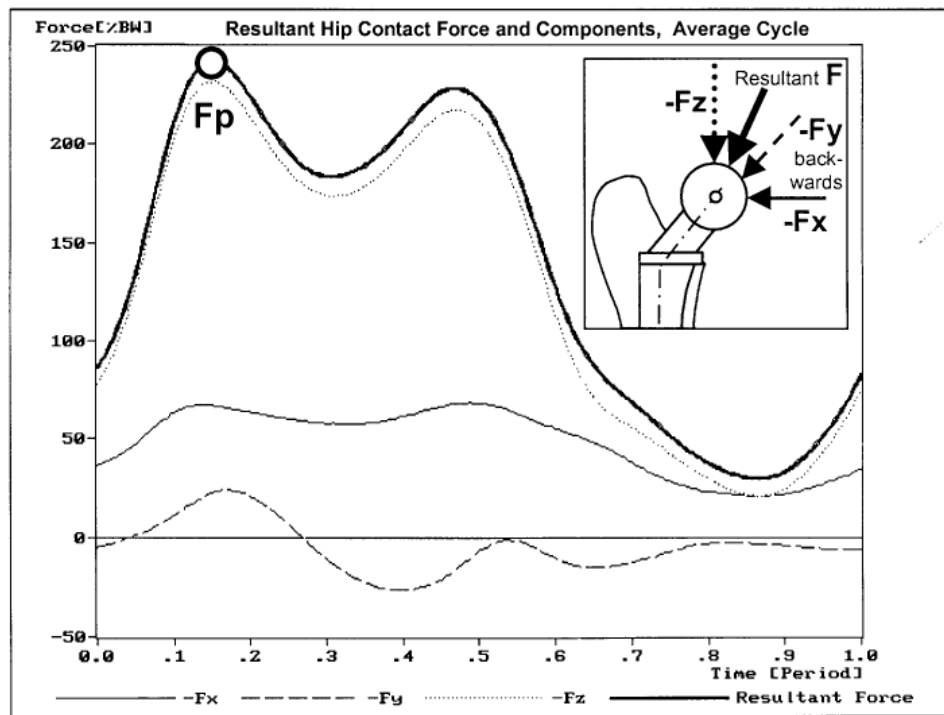


Figure 1.8 Kinetic analysis of gait cycle (Bergmann *et al.*, 2001)

Kinetic analyses of the hip joint during walking have been studied previously by using different methodologies such as implanted instruments or analytical methods. An analytical method was the base of Paul (1976) and Hashimoto and colleagues (2005) studies to predict the force transmitted at the joint by using a cine camera and force platform or a multi body dynamic system. Bergmann and colleagues (Bergmann *et al.*, 2001) monitored hip joint forces using instrumented implants in four patients for different activities. According to this study, the force that hip joint undergoes depends on the walking speed considerably. The maximum resultant force were reported to be 279% body weight for fast walking, 248% body weight for normal walking and 239% body weight for slow walking. These results can vary between studies due to study subjects and analysis methods.

### 1.2.6 Failure of hip replacements

During the early years of total hip arthroplasty, there were several reasons for the failure of the joint such as infection, dislocation, component malfunction secondary to fracture, component migration, femoral stem loosening, acetabular component

loosening, and polyethylene wear (Lombardi. *et al.*, 2000). However, currently the main concerns with hip replacements are osteolysis and long term hip stability (Lombardi. *et al.*, 2000).

Most of total hip replacements have excellent 10 years term results. However, the probability of THR failure is reported to have an inverse relationship with the age of the patients regardless of the material bearings (*National Joint Registry*, 2016). National joint registry reports 5% ten-year revision risk for woman under 55 years old whereas it is 2% for women over 75. Therefore, the main task for contemporary THR is to reduce the damage in the articulating surfaces to lengthen their lifetime.

Revision surgery is sometimes required due to failure of the original implant. Labek *et al* revealed that the rate of revision of THR from several registries around the world has been recorded to be 5% at 5 years post-surgery and 12% at 10 years post-surgery. The main cause of revision surgery was noted to be aseptic loosening (Labek *et al.*, 2011). Jassim *et al* discovered that of almost 12,500 revision surgery procedures which were performed in England and Wales in 2010, aseptic loosening (45%), pain (26%), dislocation/subluxation (15%), lysis (14%), infection (13%), periprosthetic fracture (9%) and component mal-alignment (6%) were the main reasons for the revision (Jassim, Vanhegan and Haddad, 2012).

The failure of the THRs are triggered by the following factors:

1. Poor implant design and material: this was an issue historically, where it was widely described how unsuitable shape and non-biocompatible material used within the body such as various types of metals caused undesirable reactions including corrosion and abnormal implant motion (Jassim *et al.*, 2012).
2. Biological factors: *in vivo* degradation of prosthesis occurs by means of wear processing which generates particulate debris (wear debris). Wear debris

stimulate an adverse biological reaction called osteolysis (bone loss) which is a significant threat for consideration of implant longevity (Jacobs *et al.*, 1994) because it can compromise the prosthesis fixation and bone stock. Osteolysis is widely dependant on bearing surfaces and wear debris of components (Dattani, 2007).

3. Poor surgical techniques: correct positioning of the hip replacement components decreases the instability and dislocation rate of THR. However, if the acetabular cup is implanted outside the patient's "safe zone", the dislocation rate is observed to be four times higher than implantation of the acetabular cup within the safe zone (Lewinnek *et al.*, 1978).

### **1.2.7 Dynamic separation**

There are previous studies that have focused on the difference in the performance of THRs and natural hip joints. Previous fluoroscopic studies indicate the kinematics of hip replacements would differ from the natural joint as the soft tissue supports around the hip joint are disrupted. During THR surgery, part of the supporting structure is resected or transected to facilitate surgical exposure (Dennis *et al.*, 2001). In these fluoroscopic studies, a medial/lateral separation of the THRs bearings was observed during activities such as the walking, hip abduction and adduction and pivoting activities (Lombardi. *et al.*, 2000; Komistek *et al.*, 2002). In the walking cycle, this separation (also known as microseparation or dynamic separation) is the result of sliding of the cup bearing medially/laterally during swing phase (Figure 1.9) and resulting in a smaller regional contact between the THRs bearings (Mak and Jin, 2002).

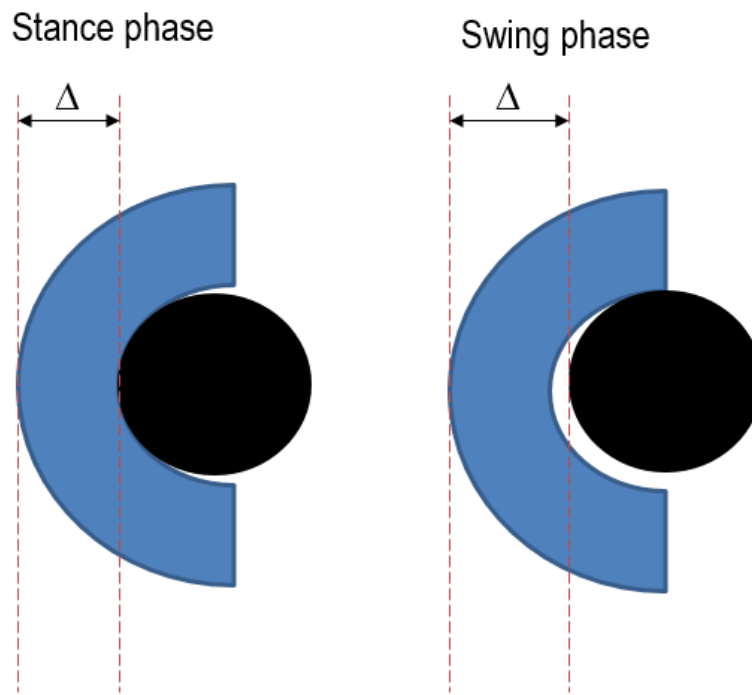


**Figure 1.9 Schematic of separation and sliding during the swing phase**

Dynamic separation is assumed to have a great effect on the kinetic and kinematic behaviour of the THRs. When the forces during gait cycle in proximal femoral replacement were analysed, it was determined that the force after heel-strike was much greater than the force just before toe-off (Taylor *et al.*, 1997). Generation of this large force between the femoral head and acetabular cup could be attributed to the dynamic separation which causes an impulse loading condition. The separation is also suspected to cause extra shear stresses on the femoral head and acetabulum cup which could cause increased wear.

As the dynamic separation occurs, contact between the rim of the cup and femoral head happens (edge loading) which generates high stresses. It has been determined that high stresses due to edge loading produce surface damage in the form of stripe wear on the components in ceramic-on-ceramic hip replacements *in vivo* and *in vitro* studies (Nevelos *et al.*, 2000). Figure 1.10 represents the stripe wear that was observed from clinical and experimental studies. On the other hand, no indication of stripe wear was observed in metal-on-metal THRs (Komistek *et al.*, 2002). However,

metal-on-metal bearings polish the surfaces themselves by wearing down the surrounding area which can remove and distinctive stripe on the head (Walter *et al.*, 2004). It is not possible to observe stripe wear on hard-on-soft bearings because of inability of polyethylene cup to damage the hard femoral head due to its softness.

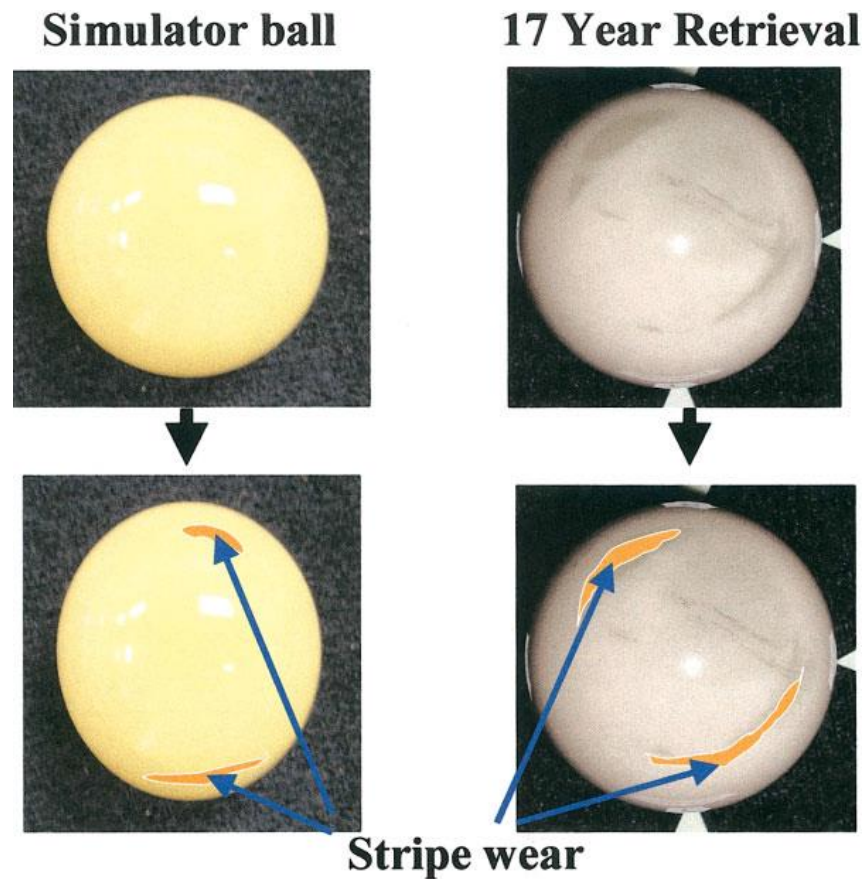


**Figure 1.10** The wear stripes on the ball in in vitro and retrieval components (Manaka *et al.*, 2004)

Lombardi *and* colleagues detected the separation in the THRs to be between 0.8mm to 2.8mm during gait cycle and 1.7mm to 3mm during leg lift (Lombardi. *et al.*, 2000). Previous studies (Komistek *et al.*, 1998) discovered the maximum separation during leg lift to be 5.4mm. Komistek *et al* (2002) determined no significant sliding of the femoral head in metal-on-metal hip replacements. Furthermore, no significant separation was observed in other common activities namely shoe tie, sit down and stand up (Blumenfeld *et al.*, 2011).

Dynamic separation was assumed to have a great detrimental effect on the wear of THRs due to the contact and loading changes. However, this idea is not well supported by *in vivo* studies as *in vivo* studies are limited to small number of patients and also there is no possible method for a comparison between the wear rate with and without separation *in vivo*. Therefore, the effect of separation and edge loading on the wear of the THRs are mainly studied *in vitro*. *In vitro* studies agreed that the wear of the THRs bearings are significantly affected by the separation (*e.g.* Williams *et al.*, 2008; Al-Hajjar *et al.*, 2010).

The increased wear in artificial joints has potentially two main disadvantages:

- 1) Changes in bearing geometry which decrease efficiency of tribological and kinematic functions.
- 2) Adverse biological reaction such as tissue reaction, osteolysis and loosening of the joint due to wear debris (Fisher, 2011).

Increased wear can lead to the requirement for revision surgery which is complicated, expensive, and involves risk to the patient. Also, currently hip replacements have been implanted in younger and more active patients and current limitations are due to rapid wear of the components (Wright and Goodman, 1995). Therefore, the need to identify the factors which increase the wear rate and approaches to minimise this wear are of primary importance.

### **1.2.8 Positioning of THR**

Miki and colleagues demonstrated that the important factors for dislocation are instability and impingement, which typically is caused by component positioning during primary THR (Miki *et al.*, 2013) or by abductor insufficiency (Dorr and Wan, 1998). In one of the studies of the factors that caused instability, it was determined

that 35.5% of the patients suffered from a malpositioned acetabular cup (Parvizi *et al.*, 2006).

The size of the THR components can be determined by using computer aided programmes. The programmes visualise the patients hip by CT scan images of patient's hip and then different sizes of components is applied to the hip to check which one is the most suitable one (Bargar *et al.*, 1998). The positioning of the components of THR can be determined by preoperative planning, sometimes using via computer aided techniques. It is recommended that the acetabular cup should be implanted in the 'safe zone' which was defined by Lewinnek *et al.* (1978). Based on his definition, the safe zone for acetabular cup allows  $15^{\circ}+10^{\circ}$  anteversion and  $30^{\circ}$  to  $50^{\circ}$  abduction. To prevent dislocation, McCollum and Gray proposed  $30^{\circ}$  to  $50^{\circ}$  abduction angle and  $20^{\circ}$  to  $40^{\circ}$  flexion angle (Mccollum and Gray, 1990). Despite all this precision, it is yet not fully possible to achieve the implantation of the acetabular cup within the safe mode neither by conventional method (even by experienced surgeon) nor by computer aid navigation system as the functional positioning of the components cannot be guaranteed due to the preoperative and postoperative changes such as in pelvic tilt. (Parratte *et al.*, 2009).

In a hip replacement, the centre of the implanted femoral head and acetabular cup should be concentric. As described previously, if the acetabular cup is not correctly positioned with respect to biomechanical loading axis and contact patch and wear does not occur within the articulating surfaces, it results in contact of the femoral head and rim of the cup (known as edge loading), and adverse tribological condition (Knahr, 2011).

Since both acetabular cup and femoral head have six independent degrees of freedom, there are different types of conditions that produce edge loading (Figure 1.11):

- Translational variation of components: which includes medial or superior translation of the centre of the cup (failure to restore cup centre), offset deficiency (failure to restore head centre), and head neck impingement.
- Rotational variation of the components: includes the inclination angle of the cup which causes intersection of rim of the cup and tribological contact patch (Fisher, 2011).

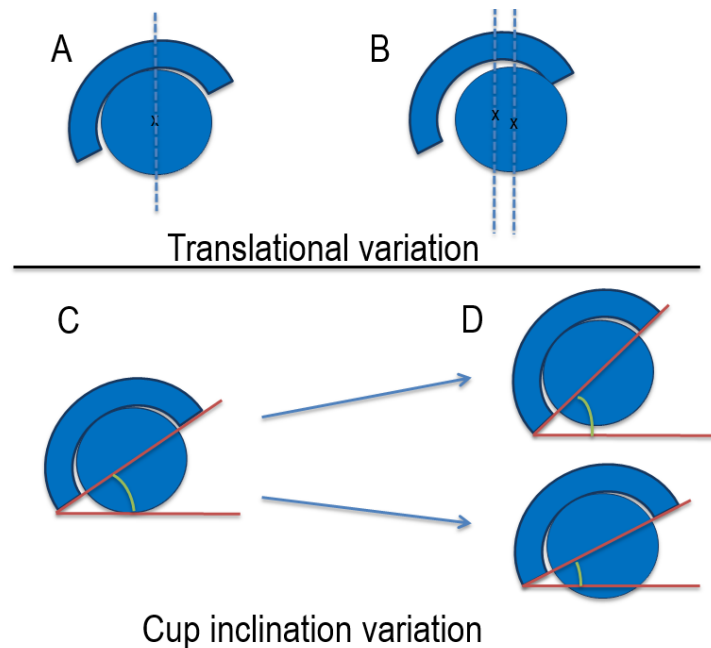


**Figure 1.11 Schematic of translational and rotational variation. Concentric bearings (A), a mismatch between the centres of the head and the cup (B), the schematic of standard (C), steep and low inclination angle (D)**

Despite the influence of material and diameter of the components used in THR, the position of the acetabular cup affects the forces on the hip joint, the range of motion, stability and wear of components (Schmalzried, 2009). Therefore, studying the effect of THR components positioning on the THR behaviour can benefit the long term performance of the device.

### **1.3 Tribology of artificial hip joint**

The critical issues of artificial joints especially hip joint failure involve the wear of the articulating surfaces (Mattei *et al.*, 2011). It is difficult to understand the effect of factors such as positioning, surrounding tissues, design, size and the load on the wear of the THRs from *in vivo* studies because each patient's artificial hip has a specific condition. Therefore, to be able to distinguish the effect of each factor, *in vitro* studies have been undertaken, based on an international standard ISO 14242 (Kaddick and Wimmer, 2001; Stewart *et al.*, 2003; Galanis and Manolakos, 2011) to test the variety of the factors with the same condition for each testing.

Biotribology is the tribological study of the human joint (Dowson and Wright, 1973). The study of interacting surfaces in relative motion between them defines tribology as being concerned with study of the friction, wear and lubrication (Jin *et al.*, 2006). Improved tribological performance can lead to greater articulating surfaces efficiency, better performance, and thereby reducing failures, number of surgeries and the lifetime costs of a THR. Research in tribology aids the product development process by informing where to modify the design. THR designers can use this data to reduce losses caused by wear where the articulation of surfaces is involved (Affatato *et al.*, 2008).

#### **1.3.1 Wear**

When there is relative motion between two surfaces, the progressive loss of the material of the surfaces is the result of this motion which is defined as wear (Jin *et al.*, 2006). Wear can be categorised as: single phase or multiple phase wear (Peterson, 1980). In single-phase wear a solid, liquid or gas causes removal of material from wearing surfaces by moving relative to a sliding surface (Affatato *et al.*, 2008). Multiple phase wear includes a carrier that produces the wear in addition to the single phase. During the wear process, worn material is expelled from the

contact between the surfaces in the form of debris which causes a biological reaction in the human body. The strategy to minimise wear rate depends on the type of wear which is presented in the surfaces (Dowson *et al*, 2000).

There are two methods of wear measurement. Volumetric wear is the volume of detached material from the bearing surfaces and linear wear (penetration) is the displacement of one bearing surface relative to another (Hall *et al*, 2001). In the laboratory, gravimetric techniques are used to measure the wear of the material before and after testing and converting the values to volume loss. In simulator studies, volumetric techniques are used as well as gravimetric techniques for wear determination. Volumetric values include changes in dimensions due to creep as well as wear (Hall *et al*, 2001).

The amount of volumetric wear ( $V$ ) can be calculated from following equation (Hall *et al*, 2001):

$$V = k \times L \times s$$

Where  $k$  is the wear factor,  $L$  is the load, and  $s$  is the sliding distance. The wear factor is a proportional constant which is dependent on the exact condition of the bearing contact including surface roughness of the materials and the material used in the bearings. As above equation indicates, greater sliding distance leads to a greater wear volume.

### **1.3.1.1 Wear studies**

Recently there have been many *in vitro* THR studies to understand the tribological performance of the surfaces under different conditions. These studies have focused on the wear of the articulating surfaces in different conditions to investigate the factors that could potentially increase the wear rate. *In vitro* studies were initiated from simple wear testing, such as a pin on disk machine, to the most advanced

simulators that replicate THR during different activities. Various *in vitro* testing of THR mechanisms by using different laboratory equipment, test methods, and measuring systems are explained below (Jin *et al*, 2006):

- 1) Pin-on disc machine: to evaluate the wear and friction of material combination under well- controlled, steady-state load conditions.
- 2) Pin-on-plate machine: to reciprocate action associated with hip joint during walking and simulates the steady sliding speed between specimens.
- 3) Joint simulator: developed according to ISO standards (14242-1:2000 to 14242-1:2014) to study different designs, bearing couples, size and volume of wear debris of the bearings in conditions similar to *in vivo*.
- 4) Joint simulator studying adverse conditions: to study effects such as separation and edge loading on the wear behaviour of THR. The most advanced versions can also feed back the effect of initial parameters that could affect the separation and edge loading as well.

The pin-on disc and pin-on-plate machines are simple screening tests which are used to rank the wear of different bearing materials (Revell, 2008). The available hip simulators consist of stations which replicate the loading and movements of an artificial hip. Namely, flexion-extension (FE), adduction-abduction (AA), and internal-external rotation (IE). Table 1.1 represents the available hip simulators and range of their motions. As Table 1.1 states, all the simulators replicate flexion/extension of the hips however, both internal/external rotation and abduction/adduction are not simulated in all the simulators. The only simulators which replicate all three degree of freedoms are multi axis testing machines (AMTI) and Electromechanical hip simulator EM13. Furthermore, the other difference between the simulators are the way that the bearings are positioned. If the bearings

are assembled with respect to the *in vivo* conditions, the cup is positioned on top of the head which is called anatomical loading. In anatomical loading simulators, the bearings are loaded through the cup. On the other hand, in non-anatomical simulators, the head is mounted on top of the cup and the loading occurs through the head.

**Table 1.1 Overview of available hip simulators The positive value in the F/E, I/E rotation and A/A represents Flexion, internal rotation and abduction and the negative value represents extension, external rotation and adduction, respectively (modified from Affatatto *et al*, 2006)**

| Author                         | Simulator      | FE | I/E rotation | A/A | Loading        |
|--------------------------------|----------------|----|--------------|-----|----------------|
| Bragdon <i>et al.</i> , 2003   | AMTI           | ✓  | ✓            | ✓   | Anatomical     |
| Saikko, 2005                   | HUT-4          | ✓  | -            | ✓   | Anatomical     |
| Smith and Unsworth, 2001       | Mark II Durham | ✓  | ✓            | -   | Anatomical     |
| Nevelos <i>et al.</i> , 2000   | Leeds PA II    | ✓  | ✓            | -   | Anatomical     |
| Barbour <i>et al.</i> , 1999   | PROSIM LIMITED | ✓  | ✓            | -   | Anatomical     |
| Pare <i>et al.</i> , 2003      | EW08 MMED      | ✓  | -            | ✓   | Non-anatomical |
| Affatatto <i>et al.</i> , 2006 | SW             | ✓  | -            | ✓   | Non-anatomical |
| Ali <i>et al.</i> , 2016       | EM13           | ✓  | ✓            | ✓   | Anatomical     |

Although the hip simulators are built to replicate the *in vivo* scenario, the relevance of the experimental studies to the *in vivo* conditions could be limited. This is due to the many differences, both between the simulators and *in vivo* conditions and between the simulators themselves that could potentially affect the wear predictions. The major difference between *in vivo* and *in vitro* studies are the testing environments that cannot be simulated in the experimental simulators, such as *in vivo* bearing positioning, synovial fluid, the surrounding tissue and ligaments. Moreover, the simulators are set to repeat millions of walking cycles to achieve a

long-term wear predictions. However, *in vivo* hip joint clearly experiences various loading and range of motions. Also, the loading of the hip joint *in vitro* usually is an axial resultant force whereas there are forces in three directions occurring on the hip joint clinically (Bergmann *et al.*, 2001).

There are hip joint simulators such as Leeds PA II, PROSIM LIMITED, and EM13 that apply separation conditions to predict the level of wear rate on the THR's due to the separation. The separation that was seen *in vivo* studies during swing phase was initially applied to the hip simulators by attaching a spring to the cup medial/laterally (Nevelos *et al.*, 2000; Stewart *et al.*, 2003; Williams *et al.*, 2003). Then, the combination of swing phase load and medial force by the spring could separate the head and the cup in the swing phase time of the gait cycle when the load is minimum. Initial *in vitro* studies evidenced stripe wear on the cup of hard-on-hard bearings under the existence of microseparation, which was previously observed in retrievals (Nevelos *et al.*, 2000). Observation of *in vitro* stripe wear increased the relevance of clinical and experimental studies. Therefore, a wide range of *in vitro* testing has been carried out to understand the effect of microseparation on the wear rate. Table 1.2 summarises the level of wear rate that could be seen in different bearing couples by these studies. In the most of the studies under separation conditions, the level of separation was applied and the resulted wear was reported. However, the wear rate that Ali et al (2016) reported, is the level of separation caused by other parameters such as translational mismatch level or cup inclination angle.

**Table 1.2 Wear rate of different bearing materials in standard and microseparation condition**

| Bearing materials | Head size | Standard condition             |                            | Adverse condition |                                |                            |
|-------------------|-----------|--------------------------------|----------------------------|-------------------|--------------------------------|----------------------------|
|                   |           | Study                          | Wear (mm <sup>3</sup> /mc) | Separation (mm)   | Study                          | Wear (mm <sup>3</sup> /mc) |
| <b>MoM</b>        | 36        | Al-Hajjar <i>et al.</i> , 2013 | 0.35                       | 0.5               | Williams <i>et al.</i> , 2013  | 1.3                        |
| <b>CoM</b>        | 36        | Reinders <i>et al.</i> , 2013  | 0.1                        | 0.5               | Williams <i>et al.</i> , 2013  | 0.36                       |
| <b>CoC</b>        | 36        | Al-Hajjar <i>et al.</i> , 2010 | 0.05                       | 0.5               | Al-Hajjar <i>et al.</i> , 2010 | 0.125                      |
| <b>CoP</b>        | 36        | Williams <i>et al.</i> , 2003  | 25                         | 0.7               | Williams <i>et al.</i> , 2003  | 5.6                        |
| <b>MoP</b>        | 36        | Ali <i>et al.</i> , 2016       | 13                         | 0.5               | Ali <i>et al.</i> , 2016       | 21                         |

As the above table shows, separation has a significant effect on the wear rate of hard-on-hard bearings. The wear rate of the hard-on-hard bearings, especially MoM, increases when a level of microseparation is introduced to the test condition. In hard-on-soft bearings, there is an obvious increase in wear rate in MoP bearings. However, this trend could not be observed in CoP bearings. The separation study on CoP bearings resulted in a locally deformed polyethylene acetabular cup on the superior edge where the edge loading occurred (Williams *et al.*, 2003). Although no significant separation was seen in this bearing couple, the observations from retrievals and experimental studies have shown significant deformation and damage on the edge of the polyethylene which could potentially result in fatigue of the polyethylene cup or fracture of the components due to concentrated stress (Williams *et al.*, 2003; Ali *et al.*, 2016; Partridge, 2016). Although, there are similar conditions in the studies stated in Table 1.2 such as microseparation level or head size, the direct comparison of wear rate between these studies are challenging as there are many differences between the studies such as range of motion, radial clearance and simulator set up.

Further studies have focused on the effect of various parameters such as translational and rotation variation of the bearings, swing phase load, head size and joint laxity to understand the effect of various factors first on the level of separation and second wear rate of the bearing (Williams *et al.*, 2003; Leslie *et al.*, 2008; Al-Hajjar *et al.*, 2013; Ali *et al.*, 2016). Another wear testing was on the modifications in material properties of the bearings that strengthen the materials against wear. For example, experimental studies showed that in polyethylene bearings, the usage of highly crosslinked polyethylene assisted the wear rate of them. In a similar manner, Biolox delta ceramics bearings generation improved the ceramic bearings performance in terms of toughness against alumina bearings (Al-Hajjar *et al.*, 2013).

The body response to the material wear debris is another factor than can lead to aseptic loosening of the device. When wear particles are produced, the body's immune system reaction to this external particles is resorption of living bone tissue. The response of human body cells to wear debris varies due to biocompatibility of the bearings material and wear debris characteristics such as size, volume, and morphology. The main adverse effect of wear debris especially in MoM and MoP bearings is the presence of metal ion level and high particle concentration that lead to cell death, osteolysis and tissue necrosis (Ingram *et al.*, 2004; Willert, 2005). Osteolysis leads to aseptic loosening of the implant and revision surgery in MoM whereas CoC bearing were introduced to prevent osteolysis. CoC bearing were shown to have less active debris than UHMWPE (Hatton *et al.*, 2003). The accumulation of micron and submicron polyethylene wear debris also leads to failure of the THR due to osteolysis (Ingham and Fisher, 2000).

### 1.3.3 Friction and Lubrication

Friction and lubrication are the two main factors that affect the wear rate of the bearing surfaces. In artificial joints, friction plays an important role in the stress generated at the bearing surfaces and force transmission from bearing surfaces to the fixation interface (Fisher *et al.*, 2006).

The wear rate of a device could be influenced by the friction and lubrication between the bearing surfaces. There are three laws of friction commonly used to model friction (Fisher *et al.*, 2006) which state that:

1. Friction is directly proportional to the applied force normal to the surface
2. Friction is independent of the apparent area of contact.
3. Frictional force is independent to sliding surfaces.

The femur and acetabulum surfaces of a natural human joint are covered by articular cartilage that has a very low coefficient of friction. The *in vitro* studies of friction, focuses on the frictional torque that is generated in the pendulum friction simulator (Brockett *et al.*, 2006). The measured frictional torque (T) is usually used to derive the dimensionless parameter called the friction factor to compare effects such as combinations of materials, implant size, implant design, load, lubrication, and motion profile (Fisher *et al.*, 2006)

Table 1.3 represents the friction factor of common hip implant material combinations. These friction factors are calculated in simulations in the presence of bovine serum as the lubrication. As this table shows, friction between coupled metallic bearings is the highest of all the bearing types and ceramic on ceramic/metal has the lowest friction factor (Brockett *et al.*, 2006).

**Table 1.3 Friction factor of typical bearings for artificial hip implants in the presence of bovine serum simulator (Jin *et al.*, 2006)**

| <b>Bearing type</b>             | <b>Friction factor</b> |
|---------------------------------|------------------------|
| <b>Metal on UHMWPE</b>          | 0.06-0.08              |
| <b>Ceramic on UHMWPE</b>        | 0.06-0.08              |
| <b>Metal on metal</b>           | 0.22-0.27              |
| <b>Ceramic/metal on Ceramic</b> | 0.002-0.07             |

Lubrication decreases the friction between the articulating surfaces by creating a film between the surfaces. The lubrication of the natural hip joint is the function of the natural synovial fluid. There are varieties of lubricants which have been used in hip simulators to replicate natural synovial fluid. It has been noted that protein has the main role in simulator lubricants because of formation of 'solid like' layers which protect the surfaces against direct contact and consequently, wear (Scholes and Unsworth, 2006) . Therefore, lubricants with no protein such as water and saline solutions were not appropriate for simulator lubrication. However, increasing protein concentration can cause gradual drop in wear rate due to protein degradation and un-physiological protection against wear (Affatato *et al.*, 2008). Currently, bovine serum is the most common lubricant that is used in hip simulators. It produces the same order of magnitude of wear as clinical data (Brown and Clarke, 2006).

There are three main lubrication modes in engineering (Dowson, 2001) based on complete separation between the bearing surfaces (fluid-film lubrication), partly separated and partly in contact (mixed lubrication), and mostly in contact (boundary lubrication). The lubrication mode between the bearing surfaces depends on the bearing material.

### **1.3.3 Contact mechanics**

Contact mechanics is the study of the behaviour of bodies when they are brought into contact. The result of contact mechanics studies is usually the contact pressure (or stress) of the bearing surfaces in contact and the contact area of them. The initial contact of two solids is at a point or a line. The contact region increases by gradual increase of load and the resultant deformation of the surfaces. The studies of tribology parameters such as wear, friction, and lubrication are all related to the mechanics of the contact.

Contact mechanics studies of human joints predict the contact pressure and contact area of the articulating surfaces when the load is applied to them. As the load increases, the surfaces of the joint start conforming to each other which leads to greater contact area and a wider stress distribution. The conformity of the surfaces depends on the material utilised in the artificial joint. The contact mechanics of artificial hip joints have been studied theoretically and experimentally to predict the level of stress, pressure, and deformation of bearings in the joint and wear of the surfaces (Mak and Jin, 2002; Williams *et al.*, 2003; Al-Hajjar *et al.*, 2010).

Hertzian theory is the theoretical method for predicting contact area and pressure in solids. In 1881, Hertz studied the stress and contact area in an elastic isotropic material with normal loading and small contact area relative to the radii of curvatures and dimensions of the surfaces (Johnson, 1985). Hertzian theory has been extended progressively to fit the particular application and has been developed to study the behaviour of bearing surfaces of artificial joints when the bearings are in contact. The geometry of the artificial hip joint has been simplified by the assumption of an equivalent ball on a plate model. To determine the contact

pressure, first the radius of the equivalent ball ( $R$ ) should be calculated using (Meng *et al.*, 2013):

$$R = \frac{R_c \times R_h}{c}$$

Where  $R_c$  is the radius of the cup,  $R_h$  is the radius of the head, and  $c$  is the radial clearance. Then the radius of the contact ( $r$ ) can be determined from following equation:

$$r = \left( \frac{3wR}{E'} \right)^{\frac{1}{3}}$$

Where  $w$  is the applied load to the bearing and  $E'$  is the equivalent elastic modulus of the bearings which can be derived from:

$$\frac{1}{E'} = \frac{1}{2} \left( \frac{1 - \nu_c^2}{E_c} + \frac{1 - \nu_h^2}{E_h} \right)$$

Where  $\nu_c$  is the Poisson's ratio of the cup,  $E_c$  elastic modulus of the cup,  $\nu_h$  Poisson's ratio of the head, and  $E_h$  is the elastic modulus of the head. Then the contact pressure ( $p_{max}$ ) of the bearings under a given load can be determined as:

$$p_{max} = \frac{3W}{2\pi r^2}$$

Contact pressure and contact area of bearing surfaces can be measured experimentally by using sensors or pressure-sensitive film. The contact area of the bearing surfaces can also be measured by using engineering 'blue'. El-Deen *et al* applied engineering blue on knee replacement to determine the contact patch between the two components and the contact patch could then be measured using Vernier callipers (El-Deen *et al.*, 2006).

Thin film transducers such as pressure sensitive film (Fuji prescale film) and electrical resistance sensor (TekScan) are used to measure both contact pressure

and contact area (Bachus *et al.*, 2006). Fuji prescale film system is based on measurement of the contact area of the stain by summing the area of stained pixels on the film from the image analysis programme. The average pressure can be calculated from the average pixel density of the film. TekScan is a digital pressure sensing device which measures the force as a change in electrical resistance at each sensel (row column intersection). Then, the contact area and eventually contact pressure can be represented on the computer during loading because of electrical isolation of each sensel (Bachus *et al.*, 2006).

The Tekscan technique has greater accuracy and reliability, can gauge a wider range of load, and produce real-time data (Revell, 2008). However, the major disadvantage of all these methods is the thickness of film or sensor which is noted to be of the order of 100µm. Therefore, these methods are not suitable for the hip implants with close conforming bearing surfaces with a decrease of less than one millimetre.

Hertzian theory equations can be used for hard-on-hard bearings used in hip replacements. However, Hertzian theory does not consider the thickness of the cup and also, it is more applicable for the nonconforming contact. Therefore, another method called simple elasticity analysis was introduced to determine more valid prediction of contact stress of hard-on-soft bearings (Jin *et al.*, 1994). This method represents that the contact pressure (p) can be determined by use of parameters such as Poisson's ratio of the polyethylene cup (ν), elastic modulus of the cup (E), thickness of the cup (d), and radial deformation (u<sub>r</sub>) which can be calculated by using the following equation:

$$\frac{p}{u_r} = \frac{E}{d} \frac{(1 - \nu)}{(1 - 2\nu)(1 + \nu)}$$

There have been experimental studies of the contact stress of THR bearings which are usually compared with the contact stresses derived from finite element modelling of joint. Table 1.4 shows the studies that have been carried out on various THR bearing couples. As this table shows, when a UHMWPE bearing is utilised, the contact pressure is significantly lower due to larger half contact area of bearing surfaces caused by the polyethylene flexibility under the load.

**Table 1.4 Contact stress of different bearing couples**

| <b>Bearing couples</b> | <b>Head diameter (mm)</b> | <b>Max. contact pressure (MPa)</b> | <b>Total contact angle (°)</b> | <b>Reference</b>                  |
|------------------------|---------------------------|------------------------------------|--------------------------------|-----------------------------------|
| <b>MoM</b>             | 14                        | 50                                 | 40                             | Jagatia and Jin, 2001             |
| <b>MoP</b>             | 11-16                     | 10-23                              | 80-100                         | Jalali-Vahid <i>et al.</i> , 2001 |
| <b>CoC</b>             | 14                        | 80                                 | 30                             | Mak and Jin, 2002                 |

The simple equations on the contact mechanics changes are not applicable for separation conditions due to higher level of complexity. The complication of the separation condition arises from the edge contact where the contact zone is less. Moreover, the prediction of contact zone is a challenging concept as only the medial-lateral separation is identified. Therefore, finite element modelling can be used to predict the more complicated contact mechanics scenarios.

## **1.4 Computational studies**

Computational modelling along with experimental testing is a useful tool for preclinical testing of the prosthesis behaviour. Such models allow the prediction of the THR behaviour under the certain conditions that are of interest. The computational predictions are used to understand the effect of a range of parameters and their severity when experimental and clinical studies of the same conditions can be time consuming, expensive and complicated.

Computational modelling allows the examination of the dynamic behaviour and contact mechanics of the articulating surfaces of total hip replacements. It also could be representative of dynamic motion of the femoral head within the acetabular cup and contact pressure distribution during an activity (Gao *et al.*, 2015). A successful computer model can either:

- Predict the outcome of an experimental run, without the expensive and time consuming process
- Direct an experimental run by providing a starting point for areas of interest within the parameters

For better understanding of hip joint tribology, the contact mechanics performance of THR such as contact area, contact stress, and pressure distribution in a hip joint are required to understand the source of the long term outcome of the device. Most of the computational analyses have been carried out using static conditions (Bartel *et al.*, 1985; Besong *et al.*, 2001; Hua *et al.*, 2012). Static contact mechanics study on its own might not be able to provide realistic data because the contact mechanics is studied based on the single static condition rather than considering the dynamic loading during an activity which could affect the contact zone. Therefore, biomechanics and tribology characteristics should be integrated to fully simulate hip joint behaviour in different positions. Integration of dynamic motion and contact mechanic studies of THR would be the best solution for a more realistic understanding.

Expensive computational cost, long computing time and appropriate simplification of the models are the challenges which are faced in coupling motion dynamics and contact mechanics. Currently, the coupling of biomechanical and biotribological analysis of human joints such as knee (Godest *et al.*, 2002; Halloran *et al.*, 2005;

Baldwin *et al.*, 2009) have been examined by using finite element methods and rigid body dynamics. Finite element method is one of the most advanced simulation techniques in solid mechanics which is used as a tool to design and analyse orthopaedic prosthesis especially THRs (Kayabasi and Ekici, 2007). However, full coupling of biomechanics and biotribology of artificial hip joints under adverse conditions has not been achieved yet. In this section, previous computational modelling such as finite element and dynamic studies on THR and other prostheses are reviewed.

#### **1.4.1 Finite element modelling of THRs**

The experimental studies and mathematical analysis provide some information on the contact mechanics of artificial hip joints such as the maximum pressure applied to the components or contact area of the articulating surfaces. However, it is necessary to use computational modelling to reproduce a wider range of the physiological conditions of daily activities and to analyse kinetic and kinematic parameters of the joint components and surrounding material. Kinetic analyses of hip replacements have been studied by finite element (FE) method to approach design optimisation and pre-clinical safety and reliability testing of artificial joints (Plank *et al.*, 2005; Jennings *et al.*, 2012). Table 1.5 represents a summary of studies on the contact mechanics analysis of artificial hip joints.

**Table 1.5 Previous computational studies on contact mechanics of THRs**

| Reference                      | Type of geometry | Focus of Study                              |
|--------------------------------|------------------|---|
| Carter, Vasu and Harris, 1982  | 2D               | Cement thickness and metal backing          |
| Bartel <i>et al.</i> , 1985    | Axisymmetric     | Conformity and plastic thickness            |
| Mak and Jin, 2002              | Axisymmetric     | CoC bearings                                |
| Kurtz, Edidin and Bartel, 1997 | 3D               | Shell/liner conformity of surfaces          |
| Korhonen <i>et al.</i> , 2005  | 3D               | Cemented THR                                |
| Plank <i>et al.</i> , 2005     | 3D               | Conventional polyethylene and UHMWPE on THR |
| Besong <i>et al.</i> , 2001    | Axisymmetric, 3D | Cementless MoM                              |
| Sariali <i>et al.</i> , 2012   | 3D               | Microseparation                             |
| Hua <i>et al.</i> , 2012       | 3D               | Microseparation in MoP                      |
| Mak <i>et al.</i> , 2011       | 3D               | Rim design under edge loading               |

It can be seen from the table that there are three different geometrical types of artificial hip joint FE models: two dimensional (2D), axisymmetric, and three dimensional (3D).

#### **1.4.2 Two-Dimensional hip models**

The early development was carried out on the 2D and axisymmetric models. The first 2D model of an artificial hip joint was undertaken (Carter *et al.*, 1982) to study the stress analysis in a conventional polyethylene acetabular cup with different cement thickness and effect of metal backing on the cup. Figure 1.12 shows the loading and material property region of THR model with 1 mm PMMA cement and metal backing. Finite element analysis of this model suggested prevention of cup loosening by use of metal-backed acetabular component (Carter *et al.*, 1982). A two dimensional model may produce a quick analysis. However, 2D models might not be reliable if the attention is on the third dimension which is not considered in two

dimensional models. For example in this study, stress distribution has been considered only on the central plane not on the inner surface of the cup. In two-dimensional models, plane strain is assumed (i.e. the strain out of the plane is assumed to be zero).

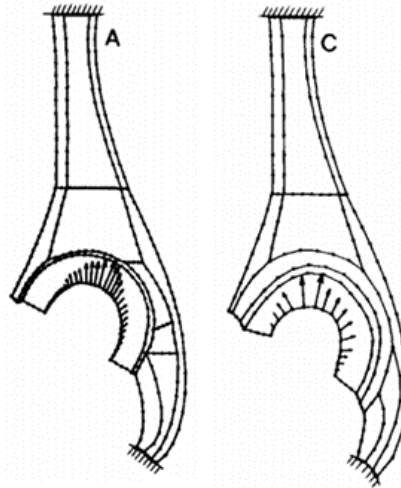


**Figure 1.12: 2D model of THR with A) 1 mm PMMA and B) with metal backing (Carter *et al.*, 1982)**

### **1.4.3 Axisymmetric hip models**

An axisymmetric model is basically suitable for the symmetric configuration about an axis and it is usually used for replacing 3D model with simple configuration to save computational resources. 2D and axisymmetric models represent high computational efficiency and lower computational storage compare to 3D models. Therefore, they are developed to establish initial estimation of the problem.

An axisymmetric contact model of UHMWPE acetabular cups against metallic femoral heads (Figure 1.13) was developed to predict the contact area and stresses in articulating surfaces under various loads. The result of this configuration was compared to the experimental measurements and simple elasticity analysis for data validation (Jin *et al.*, 1999). Another axisymmetric model (Figure 1.13) was developed by Bartel *et al* (1985) to study the effect of conformity and plastic thickness on contact stresses in metal backed plastic implants (Bartel *et al.*, 1985).

This study was based on linear elastic behaviour; however, polymers display elastic and also plastic behaviours when the yield stress is exceeded.

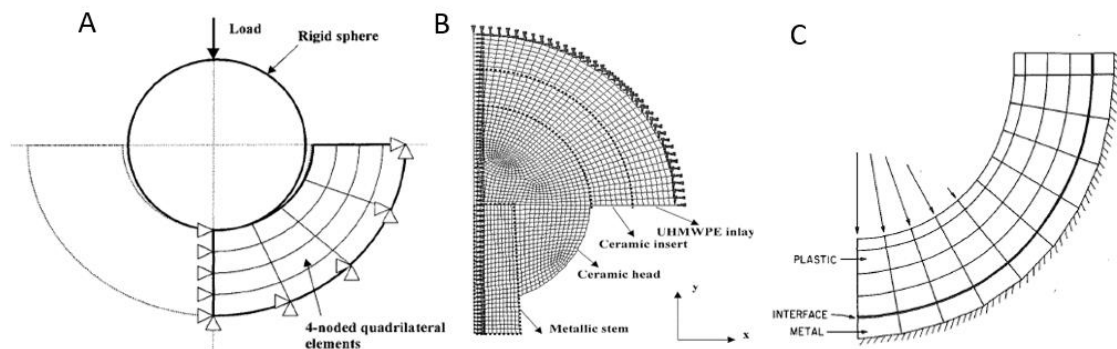


**Figure 1.13 The axisymmetric models of THR A) The axisymmetric finite element model of Jin *et al* (1999) B) Axisymmetric THR model of Mak and Jin (Mak and Jin, 2002) C) FE model of metal backed plastic cup in Bartel *et al* (1985)**

An axisymmetric finite model of CoC bearings was developed by Mak and Jin to study contact mechanics of this type of bearing (Mak and Jin, 2002). This model included ceramic insert and head, metallic stem, and a polyethylene backing secured in metallic shell for fixation purposes. Figure 1.13 shows the construction of these components. The much higher elastic modulus of the metal than the polyethylene meant that its effect was negligible for this model. This study indicated that the contact mechanics of the CoC THR largely depends on design parameters such as radial clearance and ceramic insert thickness. Furthermore, it was demonstrated that Hertz contact theory is an applicable method for validation of CoC computational models.

If the contact analysis is carried out on axisymmetric models, the hip joint has been implanted vertically to have XY axis as an axis of symmetry. However, *in vivo*, the cup is implanted with different inclination angles with respect to the femoral components. Thus, the actual assembly of the hip replacement *in vivo* is not comparable to the axisymmetric configuration.

#### **1.4.4 Three-Dimensional hip models under idealised condition**

Three dimensional models of THR have been widely developed to investigate the effect of design parameters and surgical techniques on the contact mechanics of the articulating surfaces. The running time of the 3D THR models is longer than 2D and axisymmetric models as more calculations are required compared the 2D and static models. However, these models are generally more realistic output as three dimensional effects of the kinetics and kinematics are taken into consideration in contact mechanics studies. In fact, one previous study has showcased the difference in the contact output of axisymmetric and 3D models of the THR (Besong *et al.*, 2001). The model consisted of a titanium shell, cobalt chrome femoral head and insert with 30 $\mu$ m radial clearance. The model was designed to be cementless. A 3D model was developed to consider the loading of the joint in the anatomical position. The comparison of axisymmetric and three dimensional models suggested a difference between the peak contact pressure in axisymmetric and 3D model of the THR (5MPa difference in the peak value) which is caused by the anatomical loading and axial loading in 3D model and axisymmetric model.

Three dimensional THR FE models are generally carried out on idealised conditions and the 3D modelling of separation has only recently been introduced (Sariali *et al.*, 2012; Hua *et al.*, 2014). In this section, the FE THR models under the idealised condition are reviewed. Three dimensional THR replacements mainly focus on the interfaces within the THR to predict the risk of fixation or contact failure. In addition, the effect of design, positioning and the material properties are studied for behaviour prediction. One of the studies that focuses on the interface between the polyethylene liner and metal shell due to manufacturing tolerances or locking mechanism of liner and shell was by Kurtz *et al* (1998). In this study, a three-body contact (femoral head, polyethylene liner, and the shell) was solved for quasi-static

response with four sets of liner boundary conditions: no restraints, rim restraints, equatorial restraints, and both rim and equatorial restraints. This study suggested that in nonconformities designs, deformation of polyethylene liner within the shell occurs to make a solid contact with the shell. This shell/liner interaction leads to load transfer and relative motions between the shell and liner (Kurtz *et al.*, 1998).

Korhonen *et al* studied the effect of the design and positioning of the THR by focusing on how the geometry and abduction angle affected contact pressure and area of a cemented THR (Korhonen *et al.*, 2005). In this study, a FE analysis of two clinically tested designs (IP and Lubinus eccentric shown in Figure 1.14) and two additional designs with cement mantle and femoral head were generated to predict the effect of cup clearance and thickness on contact mechanics.

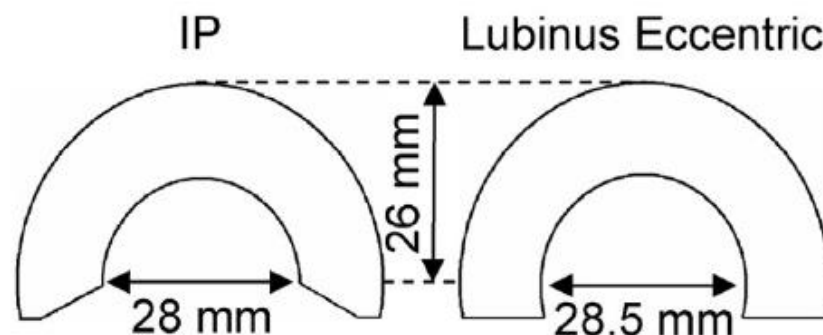


**Figure 1.14 Clinically tested IP and Lubinus (Korhonen *et al.*, 2005)**

A significant change of mechanical stresses on the acetabular cup was observed due to geometrical design, thickness, and abduction angle of the acetabular cup in the loading cycle. This analysis suggested that increased clearance leads to greater contact pressure at interfaces and also that polyethylene layer thickness and contact pressure have an inverse effect on cup-cement interface. Figure 1.15 shows validation of contact area in the numerical model and experimentally tested IP and Labrius cups which represented a fairly consistent result.

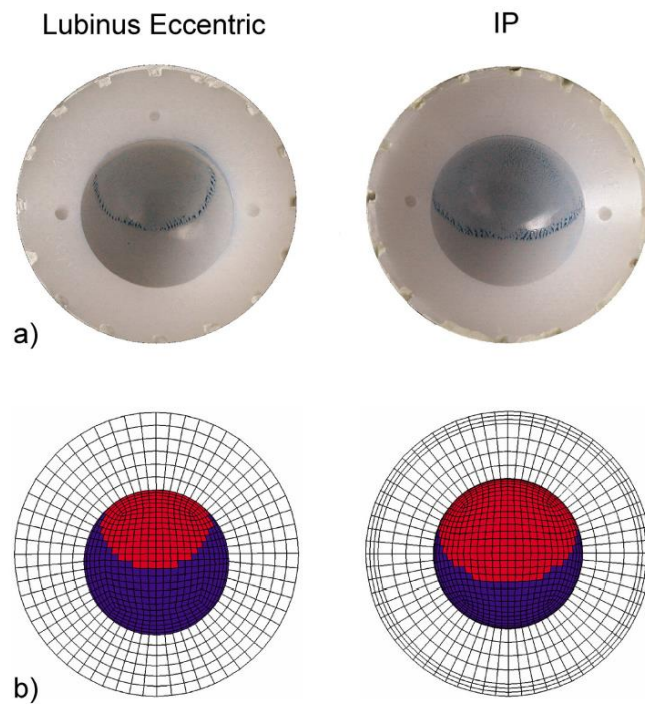


**Figure 1.15 Contact area of the Lubinus and IP cup under loading cycle in a) experimentally tested and b) numerical models (Korhonen *et al.*, 2005)**

The effect of the material properties and the bearing design were studied by Plank *et al* (2005). The contact stresses in conventional and crosslinked UHMWPE acetabular cups, different femoral head sizes and liner thicknesses were analysed. This study focused on the contact stress on the acetabular cup. Therefore, the femoral head was modelled as an analytical surface. Since the moduli of the femoral head and the shell are significantly higher than the liner, these two components were treated as rigid bodies. This approach has been taken forward in subsequent studies as it saves computational running time due to reduced element numbers (Hua *et al.*, 2012).

Plank *et al's* study suggested a lower contact stress occurred for crosslinked UHMWPE than the conventional material in all the examined sizes (Figure 1.16). It also indicated that the use of larger highly crosslinked UHMWPE head sizes with 3mm liner thickness resulted in lower stress than conjunction of smaller conventional head with 3 mm liner thickness. The FE analysis also represented a

consistent result with experimental measurement of contact pressure by use of Fuji film.

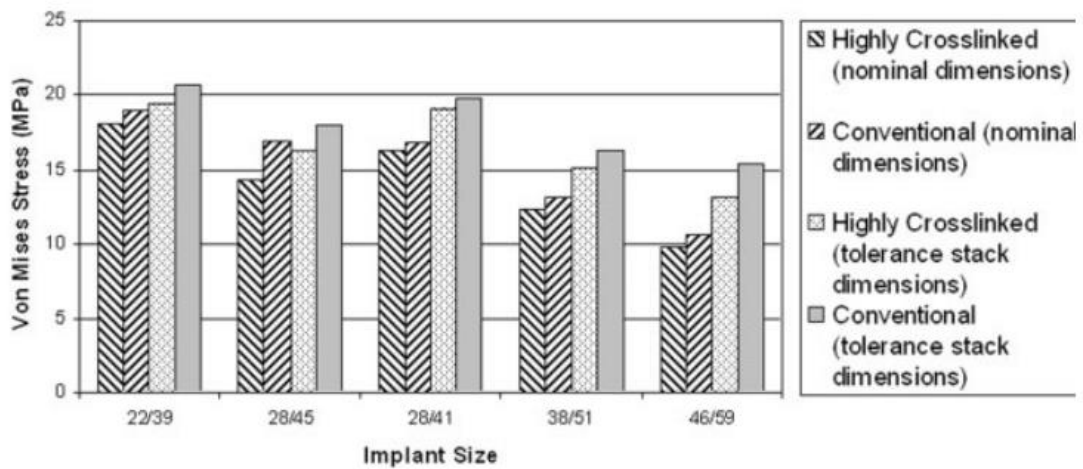
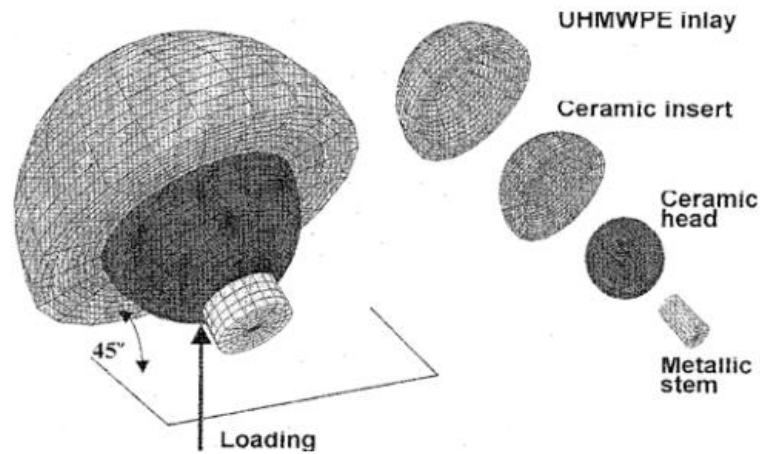


Figure 1.16 Maximum stress of FE models of THR using conventional and highly cross linked ULHMWPE (Plank *et al.*, 2005)

#### 1.4.5 Three dimensional hip models under microseparation condition

There have been a small number of three-dimensional finite element models of THR that studied the effect of microseparation, cup inclination angle, cup abduction angle, and radial clearance between the femoral head and the cup on the contact mechanics of articulating surfaces of THR (Mak and Jin, 2002; Sariali *et al.*, 2012; Hua *et al.*, 2014). Mak *et al* THR model (Figure 1.17) consisted of alumina femoral head and bearing insert, metal stem and shell, and polyethylene backing. An assumption was made that fully bonded interfaces occurred between backing and insert and also between femoral head and stem, allowing concentration on the contact of the femoral head and bearing insert in a range of different microseparation conditions. The radial clearance was assumed to be 0.04 mm and thickness of the bearing as 5mm. A simple analysis was firstly followed to determine when microseparation would lead to edge loading. Frictionless contacts were assumed.



**Figure 1.17 THR modelled by Mak et al with 45° cup inclination angle (Mak and Jin, 2002)**  
 The result of this study suggested that the microseparation which is required to cause edge loading of the THR is inversely proportional to the cup inclination angle and proportional to the radial clearance. Furthermore, it was observed that smaller microseparation is required in hard-on-hard bearings to cause edge loading due to close conformity and small clearances. This study also showed that microseparation less than 80µm does not cause edge loading. However, when the microseparation was increased to 120µm, the contact pressure was increased significantly due to the contact of the head with the edge of the cup. Furthermore, this study suggested that when microseparation was increased to 250µm, the cup with the filleted edge had a great effect on reduction of the contact pressure compared with the sharp edge.

Sariali *et al* (2012) attempted to determine the effect of high cup abduction angle on contact mechanics of articulating CoC bearings with different microseparation values. A 32mm ball with 30µm radial clearance was modelled in normal conditions (45° abduction angle and 0° anteversion angle) and for variations of cup abduction angle (45° to 90°). In the normal condition, it was indicated that lateral microseparation greater than 30µm caused edge loading. However, smaller values of microseparation caused edge loading when a larger cup abduction angle was involved. In the condition with no microseparation, the value of contact pressure

increased from 66MPa under normal conditions to 137.2 MPa in 90° cup abduction angle and up to 200MPa when 240µm lateral microseparation was obtained. Figure 1.18 shows the increase in contact pressure in the THR as the cup abduction angle increased. This study focused on the effect of microseparation on a specific point during the gait cycle (swing phase when the most microseparation occurs). However, the loading on the hip is dynamic during the gait cycle and it varies significantly with time; the contact mechanics could be affected by this variation in the loading.

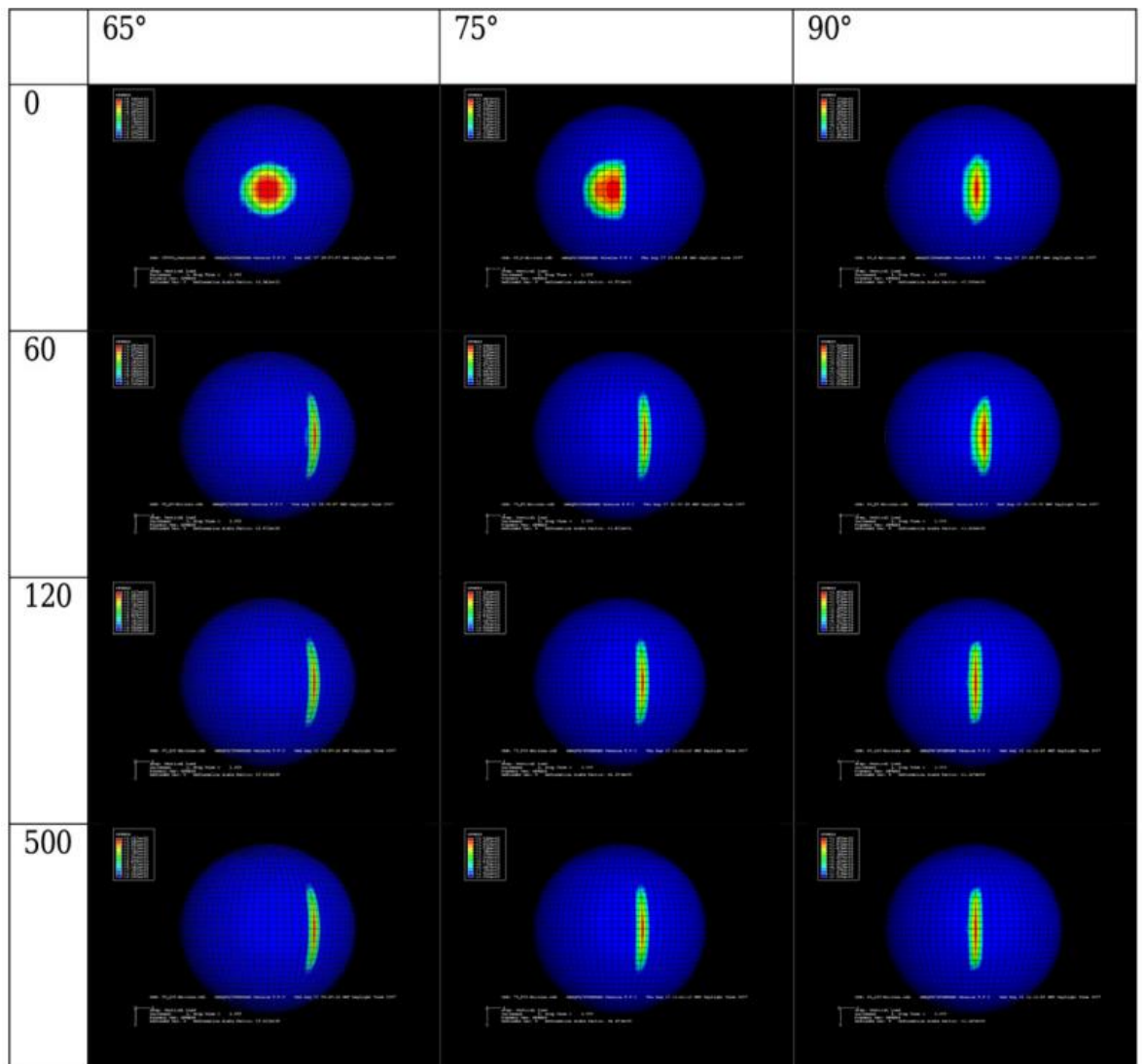


**Figure 1.18 Contact pressure analysis of the CoC THR model under 0-500 µm lateral microseparation and 65° to 90° condition (Sariali *et al.*, 2012)**

A study on edge loading of cemented hard-on-soft bearings was carried out recently to examine the effect of cup inclination angle on contact mechanics and cup fixation

of THR (Hua *et al.*, 2012). An UHMWPE acetabular cup with a 22.2mm diameter metallic femoral head and 0.1825mm radial clearance was modelled. Cup inclination angles from 45° to 65° were simulated with penetration of femoral head to UHMWPE cup ranging from 0 to 4mm. As Figure 1.19 represents, the contact pressure increases significantly when no penetration is achieved but the contact pressure with different non-zero penetration rates only slightly varied. This study suggested the sensitivity of the hard-on-soft bearings to cup inclination angle changes is less than hard-on-hard bearings (Liu *et al.*, 2005). Furthermore, the maximum von Mises stress in the cement mantle occurred at the cup/cement interface. Comparison of different conditions indicated that the highest von Mises stress in the cement mantle occurred when there is 65° inclination angle with 4mm penetration due to reduction in the cup thickness.

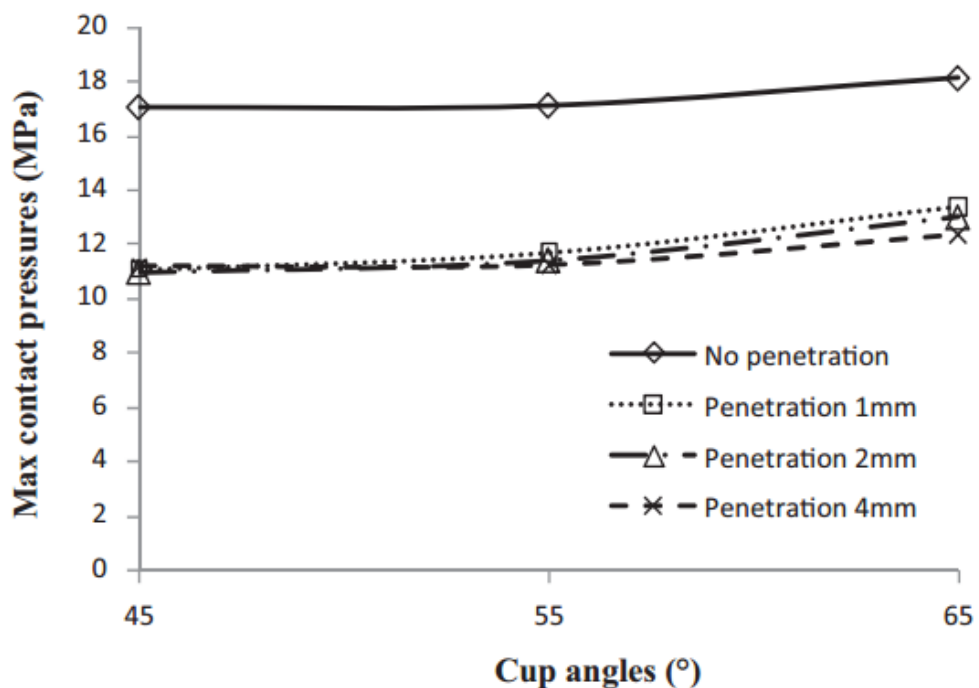


**Figure 1.19** Contact mechanics analysis of MoP THR in different penetration rate (Hua *et al.*, 2012)

The previous studies that were discussed proved that when microseparation is combined with lateral displacement or excessive cup inclination and abduction angle, the contact of rim of the cup and head occurs and this leads to increased

contact stress. A new FE model of THR was carried out to predict the effect of different cup rim geometries on the increased stress (Mak *et al.*, 2011). In this study, a 28 mm diameter CoC THR with 40  $\mu\text{m}$  radial clearance was modelled and microseparation distance was selected to be between 0 and 250  $\mu\text{m}$ . As Figure 1.20 shows, three different edge geometries were investigated: as new, worn, and chamfered (rim geometry after 1 million cycle of tested product in hip simulator under microseparation conditions). It was interesting to note that different rim geometry affected the distance for the onset of rim contact. When edge contact initiated, the maximum contact pressure was greater if the contact area was less. The maximum von Mises stress (672 MPa) under 250  $\mu\text{m}$  microseparation was the greatest in the 'as new' geometry. When the contact area becomes greater due to rim geometry changes, the contact pressures decrease to 425 MPa and 437 MPa in worn and chamfered rims, respectively.

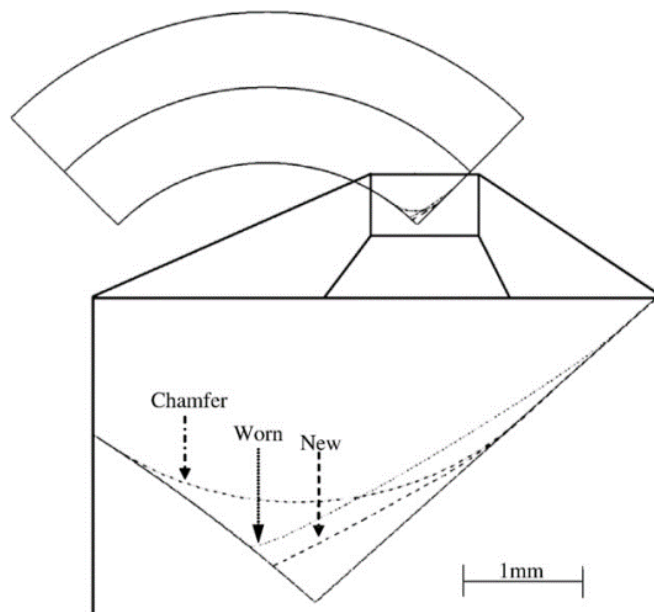


**Figure 1.20 Three different geometry of cup rim in Mak *et al.* study (Mak *et al.*, 2011)**

All of the computational studies on the contact mechanics of THR under microseparation conditions try to replicate the conditions of a specific time frame in a gait cycle using a static calculation at that time, such as the time period when maximum load occurs or when the separation is at the maximum level (minimum

axial load). However, the gait cycle is a dynamic system and therefore the THR experiences a varying load throughout the cycle. A simple static model may not report accurate data from its calculations as the location of the contact will vary due to the loading changes. Further, in these studies the position of the THR components is estimated based on the experimental separation levels or various separation levels were tested to the model directly. Then, contact mechanics of the bearings were analysed when a load is applied (Sariali *et al.*, 2012). Contact mechanics of articulating surfaces in the hip replacement have been analysed statically when a single load or series of load is applied to the prostheses. This means in previous studies, specific time frames of a gait cycle have been chosen and the loading conditions of the step were applied to the model statically. Therefore, the studies are controlled by the force rather than the motion which drives the component.

One of the other limitations of this approach is the inability to analyse the relative motions of components of the model during an entire gait cycle, instead using only the simplified loading condition. Since the details of the motion between the discrete points affect the stress state, the static models are not able to analyse the contact mechanics with real conditions especially throughout a gait cycle due to significant changes of dynamic load compared to static conditions (Kayabasi and Ekici, 2007). Consequently, the conjunction of dynamic and FE model is essential to achieve more precise understanding of contact mechanics of THR *in vivo* and *in vitro*. That means a mathematical model needs to be developed to investigate first kinematics such as motion and contact forces throughout a gait cycle (dynamics model) and then carry out static contact mechanics analysis such as contact pressure, stress, and deformation of components on each step (FE model).

### 1.4.6 Coupling of dynamic and contact mechanic analysis

Development of dynamic models of the prostheses to determine joint and contact mechanics during a dynamic loading condition is the best tool to predict the relative motion and kinematic analysis accurately. The number of dynamic studies on the THR are limited as the hip joint is a ball and socket geometry and the contact is usually stable. However, the dynamic studies of THR have been developed when the idea of edge loading and increased wear were introduced due to substantial changes in the contact condition. The most kinematic and contact mechanic integration analyses have been carried out on the total knee replacements (TKR). Table 1.6 summarises the number of these dynamic and contact mechanics studies that were carried out on knee and hip replacements.

**Table 1.6 previous studies on coupling of kinematic and FE methods of THR**

| Number | Model                          | Finite element solver method | Reference                                |
|--------|--------------------------------|------------------------------|--|
| 1      | 2D model of TKR                | Implicit                     | Reeves <i>et al.</i> , 1998              |
| 2      | 2D model of non-conforming TKR | Implicit                     | Estupinan, Bartel and Wright, 1998       |
| 3      | 3D model of TKR                | Explicit                     | Godest <i>et al.</i> , 2002              |
| 4      | 3D model of TKR                | Explicit                     | Halloran, Petrella and Rullkoetter, 2005 |
| 5      | 3D model of TKR                | Explicit                     | Baldwin <i>et al.</i> , 2009             |
| 6      | THR as a pendulum model        | Explicit                     | Liu <i>et al.</i> , 2010                 |
| 7      | 3D model of THR                | Explicit                     | Gao <i>et al.</i> , 2015                 |

In order to solve a dynamic finite element problem, the analysis requires incremental load or displacement steps (ABAQUS 6.12 documentation, 2012). In each step, several linear equations, which are represented as a system called 'stiffness matrix', need to be solved. There are two methods which can to solve these and generate dynamic solutions. One of the methods calculates the state of the incremented step from the solution of the stiffness matrix from previous step using

a forward Euler Method. This method is called an explicit solver. Another way to solve the dynamic model requires the stiffness matrix of the current state of the system, and the stiffness matrix of the incremental step. This method is called backward Euler's method which is implicit (ABAQUS 6.12 documentation, 2012).

Reeves *et al* (1998) and Estupinan *et al* (1998) studied the cyclic dynamic loading effect on UHMWPE behaviour by generating 2D and idealised 2D model of TKR implicitly. The disadvantage of using implicit solver for dynamic analysis is the long time it takes to solve the equations. Therefore, the models are restricted to two-dimensions and these 2D models might provide valid information about the central plane of contact. However, the stresses and deformation of THRs in the medial-lateral direction have not yet been investigated using this approach (Estupinan *et al.*, 1998; Reeves *et al.*, 1998).

Explicit models of joint replacements, mainly total knee replacements, have been generated to predict the kinematic and contact mechanics under dynamic loading and avoid the problems encountered by the Reeves and Estupinan groups (Godest *et al.*, 2002; Halloran *et al.*, 2005; Baldwin *et al.*, 2009). These studies used mechanical knee simulators for direct experimental validation. Therefore, the boundary conditions of the models were adjusted to simulate the mechanical knee simulator environment. In these studies, the contact force was defined to be a function of penetration distance of master into slave surface (penalty-based method). These dynamic studies are difficult to compare directly to previous static ones due to different loading, boundary conditions, and different implant geometries.

The explicit models of TKR are able to simulate the soft tissue actions which have not been considered in implicit models. The explicit models allow 'buckling' of soft

tissue whereas implicit models would cause stability problems if buckling occurs. Soft tissue behaviour was simulated differently in each study. Godest *et al* (2002) defined two planar joints to simulate the springs in the simulator that perform as soft tissues. Halloran *et al* (2005) used spring elements to constrain any internal-external and inferior-posterior displacement. In the most recent study, the tendons and ligaments around the knee were represented in a more complex but more realistic way by fibre-reinforced composite material model that consist non-linear, tension only springs embedded in a low-modulus, hyper elastic deformable 2D quadrilateral mesh (Baldwin *et al.*, 2009).

Godest *et al* (2002) studied the effect of mesh density, time steps, and coefficient friction on AP displacement, IE rotation, and internal stresses within a single analysis. At first, the axial force, anterior-posterior force, torque, and flexion angles a function of gait cycle were represented based on the boundary conditions. In this study, minor variation between the theoretical kinematic data and experimental value was seen. The exact coefficient of friction between polyethylene and metal was unknown. Also, the mass and the inertia of the fixtures of knee simulators were ignored (Godest *et al.*, 2002). In engineering, dynamic model usually involves rigid body assumptions and rigid body analysis does not calculate internal stress and strain of each element. Therefore, a softened contact which does not consider internal stress was defined when the interaction occurs (Godest *et al.*, 2002).

Halloran *et al* (2005) and Baldwin *et al* (2009) developed explicit model of Stanmore knee simulator, Purdue knee simulator, and Kansas knee simulator to study tibio-femoral and patella-femoral articulation using two different methods (Halloran, *et al.*, 2005):

- 1) Fully deformable model

## 2) Rigid body analysis

The rigid body model was used to analyse the kinematic data with significantly shorter computational time. However, a softened contact capability had to be defined to be able to study contact mechanics of the model. In both studies the kinematic data was determined and the data were experimentally validated. In the Halloran group's study, the kinematic data approached a good agreement although the same assumptions of material properties of polyethylene and same coefficient of friction as Godest *et al* study were used. Both rigid body analysis and fully deformable models gave reasonably close data (Figure 1.21). However, it should be noted that use of softened contact also requires estimation of non-linear pressure-overclosure relationship by material property data. A limitation of this method is the significant central processing unit (CPU) time usage of a fully deformable analysis.

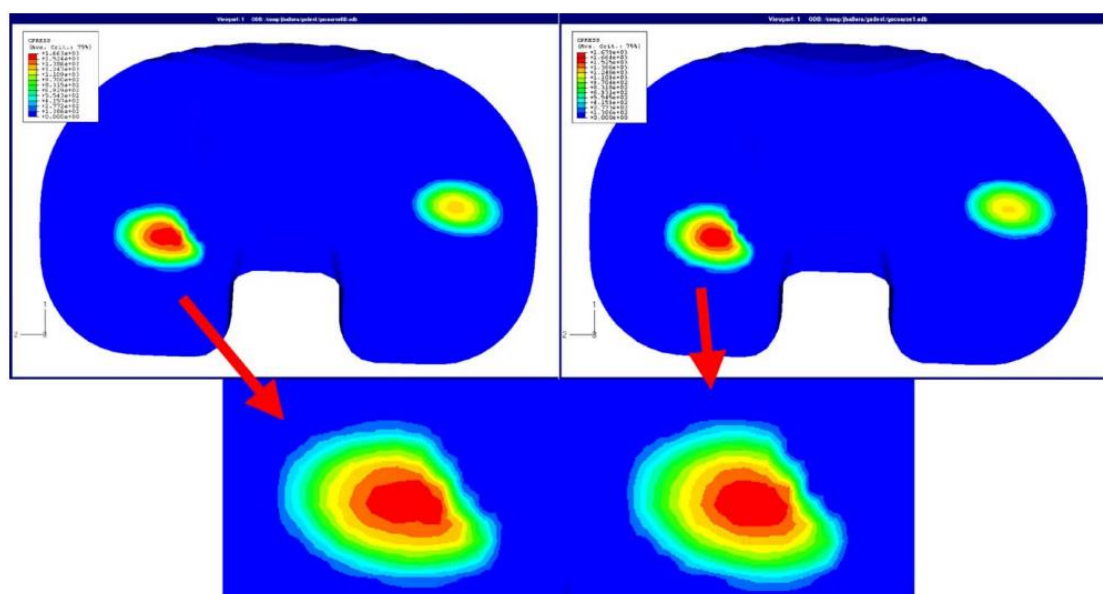


Figure 1.21 Contact pressure contour comparison during the gait cycle for both deformable (left) and rigid body (with softened contact) (right) analyses *et al*, 2005)

### 1.4.7 THR dynamic modelling

Liu *et al* (2010) tried to simulate MoM, CoC, and MoP resurfacing total hip replacement in a simple pendulum model to study THR dynamic and contact

mechanics analysis of the component interaction. The THR was simulated as a ball in socket geometry of the fulcrum and the ball was connected to a mass ball by a massless wire (Figure 1.22). Hence, different motion angles and dynamic loading of the mass ball simulated simple kinematic data that a hip joint experiences. This study was carried out using coupled (using explicit model) and decoupled (using explicit and standard) method (Liu *et al.*, 2010).

In coupled method, both dynamic and contact mechanic analyses were carried out in ABAQUS/explicit. However, in the decoupled method, the dynamic response was predicted using ABAQUS/explicit and the corresponding force predicted from explicit model was applied to the ABAQUS/standard model at different time steps to investigate contact mechanics analysis. In the coupled method, the cup was assumed to be a fully deformable model and femoral head was set as analytically rigid body whereas in the decoupled method, the cup was set as analytically rigid body for dynamic analysis. The same boundary conditions and parameters such as elements and mesh were used for both methods.

In the Liu *et al* study, the contact pressure of implicit model was compared to dynamic transient pressure of explicit model. Although both methods predicted adequately the dynamic and contact mechanics under the conditions, the decoupled method was more efficient in predicting THR performance. The main limitation of this study was the difference in the dynamic response and motion angle of the pendulum model (Figure 1.22) to the gait cycle. The pendulum model response force and motion angle were similar to sinusoidal and cosinusoidal waveforms, respectively. However, the gait cycle consists of various loading conditions including swing and stance phase and its motion is more like 'V' shape with different maximum and minimum values. Also, this study did not consider the effect of

muscle forces on the analysis. It only applied the body weight which is considered to the hip joint during a walking cycle.

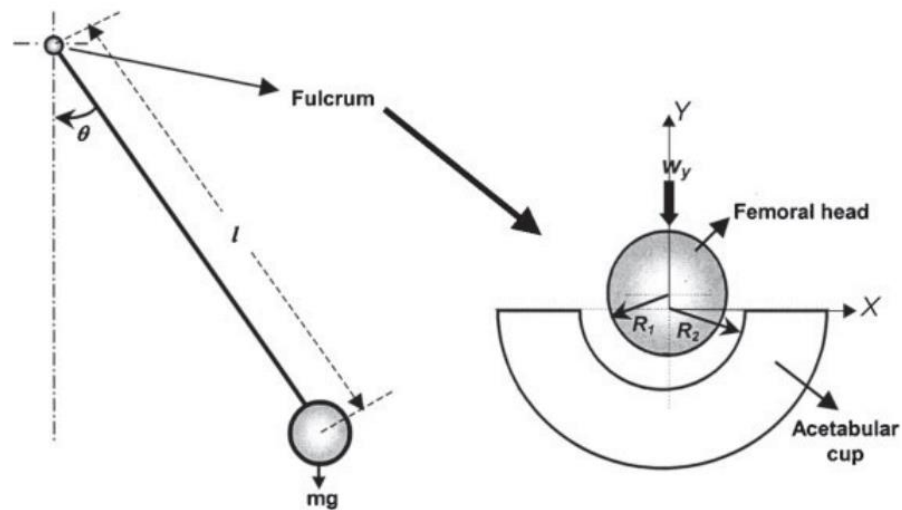


**Figure 1.22** The pendulum model used in Liu et al study (Liu *et al.*, 2010)

Three dimensional dynamic and contact mechanics modelling of the THR is still under development and most of the studies in this area only present the development criteria of this type of modelling and do not draw significant conclusions. Gao *et al.*, studied the explicit modelling of the THR under normal walking cycle (Gao *et al.*, 2015). In this study, the range of motion and anatomical loading of the THR (Figure 1.23) was applied to the explicit method model to justify the use of explicit method. The study contrasts the explicit method to the implicit and analytical methods, and also aims to show the accuracy and efficiency of the explicit method. Mesh sensitivity analysis and time steps were examined on the contact pressure and sliding distance of the hip with respect to the cup. This study shows that explicit method is a useful method to predict and capture the contact pressure and accumulated sliding distance for THR in a gait cycle. However, this study is limited to one set of normal walking activity and it does not recommend that explicit modelling is a convenient method for a range of activities when the stability is significantly less.

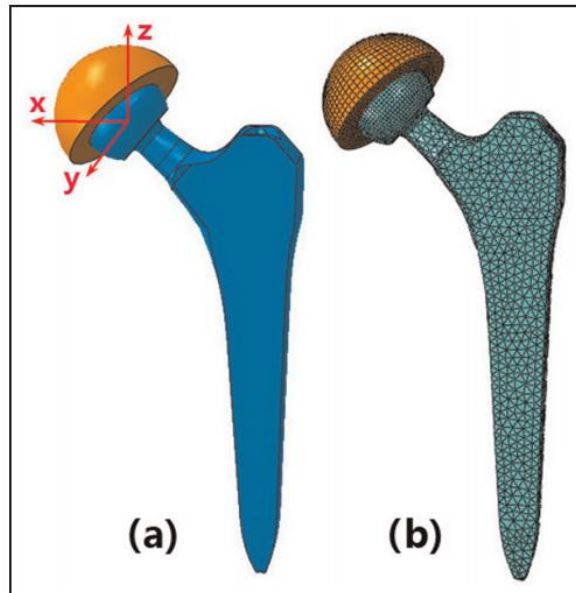


Figure 1.23 a) CAD and b) FE models of an artificial hip joint in Gao et al study (Gao *et al.*, 2015)

### 1.4.8 Wear modelling

Another type of modelling that is carried out on THRs is wear modelling. Wear modelling has focused on wear of hard-on-soft bearings, initially made from polyethylene (Maxian *et al.*, 1996; Wang *et al.*, 1998), and more recently has evolved with the technology to model hard-on-hard bearings (Liu *et al.*, 2008). In these wear models, the formula for wear prediction based on sliding distance, load and the wear factor which is assumed to be constant throughout the analysis. Other factors that are considered in wear studies are the lubrication form and the thickness which affects the wear directly (Mattei *et al.*, 2011). The wear studies are used to predict the wear scar on the bearing surfaces and the film thickness. However, the assumption of constant wear factor does not allow a realistic wear prediction against the experimental studies as the wear factor varies based on the load, velocity and the loss material volume (Mattei *et al.*, 2011).

## 1.5 Summary

The performance of THR devices can be affected by the quality of the tissues surrounding the joint or the mismatch of the component centres during hip replacement surgery. Experimental studies have shown that these factors can cause

the separation of the two components during the walking cycle (dynamic separation) followed by contact of the femoral head with the rim of the acetabular liner (edge loading), which can lead to stripe wear on the components, increased wear and shortened implant lifespan (Nevelos *et al.*, 2000; Williams *et al.*, 2003; Al-Hajjar *et al.*, 2010). It is therefore important that pre-clinical testing includes the assessment of THR devices under adverse conditions and differentiates the factors that have the most effect on the THR performance.

A precise computational model could be a useful tool to:

- 1) Provide in depth insights on THR behaviour during activities.
- 2) Understand the effects of various clinically-relevant parameters on the microseparation and contact mechanics.

As Table 1.7 represents, 2D and axisymmetric models of THRs are useful tools for gaining an initial understanding of the parameters of interest on the contact mechanics. However, the conditions of the 2D and axisymmetric models such as no consideration of third plane stress and the non-anatomical contact and load inputs limit their application for realistic simulation of THR performance.

**Table 1.7 Summary of the advantages and limitations of different FE modelling types**

| Modelling type | Main advantage  | Main limitation   |
|----------------|---|---|
| 2D             | Simple and quick solution.                                  | The stress in the third plane is neglected.   |
| Axisymmetric   | Simple and quick analysis.                                  | Central THR contact of the surfaces is assumed.   |
| 3D             | More realistic to the experimental and clinical conditions. | Separation could only be applied to the model rather than a measurement.<br>The load changes during gait cycle is not considered. |

The THR undergoes a range of loading in an activity. However, previous computational studies of the THR have modelled the loading cycles as a series of static frames that do not take account of the dynamic conditions. Previous computational studies of separation have mostly focused on the effect of microseparation on the contact mechanics of the 3D THR at a specific time of walking cycle (Hua *et al.*, 2012). There are no computational studies that focus on the effect of individual parameters on the separation and contact mechanics of THR under dynamic loading.

The idea of the integrated dynamic and contact mechanic computational model of THR has been recently introduced and there have been only limited initial studies on this area. However, the previous studies mostly report the sensitivity of the models to certain conditions and none of the previous studies incorporating dynamics and contact mechanics have focused on the separation effects.

## **1.6 Aims and objective**

The ultimate aim of this project was to develop a preclinical computational tool in order to examine the effect of clinically-relevant parameters on the separation and contact mechanics of hard-on-soft THRs as the recent analysis have shown that hard-on-soft bearings are the most common THRs that have been used in England (*National Joint Registry*, 2016).

This developed model can have variety of applications in industrial, experimental and clinical perspectives. As this model studies the direct effect of input parameters on the separation and contact mechanics, the source of THR weakness in adverse conditions can be detected and consequently, the design, material combinations and the positioning of the bearings can be optimized to reach higher tolerance to edge loading. Moreover, the durability of THR can be potentially prolonged for more

active and young patients when the component is less affected by wear due to the separation and edge loading. Although, *in vitro* testing has been carried out under adverse conditions to study the wear rate of the THR, this is the most applicable method to analyse the hip implants in a clinical and experimental environment that is cost and time effective. This model could be used as a tool to analyse the effect of wide range of parameters on the outcome and the most crucial parameters can be tested *in vitro*.

To achieve this aim, a finite element model of the THR was developed that could simulate the dynamic motion during a gait cycle and predict the THR separation and contact mechanics. The developed computational model replicates one station of an existing hip simulator so that comparisons could be made for validation purposes. The following objectives were set to achieve the aim of the project (Figure 1.24):

- Develop an explicit dynamic FE model of a simplified THR under concentric conditions that replicates one station of Leeds II hip simulator and examine the effect of computational modelling choices on the outputs (This work is presented in Chapter 2).
- Develop an explicit dynamic FE model of a Pinnacle ceramic-on-polyethylene (DePuy Synthes) THR under adverse conditions including a mechanism for separation during swing phase (This work is presented in Chapter 3).
- Study the effects of varying clinically relevant parameters, namely, the translational mismatch level, the rotational variation and the swing phase load on the dynamics of the THR. (This parametric sweep is presented in Chapter 4).

- Validate the computational model output against existing experimental data by comparing the *in vitro* and *in silico* separation (This work is presented in Chapter 4)
- Examine the effect of translational mismatch level, rotational variation and swing phase load on the THR contact mechanics including the contact pressure and stress components that cannot be measured experimentally (These additional output of the parametric sweep is presented in Chapter 5).

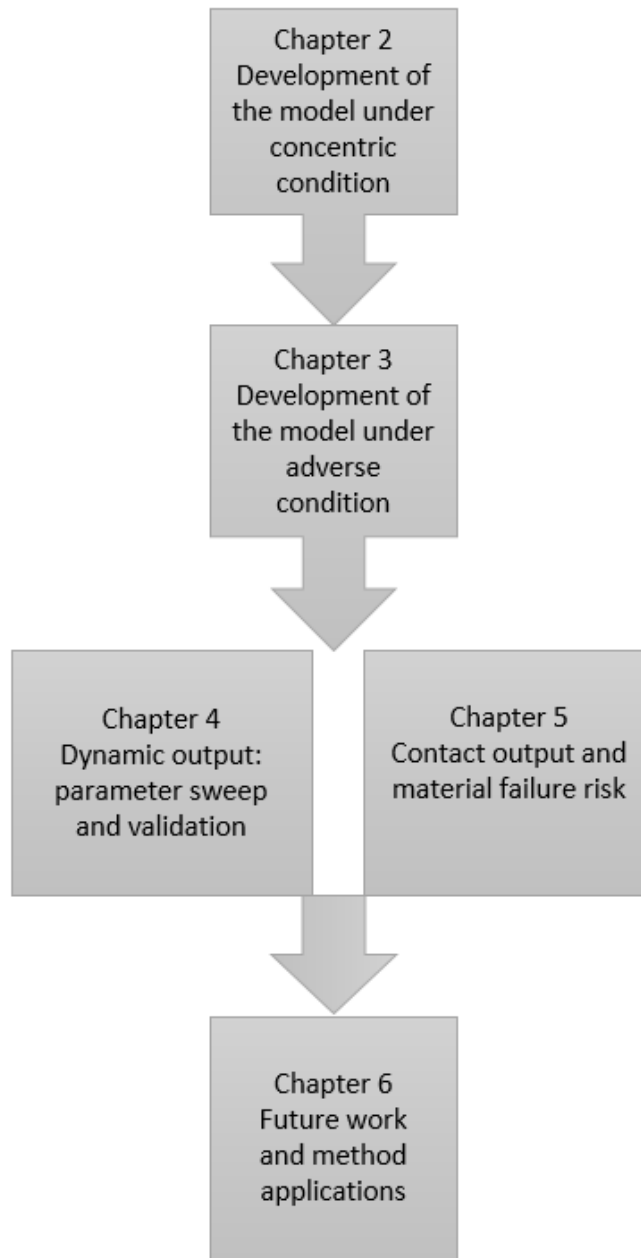


**Figure 1.24 The flowchart and order of the chapters with a brief description of the chapters focus**

## **Chapter 2    Development of the explicit model under concentric loading conditions**

### **2.1 Introduction**

The foremost aim of this project was to develop a computational model of a total hip replacement (THR) to study the effect of parameters, such as surgical malpositioning, on the contact mechanics of THR during walking. Subsequently, validation of the model with existing *in vivo* or *in vitro* studies is required in order to examine its reliability and accuracy. Therefore, for validation purposes, the computational model was established to replicate the Leeds II hip simulator. This simulator has the capability to test the effect of adverse conditions on the biomechanical and wear behaviour of THR.

To achieve a representative three-dimensional model of the Leeds II hip simulator, the features of the experimental set up need to be implemented within the model as accurately as possible. If the model is simplified to the most basic conditions, the effect of each parameter can be studied separately and gradually increase the complexity of the model. This method would allow the determination of which parameters have the most and the least effect on the analysis – i.e. the sensitivity of the model. Therefore, more engineering effort can be spent on the factors to which the model is most sensitive and less consideration to the factors which have only negligible effect on the results. The model was developed gradually by investigating a standard (concentric) scenario as well as an adverse condition scenarios. The model development under standard conditions provide information on the fundamental computing factors and provides a benchmark with which to compare results from further analyses. The effect of adverse conditions on the overall computational model behaviour can be observed when adverse conditions are

applied in the further steps. These adverse effects can be studied individually, or built into a singular model to study their interdependencies.

This chapter focuses on the initial development of the ceramic-on-polyethylene THR model under standard conditions. In this chapter the overall replication of the Leeds II experimental set up such as components movement and loading is described. To be able to achieve a computational model that produces reliable contact mechanics analysis, the components movements and axial loading should be applied to the model correctly as the contact mechanics are directly affected by the loading and the kinematics. Furthermore, the effect of computational parameters, namely mesh sensitivity analysis, contact algorithms, and loading methods, on the model outputs are is considered.

## **2.2 Experimental setup of Leeds II hip simulator**

The Leeds II simulator is a physiological and anatomical hip joint simulator that has been used to test the Pinnacle THR under standard and adverse conditions (Al-Hajjar *et al.*, 2010), specifically translational mismatch level, cup inclination variation and tissue laxity. This simulator consists of six identical stations, in each station of which, there is a stem holder that fixes the femoral stem which carries the femoral head on top (Figure 2.1). The cup unit is located at a certain inclination angle above the head and carries the metal shell and the acetabular cup in such a way that the surface of the acetabular cup articulates with the femoral head. There is a 10° difference between the clinical and simulator inclinational angle due to the 10° difference in the clinical and experimental loading angle (Williams *et al.*, 2003). An axial load is applied to the model via a load cell that is located on top of the cup holder. There is also a spring attached between the wall of each station and the cup unit horizontally to allow different levels of translational force to be applied. Each

station is filled with a lubricant (bovine serum) to replicate the lubrication of THR *in vivo* and minimise the coefficient of friction between the components.

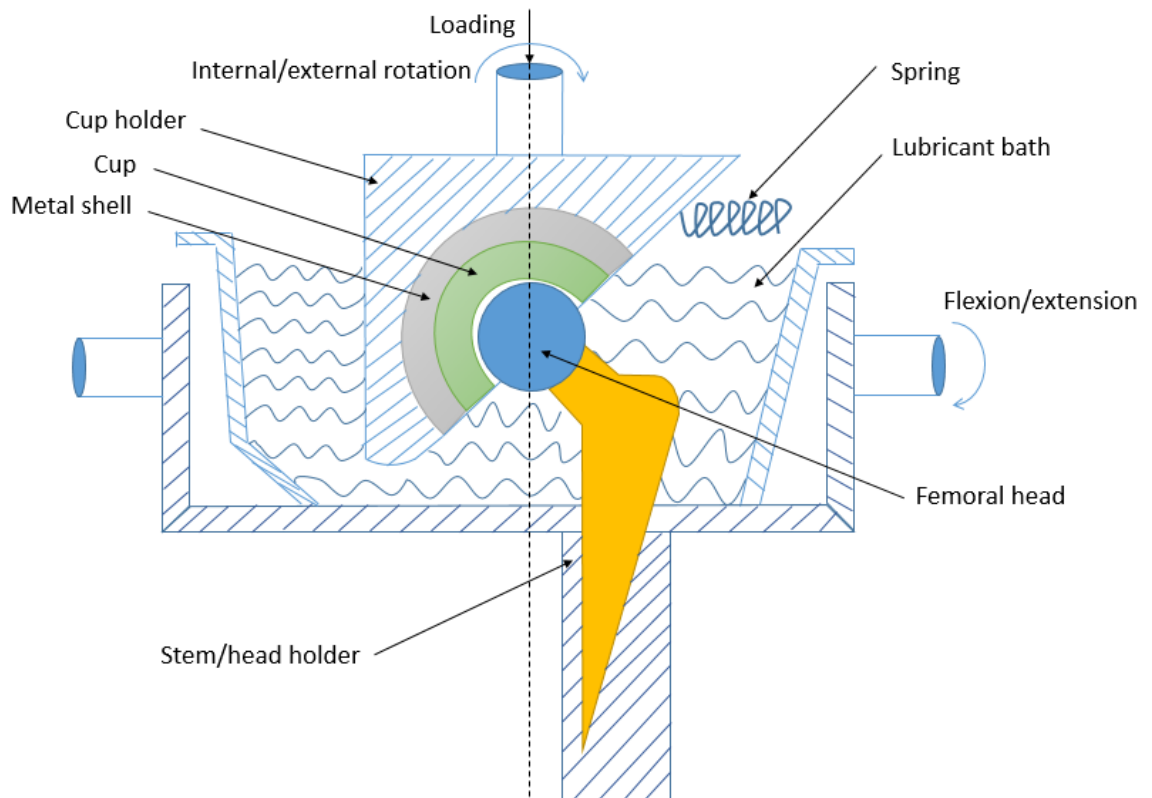


**Figure 2.1 Schematic of the experimental set up of Leeds II hip simulator with rotation and loading locations indications**

In the simulator, the THR components are taken through specific movements to simulate the walking pattern of the patient's right hip. During the gait cycle, the cup is driven to move medial-laterally and rotate internal-externally. However, the cup is free to translate anterior-posteriorly and superior-inferiorly. Moreover, the flexion-extension of the hip is implied through the femoral head. There is an axial load applied through the cup to the hip joint on each station. Figure 2.2 represents the Paul twin peak cycle load (Paul, 1976) as per ISO 14242-1 (2002) that is a representative of the load which the hip undergoes during walking. The load cell is located on top of the cup unit and it records the load applied vertically downwards on the cup. When no axial load is applied to the model, the horizontal spring separates the cup and the head and applies a translational mismatch level. Maximum

load in the stance phase causes maximum compression of the spring level, whereas low load during swing phase results in partial compression of the spring and contact of the head with the lateral edge of the cup.

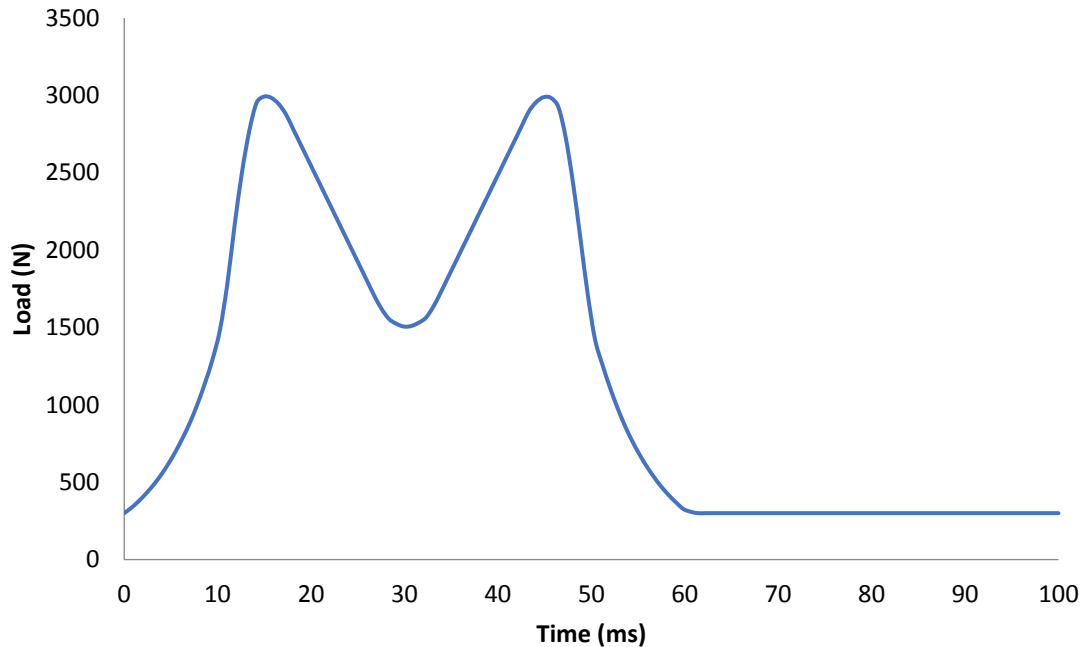


**Figure 2.2 Example of Paul cycle loading in Leeds II hip simulator (Paul, 1976; Al-Hajjar et al., 2013)**

### **2.3 Design of numerical study**

As dynamic modelling of the artificial hip joint is novel, the main aim of this analysis was to gain a fundamental understanding of dynamic analysis within the explicit ABAQUS software package (Version 6.14, Dassault Systèmes Simulia Corp., Providence, United States). The main outcome of this specific study was to investigate the level of sensitivity of contact mechanics analyses to the computational factors that can directly influence the contact mechanics of the model.

If the initial development includes the full complex geometry, a wide range of movements of the components and a holistic loading profile as well as parameters within modelling such as mesh density, contact algorithms and loading and boundary conditions, the complexity of the model will be increased considerably.

Therefore, if all the parameters are analysed at the same time, fault finding and diagnostics during the model development would be considerably more challenging. The time taken and computational cost to solve the model is increased with model complexity, and there is no guarantee at the early stages that the engineering effort is directed toward the most significant factors.

A representative dynamic model of the Leeds II hip simulator was therefore analysed for the initial results. This model consisted of simple geometry and loading with no motion, thereby eliminating the meshing and movement complexity effect for preliminary examination of the model behaviour. The results presented in this chapter are for this simple model.

Incremental development of the model in terms of loading, motion and geometry was carried out, verifying the computational results at each stage by comparison with the experimental results from the simulator.

The meshing configuration plays an important role in the reliability and efficiency of the contact mechanics output. Therefore, one of the parameters that this study focuses on is the mesh sensitivity in terms of mesh density and element ratio of the contact surfaces. Another factor that is taken into consideration is the contact algorithms between the contact surfaces. There are numbers of numerical contact solutions for contact mechanics analysis that are described later in this chapter. Also, due to dynamic modelling dependency to the running time, the effects of loading and preloading on the contact mechanics analysis are studied. Several output parameters, namely contact pressure and contact area, that are good representatives of the contact conditions are analysed. Furthermore, to understand any difference between the input and output forces, the reaction forces of the

analyses are investigated. Finally, a static loading analysis of the model with the same configuration was carried out to verify the outcome of the dynamic model.

## **2.4 Methods of Numerical Analysis**

This project ultimately focussed on the contact mechanics of the adverse loading scenario. The numerical contact calculation is directly affected by the applied contact algorithm. Hence, it is important to select a contact algorithm that represents the most robust outcome with respect to the model application. The finite element analyses were solved using ABAQUS software (Version 6.14, Dassault Systèmes Simulia Corp., Providence, United States). In this section the types of dynamic solving processors and contact algorithms available in ABAQUS are defined.

### **2.4.1 Dynamic solving processors**

ABAQUS provides two types of dynamic stress-displacement solving processors; Implicit and Explicit (ABAQUS 6.14 documentation version 2014). Figure 2.3 represents the difference in the explicit and implicit approaches.

The implicit solver is a direct integration dynamic procedure that integrates the equations of the motion. In order to solve the model using the implicit solver, inversion of the stiffness matrix ( $k$ ) and stating a set of nonlinear equilibrium equations are required at each time increment. Implicit solver uses equilibrium equations to solve for time  $t+\Delta t$  using state data at both  $t$  and  $t+\Delta t$ . The size of the stiffness matrix which depends on the degrees of freedom of the model, determines the computational time and cost of the analysis as it must be inverted at each iteration.

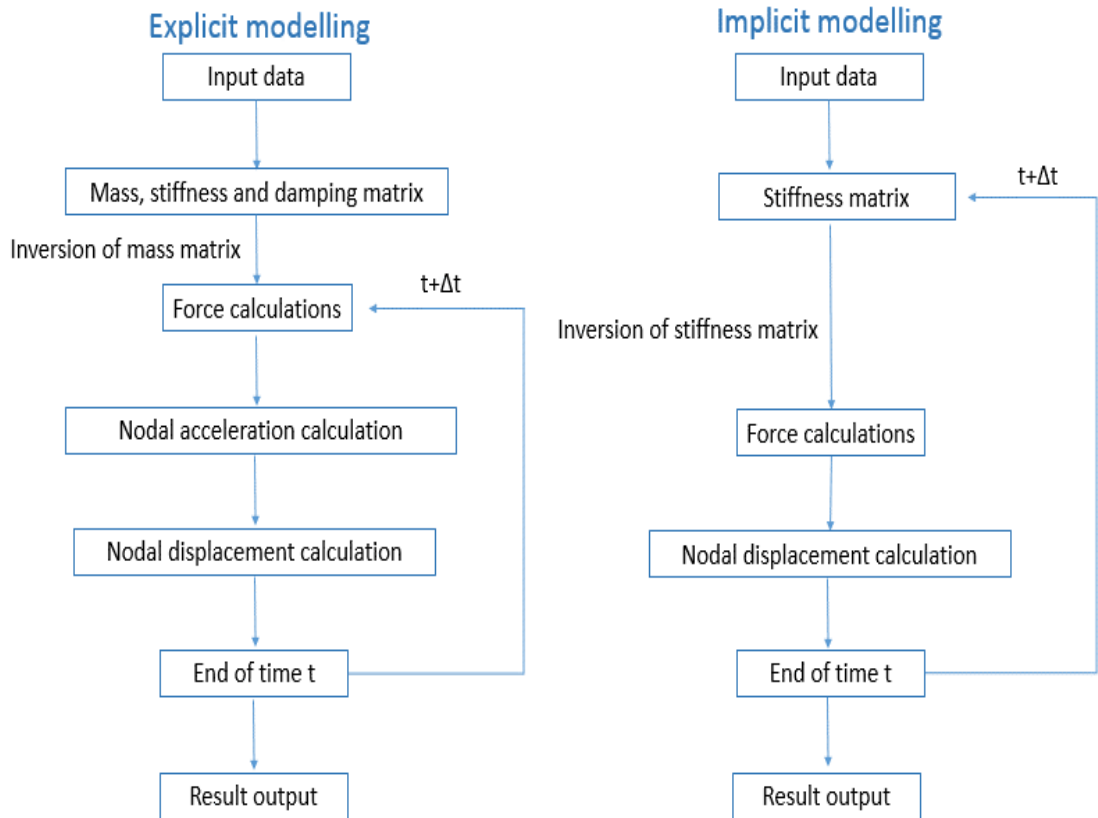


**Figure 2.3 The difference in explicit and implicit approaches of output calculation**

An explicit solver is a central-difference method that calculates the displacements and velocities at the beginning of each time increment. The explicit approach requires inversion of the lumped mass matrix instead of the stiffness matrix as in implicit. The explicit approach solves for time  $t + \Delta t$  using the state at  $t$  only. Since the explicit solver does not require to solve a set of equilibrium equations, the computations are less expensive than for the implicit solver. However, due to the nature of the explicit solver, the stability of the model for an optimum solution is strongly dependent on the time increments. Therefore, to achieve the required stability in the explicit solver, the time increments are considerably shorter. The time increment for stability in the explicit solver is conditional on the time that an elastic stress wave takes to cross the smallest element in the model. Hence, if there are very small elements in the model, the stable time increments become very short. However, there are methods such as mass scaling that artificially increases the mass

of certain elements stability, to reduce the wave speed and as a result, increase the overall stable time increments. The advantages and disadvantages of each method is presented in Table 2.1.

The model stability is not a concern in an implicit solver as equilibrium equations are an essential calculation of this solver. Moreover, a number of iterations can happen within one time step to reach a solution in an implicit solver whereas the explicit solver only calculates the solution for each time step once. If the explicit solver is suitable for the required application, the explicit solver could provide the less expensive and time consuming compared with the implicit method.

**Table 2.1 Comparison of advantages and disadvantages of implicit and explicit approaches in ABAQUS**

| <b>Method</b>   | <b>Advantages</b>   | <b>Disadvantages</b>  |
|-----------------|---|---|
| <b>Implicit</b> | <ul style="list-style-type: none"> <li>*Equilibrium equations used</li> <li>*Stability independent of time increment</li> </ul>                                   | <ul style="list-style-type: none"> <li>*Reconstructing the stiffness matrix at each increment</li> <li>*Iteration required within time increment to reach a solution</li> </ul> |
| <b>Explicit</b> | <ul style="list-style-type: none"> <li>*Updating the stiffness matrix at each increment</li> <li>*Computationally cheaper</li> <li>*Lower running time</li> </ul> | <ul style="list-style-type: none"> <li>*Less stable</li> <li>*Very small time increments required for stability</li> </ul>  |

### **2.4.2 Contact algorithms**

ABAQUS/Explicit provides two types of algorithm to define contact and interaction problems: general contact algorithm and the contact pair algorithm. Contact pair defines the possibility of contact between two defined surfaces only whereas the general contact introduces the pairing of contact between all of the surfaces.

The 'contact pair' algorithm has more restrictions on the type of surfaces which are in contact compared to the 'general contact'. In the contact pair, the surfaces must

be specified between the two surfaces. Therefore, the general contact algorithm is more convenient in model with many objects with different undefined contacts. The general contact algorithm uses only one method to minimise the overlap of surface nodes in contact while the contact pair algorithm provides an extra option to prevent the penetration of the contact surface elements. Since only the contact between two surfaces, the head and the inner surface of the cup, was of the interest in this project, it was logical to use the 'contact pair' algorithm.

#### **2.4.1.1 Contact constraint methods**

When the kinematic state of the model changes where the contact takes place, penetration of the nodes lying on the contact surfaces occurs. The contact constraint prevents excessive penetration of these contact surface nodes. The contact pair algorithm can use one of two contact methods, namely the penalty or kinematic methods, to enforce contact constraints between the surfaces. The application of the contact constraint depends on the type of contact.

One of the parameters that affects the calculation of contact constraints is the relationship between the two contact surfaces. The contact surfaces in ABAQUS are defined based on the stiffness of the surface due to their assigned material properties. The stiffer surface - usually based on relative Young's modulus value - defined as the master surface and less stiff surface as the slave surface. If there is a pure master-slave surface relationship, then the constraint is always applied to the slave surface. This means that the only penetration which is allowed is that of the master surface into the slave surface. No node on the slave surface can penetrate the master surface (Figure 2.4). If there is a balanced master-slave relationship, each surface would be considered in turn as slave surface and again as master surface. Hence, the contact constraint will be the weighted average of both calculations in

the form of constraint reaction forces. Balanced master-slave contact results in better contact constraint enforcement because of better performance in minimising the penetration between surfaces. Therefore, the balanced master-slave relationship was used in this study.

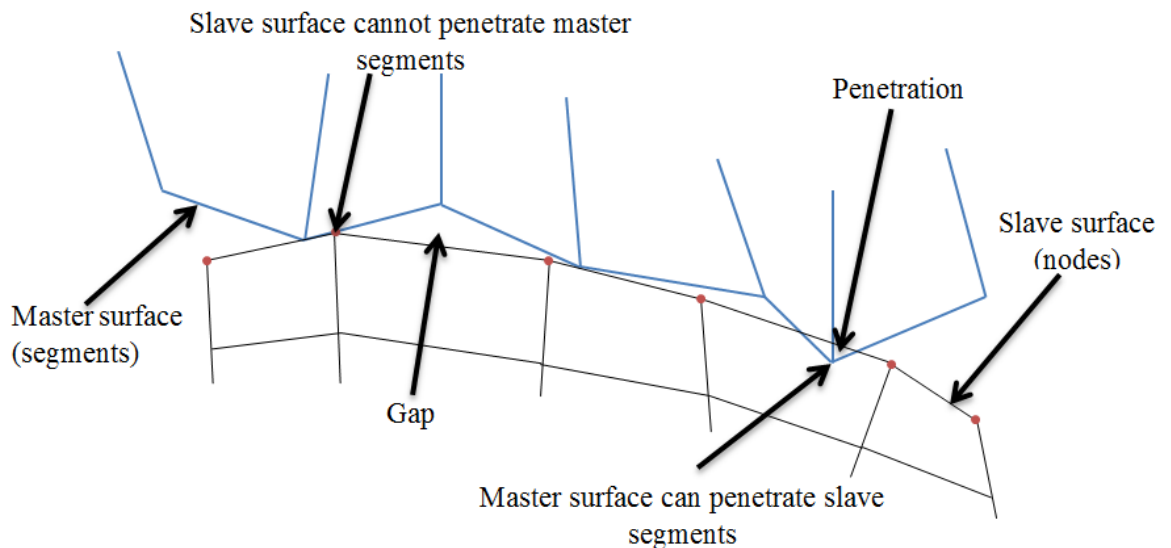


**Figure 2.4 Master-slave surfaces contact constraint in ABAQUS that represent the penetration and gap between the master and slave surface**

Penalty and kinematic contact constraints are the available algorithms for penetration prevention in ABAQUS explicit models. The penalty algorithm considers the current configuration of surfaces nodes and behaves like a spring to return the penetrated node to the contact surface. In a pure master-slave surface relationship, the penalty contact algorithm identifies the slave nodes which penetrate the master surface and applies an equal and opposite forces that are functions of penetration distance to the penetrated slave nodes and the nodes of the master surface being penetrated. The penalty algorithm with a balanced master-slave surface relationship determines the contact forces to oppose penetration using the same approach. However, one set of contact forces are calculated by assuming one surface as a master surface, and the other contact force is calculated using the same surface

as the slave surface. The balanced master-slave surface relationship considers the weighted average value of these contact forces to be applied to the model.

The kinematic contact constraint method uses a kinematic predictor to enforce contact constraint strictly whereas the penalty method applies weaker enforcement of contact constraints. In a kinematic contact algorithm with a pure master-slave relationship, the contact conditions are firstly ignored to estimate the predicted kinematic state of the model. The level of penetration of the slave nodes into master surface, the mass associated with the corresponding node and the time increment are then used to calculate the resisting force to minimise penetration. In case of element face formation of the master surface, the resisting forces and mass of the contact slave nodes are distributed over the master surface nodes to calculate the inertial mass of the contact surfaces and acceleration correction of the master surface nodes. Then acceleration correction for the master surface nodes is applied to determine the acceleration correction of slave surface nodes using the predicted penetration of the nodes and the time increment. These corrected accelerations are required to achieve a contact configuration that can be used to enforce the constraints. The balanced master-slave surface relationship with the kinematic contact algorithm also use the same method. However, the procedure is followed twice because each surface is considered once as a slave surface and another time as a master surface. Hence, the corrected value applied by ABAQUS/Explicit is the weighted average of the two cases.

The ideal contact algorithm to choose depends on the application of the model and types of bodies in contact. There are limits to the type of surfaces which can be used with the kinematic contact algorithm. For example, rigid surfaces are not allowed to be considered as slave surfaces in the kinematic algorithm whereas penalty

algorithm does not restrict rigid surfaces to be mated and therefore allows modelling of contacts between rigid surfaces. Another difference between two algorithms is that the kinematic contact does not affect the critical time increment for stability; however the critical time increment could become affected if the penalty contact is used. The penalty contact algorithm includes a “spring” stiffness which relates the contact forces to the penetration depth. The stiffness of the contact can be changed to minimise the effect of this algorithm on the time increment.

## **2.5 Development of the Numerical Model**

This section presents the methodology for the first stage of the explicit dynamic model development. The analyses that were carried out in this section are separated into three different studies. The common aspects to all models, namely geometry, material properties and boundary conditions in this part of the study are defined in this section. Also, the specifications of the three preliminary studies, mesh sensitivity, contact method effect and loading conditions, on the contact mechanics of the model are described.

### **2.5.1 Materials**

As mentioned above, the model is intended to be simplified to minimise the effect of any geometries complexity on the contact mechanics analysis. Therefore, the preliminary model is composed simply of the femoral head, acetabular cup and the cup holder. The femoral head and acetabular cup are simplified to a simple ball and socket geometry. The details of the real Pinnacle femoral head and cup are not considered at this stage of the model development. The cup unit is modelled as a half sphere which has the same mass as the actual cup unit. Figure 2.5 presents the head, the cup and the cup unit assembled vertically on top of each other.

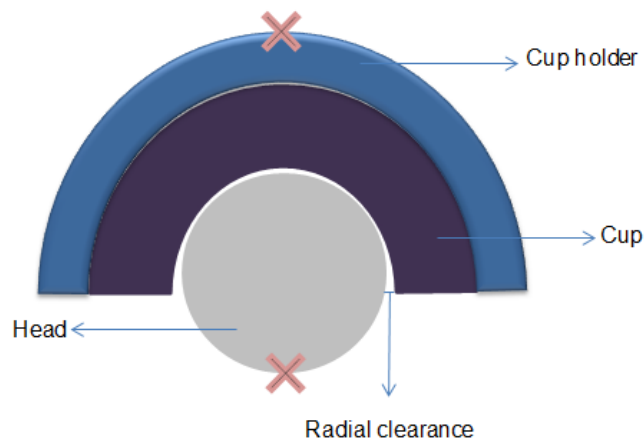


**Figure 2.5 Assembly of the simplified model. The crosses locate the boundary conditions on the head and the cup holder.**

A 'tie' constraint was generated between the inner surface of the cup unit and the outer surface of the cup to prevent all relative movement between the surfaces. To simulate the experimental movements of the components, the head was fully fixed at a point on its lower surface as it is a rigid body. An additional boundary condition preventing rotation in any direction was applied to a point at the top of the rigid cup unit. However, the cup was able to translate in any direction. Also, the loading profile was applied to the cup unit through the same point which the boundary condition of the cup unit was applied.

The dimensions and representative material properties of the components are presented in Table 2.2. The ball and cup radii were chosen to create a radial clearance of 0.25mm. Under the initial conditions, before any load was applied, the ball surface was assumed to be coincident with the cup surface at its centre for contact simplifications. However, the ball and the socket were modelled as deformable bodies. However, the cup unit was considered to be a rigid body. It should be noted that the density of the materials are scaled to lengthen the time increment for stability and reduce the running time for these initial studies. The real densities that will be applied to the model are described in later chapters.

**Table 2.2 Geometric and material properties of simplified computational model components**

| <b>Part</b>     | <b>Material</b> | <b>Young's modulus (MPa)</b> | <b>Poisson's ratio</b> | <b>Scaled Density (kg/mm<sup>3</sup>)</b> | <b>Outer radius (mm)</b> | <b>Inner radius (mm)</b> |
|-----------------|-----------------|------------------------------|------------------------|---|--------------------------|--------------------------|
| <b>Ball</b>     | Ceramic         | 350,000                      | 0.21                   | 4.37x10 <sup>-6</sup>                     | 18                       | -                        |
| <b>Cup</b>      | Polyethylene    | 1,000                        | 0.46                   | 9.23x10 <sup>-7</sup>                     | 24.25                    | 18.25                    |
| <b>Cup unit</b> | Rigid           | -                            | -                      | 8.5x10 <sup>-6</sup>                      | 27.25                    | 24.25                    |

The analyses that were carried out in the first stage of the development are presented briefly in Table 2.3. This table shows the parameters that were varied in the studies. The inputs which were constant in all cases namely geometry, material properties and boundary conditions have been excluded from this table. Detailed descriptions of the studies are given in each section that follows. The name of the 'case' of each study refers to the element size in cup divided by the element size in head.

In the analyses that are described in this chapter, several output factors were examined:

1. Contact area: Contact area is a good representative of the contact condition in different cases. The contact area can be compared at all the time points through simple observation of the predicted contact area plots. Also, the level of numerical noise in the contact mechanics can be observed by analysing the contact area data. The contact area is expected to follow clearly the loading changes. Therefore, the contact area is predicted to increase from zero to the peak value and then becomes constant at this peak value.
2. Contact pressure: The contact pressure plots on the contact surfaces provide greater visualisation of the pressure distribution in various meshing configurations. Therefore, this shows how the contact conditions can be affected by the element size and contact surfaces meshing ratio. As the

contact surfaces are symmetrical spheres, the contact pressure distribution is predicted to be circular surrounding the centre of the inner cup surface.

**Table 2.3 Full list of modelling cases of stage 1 of development namely, meshing ratio between the head and the cup inner surface, loading amplitude and contact constraint algorithm**

| Study | Case           | Mesh                     |      |                          | Loading    |               | Contact constraint algorithm |
|-------|----------------|--------------------------|------|--------------------------|------------|---------------|------------------------------|
|       |                | Global Element size (mm) |      | Total number of elements | Pattern    | Interpolation |                              |
|       |                | Head                     | Cup  |                          |            |               |                              |
| I     | Case 2:3       | 2                        | 3    | 6,220                    | Simplified | Smooth step   | Kinematic                    |
| I     | Case 1.5:1.5   | 1.5                      | 1.5  | 18,997                   | Simplified | Smooth step   | Kinematic                    |
| I     | Case 1:2       | 1                        | 2    | 43,517                   | Simplified | Smooth step   | Kinematic                    |
| I     | Case 1:1.5     | 1                        | 1.5  | 47,021                   | Simplified | Smooth step   | Kinematic                    |
| I     | Case 1:1       | 1                        | 1    | 61,205                   | Simplified | Smooth step   | Kinematic                    |
| I     | Case 1:0.75    | 1                        | 0.75 | 96,726                   | Simplified | Smooth step   | Kinematic                    |
| I     | Case 0.75:1.5  | 0.75                     | 1.5  | 104,445                  | Simplified | Smooth step   | Kinematic                    |
| I     | Case 0.75:0.75 | 0.75                     | 0.75 | 145,101                  | Simplified | Smooth step   | Kinematic                    |
| II    | Contact A      | 1                        | 1    | 61,205                   | Simplified | Smooth step   | Penalty                      |
| II    | Contact B      | 1                        | 1    | 61,205                   | Simplified | Smooth step   | Kinematic                    |
| III   | Preloading A   | 1                        | 1    | 61,205                   | Preloading | Tabular       | Kinematic                    |
| III   | Preloading B   | 1                        | 1    | 61,205                   | Preloading | Smooth step   | Kinematic                    |
| III   | Paul Cycle     | 1                        | 1    | 61,205                   | Paul cycle | Tabular       | Kinematic                    |

## 2.5.2 Study I: mesh sensitivity analysis

In this study, mesh sensitivity analysis was carried out on the model to achieve the best possible level of precision with respect to computer resources. A simplified loading profile was applied vertically downwards to the cup unit to determine the right mesh density and meshing ratio between the contact surfaces. The model was loaded up to 3kN in 0.1 seconds and the constant load of 3kN was then applied to the model for 0.4 seconds (Figure 2.6).

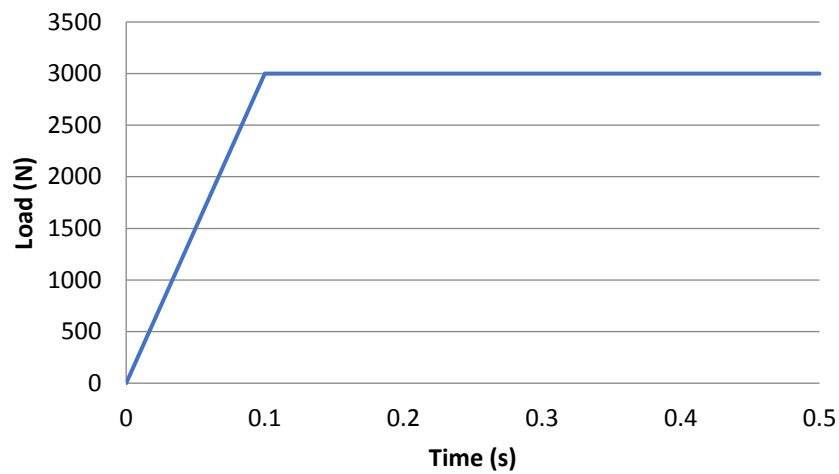


Figure 2.6 Loading condition of the study I versus time

The load variation from 0 to 3kN was defined to follow an automatic smooth ramp up (or down) of load from one amplitude value to another using a smooth step function. The amplitude ( $a$ ) between two consecutive points is derived from the equation (ABAQUS 6.12 Documentation, 2012):

$$a = A_i + (A_{i+1})\xi^3(10 - 15\xi + 6\xi^2) \quad \text{for } t_i \leq t \leq t_{i+1}$$

$$\text{Where} \quad \xi = \frac{(t - t_i)}{(t_{i+1} - t_i)}$$

This can be presented graphically as in Figure 2.7.

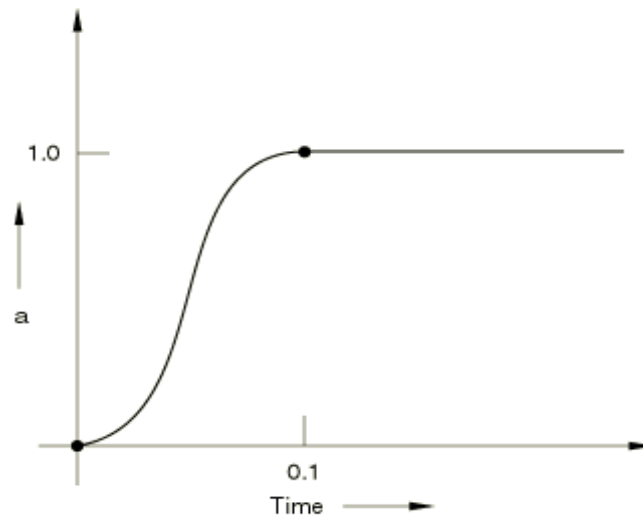


**Figure 2.7 The implementation of the variable versus time using smooth step amplitude in ABAQUS (ABAQUS 6.12 Documentation, 2012)**

For mesh sensitivity analysis, the contact pair algorithm and kinematic contact constraint enforcement was selected. As the cup unit mesh configuration would not affect the contact mechanics of the head and the cup, the same number of elements and coarse mesh configuration were defined on the cup unit for all the cases. The cup unit model consisted of 430 linear R3D4 (4-node 3-D bilinear rigid quadrilateral) quadrilateral and 14 linear R3D3 (3-node 3-D bilinear rigid quadrilateral) triangular elements. The cup and the head were meshed using linear C3D8R (continuum three dimensional 8-node reduced integration) hexahedral elements. Table 2.3 represents the different meshing ratios between the cup and the head that were assigned to the components.

### **2.5.2.1 Static loading analyses specifications**

Static analyses were investigated first and carried out for verification purposes. The static model was analysed in an attempt to replicate the dynamic model. Therefore, the same geometrical and material properties as the dynamic model were applied to the static model. Moreover, a tie constraint was specified between the inner cup and head surface. Also, a penalty contact algorithm was defined between the contact surfaces. All of the meshing cases that were applied to the dynamic model, were

tested on the static model. No translation or rotation of the head was allowed. However, movement of the cup unit was restricted to vertical translation only. When translation in more axes was applied, the static model did not converge due to stability reasons. A static load up to 3kN was applied through the cup unit.

### **2.5.3 Study II: Contact methods**

In this study, the effect of different contact constraint algorithms was investigated. As described above, there are two types of contact constraint enforcement that are available in ABAQUS/explicit. To understand the effect of these contact constraints on the contact mechanics and numerical noise, both contact constraints were tested on the contact surfaces.

Similar assumptions of boundary conditions, loading conditions and contact methods as in study I are conducted in this analysis. The analysis was carried out on the best meshing configuration from the mesh sensitivity analysis (study I). The balanced master-slave relationship was chosen for these analyses. The following contact algorithms with contact constraint enforcements were applied to the model:

1. Contact pair algorithm with penalty contact constraint
2. Contact pair algorithm with kinematic contact constraint

### **2.5.4 Study III: Loading**

A study was carried out to determine the effect of preloading on the initial oscillation of the contact areas of the analysis. This study also demonstrated how this method is applicable for Paul cycle loading. All of these analyses were carried on the same meshing configuration and boundary condition as for study II. The considered loading conditions are:

**Preloading** (Table 2.4): a magnitude of 1N was applied to the model through the cup unit vertically downwards in 0.1 seconds using tabular (linear relationship of

amplitude between the consecutive points) and smooth step amplitude. Then, a constant load of 1N for 0.2 seconds was applied following increase load of up to 3kN in 0.1 seconds.

**Table 2.4 The loading conditions of the preloading study at the specific time points (study III)**

| Time (s) | Load (N) |
|----------|----------|
| 0        | 0        |
| 0.1      | 1        |
| 0.2      | 1        |
| 0.3      | 3000     |

**Paul Cycle loading:** To understand the effect of the Paul walking cycle on numerical noise and contact mechanics, the loading data exported from one station of the Leeds II hip simulator (Figure 2.8) was applied to the model using tabular amplitude data. There were 68 data points that represented the stance phase loading of the Paul cycle (Paul, 1976; Al-Hajjar *et al.*, 2013). However, two data points were defined for the loading during the swing phase as the load during the swing phase was constant at the load level of 300N. Also, a 5ms step was applied at the beginning of the loading cycle to increase the load from 0 to the initial point of the Paul cycle.

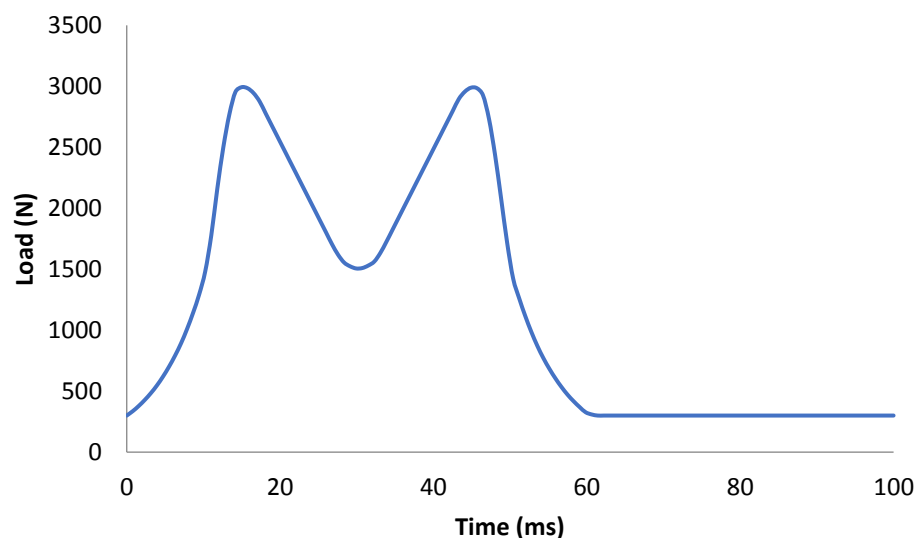


**Figure 2.8 Paul cycle loading. The graph represents the twin peak load that is applied to the Leeds II hip simulator axially.**

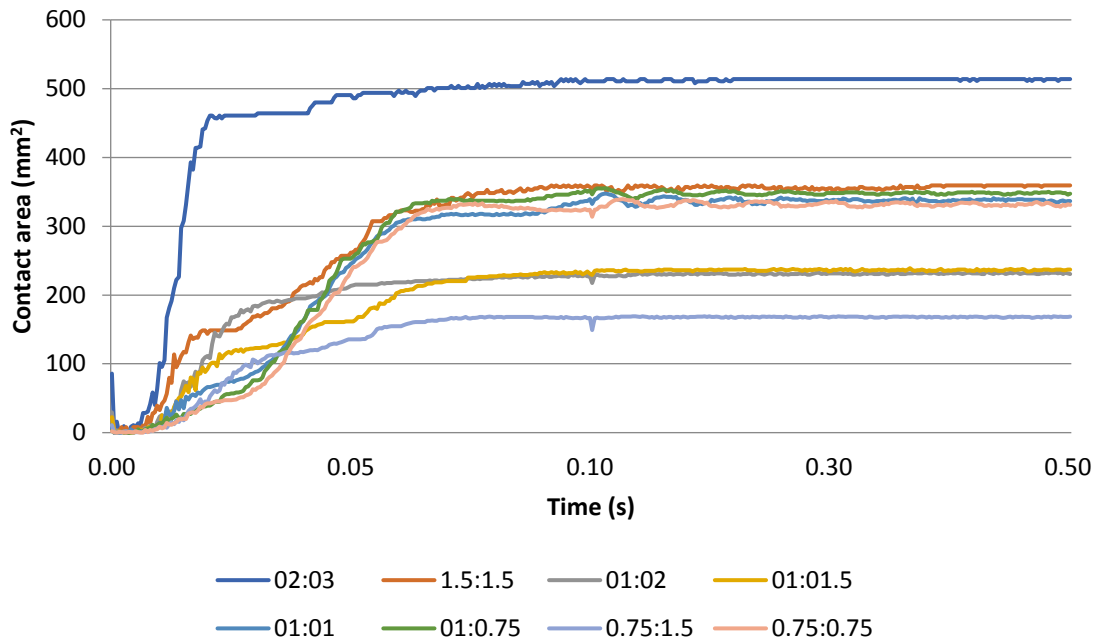
## **2.6 Results of concentric loading condition**

This section presents all the results from the preliminary analyses defined previously.

### **2.6.1 Study I: Mesh sensitivity analysis**

ABAQUS Explicit provides two sets of contact area plots which presents the contact area on each of the surfaces where the contact occurs. As Figure 2.9 shows, the contact area on the head seems to increase in all the plots as the load is increased (from 0 up to 0.1s). Furthermore, the contact area on the head undergoes a level of oscillation as the load is constant. However, the oscillations are damped as time progresses, and eventually the constant contact area reaches a steady state. As the number of elements increase, the contact area tends to decrease. However, the contact area is more sensitive to changes in the meshing ratio between the surfaces.

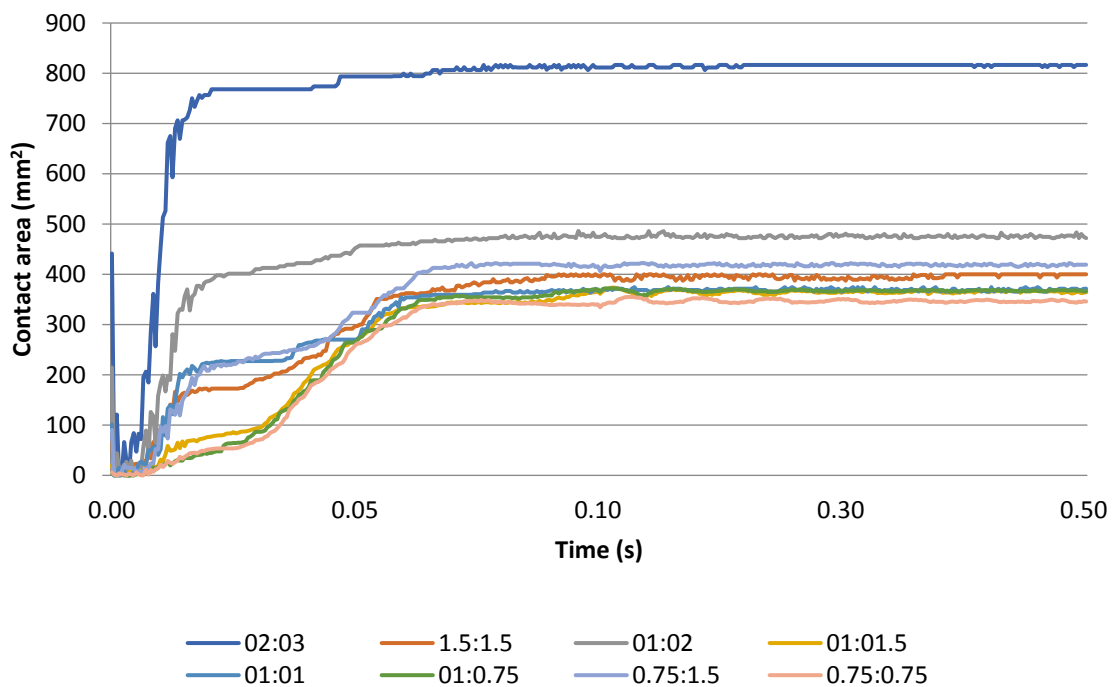
The contact area during the constant load phase varied between approximately 310mm<sup>2</sup> to 360 mm<sup>2</sup> when the same element size on the head and cup surfaces was used. Figure 2.9 shows that there is only a slight difference in contact area when the same meshing ratio on both surfaces was applied (plot 1.5:1.5, 1:1 and 0.75:0.75). However, when the meshing ratio on the cup to the head element size has a double ratio (plot 2:3, 1:2 and 0.75:1.5), the changes in the contact area are extensive ranging from 180 mm<sup>2</sup> to 510 mm<sup>2</sup>.



**Figure 2.9 Contact area on the head, for different mesh resolution combinations. Each plot represents each meshing ratio condition that was carried out**

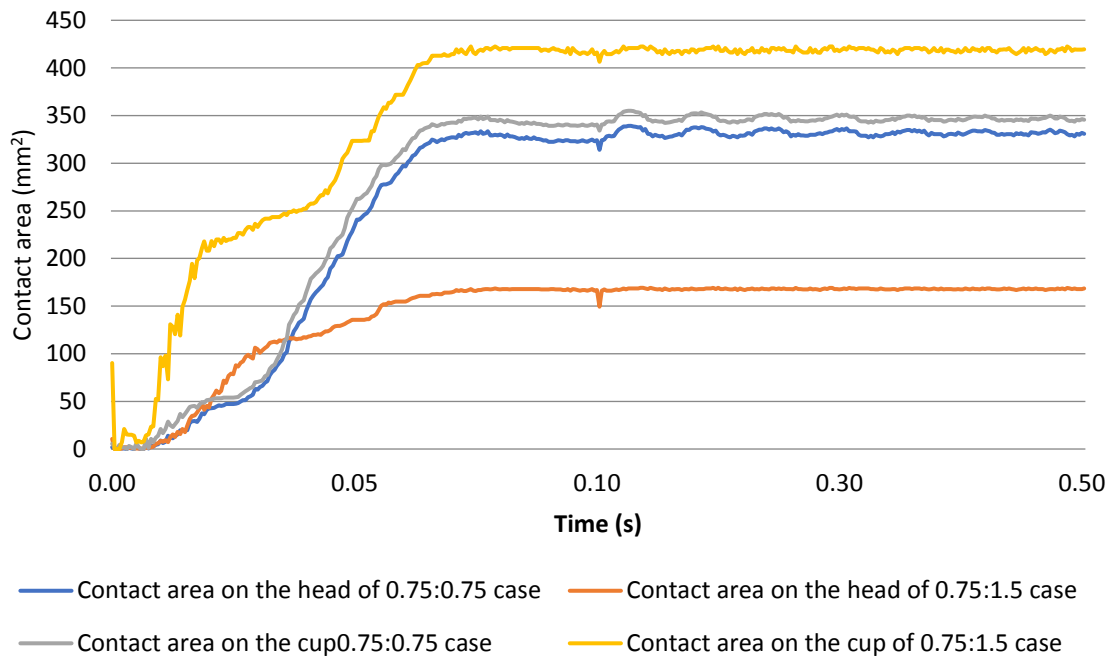
Figure 2.10 demonstrates that the contact area on the cup follows almost the same trend as the contact area on the head. It can be seen that the contact area increases to the maximum level when the load is ramped up to the maximum value. Then, a constant contact area was achieved when the load is held constant. Throughout the analysis there was a constant numerical noise. The level of noise was highest when the initial load was applied, and reduces as the model reaches a steady state. Plots 1:2 and 0.75:1.5 which are when the head that has half the element size of the cup, produced the highest values of contact area when the load is constant (ranging from 410 mm<sup>2</sup> to up to 910 mm<sup>2</sup>). As the difference between the element size on the bearings decreases, the difference between the contact areas of the different cases decreased as well. The highest number of elements with the same meshing ratio (plot 0.75:0.75) resulted in the lowest values of the contact area. A comparison of plot 0.75:0.75 with other plots that have the same meshing ratio (1.5:1.5 and 1:1) indicates that the contact area of the plots are not affected substantially by using a

greater number of elements (contact areas range between 340 mm<sup>2</sup> to 400 mm<sup>2</sup> when the load is constant).



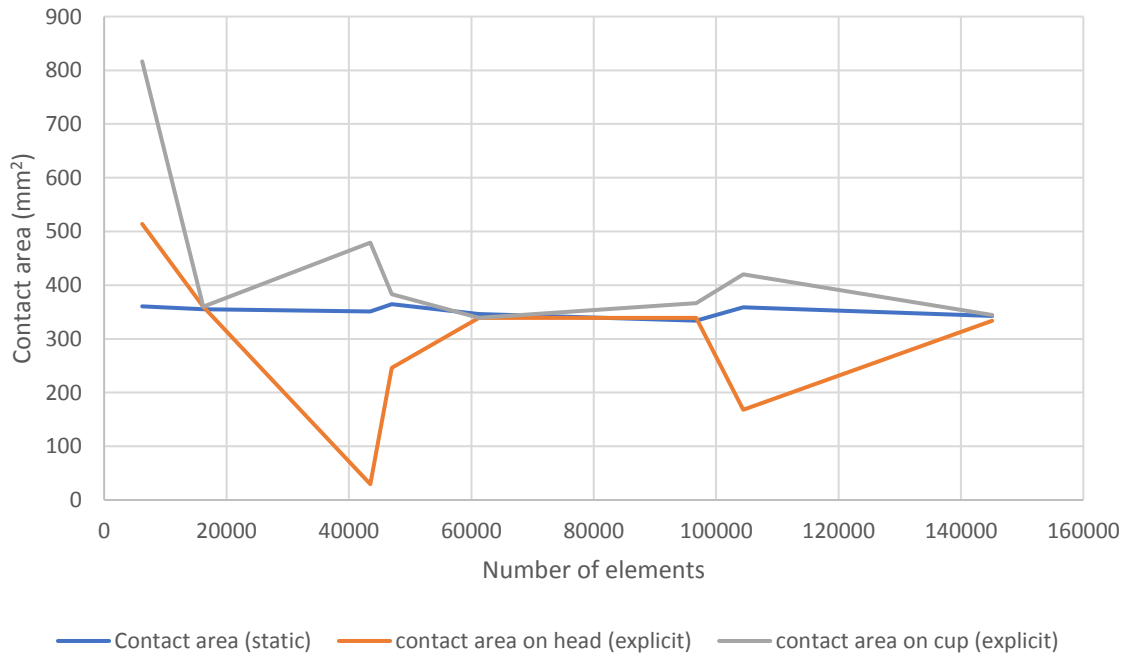
**Figure 2.10 Contact area on the cup inner surface for different mesh resolution combinations under standard condition**

Figure 2.11 illustrates the differences between the contact area generated on the head and the cup when various meshing ratios were applied. Different element size on the contact surfaces can affect the contact area. For example, mesh configuration 0.75:1.5 which has 0.75 (head) to 1.5 (cup) element size results in a large difference between the contact area produced on the contact surfaces of this mesh configuration. However, if the element size on the two surfaces is similar or minimally different, the contact area on the two surfaces is also closer to each other. Moreover, this comparison indicates that there is a linear contact area change during the ramp up load step in the analysis with the same element size on the contact surfaces (1.5:1.5, 1:1 and 0.75:0.75). However, a meshing ratio of 0.75:1.5 affects the contact area variation at the load ramp up step and produces a less consistent contact area on the head and the cup.



**Figure 2.11 Comparison of contact area generated on the contact surfaces using 0.75:0.75 and 0.75:1.5 cases under standard condition.**

Figure 2.12 compares the contact area for static loading with the mean contact area for dynamic loading of the contact surfaces when the load remains constant.



**Figure 2.12 Contact area values versus number of elements, across all mesh cases with both static and dynamic loading under standard condition**

According to the data presented in Figure 2.12, as the number of elements increases the agreement between the contact area using static and dynamic loading becomes

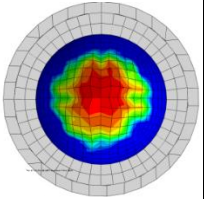
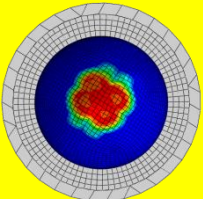
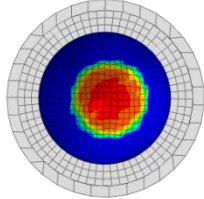
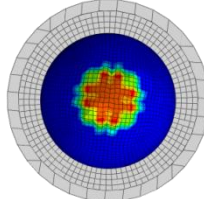
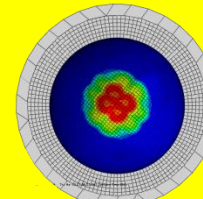
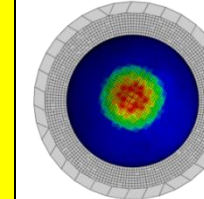
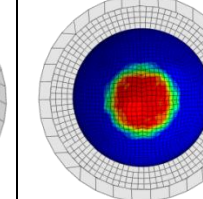
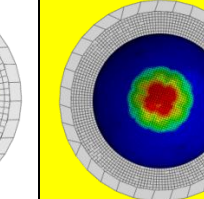
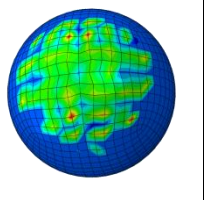
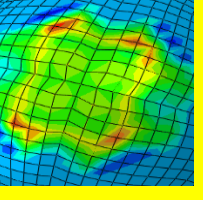
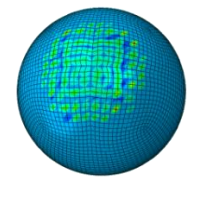
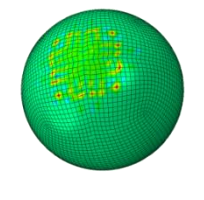
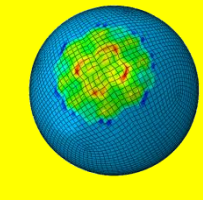
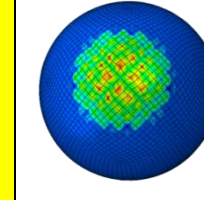
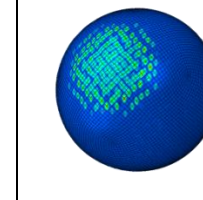
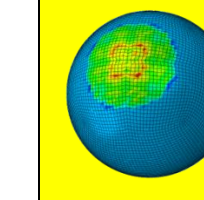
better with less than 1% disagreement, except when 104,445 elements were used. This meshing configuration consists of the element sizes of 2mm on head and of 1mm on cup. It was illustrated previously that the 2:1 meshing ratio causes a large difference between the contact area on the head and the cup. However, there is still a good agreement between the contact area produced on the head using dynamic loading and static loading are for this mesh configuration. Although finer meshing leads to a better agreement the contact area using static and dynamic analysis, the agreement between the contact areas depends mainly on the meshing ratio of the contact surfaces as the cases with the same meshing ratio have better agreements.

One of the other criteria for selecting the best mesh configuration is the distribution of the contact pressure on the surfaces. Since the contact is occurring in the centre of the cup surface (about which the contact is symmetric), the ideal contact pressure should be distributed symmetrically along the surface. The contact pressure is expected to be circular due to the shape of the contact faces which are both spherical. The pressure distributions of the contact surfaces in the last step of the analysis for each meshing configuration are presented in Table 2.5. The contact pressure distribution depends on the element size ratio of the contact surfaces. For example, the element size ratio of 1.5 (cup) to 1 (head) causes the contact pressure distribution on the surface to be more four-sided than circular (Case 2:3 and 1:1.5) whereas a circular contact patch is predicted due to the conforming where of the spherical contact surfaces. According to this table, a circular pressure distribution is achieved on the cup surface when the element size on the head is half the cup element size (mesh configuration 1:2 and 0.75:1.5). However, the majority of the contact area appears under the maximum pressure (red area of the pressure distribution). Furthermore, the contact pressure on the head surface does not seem

to be continuous for these cases which could be due to different element sizes on the contact surfaces.

When the same element size is applied to both surfaces (highlighted columns on Table 2.5), the contact pressure on the cup surface gradually increases from the boundaries to the centre. Although the contact pressure is not as circular as the one with different element sizes the contours of contact pressure appeared to be more reasonable. The contact pressure on the head in the same meshing ratio cases (1.5:1.5, 1:1 and 0.75:0.75) appears to be more distinct than the meshing ratio cases 1:2 and 0.75:1.5. Nevertheless, the pressure distributions on the head surface is as well distributed as on cup surface on no occasion. Therefore, the conclusion was drawn that finer mesh on the cup could produce better pressure distribution on the head surfaces (1:0.75). As contact pressure analysis of case F shows, this meshing configuration resulted in random elements on the head surface to have the maximum pressure values. Finer mesh on the cup surface than on the head surface also causes the distribution of the pressure on the cup surface to be less concentric which is not ideal.

**Table 2.5 Pressure distributions for different mesh configurations under standard condition. The analyses that were carried out with the same element size on the bearing surfaces are highlighted.**

| Case                               | A  | B  | C  | D   | E  | F  | G  | H  |
|------------------------------------|--|--|--|---|--|--|--|--|
| Cup mesh size (mm)                 | 3  | 1.5  | 2  | 1.5   | 1  | 0.75   | 1.5  | 0.75   |
| Head mesh size (mm)                | 2  | 1.5  | 1  | 1   | 1  | 1  | 0.75   | 0.75   |
| Cup contact pressure distribution  |   |   |   |   |   |   |   |   |
| Head contact pressure distribution |  |  |  |  |  |  |  |  |

To compare the produced contact pressure distributions with different meshing ratios, the pressures along the line of the nodes aligned with the z axis through the centre of the contact were plotted (Figure 2.13). This procedure was conducted for the 0.75:1.5 and 0.75:0.75 mesh configurations because these cases generated the most ideal contact pressure distribution out of all the cases.

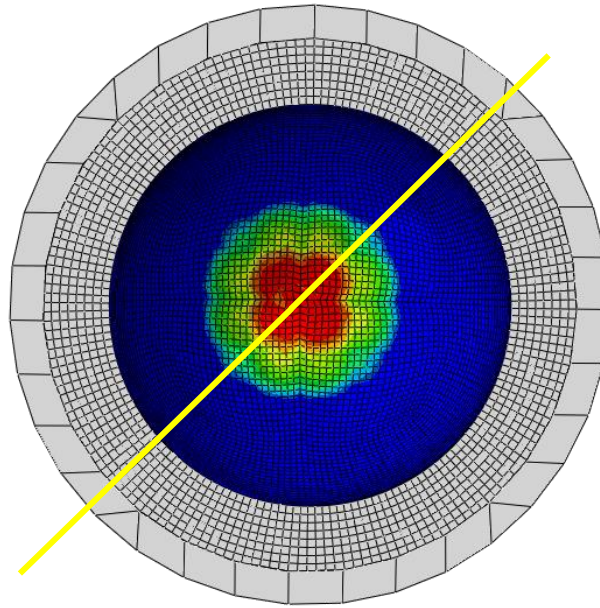


**Figure 2.13 Position of the selected nodes which their nodal pressure was recorded to compare the contact pressure distribution of different meshing ratios**

As Figure 2.14 presents, the contact pressure of both these cases is symmetric. However, the pressure distribution using same element size on both surfaces indicates a smaller area. Although a larger area is covered in the red plot than blue plot and wider area for maximum pressure is visualised on the red plot than blue one. However, the ratio when the pressure goes from zero to maximum contact pressure with when the pressure remains at maximum value seems to be more equivalent in the plot with 0.75 element size on both surfaces than other mesh configurations. Moreover, it was presented in Figure 2.12 that the ratio of 0.75:0.75 produced the similar contact area to the static loading.

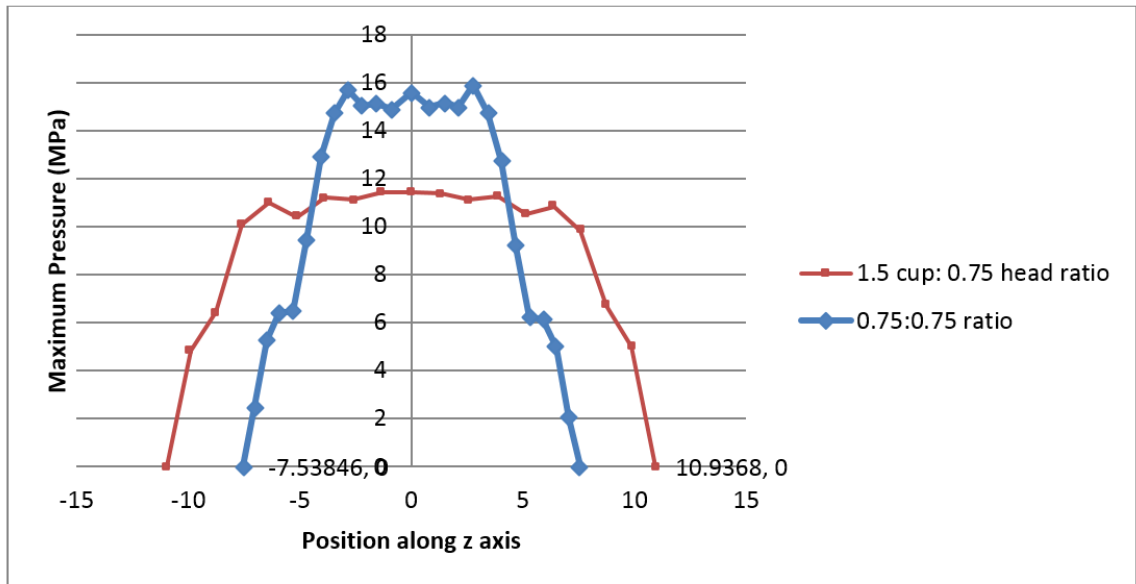


**Figure 2.14 The nodal Pressure distribution along the line aligned with z axis for meshing ratio of 0.75:0.75 and 1.5:0.75 under standard condition**

### 2.6.2 Study II: Contact methods

The main concern of this analysis was to focus on the effect of contact constraint enforcement on the contact mechanics and the level of numerical noise generated on the contact area. Results from study I indicated that the same element size on both contact surfaces produces more reliable outcomes than different element size on the contact surfaces. Therefore, the 0.75:0.75 meshing configuration of study I which consists of 0.75mm element size on both contact surfaces was chosen to investigate the effect of the contact method.

Figure 2.15 represents the predicted contact area on the two contact surfaces using the penalty and kinematic contact constraint methods. As this figure indicates, the kinematic contact constraint method predicts lower contact area throughout the analysis. Furthermore, even when the load is constant, oscillation in the contact area values occurs in all cases. However, the oscillations using the penalty constraint enforcement appear to be higher. These oscillations reduce with time. The final contact area value on the cup surface (when the contact area has reached a stable value) using the kinematic enforcement is 345.6 mm<sup>2</sup> whereas the area using the

penalty enforcement is 419.6 mm<sup>2</sup>. A comparison of the contact area when the maximum load is applied with the static loading (Figure 2.12) shows the area values determined by the kinematic constraint enforcement are closer to the static values than area from the penalty method.

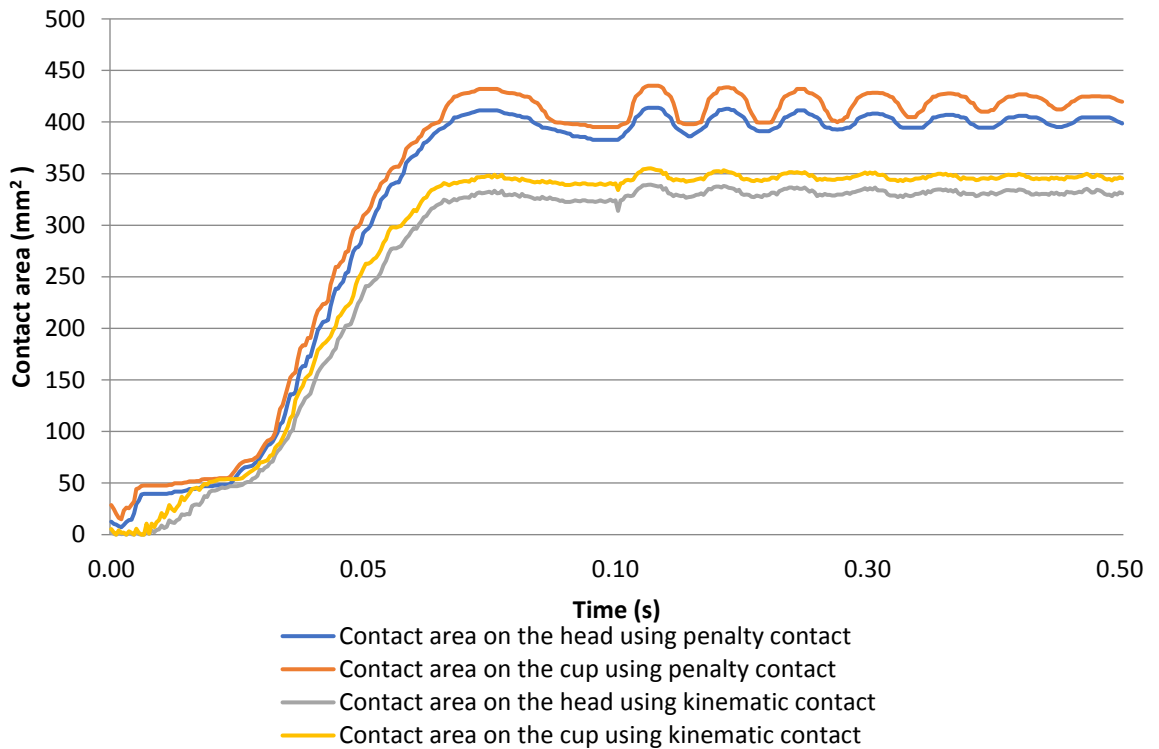


**Figure 2.15 Predicted contact area on the head and cup inner surface using different contact constraint enforcement methods namely penalty and kinematic contact constraint enforcement under standard condition**

The other factor of comparison between the constraint enforcement methods is the contact pressure distribution on the surfaces. Figure 2.16 illustrates the contact pressure distribution on the cup surface using the two constraint methods. The pressure varies from minimum (blue contours) to the maximum (red contours). The kinematic contact enforcement method produces a circular pressure distribution that gradually reaches the peak contact pressure from zero. A half fraction of the pressure distribution consists of the maximum pressure value. Moreover, the penalty contact constraint also generates a circular contact pressure distribution.

However, the pressure variation mainly consists of the low contact pressure and the maximum pressure patch is not symmetrical.

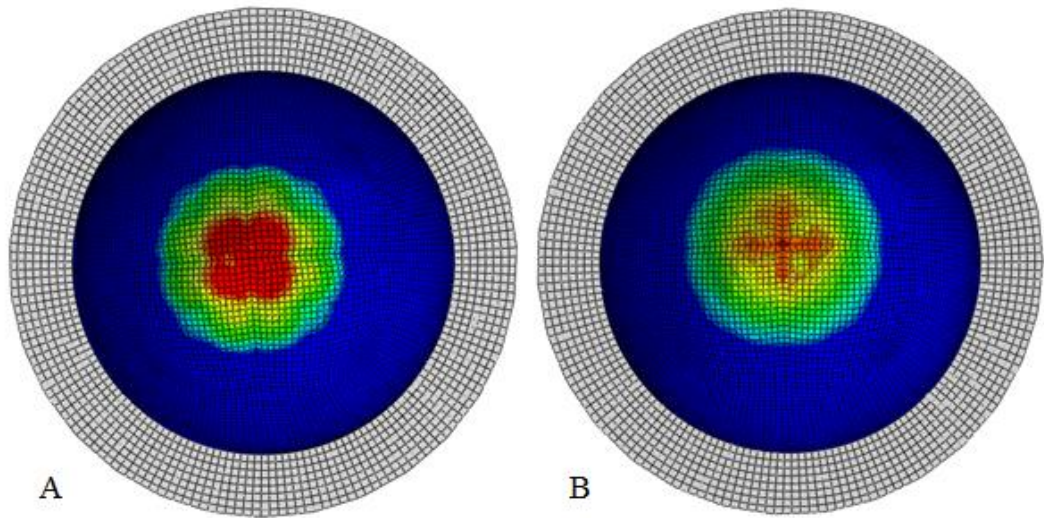


**Figure 2.16 Contact pressure distribution on the cup surface using A) Kinematic and B) Penalty contact constraint method under standard condition**

Comparison of pressure distribution on the head surface indicates that better pressure distribution is achieved by using the penalty constraint enforcement (Figure 2.17). The pressure distribution on the head using penalty contact constraint method could be expected to be better distributed if smaller element size is used on both surfaces.

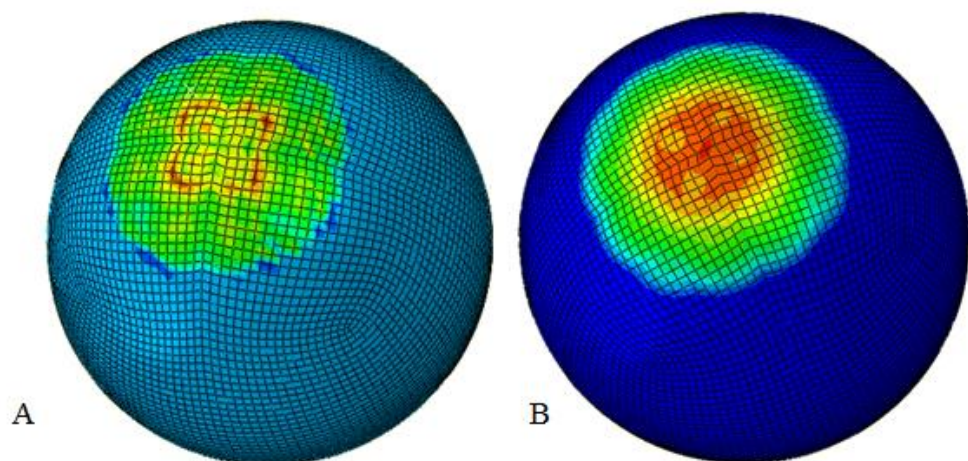


**Figure 2.17 Contact pressure distribution on the head surface using A) Kinematic and B) Penalty contact constraint method under standard condition**

### 2.6.3 Study III: Loading condition

The result of study I analysis shows that there is numerical noise when the load just starts to be applied to the model. There is a possibility that this noise is produced as the code attempts to maintain the initial contact or increases this due to the rapid loading of specific elements. Therefore, preloading of the model is the best way to understand if the initial contact is the factor which increases the noise. Figure 2.18 shows the predicted contact area on the two contact surfaces when preloading of the model occurs by either using tabular or smooth step amplitude loading. As this figure shows, there is a high level of noise in the preloading steps and as the actual load starts increasing, the oscillations are reduced substantially. This supports the hypothesis of the effect of preloading on the noise produced. The main difference between the behaviour of the contact area on the surfaces is at the end of the second step when the load is constant at 1N. A level of contact area difference between the head and the cup was also produced in the previous study.

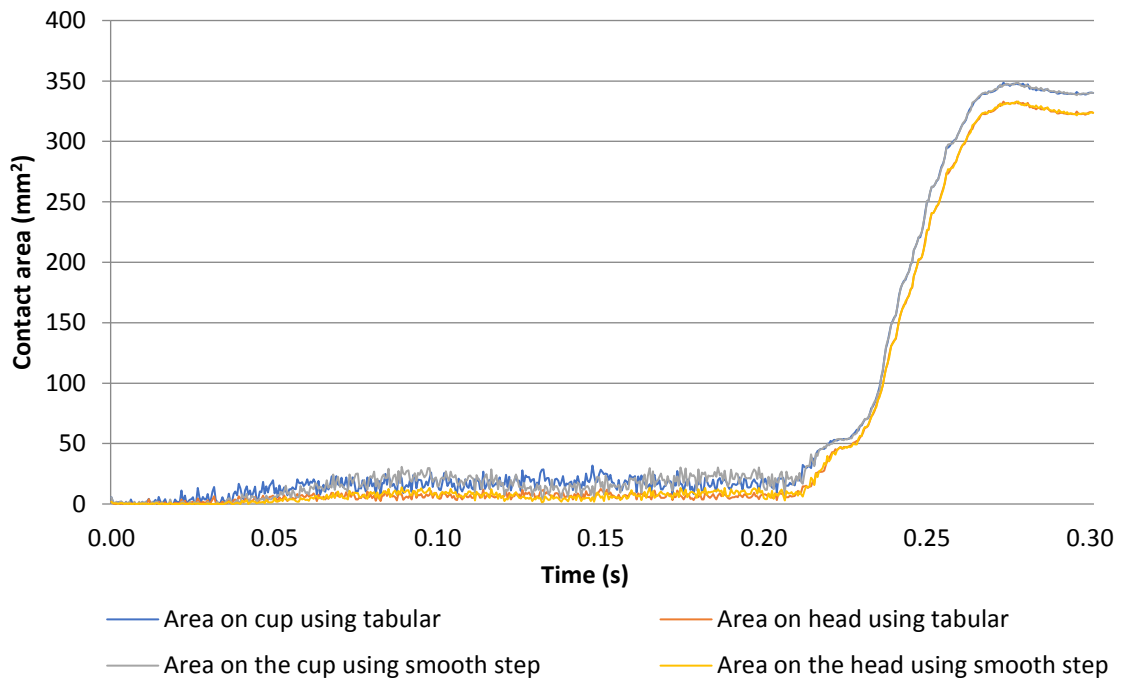


**Figure 2.18 Contact area using preloading of the model on the head and the cup inner surface using tabular and smooth step loading amplitude under standard condition**

To understand the contact area behaviour when different pre-loads are applied to the model, the predicted contact area from the preloading step is illustrated in Figure 2.19. Initially surfaces do not easily maintain contact as can be seen before load ramp up as the contact area is very low. However, it is expected that the contact area will increase as the load increases. Although the load should be increasing gradually, application of the load within a simple step could be another factor to affect the contact area.

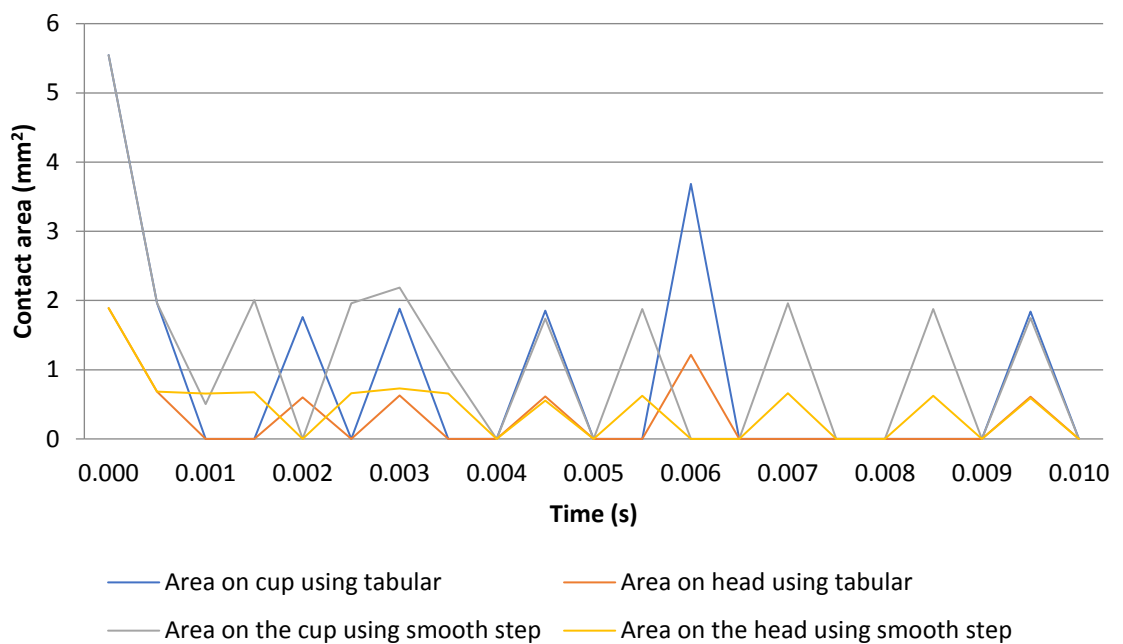


**Figure 2.19 Contact area during preloading step on the head and the cup inner surface based on tabular and smooth step loading amplitude under standard condition**

The reaction forces of the analyses at the fixed point of the head were extracted and plotted, the reaction force is identical in both cases and since the value of reaction force in the preloading step is low (due to the low applied load), the graph is not able to illustrate the difference of reaction forces values in preloading steps. Hence, the reaction force of the models in preloading step is only shown. Figure 2.20 indicates that the both tabular and smooth step load amplitude produce similar initial reaction forces. However, the tabular amplitude method increases the load steadier in the fixed time length than the smooth step. The smooth step amplitude causes

slow increase of load initially for smoother contact and at this point, rapid change of the load takes place. The same behaviour of smooth step amplitude occurred in Figure 2.20 when the load was overestimated during the actual load step. Then, decrease of the load occur which causes final underestimation of the force.

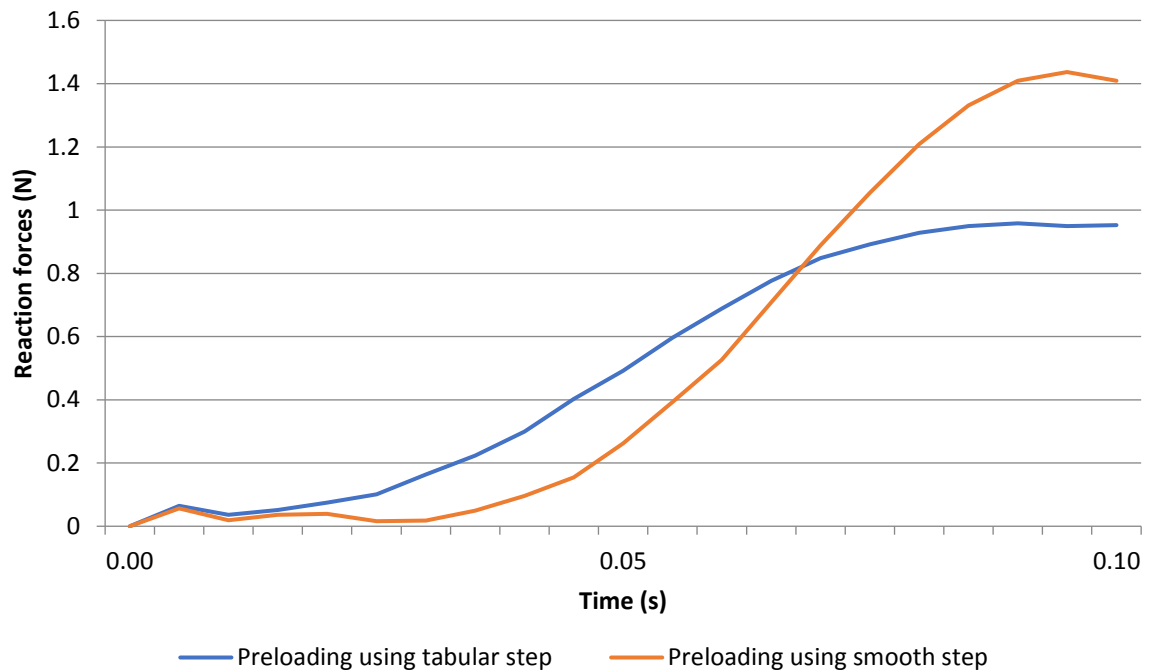


**Figure 2.20 Reaction force in preloading step using different load amplitude under standard condition**

The Paul cycle loading was applied to this model to examine in the effect of a realistic load cycle on the predicted reaction forces. As Figure 2.21 illustrates, the reaction force created by the model experiences a level of oscillation mainly between the first and second peak load, and during swing phase load. However, the oscillations in swing phase appear to improve and become steadier with time. The oscillations in reaction forces must be minimised to achieve the most stable outcome. Therefore, the factors which eliminate these oscillations such as damping and filtering the result should be investigated further.

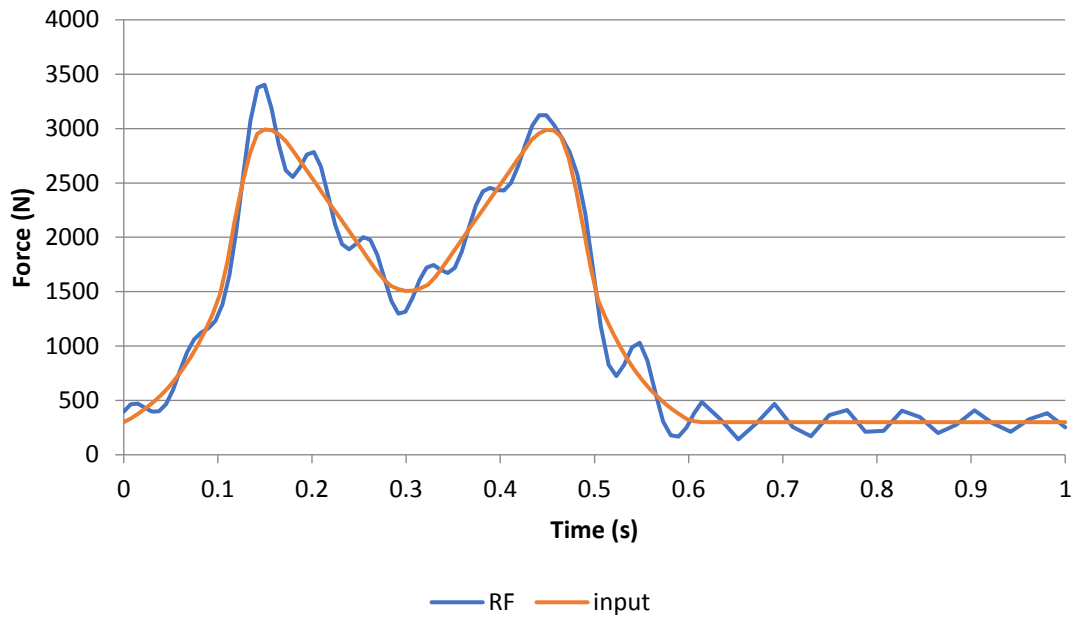


**Figure 2.21 Input loading and predicted reaction force (RF) of the analysis using Paul cycle loading under standard condition**

Although Figure 2.20 indicated that tabular amplitude resulted in underestimation of the load, overestimation of the first peak load occurred when tabular amplitude was applied for Paul cycle loading (Figure 2.21). This disagreement could suggest that the difference between the input load and reaction force could not be affected by the load amplitude for high input loads.

## 2.7 Discussion

This chapter focuses on the general validation of the computational solutions that were chosen for this study. The main aim of this chapter was to confirm the suitability and reliability of the parameters that will be implemented in the future model developments.

In the mesh sensitivity study, the contact area changes were expected to follow the loading changes as the contact condition remained constant and as predicted, the contact area increased generally as the loading magnitude increased. The comparison of the contact area on the contact surfaces demonstrated that the area generated on the cup is predicted to be slightly larger than the area on the head. However, this difference is much less in the analyses with the same meshing ratio (1.5:1.5, 1:1 and 0.75:0.75). There was numerical noise in the analysis results which were due to the nature of the dynamic modelling.

The ultimate aim of this project was to focus on ceramic-on-polyethylene THRs. As the Young's modulus of the ceramic head is significantly higher than the cup, the severity of the contact predicted to be more severe on the polyethylene contact surface, which has a much lower hardness. The main interest was the contact mechanics that were generated on the acetabular cup as the head was modelled as a rigid body due to its high Young's modulus. Therefore, it is not a great concern that the contact result for the head were different.

As Figure 2.12 indicated, when a finer element size was used on the head surface than on the cup surface, it seems to produce a larger contact area on the cup surface than on the head surface. This difference could be due to elements with larger area on the cup surface. When the contact occurs, the head which is made of stiffer material and has a finer mesh tend to penetrate the cup surface. The penetration of

each node of the head surface into the cup surface resulted in the selection of the whole element where the penetration occurred as being in contact even if the whole element was not in contact. Therefore, more elements appear to be in contact on the cup surface. However, if the same meshing ratio was varied on the two contact surfaces, the penetration of the head nodes on the cup surface is more accurately controlled because of similar node configurations on both the surfaces.

As expected, the contact area of the surfaces was affected by the element numbers. As comparison of static and dynamic maximum contact areas revealed, all of the meshing configuration resulted in a reliable maximum contact area because the maximum contact area variation between the static and dynamic cases was minimal (31 mm<sup>2</sup>). However, in the dynamic explicit analyses, the maximum contact area depends strongly on the meshing ratio between the contact surfaces. The contact surfaces with significantly different element sizes predict considerably different contact areas. On the other hand, generally, when the element size on both surfaces is equal or minimally different, the surfaces contact area is not affected. Moreover, when the refinement of the meshes with the same meshing ratio of the surfaces occurred, the maximum contact area was slightly affected by the refinement. This suggests that if the same meshing ratio is used on the contact surfaces, fewer elements can be applied for a reliable contact mechanics results that could save substantial computational time and cost. The usual running time of these analyses was 150 minutes as significant mass scaling was applied for these initial studies by increasing the density of the materials. Therefore, the running time of the future models will be significantly higher than for this initial study. Hence, the same meshing ratio on both surfaces with the highest element size (1.5mm) is recommended to use for future studies. Gao *et al.* also used the same meshing ratio

between the contact surfaces of the hip replacement in his explicit analyses (Gao *et al.*, 2015).

The contact surfaces in this study are conforming due to quite large contact area between the surfaces, the simple loading regime and a deformable component (polyethylene cup). Therefore, a circular well distributed pressure distribution is predicted to occur. The kinematic contact constraint enforcement method produced a more distributed pressure on the cup surface than the penalty method. However, the penalty enforcement resulted in a better pressure distribution than kinematic enforcement on the stiffer surface (head) with a more uniform distributed pressure. Increasing the number of the elements in the model could affect the pressure distribution on the head positively. However, increasing the element number requires more computing source and cost whereas lower number of elements still produces reliable results on the cup by using the kinematic enforcement of constraint.

It was demonstrated that the level of numerical noise in the contact area was significantly less than that in the preloading step and the output is affected by the loading amplitude. As Figure 2.18 showed, the smooth step amplitude caused 40% overestimation of the full load at the end of the step. The tabular amplitude step does not cause overestimation of the force which increases constantly during the step. Moreover, the load is underestimated by a factor of 0.048% which is very low compared to the overestimation of by the smooth step amplitude method by a factor of 40%.

## **2.8 Key points**

- For accuracy at reasonable computational cost, the optimum meshing ratio between the head and the cup surfaces should be set to 1.5mm.

- The kinematic contact constraint between interacting surfaces provides more consistent contact information.
- As the smooth step amplitude produced substantial overestimation of the load, the tabular step amplitude method will be used in the future studies.
- The next step of this study is to develop the model under adverse conditions to replicate separation during the gait cycle.

## Chapter 3 Model development under adverse conditions

### 3.1 Introduction

The previous chapter illustrated the fundamental development of the model under concentric loading conditions. This provided an insight to essential explicit modelling techniques, such as meshing configuration and contact algorithms, and defined them in terms of an integrated dynamic and contact mechanic model of a THR. This chapter focuses on modifying that model to implement the parameters that result in adverse loading conditions.

The technical background is presented to describe the spring representation and damping methods in ABAQUS explicit. Also, the meaning of stability in this study is discussed in the technical background section. Furthermore, the materials and methods used in this study to replicate the experimental events to the computational package is explained. There are four separate studies that focus on the spring representation, damping methods, mass effect and spring compression effect. Finally, the output of each study and its significance are presented in the result and discussion section, respectively.

A representative geometry of the specific Pinnacle THR hard-on-soft bearing was obtained from DePuy Synthes, thereby reducing the number of assumptions and allowing for more accurate dynamic and contact mechanics prediction of *in vitro* studies. On wear test simulators, there are a set of parameters that are tested for their effect on the THR wear, these are: translational mismatch, rotational orientation and swing phase load. Peer reviewed data from a range of studies that focused on the effect of specific parameters were implemented into the computational model.

Prior to implementation of the adverse conditions, it was necessary to implement the *in vitro* separation method in the computational model. Previous *in vitro* studies initially focused on only the effect of separation on the wearing of the THR bearings (Williams *et al.*, 2003; Al-Hajjar *et al.*, 2010). The separation of the head and the cup was replicated in the early studies by using a pre-defined spring on the cup holder which was kept at constant throughout the analyses. The spring maintains the separation between the bearing surfaces at a constant load. In these studies, the separation level was set by varying the spring compression. Therefore, the next development step revolves around the integration of the spring into the present computational model. However, implementation of the spring in the model is a challenging task as the changes in the spring length can cause instability of the explicit model. Furthermore, the spring could potentially be a source of undesired oscillations which can make the true dynamic prediction problematic.

The effect of different spring representation methods, namely the ABAQUS spring element and truss element was investigated. Moreover, different methods of damping were introduced to the model to control the oscillations caused by the spring. This chapter mainly focuses on the dynamic aspects of the model to predict a realistic dynamic separation profile during the gait cycle.

Once the method to implement the spring is finalised and the inclusion of damping is defined, the effect of mass on the output result was tested. Whereas in the previous chapter, the mass of the components were increased by scaling up the material densities (decreasing the run times significantly), in this chapter the effect of the mass of components on the separation predictions and the computational perspectives is assessed.

Various methods are used in an experimental environment to implement adverse conditions *in vitro*. For example, the effect of swing phase load on the THR was predicted by varying the swing phase load during the gait cycle from 50N to 300N. Different rotational orientation is applied by varying the cup inclination angle with respect to the horizontal axis (35° to 65° inclination angle). To apply the translational mismatch, a level of medial/lateral mismatch is set between the bearings centres and then, the relaxed spring is assembled into the station. The experimental studies have shown that the wear rate of the THR bearings is affected by changes in the above parameters (Al-Hajjar *et al.*, 2013; Ali *et al.*, 2016). Therefore, the computational model was expected to present a level of sensitivity to the variation of the parameters. Therefore, within this chapter, the effect of varying the translational mismatch is explored to test if the model can distinguish the effect of these changes.

The chapter proceeds to discuss the final developmental stage of the model to assess whether the model was sufficiently reliable to perform parametric testing of the adverse conditions and to validate the output against the experimental studies.

## 3.2 Technical Background

The explicit method is suitable for solving dynamic models as the time steps can be defined in very small increments. Although the explicit model can solve these with relative ease, the large number of time increments causes very long run times. Therefore, explicit modelling can achieve a realistic outcome despite the rapid changes in the system. In this project, as the loading changes quite rapidly, small time increments are required to obtain a stable output. Therefore, the explicit approach is the most suitable method for this application.

The duration of the time increments is a crucial factor in the explicit approach. Although small increments can be solved the stability issue in the dynamic analysis, there are issues associated with a time increment that is either too high or low. If the time increment is longer than a critical value, known as the stability limit, the model becomes unstable resulting in assumptions made between calculations causes an unrealistic output. Therefore, it is less likely to have an unstable model if the time increments are smaller than the stability limit. The cost for the more reliable model is the running time and computational cost. The smaller the time increment is, the more equations are required to be solved. The explicit method is restricted to solving the dynamic equations for small time increments, the stability limit is the longest the time increment could be to avoid instability.

In this section, the time incrementation method used in ABAQUS is described. Other potential factors for instability such as spring and damper in the model are mentioned and reviewed.

### 3.2.1 Stability and time incrementation

ABAQUS explicit method determines the time increments automatically based on the stability limit ( $\Delta t_{\text{stable}}$ ) that is calculated in ABAQUS. The stability limit of the model can be defined in two ways (ABAQUS 6.12 documentation, 2012):

1. Global stability limit: That is defined as a proportion of the highest natural frequency ( $f_{\text{max}}$ ) in the system. However, the highest frequency is difficult to calculate as it is the result of various interrelated factors.

$$\Delta t_{\text{stable}} = \frac{2}{f_{\text{max}}}$$

2. Element-by-element stability limit: In this method, the stability limit is defined by predicting the highest frequency in each element which is directly influenced by the **element length ( $L^e$ )** and inversely affected by **the elastic wave speed of the material ( $c_d$ )** of that element.

$$\Delta t_{\text{stable}} = \frac{L^e}{c_d}$$

Also, the elastic wave speed of the material is equal to the square root of the **Young's modulus of the material ( $E$ )** and divided by **the mass density ( $\rho$ )** for an element with no Poisson's ratio.

$$c_d = \sqrt{\frac{E}{\rho}}$$

Figure 3.1 depicts a strategy for reducing the size of the time increments of a dynamic model. The time increment is mainly affected by the minimum element size based on meshing and the material properties of the element namely, density and Young's modulus.

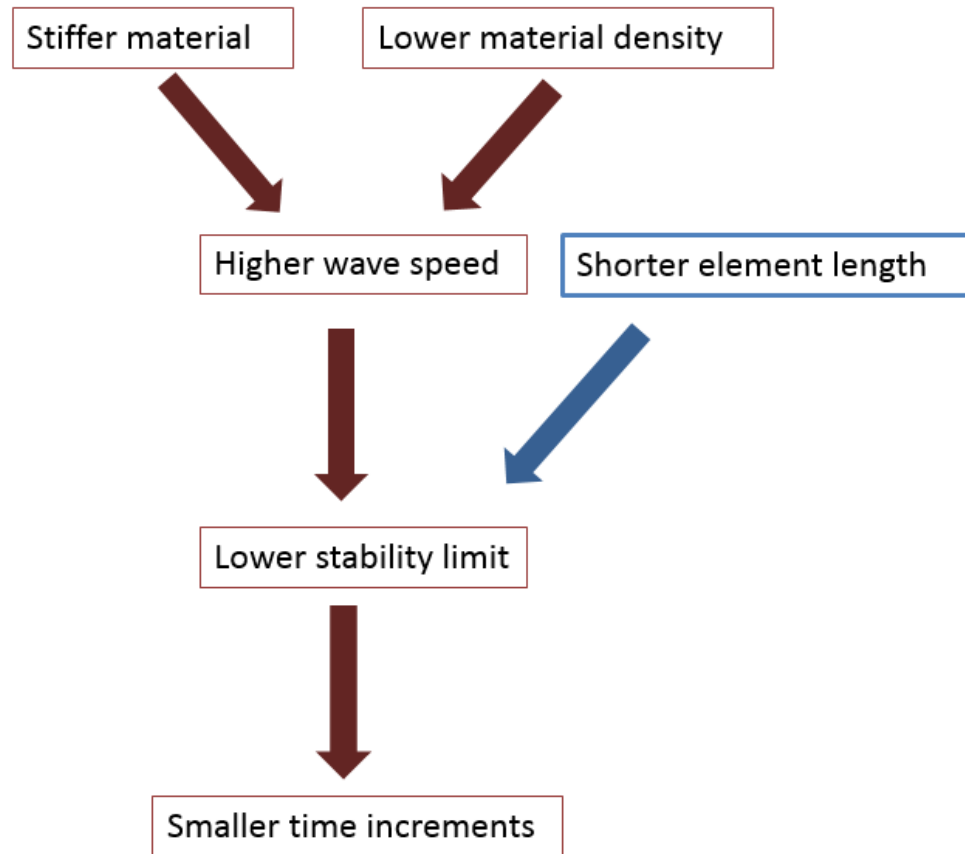


Figure 3.1 The effect of meshing and material properties on the stability limit of the computational analysis

### 3.2.2 Spring representation

The mechanical behaviour within the spring is not the primary interest of this study. The focus is the effect that the spring can have on the behaviour of the system. For situations, such as this, where the spring is used as a tool to represent a phenomenon, using a simplified spring representation is good practice as it avoids any unnecessary complexity due to the spring geometry. In ABAQUS explicit, there are two techniques to model the spring without spring geometry to use:

**Truss element (TE):** In this method, the spring is modelled as one truss element and this element is assigned with material properties to replicate the spring stiffness.

**Spring element (SE):** This is one of ABAQUS explicit built in features to replicate a spring by using two nodes that represents the spring ends and the spring stiffness.

The main difference between the TE and SE methods are in the nature of the elements. The stability limit behaviour of a system varies if truss or spring element is used in the system. TE consists of the mass and stiffness. Since mass and stiffness of the elements are the main requirements to calculate the stable time increment, it is assured that the time increment for the analysis is within the stable time increment by using a truss element. The stability limit of the truss element alters during the analysis. As the spring becomes compressed or extended, the length of the truss element becomes smaller and longer, respectively. As it was shown in the previous section, the stability limit of the element is affected by the element length. For example, if the spring is compressed, the stability limit becomes smaller and the time increments becomes smaller.

In contrast, there is no mass associated with SE so it is not considered by ABAQUS during the stable time increment calculation. Therefore, the possibility of instability in a model with SE is potentially higher than truss element. The stability limit of a SE can be predicted by using the stiffness of the spring and the mass of the element that the spring is attached to. When SE is applied, the stability limit of the system is constant as the stiffness of the spring and the mass of the element does not alter during the analysis. The features of both spring and truss elements are presented in Table 3.1.

**Table 3.1 The summary of the truss and spring element features to use as the experimental spring**

| <b>Element</b> | <b>Mass</b>  | <b>Stiffness</b> | <b>Stability limit</b> |
|----------------|--|------------------|------------------------|
| <b>Truss</b>   | ✓  | ✓                | Varies                 |
| <b>Spring</b>  | ✗<br>(can be calculated by attaching a mass element) | ✓                | Constant               |

### 3.2.2 An oscillatory system

If an under damped spring is part of the dynamic system, a level of oscillation is expected, as there is no energy dissipation inherent to the system. As such, when a load is applied the model will overshoot and oscillate with an amplitude proportional to the original load. As the loading changes in this model varies rapidly, the spring is unable to reach the stable condition which would result in false output. The noise due to the oscillations can be reduced by damping the system. Therefore, the oscillations in the system must be either prevented, by critically damping the system, or otherwise reduced by a damping figure close to the critical. Once the system is damped, an accurate value of the output can be recorded with minimum noise. As the damping in the experimental set up is unknown, calculations were used to obtain a critically damped model for all of the cases.

$$\mathbf{1} = \frac{c}{2\sqrt{mk}}$$

Where  $c$  is the dashpot coefficient,  $m$  is the mass of the system and  $k$  is the spring stiffness. The damping equation is used for a spring-mass system which is an extreme simplification of the model. However, the equation provides some predictions about the level of damping.

An oscillatory system with no damping oscillates within the natural frequency of the system however, in a damped system the amplitude of oscillations decreases gradually from the maximum amplitude to a stable constant value to reach the equilibrium. The critical damping in a system is for the spring to return to equilibrium as quickly as possible and eliminate oscillations without overdamping the system. It is crucial to achieve a critically damped system because overdamping the spring might cause underestimation of the output.

One major problem in any dynamic analysis is the tendency for the components of the model to display oscillatory behaviour due to their inherent dynamic characteristics. Such oscillatory behaviour can sometimes obscure the main trend in the results. There are two strategies to reduce such effects: 1) addition of damping to the FE model and 2) filtering of results in post analysis stage. To damp a model in ABAQUS explicit, there are three different approaches described below and compared in Table 3.2:

**Bulk viscosity damping:** This damping is a purely numerical effect that is associated with volumetric straining and affected the whole model. Bulk viscosity damping is mainly used for high speed dynamic events. Two different types of bulk viscosity damping (linear and quadratic) can be used in analysis based on the nature of the elements and the volumetric strain rate. There is a default value of bulk viscosity damping in all the explicit analysis carried out by ABAQUS. Increased value of bulk viscosity affects the running time of the analysis negatively.

**Material damping:** The material damping method in ABAQUS is called Rayleigh damping which is also known as, mass and stiffness proportional damping. The mass proportional damping considers the mass matrix of the element and applies the damping force based on the element velocity. The stiffness proportional damping produces damping stress based on the total strain rate calculated by using the elastic material stiffness. The value of the mass and stiffness coefficients are challenging to choose in the model with many degrees of freedom because of changes in frequency and modal mass participation as the mode of vibration changes. These two factors directly affect the critical damping and the damping ratio of the analysis. Therefore, the damping ratio arising from the Rayleigh damping method potentially varies throughout one analysis.

**Discrete dashpot:** The individual dashpot element is available to use in conjunction with the spring element. The damping force produced by the dashpot element is based on the relative velocity of the nodes at either end of the element. This feature allows the damping force to be applied only in the position where it is critical to have damping. The dashpot element is usually used in conjunction with a spring element. In this model, as the source of the noise oscillation is the SE, the dashpot element can be attached in parallel to the spring element to reduce the oscillation. The dashpot element, same as spring element, is not considered for the stability limit calculation which could increase the possibility of instability.

**Table 3.2 Summary of the damping methods available in ABAQUS and the advantages and disadvantages of each method**

| <b>Damping</b>                | <b>Method</b>  | <b>Advantage</b>  | <b>Disadvantage</b>   |
|-------------------------------|--|---|---|
| <b>Bulk viscosity damping</b> | Based on volumetric straining of elements                    | General ABAQUS damping method   | Doesn't apply the physical damping to any specific area.<br>Increase the running time |
| <b>Material damping</b>       | Mass and stiffness proportional damping (Rayleigh damping)   | Included in stability limit calculation<br>Directly applied to the source of oscillations | Complicated to use<br>The material damping parameters are generally unknown           |
| <b>Discrete dashpot</b>       | Relative velocity of the element nodes of the spring element | Simple to use.<br>Directly applied to the source of oscillations                          | Excluded in stability limit calculation   |

### 3.3 Materials and methods

#### 3.3.1 Geometry and alignment

The components of the THR were aligned as illustrated in Figure 3.2. In this chapter, the simplified geometry of the Pinnacle Ceramic-on-polyethylene THR was implemented. CAD models of commercially available implant geometries were used (Pinnacle® 100 series shell, outer diameter 56mm, Pinnacle® neutral polyethylene liner, bearing diameter 36mm, BioloX Delta® femoral head, bearing diameter 36mm, DePuy Synthes, Leeds, UK) modified for model simplicity by removing anti rotation devices on the cup and the shell.

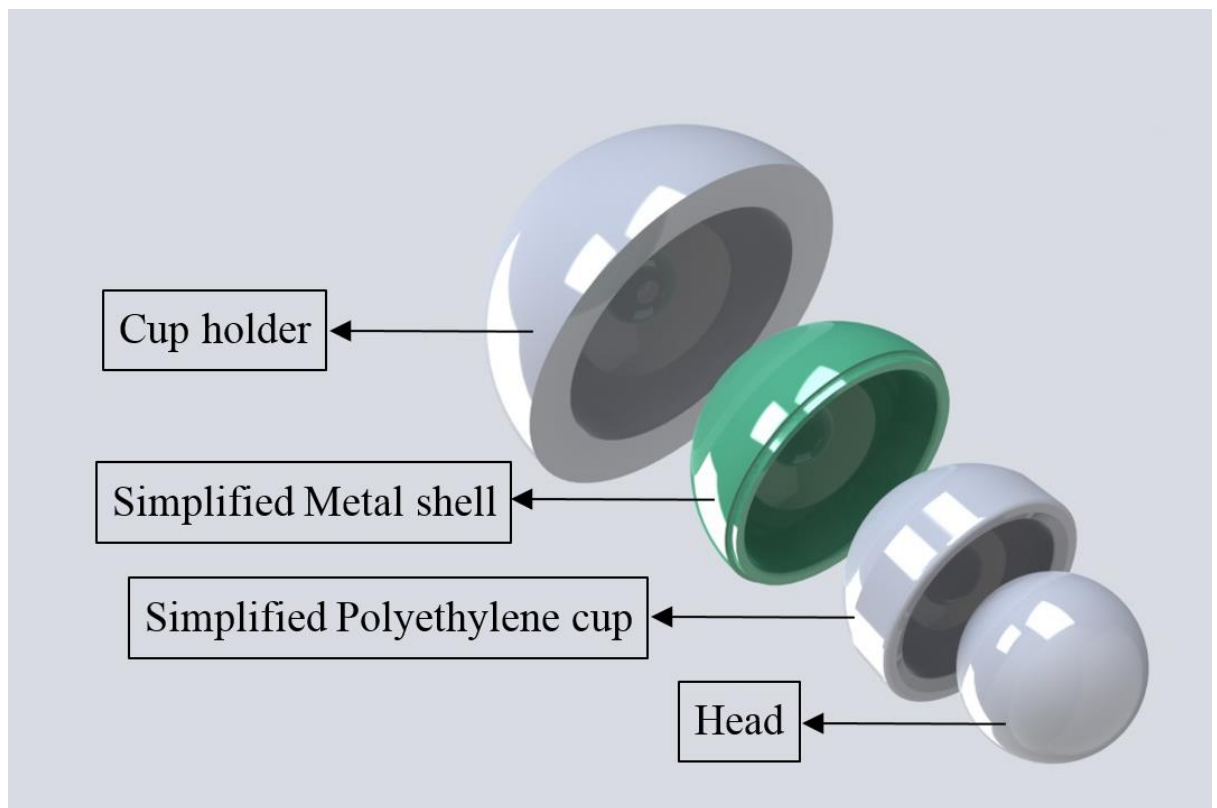


**Figure 3.2** Simplified cup holder, Pinnacle® 100 series shell, outer diameter 56mm, Pinnacle® neutral polyethylene liner, bearing diameter 36mm, BioloX Delta® femoral head, bearing diameter 36mm (DePuy Synthes, Leeds, UK).

#### 3.3.2 Assembly

The assembly of the components were designed to replicate the *in vitro* configuration as shown in Figure 3.3. A spring is attached to the cup holder and the cup holder, metal shell and the acetabular cup have tie constraint between the

interactive surfaces with 45° inclination angle. To simplify the cup holder geometry, it was designed as a semi-hemisphere.

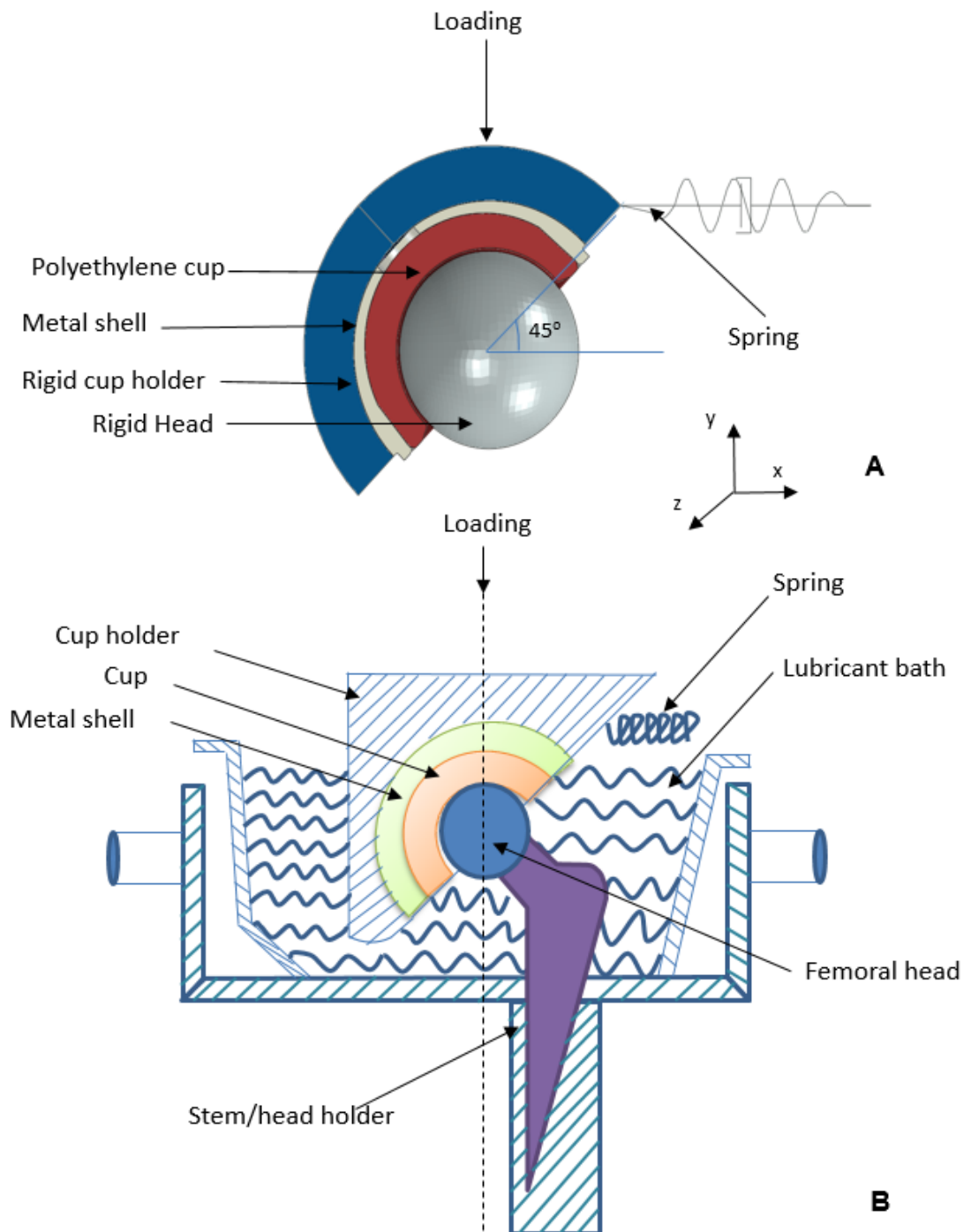


**Figure 3.3** The assembly in the computational model (A) and schematic of the experimental set up (B)

### 3.3.3 Material properties

The material properties of the components are shown in Table 3.3. As the size of the cup holder is simplified significantly, the mass point which assigns the total mass of the cup holder was defined on the reference point of the cup unit (The centre of the

head). In this study, the density was scaled up to increase the time step for computational efficiency as the higher density results in a larger time increment for stability.

**Table 3.3 Material and geometric properties of the components**

| Components | Material     | Young's modulus (MPa) | Poisson's ratio | Density (kg/mm <sup>3</sup> ) | Outer radius (mm) | Inner radius (mm) |
|------------|--------------|-----------------------|-----------------|-------------------------------|-------------------|-------------------|
| Head       | Rigid        | -                     | -               | 4.37x10 <sup>-6</sup>         | 18                | -                 |
| Cup        | Polyethylene | 670                   | 0.46            | 9.23x10 <sup>-7</sup>         | -                 | 18.524            |
| Shell      | Titanium     | 114,500               | 0.34            | 4.43x10 <sup>-6</sup>         | 56                | -                 |
| Cup holder | Rigid        | -                     | -               | 8.5x10 <sup>-6</sup>          | 27.25             | 24.25             |

In addition, the UHMWPE cup was assigned with a nonlinear behaviour by using elastic-plastic material model in ABAQUS that requires the stress and strain behaviour of the model only. This material model was used previously (Hua *et al*, 2014) and the elastic-plastic behaviour of the UHMWPE was provided by DePuy Synthes in house testing (Figure 3.4).

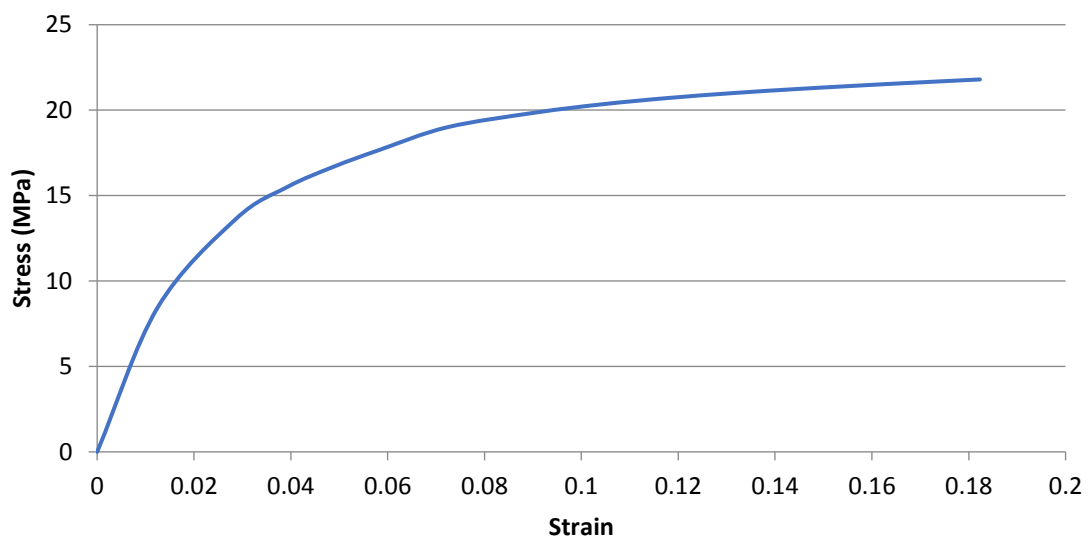


**Figure 3.4 Nonlinear Stress-strain behaviour for UHMWPE (1050 GUR)**

### 3.3.4 Finite element mesh

The meshing configuration of this study was chosen based on the previous analyses (presented in chapter 2). In line with the conclusions of chapter 2, a meshing ratio of 1.5:1.5 was assigned on the contact surfaces globally (ratio of element size on the acetabular cup to that on head). The cup holder and the shell have a slightly coarser mesh of 3mm and 2mm, respectively. Table 3.4 represents the details of the components elements. All of the elements have explicit, linear and reduced integration features.

**Table 3.4 The details of the components elements**

| <b>Part</b>       | <b>Global size (mm)</b> | <b>Element shape</b>       | <b>ABAQUS Code</b> | <b>Number of elements</b> |
|-------------------|-------------------------|----------------------------|--------------------|---------------------------|
| <b>Head</b>       | 1.5                     | Hexahedral                 | R3D4               | 2,228                     |
| <b>Cup</b>        | 1.5                     | Hexahedral                 | C3D8R              | 8,960                     |
| <b>Cup holder</b> | 3                       | Hexahedral and tetrahedral | R3D4 and R3D3      | 2,211                     |
| <b>Shell</b>      | 2                       | Hexahedral                 | C3D8R              | 2,820                     |

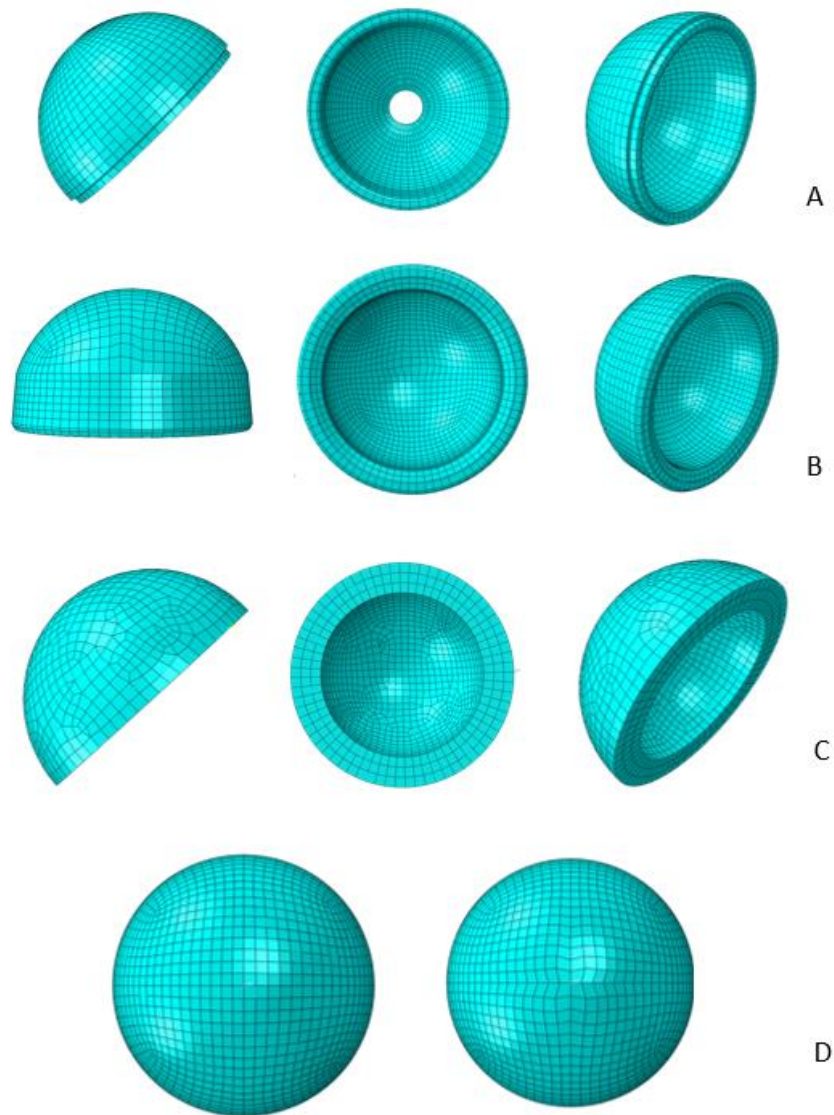


**Figure 3.5 Meshing of each component A) Metal shell, B) Polyethylene cup, c) cup unit and D) head**

### **3.3.5 Methods**

In this chapter, four studies are reported:

1. Spring representation
2. Inclusion of damping
3. Mass effect
4. Model input sensitivity

The construction of each study is based on the conclusion of the previous study. Figure 3.6 represents the flow and the order of the studies. As this figure shows, two approaches, spring element and truss element, were used to introduce the spring

behaviour into the model. Then, dashpot discrete damping method was applied to represent the spring in a more efficient way by achieving critical damping. Furthermore, the critically damped spring was taken forward to understand the effect of true mass rather than artificially increased mass and gait cycle loading on the analysis. Finally, the most reliable model up to this point was chosen for model input sensitivity analysis.

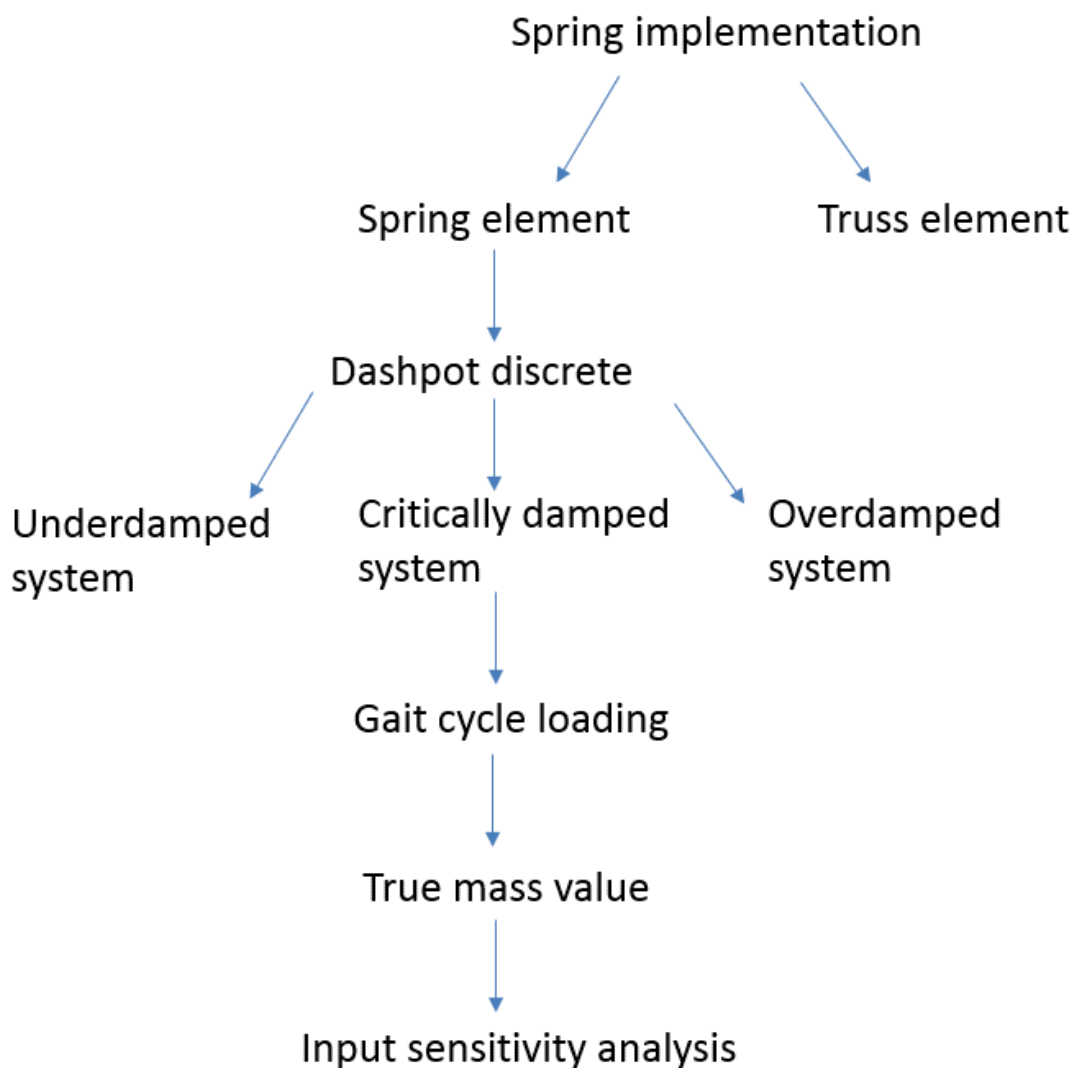


**Figure 3.6 Flowchart of the chapter 3 studies**

The overall details of the analyses, namely mismatch level, stabilisation time, dashpot coefficient and the mass of the system, that are reported in this chapter are presented in Table 3.5.

**Table 3.5 The variation and details of the studies that were carried out in chapter 3 based on the main variables namely, spring representation method, mismatch level, stabilisation time, dashpot coefficient and component mass condition**

| Study                   | Spring representation | Mismatch level (mm) | Stabilisation time (s) | Dashpot coefficient (mmN/s) | Mass state |
|-------------------------|-----------------------|---------------------|------------------------|-----------------------------|------------|
| Spring representation   | Truss element         | 3                   | 20                     | 0                           | Artificial |
|                         | Spring element        | 3                   | 20                     | 0                           | Artificial |
| Inclusion if damping    | Spring element        | 3                   | 2                      | 0                           | Artificial |
|                         | Spring element        | 3                   | 2                      | 1                           | Artificial |
|                         | Spring element        | 3                   | 2                      | 10                          | Artificial |
|                         | Spring element        | 3                   | 2                      | 20                          | Artificial |
|                         | Spring element        | 3                   | 2                      | 40                          | Artificial |
|                         | Spring element        | 3                   | 2                      | 60                          | Artificial |
|                         | Spring element        | 3                   | 2                      | 80                          | Artificial |
|                         | Spring element        | 3                   | 2                      | 90                          | Artificial |
| Mass effect             | Spring element        | 3                   | 0.2                    | 1                           | True       |
|                         | Spring element        | 3                   | 0.2                    | 3                           | True       |
|                         | Spring element        | 3                   | 0.2                    | 4                           | True       |
| Model input sensitivity | Spring element        | 1                   | 0.2                    | 3                           | True       |
|                         | Spring element        | 4                   | 0.2                    | 1                           | True       |

### 3.3.6 Spring representation

As mentioned above, the spring is used in the experimental set up to represent any medial-lateral mismatch between the head and the cup of the THR. In this study the spring is represented in the model by using two different methods as follows:

**Truss element:** A truss element of 50mm length was attached to the edge of the cup unit. The material properties given in Table 3.6 were assigned to the truss element. The Young’s modulus of the elements was calculated based on the predicted stress and strain level of the spring to produce the same spring stiffness as the *in vitro* studies (100 N/mm). Therefore, the Young’s modulus of the truss element was calculated from the predicted from strain and force level based on the fixed stiffness. A 2-node linear 3-D truss (two dimensional element in three dimensional space) was allocated to this element.

**Spring element:** In this method, two ends of the spring were selected by using reference points where one end is attached to the cup unit (attached end) and the other end is unattached to any entity. The properties that were assigned to the spring element are also presented in Table 3.6.

**Table 3.6 Truss and spring element properties to represent the experimental spring**

| Property             | Truss element                         | Spring element |
|----------------------|---------------------------------------|----------------|
| Young’s modulus      | 500 MPa                               | N/A            |
| Cross sectional area | 10 mm <sup>2</sup>                    | N/A            |
| Length               | 50 mm                                 | 50 mm          |
| Density              | 9x10 <sup>-6</sup> kg/mm <sup>3</sup> | N/A            |
| Stiffness            | 100 N/mm                              | 100 N/mm       |

### 3.3.7 Boundary conditions, loads and analysis steps

All of the analyses consisted of four steps:

1. Pre-contact: The analysis starts with a concentric head and the cup. In this step, the head is translated upward for the amount of radial clearance in order to establish initial contact (Figure 3.7).

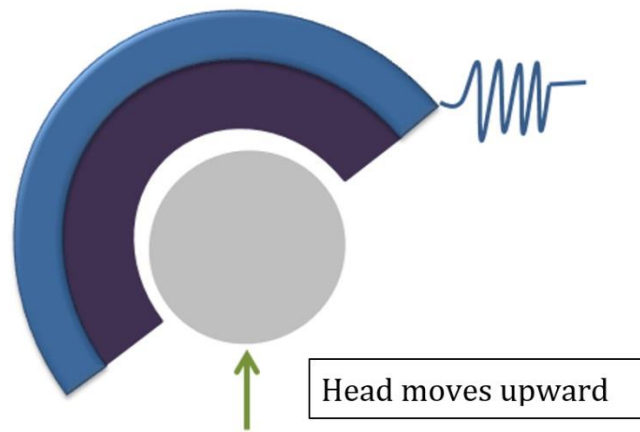


**Figure 3.7 Illustration of precontact step: vertical movement of the head.**

2. Spring compression: During this step, the spring becomes fully compressed (3mm for 3mm translational mismatch) in isolation by translating the lateral end (Figure 3.8). At this step, the head and the cup components are held in place by fully constraining them.

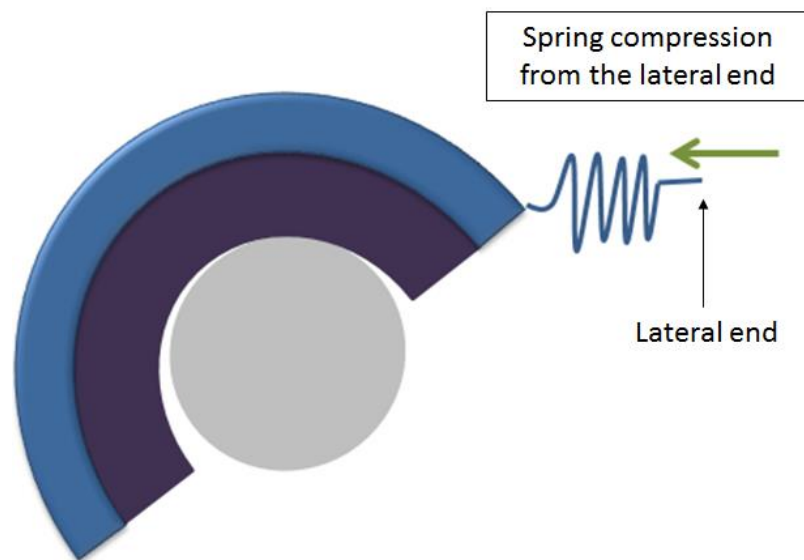


**Figure 3.8 Spring compression step illustration: Compression of the spring medial/laterally**

3. Spring stabilisation: The Fixation of the cup unit is released and the lateral end of the spring is fixed. Therefore, the equilibrium position of the cup with respect to the head is determined. Also, there is a vertical force applied through the cup unit to stabilise the joint (Figure 3.9).

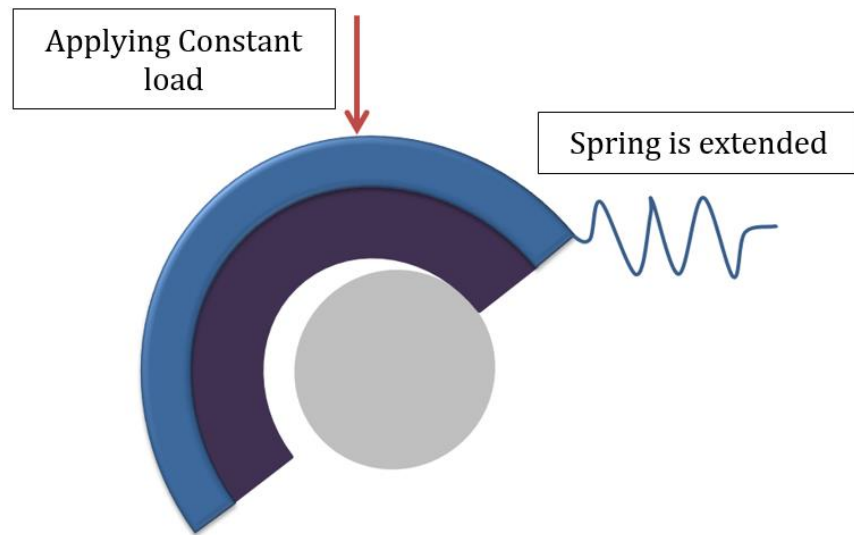


**Figure 3.9 Spring stabilisation step illustration: Cup moves away from the head and the spring extends**

The details of the steps, loading and boundary conditions are shown in Table 3.7. In the pre-contact step, only vertical displacement of the head is allowed. As the spring compresses in isolation in the spring compression step, the only movement in this step is the horizontal translation of the lateral spring end.

As the stabilisation step starts, the lateral end of the spring becomes fixed. The spring attached end, cup unit, metal shell and cup liner are allowed to translate horizontally and vertically to determine the equilibrium cup location with respect to the head. Moreover, a constant vertical load of 300N is applied during this step. 300N is the minimum load that is applied during the swing phase of the standard gait cycle.

**Table 3.7 Steps, loading conditions and boundary conditions of the analyses**

| Steps                       | Duration (s) | Axial load    | Boundary conditions |                                     |                                     |                 |
|-----------------------------|--------------|---------------|---------------------|-------------------------------------|-------------------------------------|-----------------|
|                             |              |               | Head movement       | Cup movement                        | Spring movement                     |                 |
|                             |              |               |                     |                                     | Medial end                          | Lateral end     |
| <b>Pre-contact</b>          | 0.05         | -             | 0.54mm upward       | Fixed                               | Fixed                               | Fixed           |
| <b>Spring compression</b>   | 0.05         | -             | Fixed               | Fixed                               | Fixed                               | 3mm compression |
| <b>Spring stabilisation</b> | 2            | Constant 300N | Fixed               | Horizontal and vertical translation | Horizontal and vertical translation | Fixed           |
| <b>Loading</b>              | 2            | 2 Paul cycle  | Fixed               | Horizontal and vertical translation | Horizontal and vertical translation | Fixed           |

In the fixed loading step, the twin peak Paul cycle loading that was applied in the experimental set up (shown in chapter 2) is applied in the model with similar boundary conditions as in the stabilisation step. The Paul cycle is repeated twice in these analyses in order to examine the level of noise in repetitive cycling.

### **3.3.8 Inclusion of damping**

A dashpot coefficient was added to the spring element to minimise the dynamic oscillations of the spring and study the effect of damping on the dynamic output. Various dashpot coefficients were tested to determine the value which would

produce a critically damped system. Table 3.8 represents the dashpot coefficients of each case. The duration of the stabilisation step is 2s for all the cases.

**Table 3.8 Dashpot coefficient assigned for each case with spring element as the spring**

| Case | Dashpot coefficient (Ns/mm) |
|------|-----------------------------|
| A    | 0                           |
| B    | 1                           |
| C    | 10                          |
| D    | 20                          |
| E    | 30                          |
| F    | 40                          |
| G    | 60                          |
| H    | 70                          |
| I    | 80                          |

### 3.3.9 Mass effect

The effect of the mass was tested on the dynamics and contact mechanics analysis to justify if the model with artificial mass (heavier than true mass values to increase the time step) could produce as valid output as the true mass values. The mass of the elements is the main parameter to calculate the maximum time increment for stability and there is an inverse relationship between the mass and the time increments for stability. Therefore, the greater the density is, the longer the time increment for stability is and consequently, the shorter the run time of the analysis. The material densities shown in Table 3.9 were assigned to the corresponding component. Initial studies on the analyses with true mass values indicated that due to the mass changes, the time taken for the spring to become stable during stabilisation is considerably reduced. Therefore, the stabilisation step time was assigned to be 0.2s for true mass value analyses.

**Table 3.9 True mass values of the components and the material used for each component**

| Components | Material     | Density (kg/mm <sup>3</sup> ) |
|------------|--------------|-------------------------------|
| Head       | Rigid        | 4.37x10 <sup>-9</sup>         |
| Cup        | Polyethylene | 9.23x10 <sup>-10</sup>        |
| Shell      | Titanium     | 4.43x10 <sup>-9</sup>         |
| Cup holder | Rigid        | 8.5x10 <sup>-9</sup>          |

To understand the effect of dashpot coefficient on the output of the model with true mass values, variation of dashpot coefficients of 1, 3 and 4 Ns/mm were applied to the model.

### 3.3.10 Model input sensitivity

Two cases that represents the extreme best case and worst case input circumstances based on the translational mismatch matrix were tested on the model with the spring element with different dashpot coefficients. The purpose of this study is to determine if the model can differentiate between the input parameters with no instability. Furthermore, it would indicate whether the chosen methodology can work on a wider parametric range. Table 3.10 represents the differences between each case. The mismatch level, cup inclination angle, swing phase load of the gait cycle and the dashpot coefficient vary in the cases. In this study, the true mass values of the components were applied.

**Table 3.10 Description of the variables namely mismatch level, cup inclination angle, swing phase load, stabilisation load and dashpot coefficient on both cases**

| Cases | Mismatch level (mm) | Cup inclination angle (°) | Swing phase load (N) | Stabilisation load (N) | Dashpot coefficient (mmN/s) |
|-------|---------------------|---------------------------|----------------------|------------------------|-----------------------------|
| A     | 1                   | 45                        | 300                  | 300                    | 3                           |
| B     | 4                   | 45                        | 300                  | 300                    | 1                           |

### 3.3.11 Model output measures

At this stage, the primary factor that was investigated was the dynamic behaviour of the system in order to study the methods of mitigating the oscillations. A decision was made to determine a suitable response that could be compared to the experimental simulation for validation purposes. In the experimental set up, the measured separation, i.e. the Medial/Lateral displacement (M/L displacement), between the centre of the head and the cup (Williams *et al.*, 2003; Al-Hajjar *et al.*, 2010; Ali *et al.*, 2016), is exported from the testing. Hence, the M/L displacement of the cup throughout the analysis is recorded during the experiment and can be compared to the simulation results without any extra engineering effort. In experimental and clinical studies, the highest separation occurs during the swing phase load when the vertical force is a minimum. Moreover, lower separation was recorded during the stance phase causing a more concentric contact between the contact surfaces due to the highest vertical loading (Komistek *et al.*, 2002; Al-Hajjar *et al.*, 2010). The M/L displacement of the cup represents the separation because the head and cup are initially concentric and the head is fully fixed during the analysis. This measure only takes into account the separation in one medial-lateral direction and does not include the movement of the cup in the other directions. In terms of the contact mechanics analysis, the contact area on the cup surface is also studied to understand if there is any contact instability or loss of contact between the bearing surfaces during the loading cycle.

### 3.4 Results

The output of the analyses are presented in the same order as the description of the methodology.

#### 3.4.1 Spring representation

Two simplified methods were used to represent the experimental spring in the computational model. The predicted M/L displacement of the cup is presented in Figure 3.10 and Figure 3.11 with truss and spring elements, respectively.

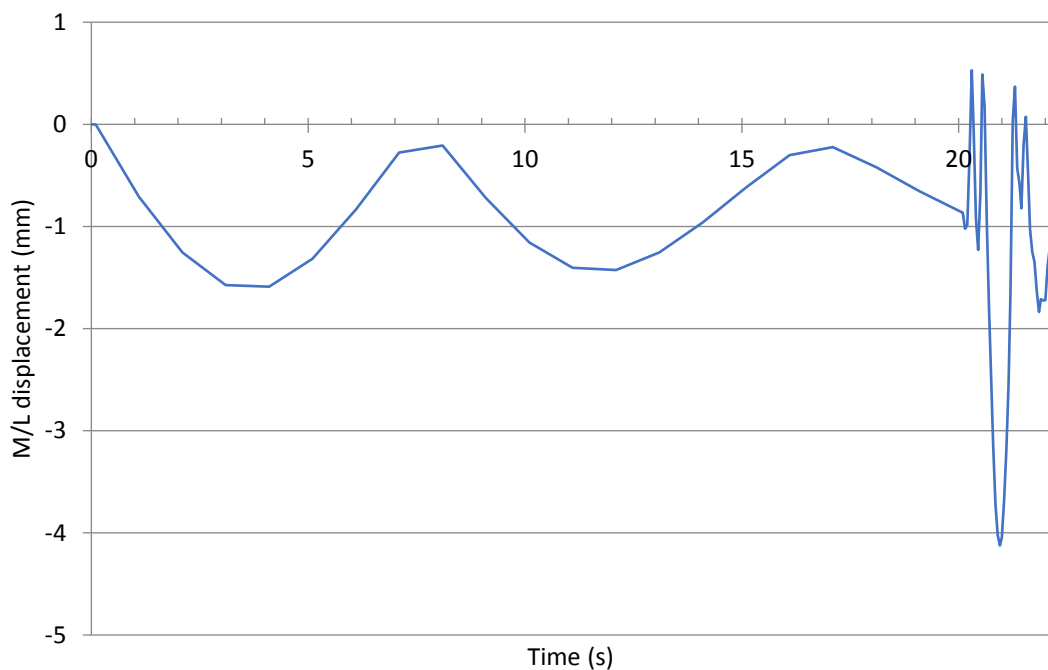


**Figure 3.10 Medial/lateral displacement of the cup using a truss element as the spring with 3mm translational mismatch level and 300N swing phase load**

At this stage of development, the focus is on the M/L displacement during stabilisation because this behaviour indicates the dynamic stability of the system. Moreover, the M/L displacement during the gait cycle is monitored to determine whether the displacement of the model is practical. The M/L displacement of the cup unit indicates a large noise during the spring stabilisation step when a truss element was used. The oscillation that was produced by the truss element in this step has a large time period of about 8s and the amplitude of the oscillations is reduced gradually with time. As expected, the oscillations generated by the truss

element seem to lessen with time which suggest that the system naturally becomes more stable with time.

When the Paul cycle is applied, the minimum M/L displacement during stance phase is expected especially at the two peak loads because of the high vertical loading. Furthermore, the M/L displacement during the swing phase is expected to be the maximum as the axial loading is minimum. The minimum axial load should allow the cup to move in M/L direction as the M/L force is less in swing phase.

As gait cycle loading is applied, the M/L displacement follows a similar trend as stance loading. However, when the swing phase load was applied (constant 300N load), the medial-lateral displacement initially decreases (time 20.6s to 20.8s in Figure 3.10) and then increases dramatically (20.8s to 21s) and doesn't become constant. Moreover, the oscillations in the medial-lateral displacement of the cup during the second gait cycle loading become more moderate particularly in the swing phase load.

The spring element underwent an oscillations with an amplitude that decreases by the time during the spring stabilisation step. The number of the oscillations during stabilisation is more for the spring element than for the truss element. Thus, the time period of the oscillations for the truss element is substantially longer than for the spring element. The Paul cycle undergoes two peak loads for which the M/L displacement is expected to be zero. During the swing phase load, the M/L displacement of the model increases. However, the M/L displacement during the swing phase load of the second Paul cycle is substantially higher than in the first Paul cycle loading of the truss element model.

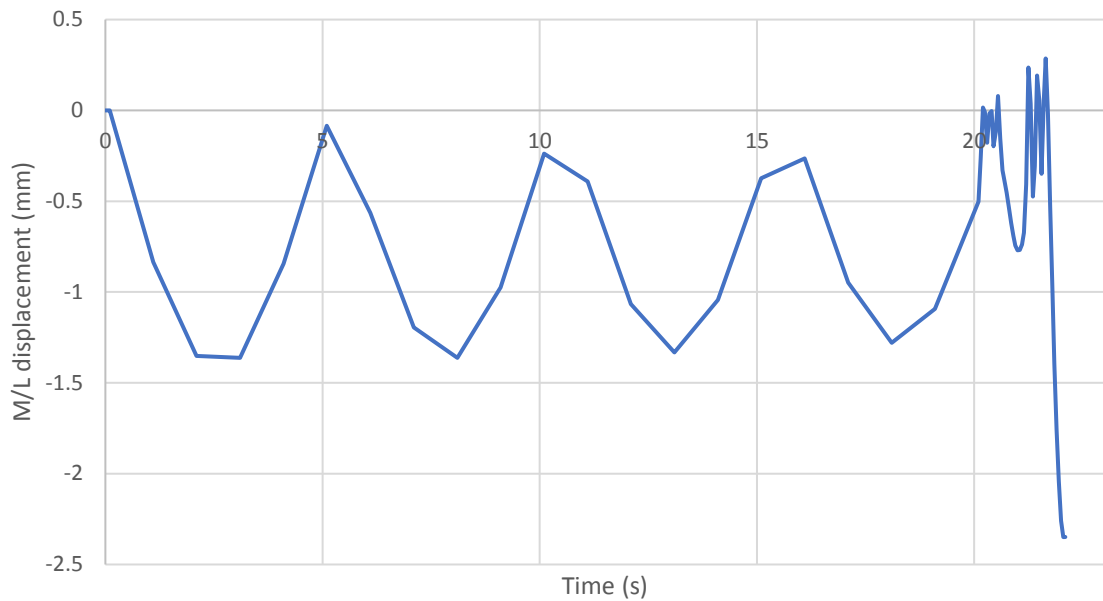


**Figure 3.11 Medial-lateral behaviour of the model with ABAQUS spring element as the spring with 3mm translational mismatch level and 300N swing phase load**

The dynamic output of both the truss and spring element models indicated that the M/L displacement could potentially be affected by numerical noise level which could make the prediction of the separation unreliable. It is important to be able to predict the level of M/L displacement during the swing phase load as the dynamic separation that is recorded from the *in vitro* studies is measured during the swing phase. Therefore, additional damping was introduced to the model to understand to that extent the numerical noise can be minimised by damping. To implement a level of damping in the truss element model, Rayleigh's damping coefficients need to be calculated. However, damping can be applied to the spring element simply by attaching a damper in parallel to the spring. Therefore, further analyses are carried out on the spring element only.

### 3.4.2 Inclusion of damping

Different dashpot coefficient values were applied to the model with the spring element to understand the importance of damping effects on the output. Figure 3.12 represents the results of several analyses carried out with different dashpot coefficients. Even the minimum level of dashpot coefficient that was applied

resulted in a large decrease in the amplitude of the oscillations compared to the no dashpot case. The consistency in the oscillations is more obvious for the spring element model as the wavelength of the oscillations for spring element model is shorter than for the truss element model. The underdamped system behaviour is more obvious when a level of dashpot coefficient is applied to the spring element. Moreover, the dashpot coefficient causes stabilisation of the spring in a shorter time. Although the initial results suggest an underdamped system up to the dashpot coefficient of 60 Ns/mm, the overall displacement behaviour is considerably affected by the value of the dashpot coefficient. It can be seen that various dashpot coefficients were applied to the model to achieve a critically damped system. As the dashpot coefficient increased up to 70 Ns/mm, the amplitude of oscillations decreased during stabilisation time. When a dashpot coefficient of 80 Ns/mm was used, the cup unit is moved medial-laterally to the stable point in a shortest time (0.5s). Thereafter, no further oscillations are recorded when the cup unit is displaced to its maximum level which is an indication of a critically damped spring system. A higher dashpot coefficient of 70 Ns/mm caused a different behaviour during stabilisation. The cup unit ultimately attempted to reach the same stable point. However, the time taken to reach the point is longer. Although, no noise was seen for a dashpot coefficient higher than 70 Ns/mm, the time taken and the shape of M/L displacement graph indicate an over damped system which may under predict the magnitude of the displacement in the time period.

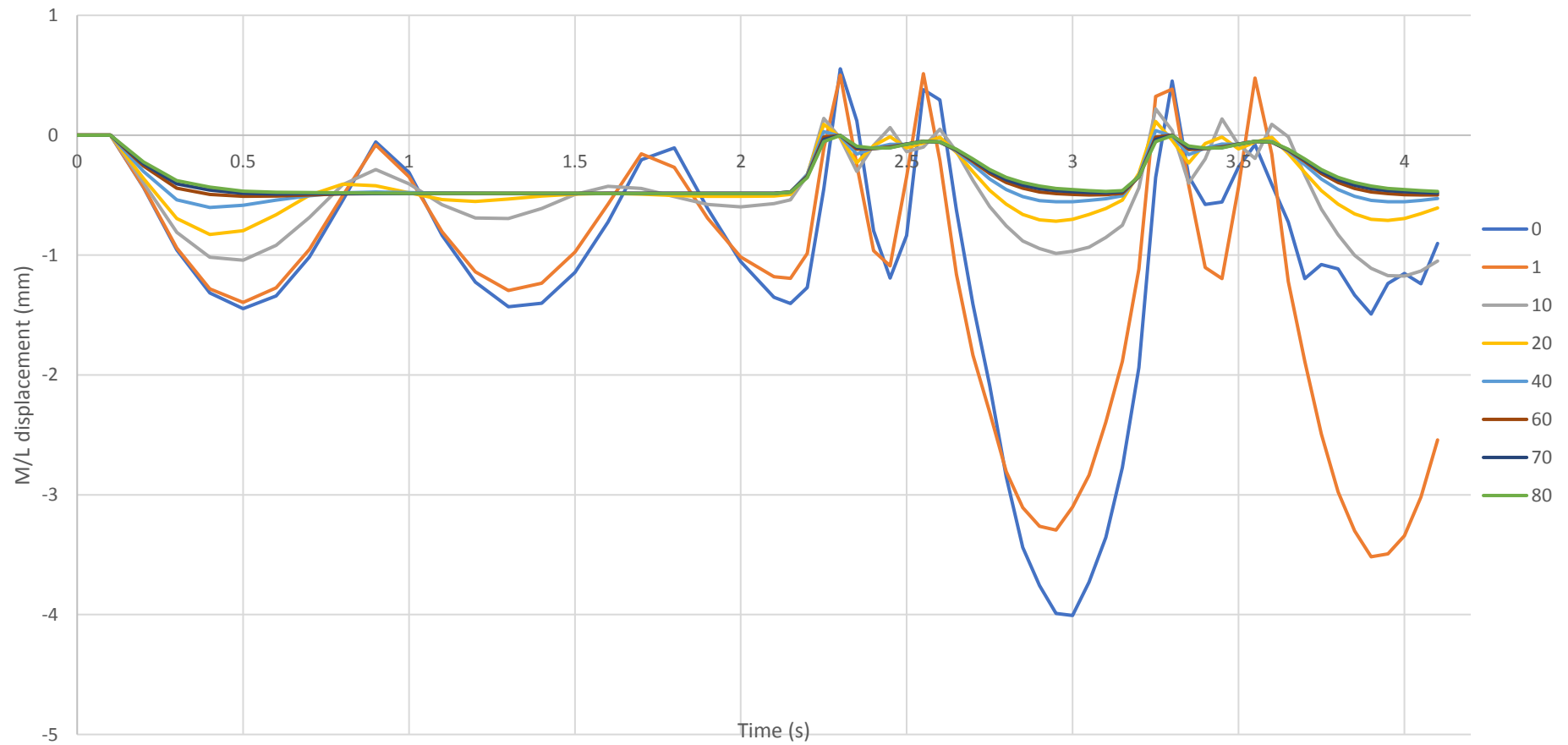


**Figure 3.12** The effect of damping on the M/L displacement of the model with specific dashpot coefficient, 3mm translational mismatch level and 300N swing phase load. Each plot represents the value of dashpot coefficient (Ns/mm).

After the damping analysis, the next step is to investigate the effects of gait cycle loading on the dynamics and contact mechanics of the explicit model (Figure 3.12). The analyses that were carried out in inclusion of damping study underwent gait cycle loading to understand the effect of damping condition on the M/L displacement during the loading. Therefore, two modified vertical Paul loading cycle were applied to the model. When the Paul cycle loading is applied, the M/L displacement initially decreased as the load reached the first peak. Then a moderate increase and then decrease of the displacement between the two peak loads were observed. After the second peak load, a substantial increase in the M/L displacement occurred during swing phase load (minimum axial load of the cycle). The major differences between different damping conditions caused by increasing the dashpot coefficient are:

- Changing of three zero point to two zero point: The damping resulted in the two points during gait cycle in which the separation is minimum as the load is maximum (the twin peaks)
- No overshooting of the M/L displacement in the critically damped model
- Moderate changes of M/L displacement between the two peak stance phase loads
- Minimisation of oscillations during the swing phase
- Substantial decrease in the M/L displacement during swing phase.

Moreover, it was also seen that if a dashpot is added to the model, M/L displacement during the first and second Paul cycle is similar and hence greater consistency and stability after only one cycle.

The critically damped system produced the ideal dynamic behaviour computationally as no noise and no overshooting were observed in the critically

damped model. Moreover, the M/L displacement behaviour in swing phase load was clearer which resulted in a clearer displacement prediction. The cases with lower dashpot coefficient displayed oscillations during the swing phase whereas the displacement decreased and stayed constant during the swing phase in the critically damped model.

The contact area predicted by the model is shown in Figure 3.13. Large oscillations could be seen as the spring reached its initial stabilisation point. Later, the amplitude of the oscillations was substantially less. However, the mean value of the oscillation peak alters during this step. Similar to analyses that were reported in chapter 2, oscillation also occurred during Paul cycle loading and the oscillation pattern is similar in first and second Paul cycle. As the dynamic and contact mechanics behaviour does not vary in the second Paul cycle, future analyses will be carried out on only one Paul cycle loading.

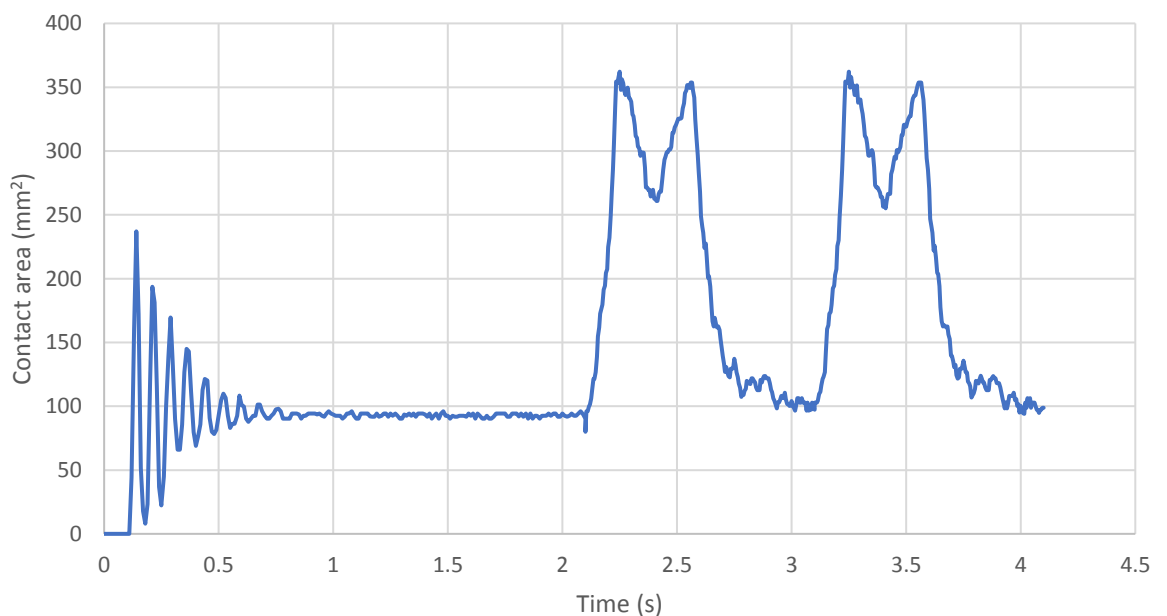


**Figure 3.13 contact area versus time for the model with 3mm mismatch level, 300N swing phase load, 45° inclination angle and 70 Ns/mm**

### 3.4.3 Mass effect

Figure 3.14 represents the M/L displacement of the model with true mass values for the 3mm mismatch case. Zero displacement in the pre-contact and spring compression steps is expected as no horizontal movement resulted from these steps. Dashpot coefficients varying between 1 Ns/mm and 4 Ns/mm were tested on this model. The minimum dashpot coefficient that resulted in no oscillation was 3 Ns/mm. Although the critical value of the dashpot coefficient differed between the true and artificial mass models, the same damping behaviour is observed for both mass conditions. The spring seems to become stable in a significantly shorter time than for the artificial mass values with a minimum level of oscillation. In gait cycle loading, the M/L displacement with true mass values, as for the artificial mass values, followed the axial loading changes. The displacement at the peak loads are the same and no overshooting of the displacement was observed.

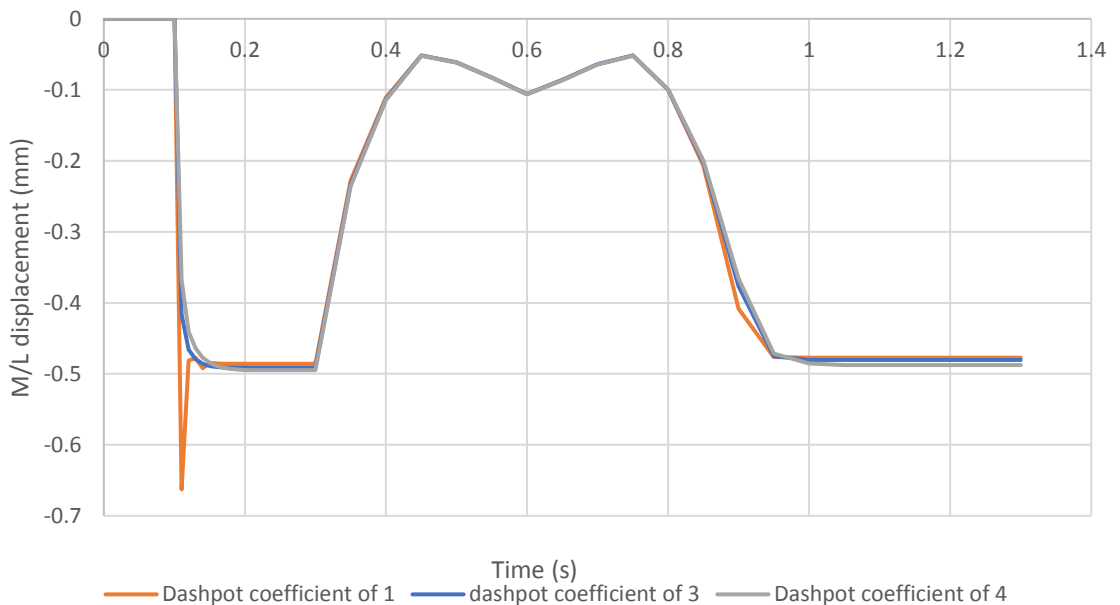


**Figure 3.14 M/L displacement behaviour for various dashpot coefficient with true mass values, 3mm translational mismatch level and 300N swing phase load**

Figure 3.15 indicates the difference in M/L displacement under cyclic load when artificial and true mass values are applied. Although the overall M/L displacement

pattern is similar in both cases, the following differences between the true and artificial mass model with respect to the M/L displacement were observed:

- Time delay in M/L displacement response only in model with artificial mass value.
- Different M/L displacement value for two peaks in the model with artificial mass value whereas true mass values resulted in the same M/L displacement for both peaks.
- During the swing phase, the analysis carried out on the model with true mass values resulted in constant M/L displacement. However, the artificial mass value resulted in gradual decrease in M/L displacement throughout the whole swing phase.

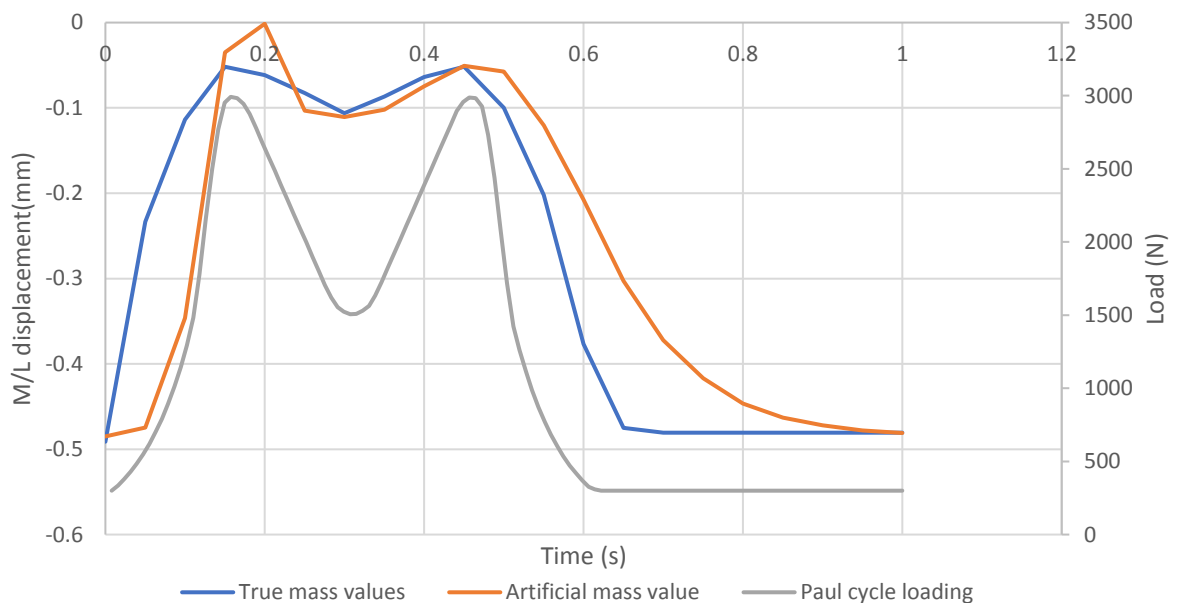


**Figure 3.15 Critically damped model of artificial and true mass on M/L displacement behaviour with sampling frequency of 20 with 300N swing phase load and 3mm translational mismatch level**

The contact area predicted by both models (Figure 3.16) showed the same numerical noise. However, the amplitude of the noise is very small and the general trend of contact area is obvious. The major differences in contact area between the cases occurred at the beginning of the stance phase and during the swing phase. The

analysis with true mass values resulted in a slightly higher contact area as the load reached its first peak. Moreover, contact area changes during the swing phase in the artificial mass model gradually decreased whereas the contact area in the true mass model is constant throughout the swing phase.

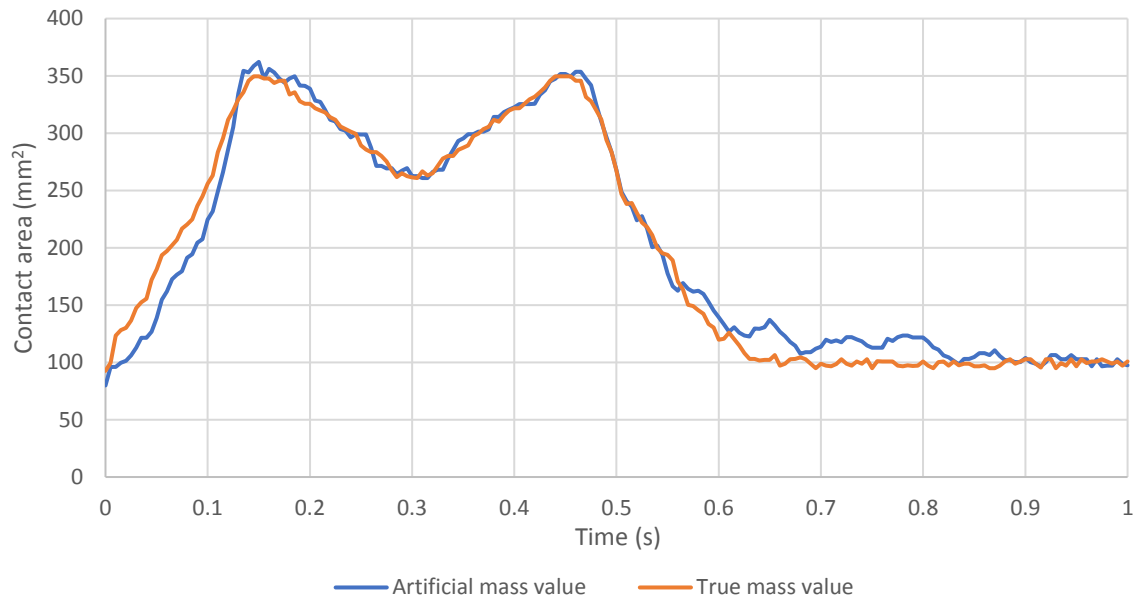


**Figure 3.16 Contact area comparison using true and artificial mass values for the analyses with 3mm translational mismatch level and 300N swing phase load**

### 3.4.4 Model input sensitivity

The two cases that could represent the best and the most crucial output conditions (1mm and 4mm mismatch) were analysed and the M/L displacement time history for each is presented in Figure 3.17. Once more, the expected behaviour was seen for each of the pre-contact, spring compression and stabilisation steps and the analyses were critically damped so no oscillation or long term gradual stabilisation was observed. The general trend of the M/L displacement in all the cases followed the axial loading changes and the M/L displacement behaviour seemed to be similar to the previous analysis with 3mm mismatch level and critically damped system.

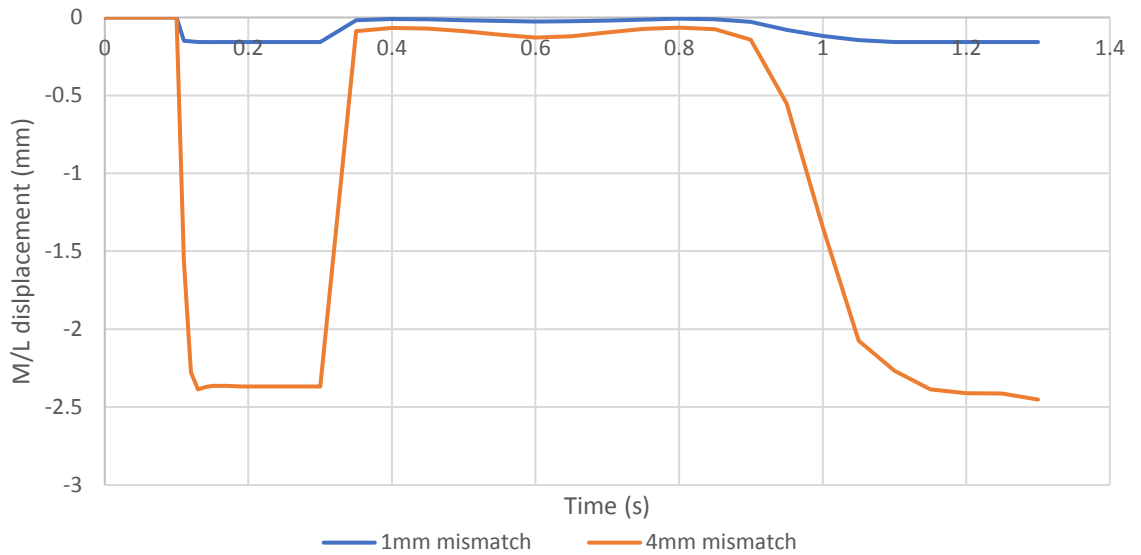


**Figure 3.17** The M/L displacement of the cases that represent the analyses with 1mm and 4mm translational mismatch level, 45° inclination angle and 300N swing phase load

The contact area changes during Paul cycle loading for the 1mm and 4mm mismatch level is presented in Figure 3.18. Both analyses resulted in virtually the same maximum contact area at the peak loads. However, the contact area derived during the swing phase was less for the 4mm mismatch than for the 1mm mismatch. The difference in contact area value during the swing phase agreed with the changes in M/L displacement. The difference in contact area occurred due to the higher lateral separation in 4mm mismatch case resulting in a smaller contact area close to the lateral edge of the cup.

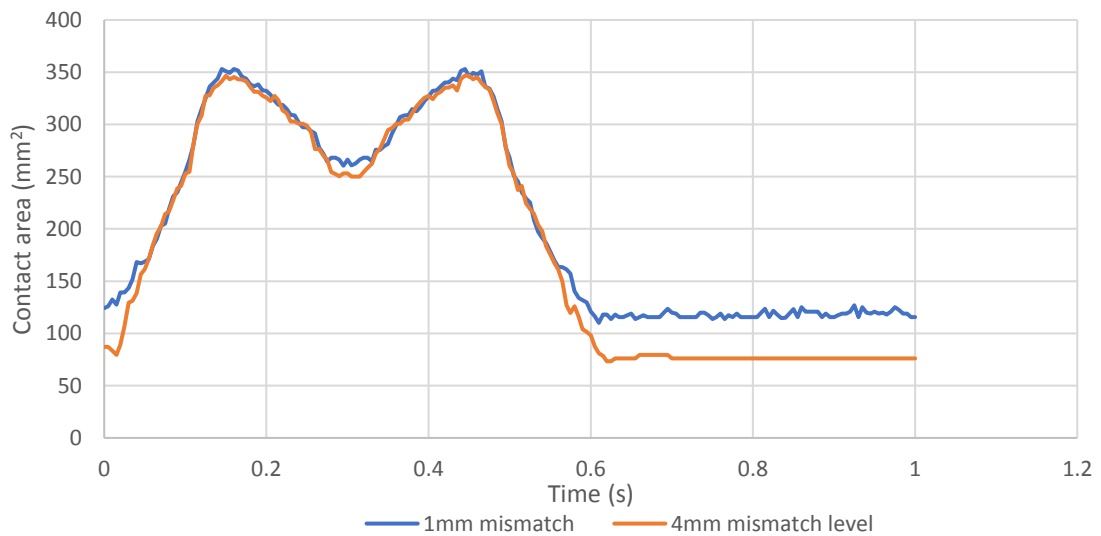


**Figure 3.18** Contact area derived from analyses versus time with 300N swing phase load, 45° inclination angle and translational mismatch variation of 1mm and 4mm

### 3.5 Discussion

The analyses reported in this chapter focused on the reliability of the chosen methods based on the applications. The model is required to predict the level of M/L displacement for validation proposes against *in vitro* testing as described in the next chapter. Once the model is validated against *in vitro* studies, the reliability of the model can be assured in order to predict the effect of a wide range of parameters on the dynamic and contact mechanics of the THRs. As dynamic separation and edge loading are multifactorial scenarios (Fisher, 2011), *in vitro* studies are expensive and it is time consuming to test all the potential factors or combination of the factors on THR behaviour due to simulator preparation time, long duration of simulator testing, maintenance of the simulators and number of tests required. However, a validated computational model can provide a useful insight to the THR performance during an activity. A wide range of parametric testing can also be carried out on the computational models to estimate which parameters can potentially have the most effect on the THR performance under adverse conditions. Furthermore, those parameters can be taken forward in experimental studies.

The computational model also needs to estimate reliable contact mechanics information. The contact mechanics output provides information about which area of the bearing undergoes the most severe contact behaviour that could lead to permanent damage and potentially failure of the device. The model can be used to determine at which stage of the gait cycle the bearing is potentially at the most risk of damage. The insight from the contact mechanics information about the bearing behaviour during an activity helps to navigate and focus on the damaged zone for improvement of future joint designs.

*In vitro* studies cannot provide contact mechanics information for the bearing during a gait cycle. The dynamic parameter that is measured in these simulator studies is the dynamic separation within the cycle. Therefore, the dynamic separation is the only factor that can be readily compared between the *in vitro* and computational studies. In this chapter, the computational model is developed to simulate the experimental configuration simply by considering the efficiency of the computational method.

There is an element of damping (energy loss) due to mechanical friction or other tribological effects in all real systems. In the simulators, no additional damping is attached to the spring and the damping in the experimental studies is provided by friction and other aspects of the total components behaviour such as mass. Therefore, there is no direct measurement of the damping in the experimental set up and it is a very challenging task to quantify the *in vitro* damping. In computational studies, damping is modelled mathematically to align the model more closely to the real-world scenario and to reduce the system noise. In this application, as the spring is the primary cause of the oscillation in the M/L displacement, the damping is directly applied by adding a damper parallel with the spring.

There are different numerical damping methods that were discussed in the technical background section of this chapter. Bulk viscosity applies the damping to the whole system regardless of the individual components. ABAQUS applies a small level of bulk viscosity by default to decrease the numerical noise of the system. Material damping can be applied only when using a truss element as the spring. However, the prediction of mass and stiffness proportional Rayleigh damping is very challenging for a system with many degrees of freedom. The most ideal option is to add the

discrete dashpot to be used in parallel with spring element to add damping in addition to the default bulk viscosity damping.

The spring/dashpot system is the simplest method to implement the experimental spring behaviour as it only requires a simple calculation prior to analysis whereas the material damping/truss element system requires a complex initial calculation to find the Rayleigh damping factors. On the other hand, the spring element is not considered in the ABAQUS stability time step calculation due to the lack of spring element mass. This could cause a level of instability in the whole system. This effect is substantial when considering a damper/spring system because of continuous spring movement. However, the spring/dashpot system does not appear to experience any dynamic instability throughout the analysis although numerical oscillation still occurs for low values of dashpot coefficients

The damping conditions have a great effect on the M/L displacement of the model. Maximum M/L displacement (during the swing phase) varies based on the damping factor. The critically damped model predicts the maximum M/L displacement with no oscillations present. The results from an over/under damped system are not as reliable as from the critically damped model as the dynamic effects could potentially be underestimated in the over damped system and overestimated in the underdamped system. There is not a specified level of damping that can be extracted from the experimental set up. If a fixed dashpot coefficient is assigned for all the cases, it could either be an estimation or predicted from the certain conditions based on the experimental behaviour. However, this approach is challenging as it would involve a whole series of analyses to be carried out at much longer computational time and cost.

As increased mass has the inverse effect on the time increments for stability, the effect of mass scaling was examined to shorten the running time of the analysis. The main effect of mass on the dynamics of the model is during the swing phase. The M/L displacement during the swing phase seems to be constant in the analysis with true mass values as the swing phase load is constant. However, artificial mass values resulted in continuous increase in M/L displacement during the swing phase. Higher mass values results in longer time to stabilise the output than true mass values. The asymptotic behaviour of M/L displacement during the swing phase for the artificial mass model could be explained by the lack of sufficient time during the swing phase to reach a stable value.

Artificial mass values also result in substantial changes in the M/L displacement between the two peak loads during the stance phase whereas true mass values cause only a slight change during that time. This difference in dynamic behaviour is due to the inertia in two systems. True mass values results in lower inertia and therefore, takes less time to settle to a stable position than higher inertia for the artificial mass model. For future analyses, true mass values for all the components are specified as the differences between the M/L displacement in the true and artificial mass analyses are substantial even though the run time of the true mass analyses are much higher.

In the model input sensitivity study, the analyses positively reacted to the changes in the cases. There was a definite differentiation between the attempted cases. As expected, the maximum M/L displacement increased as the translational mismatch level increased. Moreover, no oscillations or instability of the dynamic and contact mechanics data were observed throughout the analyses when critical damping was applied. Although no noise in the analysis simplified the output reading, pre-

damping analysis is required for each case to predict the dashpot coefficient level that produce a critically damped system. The output observation indicated an acceptable overall dynamic and contact mechanics behaviour. Therefore, the next step would be validating the output by comparison with *in vitro* data followed by parametric testing.

### **3.6 Key findings**

- ABAQUS built in spring element with dashpot in parallel was found to be the best method to represent the *in vitro* spring.
- The dynamic and contact mechanic are directly affected by the mass of the system. Therefore, true mass values will be applied to the model for all future analyses even though the run time was over 20 hours for the analyses with true mass values.
- As determined, the true damping ratio of the simulator is a challenging task, critically damping was assigned to the spring to minimise oscillation of the M/L displacement. However, damping calibration is required for each individual cases to reach critically damped model.
- The M/L displacement of the model behaved expectedly. Therefore, the next step is to perform model validation and parametric testing.

## Chapter 4 Parametric sweep, validation and sensitivity testing

### 4.1 Introduction

In line with the conclusion of Chapter 3, the method of the explicit finite element model of THR under adverse condition is mainly developed and finalised. The agreed method consisted of a spring element that initially is compressed for the desired translational mismatch level and then is released to maintain the stability. After the stabilisation of the spring, the model is loaded with the gait cycle axially. Implying the dashpot coefficient assisted the model to eliminate the effect of noise on the results. The recorded separation had an inverse relationship with the loading during the gait cycle which resulted in the highest separation during swing phase and consequently, the lowest contact area in the cycle.

The results that were exported from the chosen method followed the sensible trends as the experimental methodologies, and so enabled the next step of the development which was applying the parametric sweep of testing and validate the outcome against *in vitro* studies. The aim of testing parametric sweep and validation was to test the reliability of the method that leads to confidence in the conclusion resulted from the model output.

The parametric sweep focussed on the following key areas:

- 1 Translational mismatch level: A level of mismatch between the centre of the head and the cup
- 2 Rotational variation: variation in cup inclination angle
- 3 Tissue laxity: by varying swing phase load

In this chapter, the dynamic effect of the parameters such as dynamic separation predicted by the finite element model is compared to separation values measured in independent *in vitro* tests undertaken by another researcher (Ali et al, 2016; Appendix). The results from thirty two independent conditions data points were compared to the experimental results for the same set of conditions as part of the validation process.

The validation of the model is discussed based on the *in vitro* testing carried out on an iMBE electromechanical hip simulator (Prosim EM13 hip simulator) which has previously been used to test metal on polyethylene hips under standard conditions. For the purposes of the validation of this computational model of edge loading, the test conditions and study reported in the Appendix was used, As the model is set to replicate a physical hip simulator, the overall assembly of the experimental set up was replicated in the computational model to simplify the validation process.

Furthermore, as friction occurs in the bearing in the experimental simulator and the precise value is not known, the model was tested for sensitivity to variation in the coefficient of friction on the contact surfaces was carried out on the model to understand the effect of friction on the extreme cases in the input parameters. Friction and lubrication of the bearing materials have an effect on the contact mechanics and wear of the material bearings *in vitro* studies (Brocket et al, 2007). The aim of the sensitivity test is to examine if friction at the bearing surfaces plays an important role in this application.

The layout of this chapter also, consists of the description of the methodology (section 4.2), the computational and experimental result presentation (section 4.3), discussion of the results (section 4.4) and the key finding of the studies (4.5), respectively.

## 4.2 Methodology

The model specification used in these analyses is fully described in previous chapters. The geometry, material properties, assembly, contact conditions, boundary conditions and element size are described in Chapter 3 methodology. To summarize the model development, Figure 4.1 represents the assembly of the components in the model.

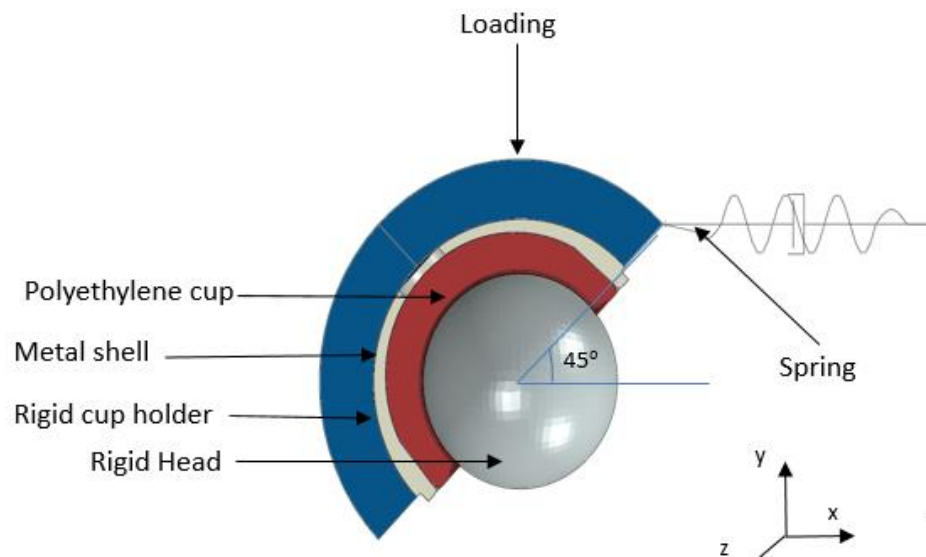


**Figure 4.1** The assembly of the components in the computational model for the parametric testing purposes

Furthermore, the material properties of the components and meshing configurations are available in Table 4.1 and Table 4.2, respectively.

**Table 4.1** Material properties of the components the computational analyses in the parametric sweep of chapter 4

| Components | Material     | Young's modulus (MPa) | Poisson's ratio | Density (kg/mm <sup>3</sup> ) | Outer radius (mm) | Inner radius (mm) |
|------------|--------------|-----------------------|-----------------|-------------------------------|-------------------|-------------------|
| Head       | Rigid        | -                     | -               | 4.37x10 <sup>-9</sup>         | 18                | -                 |
| Cup        | Polyethylene | 670 (Elasticity)      | 0.46            | 9.23x10 <sup>-10</sup>        | -                 | 18.524            |
| Shell      | Titanium     | 114,500               | 0.34            | 4.43x10 <sup>-9</sup>         | 56                | -                 |
| Cup holder | Rigid        | -                     | -               | 8.5x10 <sup>-10</sup>         | 27.25             | 24.25             |

**Table 4.2 The meshing configurations and the element size of the components in the computational analyses in the parametric sweep of chapter 4**

| <b>Component</b>  | <b>Global size (mm)</b> | <b>Element shape</b>       | <b>Code</b>   | <b>Number of elements</b> |
|-------------------|-------------------------|----------------------------|---------------|---------------------------|
| <b>Head</b>       | 1.5                     | Hexahedral                 | R3D4          | 2,228                     |
| <b>Cup</b>        | 1.5                     | Hexahedral                 | C3D8R         | 8,960                     |
| <b>Cup holder</b> | 3                       | Hexahedral and tetrahedral | R3D4 and R3D3 | 2,211                     |
| <b>Shell</b>      | 2                       | Hexahedral                 | C3D8R         | 2,820                     |

Moreover, the same set of progressive dynamic steps and boundary conditions which are presented in chapter 3 is used and presented in Table 4.3.

**Table 4.3 The boundary and loading conditions on each step of the computational analyses in the parametric sweep of chapter 4**

| <b>Steps</b>                | <b>Duration</b> | <b>Axial load</b> | <b>Boundary conditions</b> |                                     |                                     |                    |
|-----------------------------|-----------------|-------------------|----------------------------|-------------------------------------|-------------------------------------|--------------------|
|                             |                 |                   | <b>Head movement</b>       | <b>Cup movement</b>                 | <b>Spring movement</b>              |                    |
|                             |                 |                   |                            |                                     | <b>Lateral end</b>                  | <b>Medial end</b>  |
| <b>Pre-contact</b>          | 0.05            | -                 | 0.542mm upward             | Fixed                               | Fixed                               | Fixed              |
| <b>Spring compression</b>   | 0.05            | -                 | Fixed                      | Fixed                               | Fixed                               | Spring compression |
| <b>Spring stabilisation</b> | Alters          | Constant 300N     | Fixed                      | Horizontal and vertical translation | Horizontal and vertical translation | Fixed              |
| <b>Loading</b>              | 2               | 2 Paul cycle      | Fixed                      | Horizontal and vertical translation | Horizontal and vertical translation | Fixed              |

### 4.2.1 Input parameters

For validation purposes, the same input parameters that were tested experimentally, surgical translational mismatch, rotational variation and tissue laxity, were adjusted to the models as an input (Appendix).

Table 4.4 is the matrix describing the full set of test cases that were carried out in this chapter. For the parameter sweep study, total of 32 cases with variety in translational, rotational variation and swing phase were carried out. Moreover, the cases which friction studies were tested on are also shown. The running time taken to carry out each of the analysis was approximately 21 hours.

**Table 4.4 The full set of test cases in the parameter sweep based on various translational mismatch level, swing phase load and cup inclination angle**

|                  |      | Swing phase load   |  |  |  |
|------------------|------|--|--|--|--|
|                  |      | 70N  | 100N                                   | 200N                                   | 300N   |
| Lateral mismatch | 1 mm | Inclination = 45°<br>Inclination = 65°                     | Inclination = 45°<br>Inclination = 65° | Inclination = 45°<br>Inclination = 65° | Inclination = 45°<br>Inclination = 65°                     |
|                  | 2 mm | Inclination = 45°<br>Inclination = 65°                     | Inclination = 45°<br>Inclination = 65° | Inclination = 45°<br>Inclination = 65° | Inclination = 45°<br>Inclination = 65°                     |
|                  | 3 mm | Inclination = 45°<br>Inclination = 65°                     | Inclination = 45°<br>Inclination = 65° | Inclination = 45°<br>Inclination = 65° | Inclination = 45°<br>Inclination = 65°                     |
|                  | 4 mm | Inclination = 45°<br>Inclination = 65°<br>[+friction test] | Inclination = 45°<br>Inclination = 65° | Inclination = 45°<br>Inclination = 65° | Inclination = 45°<br>Inclination = 65°<br>[+friction test] |

The implementations of input parameters that are mentioned in Table 4.4 are explained as follows:

**Surgical translational mismatch:** The translational mismatch level is presented in the model by setting a mismatch between the centre of the head and cup which causes the spring to compress. The same translational mismatch level of 1mm, 2mm, 3mm and 4mm, that were used experimentally, were applied. Surgical translational

mismatch represents a level of mismatch between the cup and the head centre. Figure 4.2 represents the schematic of translational mismatch level in the computational model

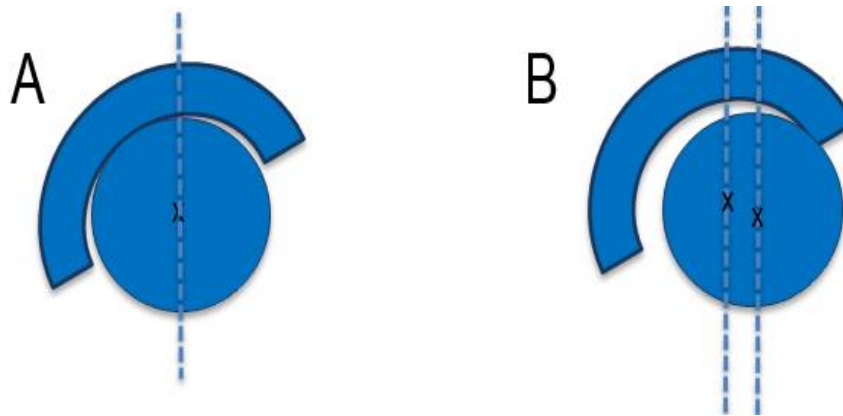


**Figure 4.2** The difference in assembly of fully concentric (A) where the head and the cup have the same centre and THR bearing with translational mismatch level (B) where there is a translational distance between the bearing centres

**Surgical rotational variation:** Surgical rotational variation effect has been studied *in vitro* by varying the cup inclination angle. Two different cup inclination angles are tested *in vitro*: 1) 45° inclination angle that is assumed to be in the safe zone and 2) 65° inclination angle which is defined as a steep inclination angle. To apply surgical rotational variation, the polyethylene cup, metal shell and the cup holder are assembled to have 35° angle with respect to horizontal axis to represent 45° clinical inclination angle. To implement a surgical rotational mismatch of 65°, the inclination angle of 55° is applied (Figure 4.3). The 10° difference between the cup inclination angles clinically and experimentally is due to the difference in loading angle *in vitro* and *in vivo* (explained in chapter 2). The cup inclination angle reported throughout this chapter is referenced to the clinical cup inclination angle.

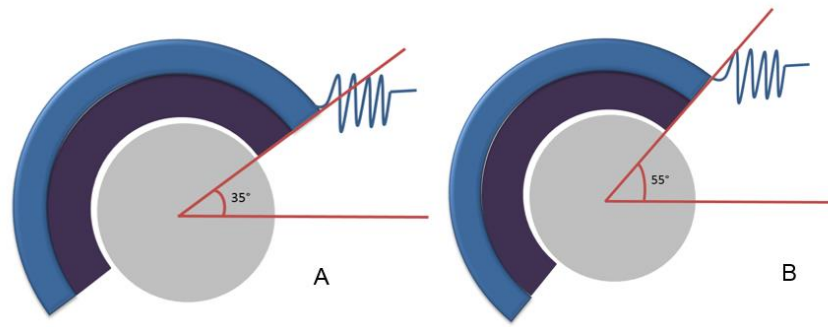


**Figure 4.3 Rotational mismatch configuration. A) 45° inclination angle clinically B) 65° inclination angle clinically**

**Tissue laxity:** Tissue and muscle laxity seen *in vivo*, is represented *in vitro* and *in silico* by varying the swing phase load of the gait cycle. The swing phase loads of 70N, 100N, 200N and 300N are tested *in vitro* which is within the range of patient's swing phase load range in the Bergsmann study (Bergsmann *et al.*, 2001). The same experimental variation of swing phase loads are applied to the model. The gait cycle loading of each case which is extracted from experimental testing is presented in Figure 4.4.

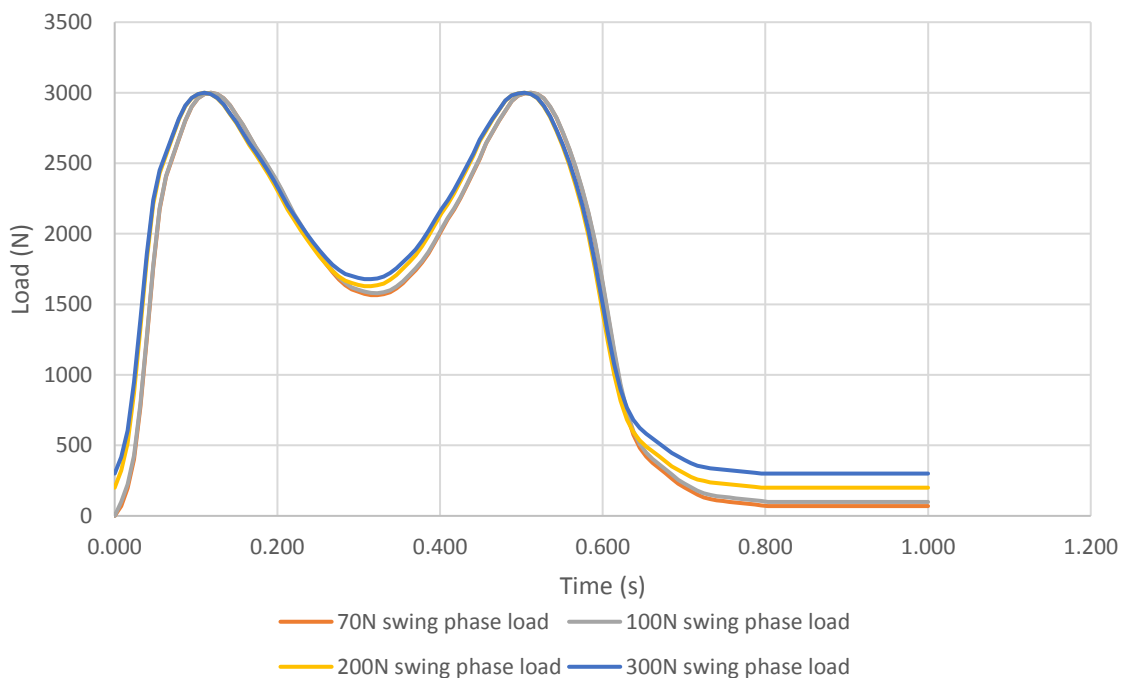


**Figure 4.4 The input gait cycle loading versus time for each swing phase load of 70N, 100N, 200N and 300N**

**Case-specific model specifications:** The constant force that was applied during stabilisation time (to fasten the stabilisation) differs from each condition to match the swing phase loads applied throughout the gait cycle of the specific analysis.

In line with the conclusion of Chapter 3, the choice of dashpot coefficient for critical damping of the spring was affected by the mass of the system the translational mismatch level (due to the variation in the resultant force and the cup position in relation to the head). In these analyses, although the mass of the system was constant, the translational mismatch was varied. It is expected that this will result in variation of the coefficient of damping between cases, so an initial dashpot coefficient analysis was carried out to achieve critically damped spring in each case. The table of dashpot coefficient for analysis carried out with 45° inclination angle is presented in Table 4.5 and 65° inclination angle is represented in Table 4.6. Before gait cycle loading, a series of analyses were carried out on each condition to achieve a critically damped system.

**Table 4.5 Dashpot coefficient of analysis with 45° inclination angle, translational mismatch level of 1mm to 4mm and swing phase load of 70N to 300N**

| Mismatch (mm) | 70N  | 100N | 200N | 300N |
|---------------|------|------|------|------|
| 1             | 1.85 | 1.8  | 2.1  | 2.5  |
| 2             | 1.5  | 1.8  | 1.4  | 2.35 |
| 3             | 1.2  | 1.1  | 2.25 | 3.1  |
| 4             | 1.1  | 1.2  | 1.2  | 1.3  |

**Table 4.6 Dashpot coefficient of analysis with 65° inclination angle, translational mismatch level of 1mm to 4mm and swing phase load of 70N to 300N**

| Mismatch (mm) | 70N  | 100N | 200N | 300N |
|---------------|------|------|------|------|
| 1             | 1.25 | 1.4  | 1.35 | 2.5  |
| 2             | 1.5  | 1.1  | 1.4  | 2.1  |
| 3             | 1.2  | 1.2  | 1.1  | 1    |
| 4             | 1    | 1.1  | 1    | 0.8  |

## 4.2.2 Outputs and experimental comparison

### 4.2.2.1 Maximum dynamic separation

The highest dynamic separation value throughout the gait cycle which occurs during the swing phase load was recorded for validation purposes.

**Edge loading definition:** If the maximum dynamic separation was greater than the radial clearance (0.5mm), the separation is defined to cause head contact with the rim of the cup and a level of edge loading.

Experimental measurement: The *in vitro* dynamic separation was recorded from the biomechanical testing on Pinnacle metal-on-polyethylene THRs on the electromechanical hip simulator (EM13). The experimental maximum separation was taken as the mean value of the separation recorded from three samples. For the validation and comparison purposes, the maximum dynamic separation was exported from the explicit finite element model. The dynamic separation *in vitro* was measured from the point where the cup and the head were in contact with no spring compression (Figure 4.5).

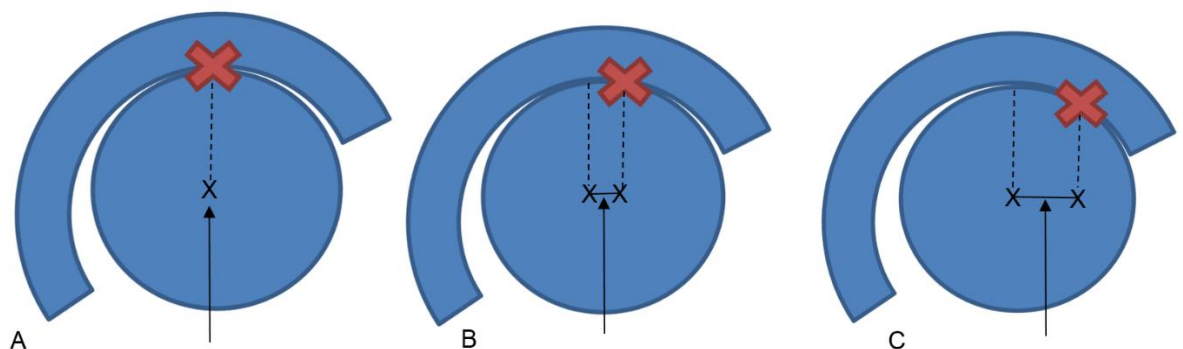


**Figure 4.5** The schematic of dynamic separation measurement *in vitro*. A) The point where the separation is measured from (concentric cup and head and no spring compression), B) Minimum dynamic separation and C) Maximum dynamic separation (edge loading)

### 4.2.2.2 Maximum load at the rim

In the conditions that edge loading occurs, the maximum load that the rim of the cup undergoes, is recorded in two different time points:

1. When the input load is increasing to the first peak and the head is relocating to the concentric condition.
2. When the input load is decreasing from the second peak to the swing phase load and the head is separating from the concentric condition.

**Computational measurement:** to calculate the load at the rim, firstly, the point at which the separation is at the minimum level (including 0.5mm) is recorded. Secondly, the corresponding time point in which the separation would be 0.5mm is calculated by using linear interpolation. Finally, the input load at the time in which the recorded separation level occurred is measured. Figure 4.6 illustrates the time point at which the separation and the load are measured.

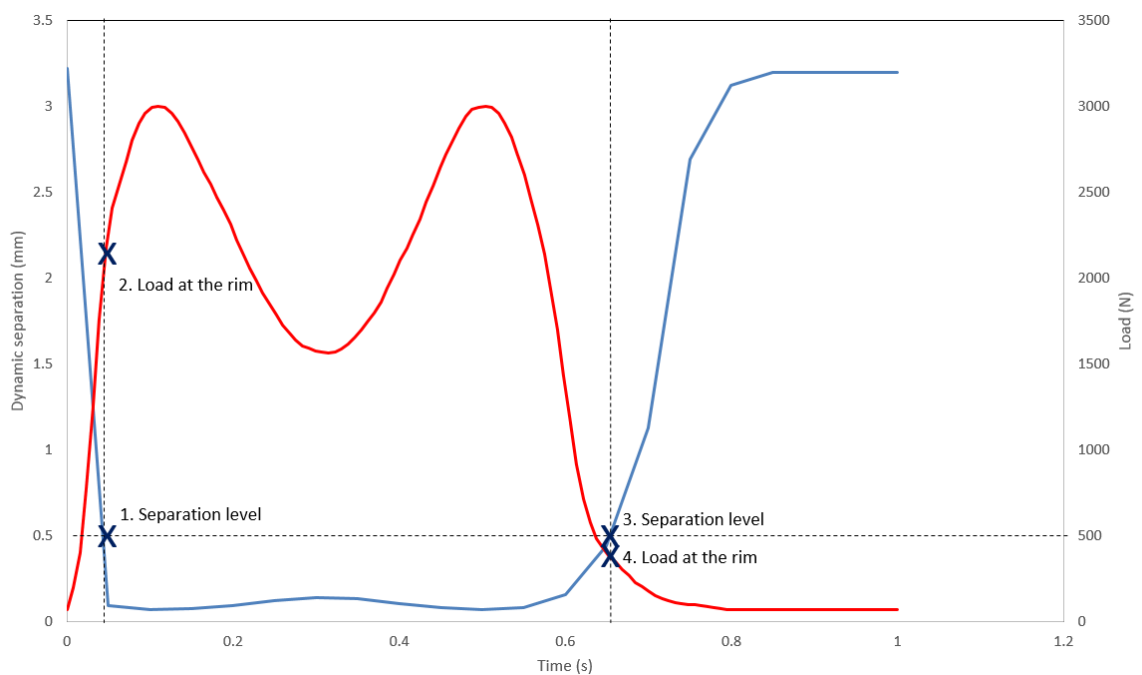


**Figure 4.6 The intersection of the load and the separation for maximum load at the rim calculations. The corresponding load to the dynamic separation of 0.5mm is recorded as the maximum load at the rim**

**Experimental measurement:** The experimental measurement method used to determine maximum load at the rim was similar to the computational measurement. The load at the rim was determined as the axial force measured from the load cell at

a specified dynamic separation (Appendix). However, the maximum load at the rim is only taken when the head is relocating to the concentric condition.

### **4.2.3 Friction sensitivity test**

Four cases were selected for a friction sensitivity test, where a friction coefficient of 0.1 was applied to the contact between the bearings surfaces based on the range of friction coefficient of the bearing presented in the study by Jin *et al* (2006). The selected cases are marked in Table 4.4. The difference in the separation data output between the computational and experimental results for these cases was the highest. Friction testing was carried out specifically on these cases to see if the difference between the results could be explained by friction. Based on the dynamic separation of the all conditions, the friction analyses were carried out on the chosen one due to their dynamic behaviours. The friction testing was carried out on the four conditions with:

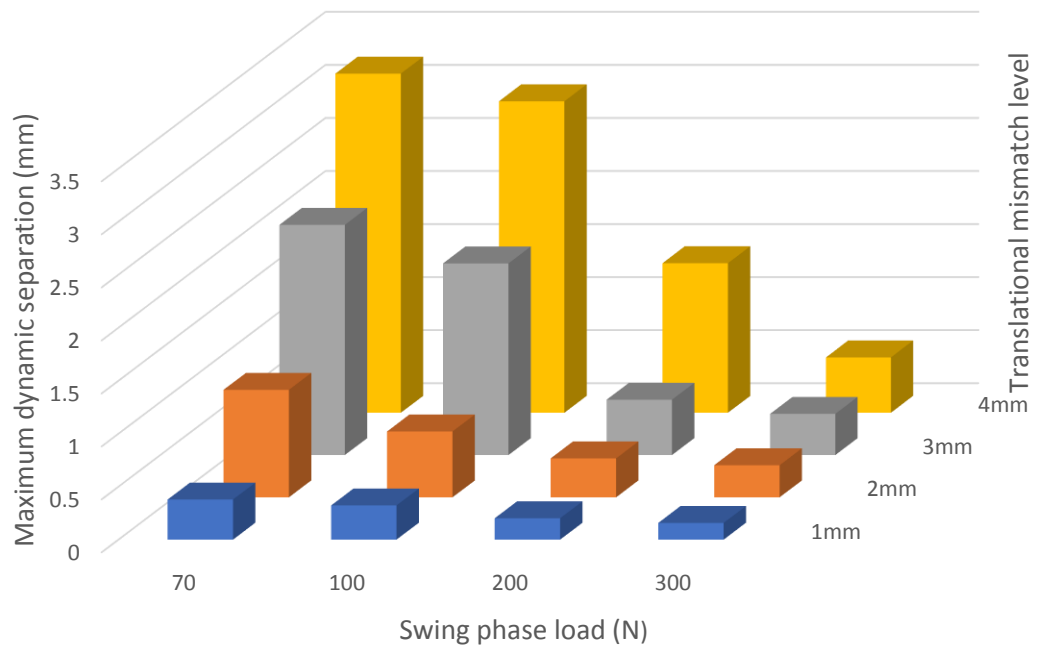
- 4mm translational mismatch
- 70N and 300N swing phase load
- 45° and 65° cup inclination angles

### **4.3 Results**

This section of chapter is divided into three sections that firstly focus on the dynamic results of the computational model. Secondly, the comparison and validation of the computational results against the experimental testing is carried out. Finally, the effect of friction in the bearing on the selected conditions are described.

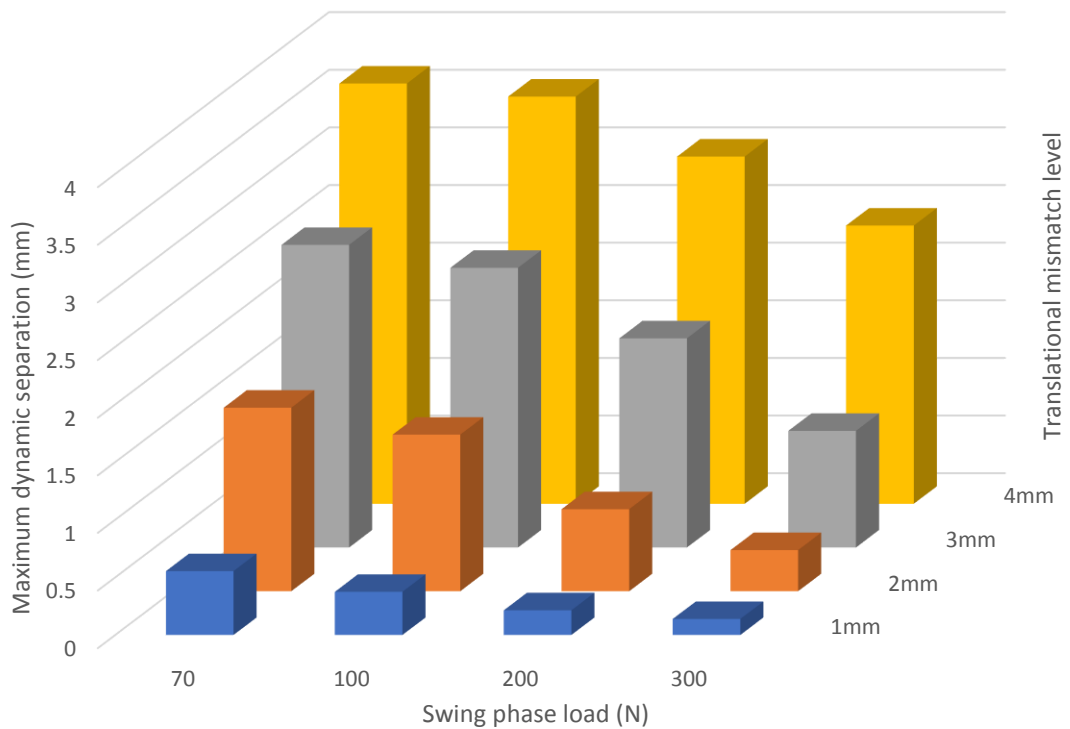
#### **4.3.1 *In silico* parameter sweep**

The *in silico* maximum dynamic separation caused by surgical translational mismatch level, rotational variation and swing phase load of the THR are all plotted and compared. Figure 4.7 represents the maximum dynamic separation resulted from various translational mismatch and swing phase loads in 45° cup inclination angle. For this cup inclination angle, the combination of 1mm translational mismatch level and 300N swing phase load results in a best separation case (0.1mm). Moreover, the worst separation case (3.1mm) occurred with the combination conditions of 4mm mismatch level and 70N swing phase load. The separation increased as the translational mismatch increased for a fixed swing phase load. Also, increase in swing phase load for a specific translational mismatch decreased the separation level. Based on the definition of the edge loading that was defined in methodology (section 4.2), 7 out of 16 conditions underwent a separation of greater than 0.5mm and some degree of edge loading with 45° inclination angle.



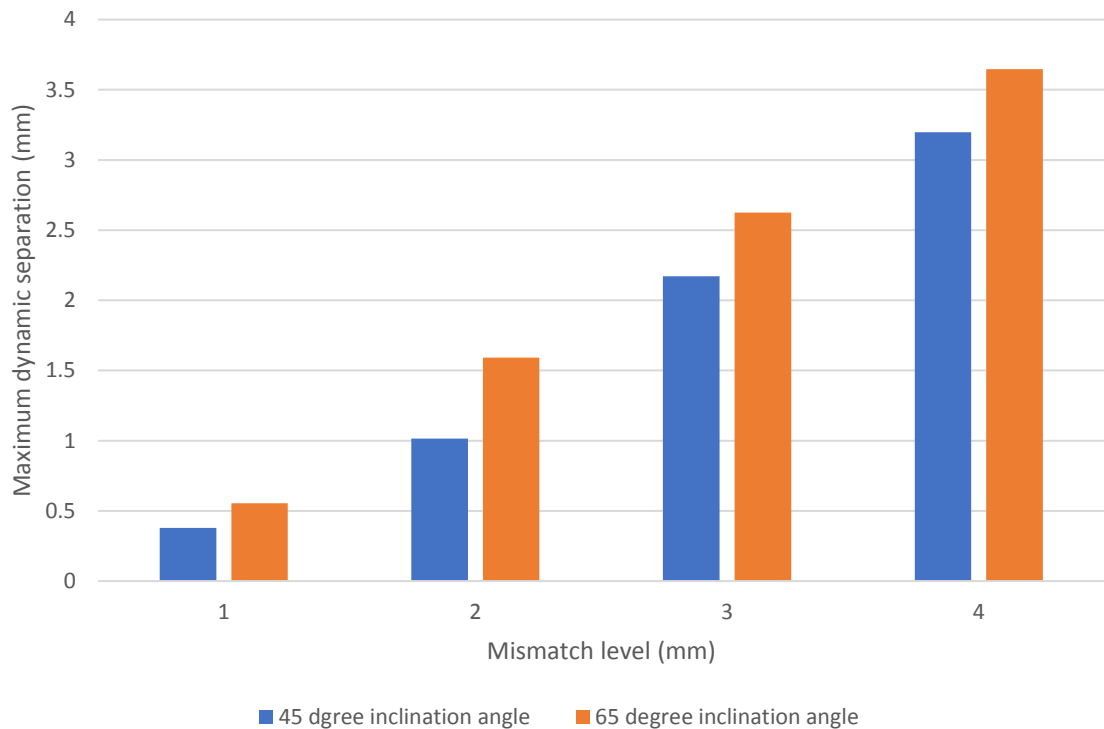
**Figure 4.7 Maximum dynamic separation versus the variation of translational mismatch levels (1mm to 4mm) and swing phase loads (70N to 300N) and 45° inclination angle**

Figure 4.8 illustrates the maximum dynamic separation of various translational and swing phase loads in 65° cup inclination angle. The same trend of the lowest and highest separation levels were observed in the similar cases as 45° inclination angle. However, the range of separation level varies from 0.1mm to 3.5mm. Moreover, lower swing phase load and higher translational mismatch level resulted in higher separation levels. In 65° inclination angle conditions, a separation of greater than 0.5mm and some degree of edge loading occurred in 11 out of 16 conditions.



**Figure 4.8 Maximum dynamic separation versus the variation of translational mismatch levels (1mm to 4mm) and swing phase loads (70N to 300N) and 65° inclination angle**

Furthermore, the effect of cup inclination angle on maximum dynamic separation was considered. As Figure 4.9 shows, a 70N swing phase load produced dynamic separation of 0.4mm to 3.1mm under standard cup inclination angle (45°) and 0.5mm to 3.6mm for steep inclination angle (65°). The dynamic separation level increased as the translational mismatch level increased in both cup inclination configurations. Steeper cup inclination angle results in a higher dynamic separation than standard cup inclination angle for different translational mismatch level.



**Figure 4.9 The effect of standard and steep cup inclination and translational mismatch of 1mm to 4mm on the maximum computational dynamic separation with 70N swing phase load**

Figure 4.10 illustrates that the same trend of maximum dynamic separation changes occurred for different cup inclination angles when 300N swing phase load was applied. Although the dynamic separation increased as the translational mismatch level increased for both cup inclination angle, the maximum dynamic separation for all translational mismatch level for 45° inclination angle is less than 0.5mm (radial clearance). The maximum dynamic separation with 65° inclination angle increased substantially as the dynamic separation became greater than radial clearance (up to 2.45mm separation). Additionally separation of greater than 0.5mm and edge loading occurred more frequently with the 65 degree inclination angle.

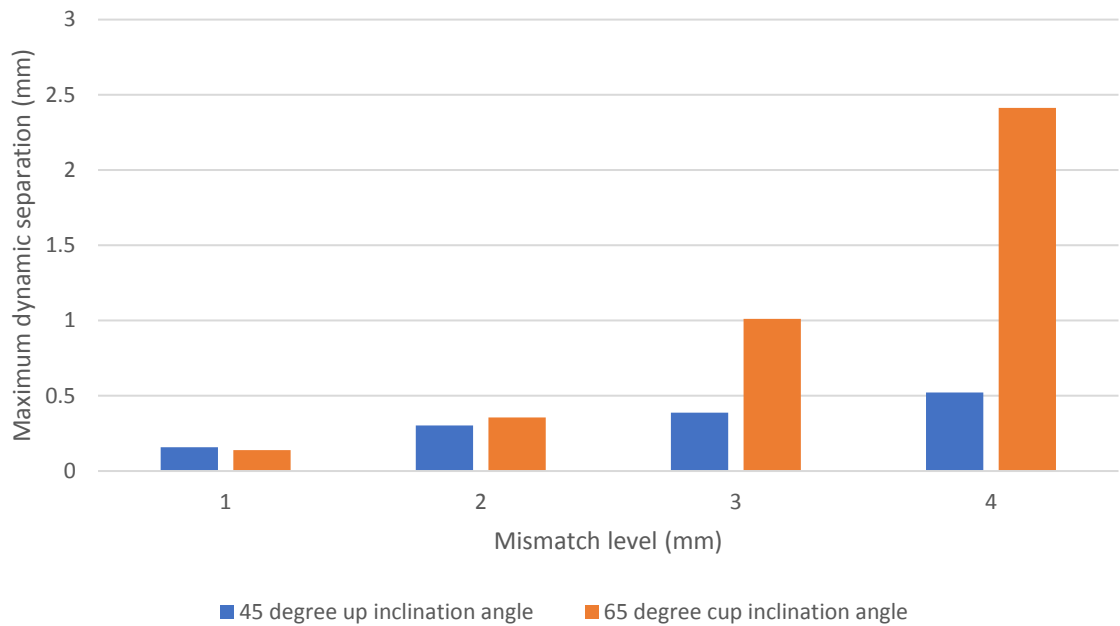


**Figure 4.10 The effect of cup inclination and translational mismatch on the maximum computational dynamic separation with 300N swing phase load**

### 4.3.2 Comparison of *in vitro* and *in silico*

Figure 4.11 illustrates the overall comparison of computational and experimental maximum dynamic separation value for all the frictionless cases tested. As Figure 4.11 demonstrates, mostly, the model overestimated the separation level compared to the experimental values. The results indicated that there is an overestimation of the separation by the computational model for high separation levels and slight underestimation of the separation by the computational model for lower separation level.

This graph doesn't present the specific separation level under different translational mismatch level which indicates that the overestimation of the separation doesn't seem to be only dependant on the cup inclination angle or swing phase load. Figure 4.11 does not represent the variation of the separation level in experimental testing and the variation will be demonstrated later in this chapter.

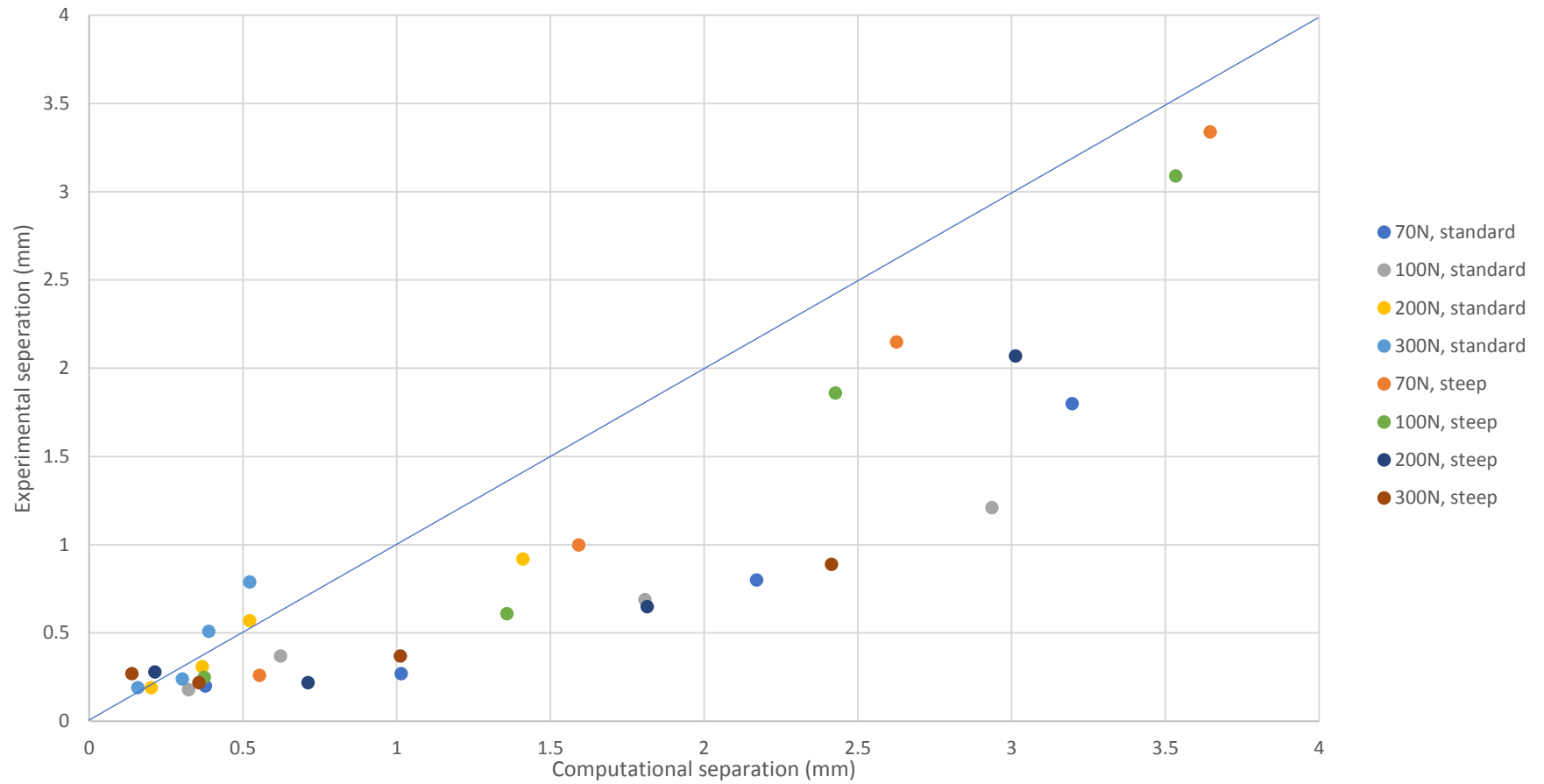


**Figure 4.11 Comparison of computational dynamic separation and experimental dynamic separation. The legend represents the swing phase load and the cup inclination angle. Standard is referred to 45° inclination angle and steep is referred to 65° inclination angle**

Figure 4.12 and Figure 4.13 illustrate the maximum dynamic separation versus the surgical translational mismatch for different swing phase loads under standard cup inclination angle and steep inclination angle, respectively. The bars on the experimental data represents the variation of maximum separation in *in vitro* testing.

The comparison of computational and experimental separation for standard cup inclination angle indicates that the separation predictions are in a good agreement for all the translational mismatch levels in a higher swing phase loads than lower swing phase loads. The most overestimation occurs for the cases with low swing phase loads especially high translational mismatch levels (70N and 100N).

In standard cup inclination angle condition, it is difficult to compare the separation values under 1mm translational mismatch level because the experimental result does not vary considerably due to a low separation level. There is a good agreement for all swing phase loads when 2mm translational mismatch was applied except 70N swing phase load. The experimental value does not follow the actual theoretical trend in this specific case (the experimental separation does not increase as the swing phase decreases). In the cases with 3mm and 4mm translational mismatch level, good agreement was seen under high swing phase loads (200N and 300N). However, the most overestimation was observed under low swing phase loads.

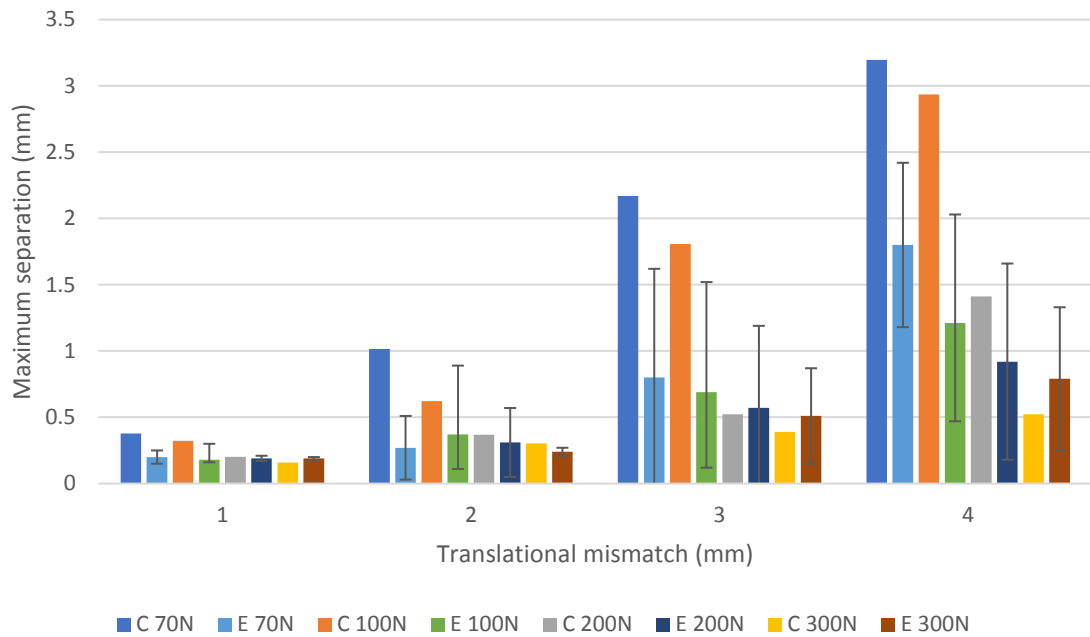


**Figure 4.12 The effect of translational mismatch and swing phase load on the maximum dynamic separation of the THR *in vitro* and in silica under 45° inclination angle. The letters E and C in the legend section represents experimental and computational data, respectively (in vitro testing was carried out by Murat Ali, Appendix)**

Figure 4.13 indicates the computational maximum dynamic separation of up to 0.5mm for 1mm mismatch level, 1.55mm for 2mm, 2.55mm for 3mm and 3.55mm for 4mm translational mismatch level in steep cup inclination angle. The inverse relationship between swing phase load and maximum dynamic separation is also observed for a fixed translational mismatch level. In contrast to standard cup inclination angle, there is a great agreement between the experimental and computational separation when lower swing phase loads were applied (70N and 100N). Furthermore, higher swing phase loads (200N and 300N) resulted in the overestimation of the computational separation. Although, there an overestimation of the output, the experimental and computational separation follow a similar trend between the different conditions. The potential reasons for the differences between the computational model and the experimental results are described in the discussion

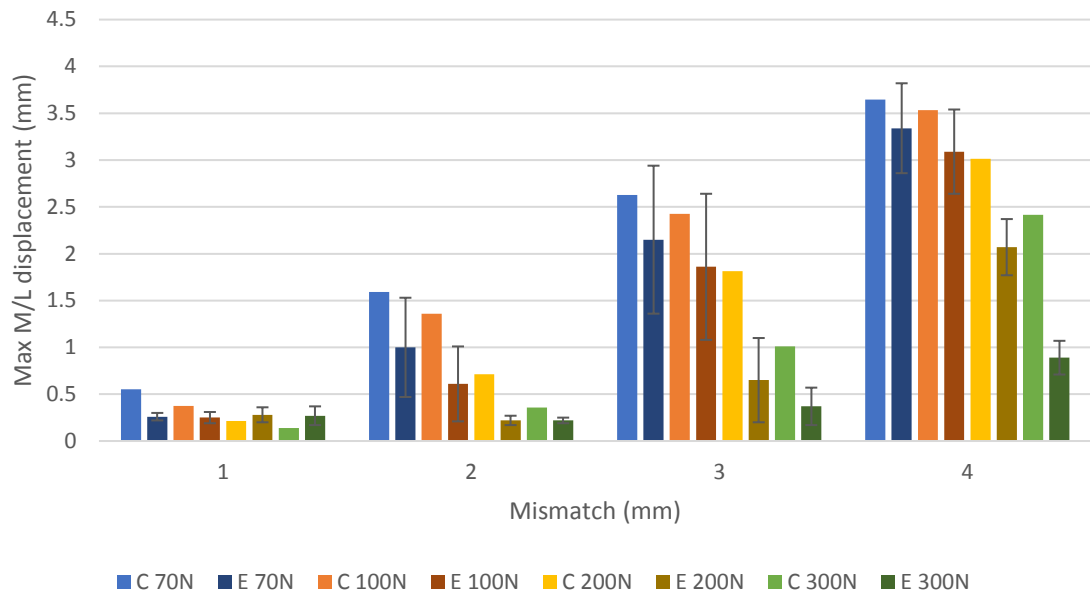


**Figure 4.13** The effect of translational mismatch and swing phase load on the maximum dynamic separation of the THR *in vitro* and in silica under 65° inclination angle. The letters E and C in the legend section represents experimental and computational data, respectively (in vitro testing was carried out by Murat Ali, Appendix)

### 4.3.3 Friction sensitivity test

The effect of friction on the maximum dynamic separation is also studied. The maximum separation generated by using friction coefficient of 0.1 under the specified conditions are presented in Figure 4.14. As the dynamic separation of the chosen conditions show, the maximum overestimation of the separation occurred under standard cup inclination angle, 4mm translational mismatch level and 70N swing phase load. And also under steep cup inclination angle, 4mm translational mismatch level and 300N swing phase load. Therefore, primarily these conditions were chosen for friction analysis. Moreover, friction analyses were carried out on two other conditions (same translational mismatch level with 70N and 300N swing phase load under steep and standard cup inclination angle, respectively) to understand if friction could affect the level of validation agreement for these cases.

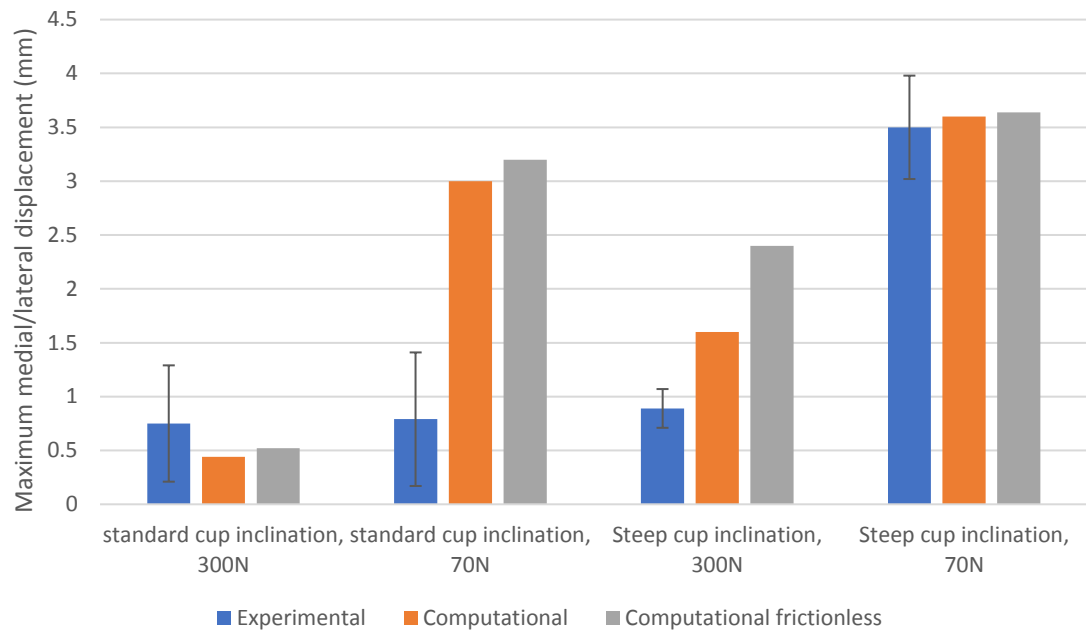


**Figure 4.14 Comparison of computational and experimental maximum dynamic separation under steep inclination angle (friction coefficient of 0.1). Experimental bars represents the dynamic separation *in vitro*, Computational bars represent the maximum dynamic separation with friction coefficient of 0.1 between the contact surfaces and computational frictionless bars represents the maximum dynamic separation with no friction between the contact surfaces**

Slightly reduced maximum dynamic separation was obtained in the both standard cup inclination conditions and 70N swing phase load under steep cup inclination angle. However, the bearing friction in the model had a great effect on the level of dynamic separation for the higher swing phase load under steep cup inclination angle (0.8mm reduction).

As Figure 4.14 demonstrates, although friction coefficient decreased the maximum dynamic separation in comparison with frictionless analyses, the underestimation of the computational dynamic separation in comparison with experimental results is still observed on the same cases as frictionless analyses.

#### 4.3.4 Maximum load at the rim

In this section, the comparison of the maximum force on the rim of computational and experimental data is shown. Firstly, the computational maximum force on rim for 45° and 65° inclination angles are presented in Figure 4.15 and Figure 4.16, respectively. As Figure 4.15 illustrates, the maximum force on the rim under

standard cup inclination varies between zero to 1980N. As it was described in methodology, no edge loading was assumed for the conditions which had separation level of less than 0.5mm. Therefore, the maximum force on the rim for these conditions are shown in graph with no load at the rim. However, the maximum force on the rim increased by increasing the swing phase load and increasing the translational mismatch level.

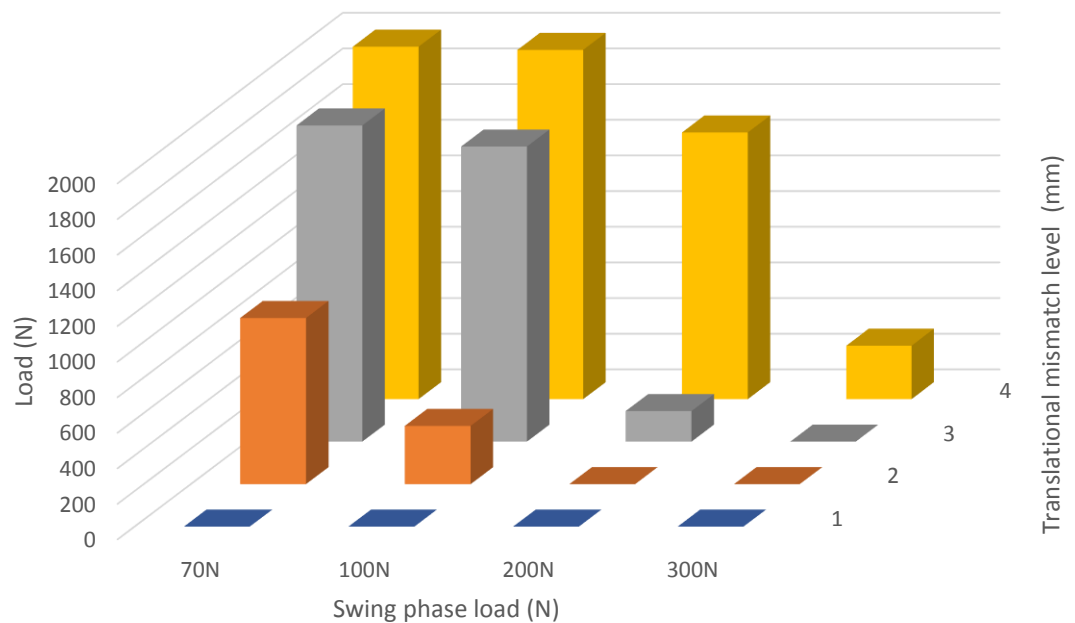


**Figure 4.15 Computational maximum force on the rim with different translational mismatch level and swing phase loads under 45° inclination angle**

The range of maximum force on the rim for all the conditions under steep cup inclination angle (Figure 4.16) is demonstrated to be between zero to 2020N. The similar trend that was found with standard cup inclination angle was also found with steep cup inclination angle. Therefore, higher swing phase load and higher translational mismatch level increased the value of maximum load at the rim. However, the swing phase load did not have a substantial effect when 4mm translational mismatch was applied.

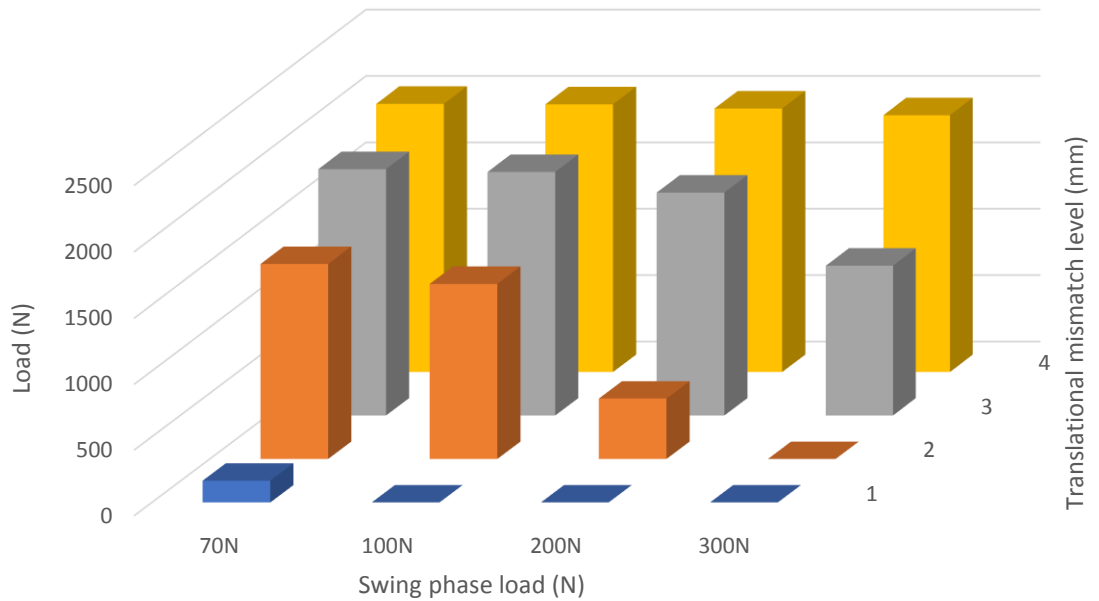


**Figure 4.16 Computational maximum force on the rim versus translational mismatch level of 1mm to 4mm and swing phase loads under 65° inclination angle**

In the next step, the maximum load at the rim at the relocation to concentric point from the edge and the separation from the concentric point to the edge were compared. As Figure 4.17 represents, under standard cup inclination angle, the maximum load at the rim at the relocation time is substantially higher than the separation time. When the head is relocating into the concentric condition, the maximum load at the rim could be five times higher than the load at the rim when the head is separating from the cup. The conditions that have the similar relocation and separation maximum load at the rim contain high swing phase load (200N with 3mm mismatch and 300N).

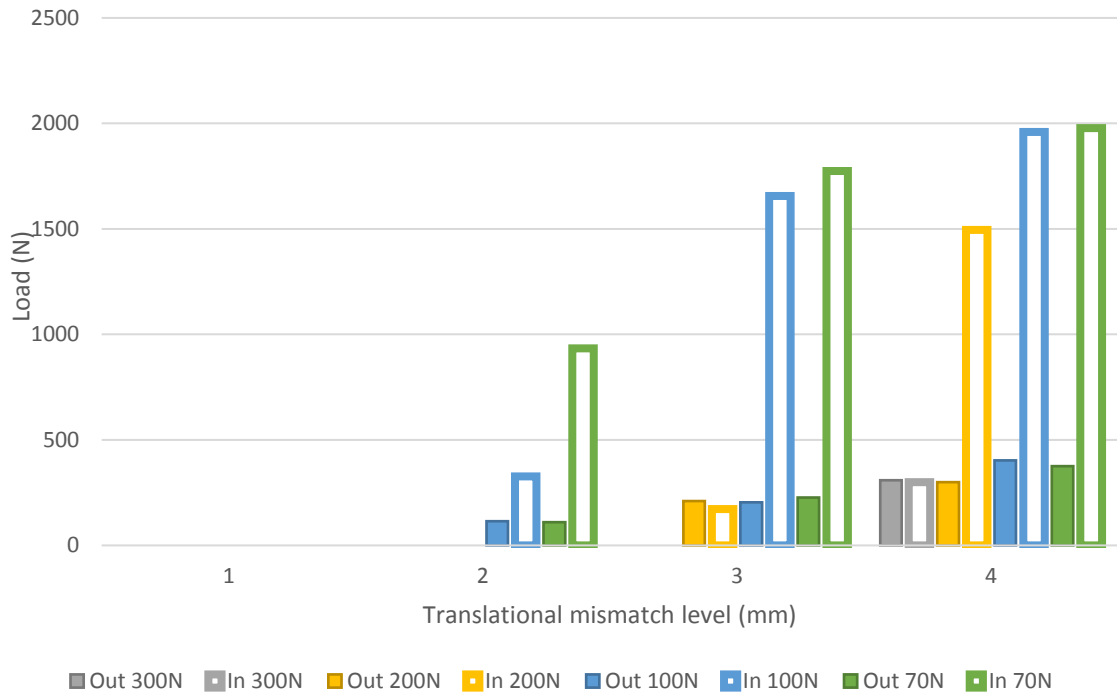


**Figure 4.17 Comparison of the load the rim when the head is moving to concentric condition and when the head is moving to the edge under standard cup inclination angle. At the legend of this graph, the word 'in' represents the maximum load at the rim when the head was relocating into the cup and the word 'out' represents the maximum load at the rim when the head was separating out of the concentric point**

Similar observation could be seen from the maximum load at the rim comparison under steep cup inclination angle. However, all the conditions resulted in a substantially higher maximum load at the rim at the relocation point than the separation point. The range of maximum load at the rim at the relocation point is between zero to 2020 whereas the maximum load at the rim at the separation point is between zero to 800N.

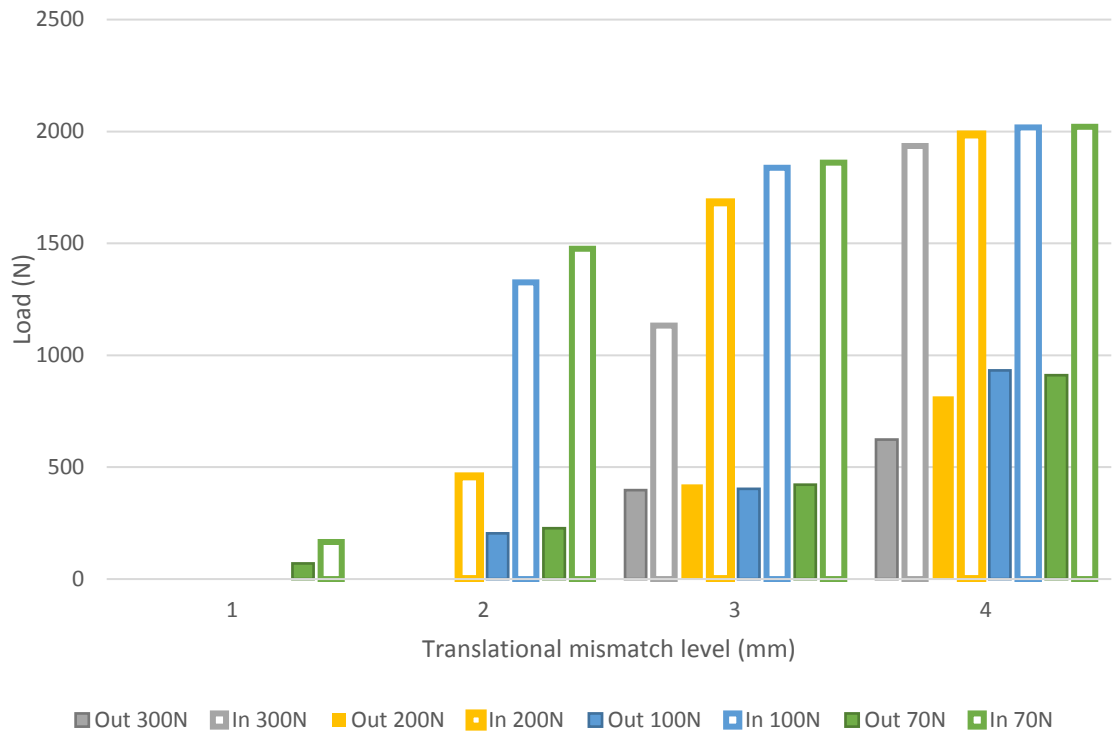


**Figure 4.18 Comparison of the load the rim when the head is moving to concentric condition and when the head is moving to the edge under steep cup inclination angle. At the legend of this graph, the word 'in' represents the maximum load at the rim when the head was relocating into the cup and the word 'out' represents the maximum load at the rim when the head was separating out of the concentric point**

The difference between the computational and experimental maximum load at the rim was also studied. The maximum force on the rim is dependent on the occurrence of edge loading. If the separation is less than 0.5mm, the maximum force on the rim is not calculated *in vitro* as there is no contact of the head with rim surface. Therefore, the computational maximum load at the rim that are presented in the following figures are for the available experimental maximum load at the rim conditions. No maximum load at the rim was found in *in vitro* studies for 1mm and 2mm translational mismatch level. Then, the comparison graphs only illustrate the maximum load at the rim for 3mm and 4mm translational mismatch levels.

Figure 4.19 represents the maximum force on the rim under 70N swing phase load. The computational method produce substantially higher maximum load at the rim than the experimental load at the rim. However, lower mismatch level and cup

inclination angle decreased the load at the rim in both computational and experimental methods.

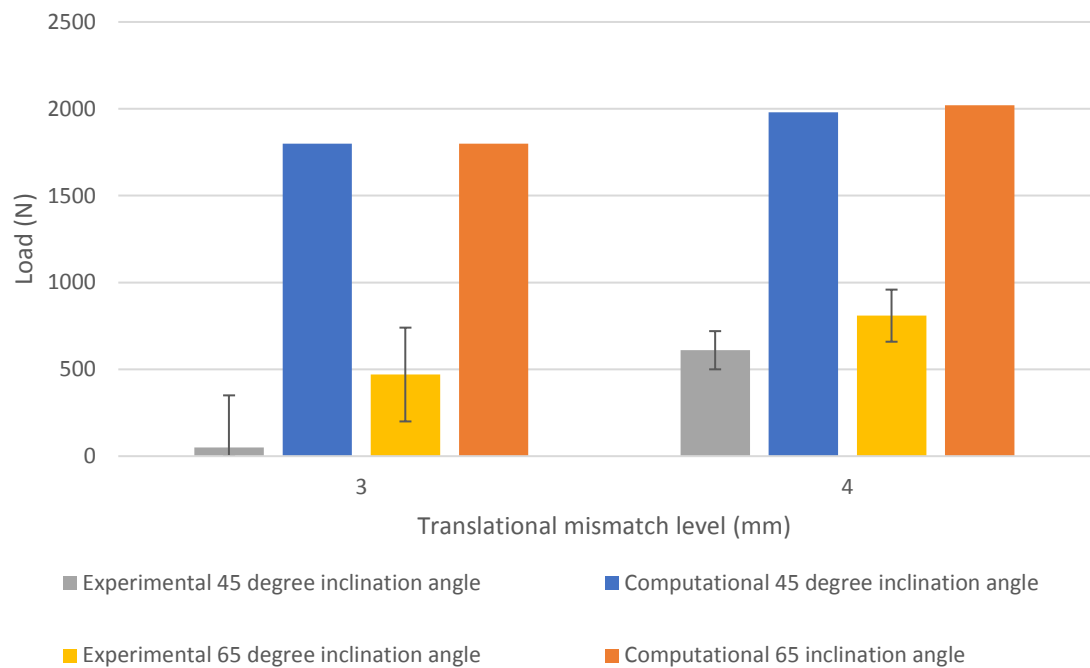


**Figure 4.19 Experimental and computational maximum force on the rim under 70N swing phase load, standard (45°) and steep (65°) cup inclination angle, and 3mm and 4mm translational mismatch level (Appendix)**

The same trend of experimental and computational maximum load at the rim for 70N swing phase load (Figure 4.20) was found for 100N swing phase load. The overestimation of the computational load at the rim occurred. However, both experimental and computational methods agreed that the load at the rim decreased as the translational mismatch level and inclination angle decreased.

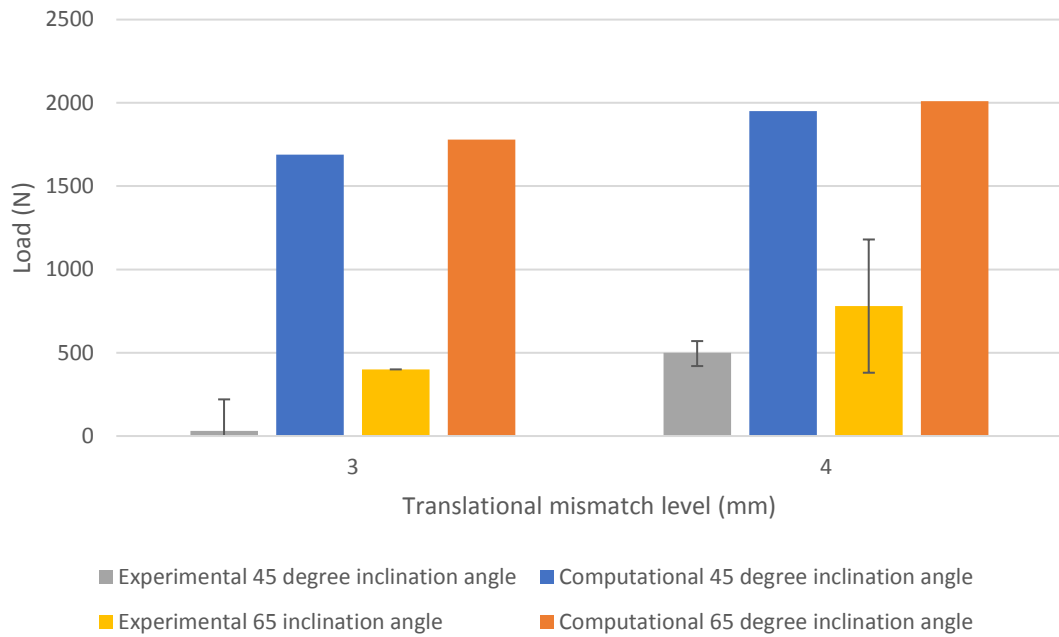


**Figure 4.20 Experimental and computational maximum force on the rim under 100N swing phase load, standard (45°) and steep (65°) cup inclination angle, and 3mm and 4mm translational mismatch level (Appendix)**

The comparison of the maximum load on the head for 200N swing phase load (Figure 4.21) also indicates the same trend as previous analyses between the experimental and computational data. However, no load at the rim occurred experimentally under standard cup inclination angle.

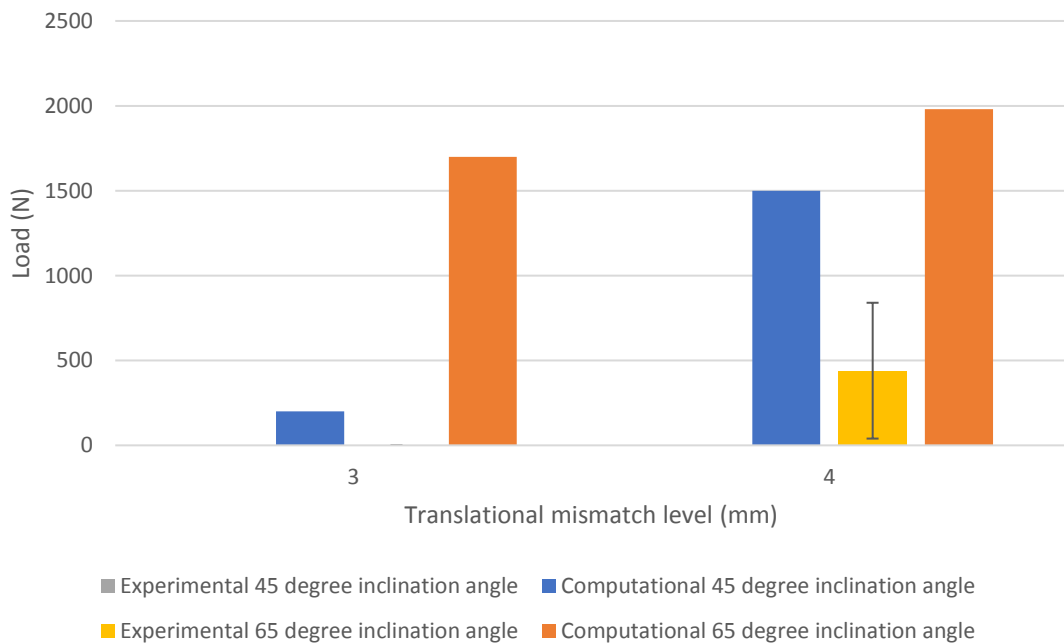


**Figure 4.21 Experimental and computational maximum force on the rim under 200N swing phase load, standard (45°) and steep (65°) cup inclination angle, and 3mm and 4mm translational mismatch level (Appendix)**

The rim did not undergo any load under any cup inclination angles when swing phase load of 300N was applied. Therefore, no experimental and computational comparison of the maximum load at the rim was carried out with 300N swing phase load.

#### **4.4 Discussion**

The dynamic finite element model has been used to predict medial-lateral separation as it occurred during the gait cycle, including cases where the femoral head was in contact with the rim of the cup. The development of such a computational model allows the preclinical testing of THR to examine the factors that could affect the separation and edge loading the most. Additionally, the validity of the model has been tested by comparison with an *in vitro* experimental simulation. The comparison of experimental and computational results could indicate if the numerical method is capable of predicting the important dynamics and contact mechanics data and also giving an overall indication of the model reliability for future parameters. Therefore, the parameters that have been tested *in vitro* experimentally have been applied to the computational model and the effects of these factors such as surgical translational mismatch, rotational variation and swing phase load on the dynamic separation are studied.

It has to be recognised both the computational model and the experimental model are both representations of more complex and variable conditions which occur clinically, their main value is in predicting the effect of detain biomechanical and surgical variables on the performance of the hip joint. Direct comparison with the clinical results can only be made by comparison of wear rates and wear scars and mechanisms between experimental simulation and retrievals. The development of the computational model and comparison of the computational and experimental simulations, will enable wider sets of conditions to be investigated computationally and more rapidly and most importantly enable the computational models and predictions to be run in the design phase (including parametric design studies) of new product development before actual prototypes are manufactured for testing.

#### 4.4.1 Computational results

The computational separation results (maximum M/L displacements) indicated the primary factors that cause more separation level under the same cup inclination angle are low swing phase load and high translational mismatch. The resultant force of the medial spring force and the axial force determines the position of the cup with respect to the head. The combination of low swing phase load (low axial load) and high medial load causes the edge contact as the cup sits more toward horizontal axis (Figure 4.22).

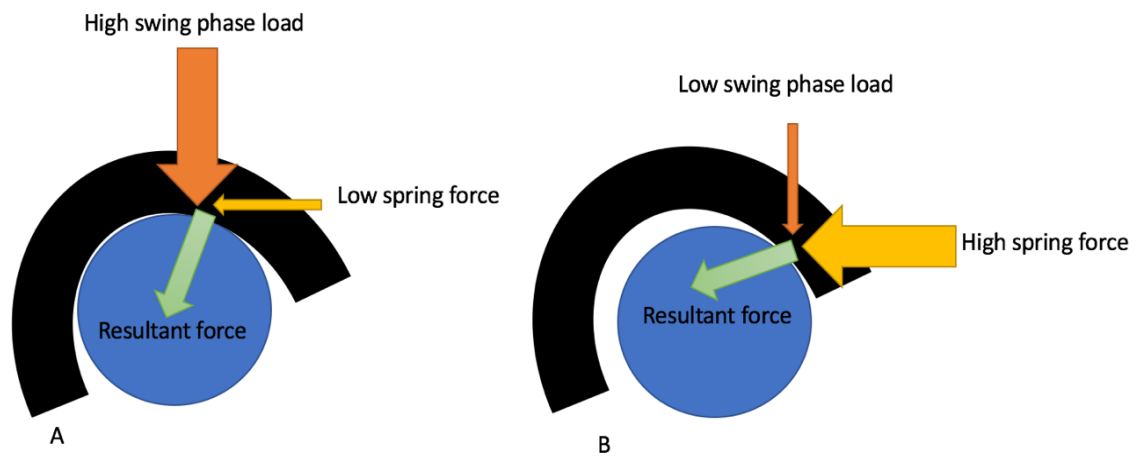


**Figure 4.22 The cup positioning with respect to the resultant force. A) Resultant force caused from high swing phase load and low spring force B) Edge contact due to low swing phase load and high spring force**

Moreover, the standard cup inclination angle generally causes lower separation level than steep inclination angle under the similar parameters. In standard cup inclination angle, the inner curvature of the liner could be acting as a resistance to the medial movement in comparison with steep cup inclination angle (Figure 4.23). Additionally, the distance that needs to be travelled by the cup from the concentric condition to the edge loading condition is longer in standard cup inclination angle due to the liner edge location with respect to the centre.

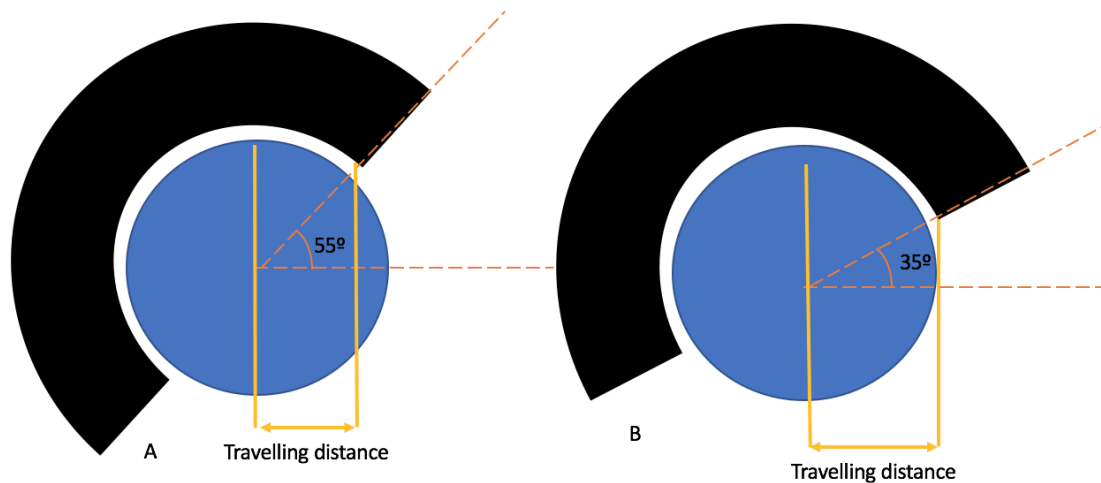


**Figure 4.23 Horizontal travelling distance by the cup with different cup inclination angle. A) Steep cup inclination angle and B) standard cup inclination angle**

It is indicated that the steeper inclination angle and higher spring compression resulted in increased dynamic separation with the same axial loading (70N swing phase load). The effect of 20° changes of the inclination angle have the maximum effect of 0.2mm on the dynamic separation whereas the minimal increase of the translational mismatch can increase the dynamic separation up to two times. The same pattern was seen in the previous dynamic computational study that was carried out on the ceramic-on-ceramic THR (Leng *et al.*, 2017). Therefore, it can be concluded that translational mismatch has greater effect than rotational variation on the level of dynamic separation under low swing phase load. However, steep inclination angle has the greater effect on the dynamic separation if high swing phase load is applied.

Tissue laxity, which is represented by various swing phase loads, is the other parameter studied on the computational model. Higher dynamic separation is achieved by lower swing phase loads for standard cup inclination angle. When minimum axial load (during swing phase) was applied, the direction of the resultant force between this force and the medial spring load become closer to the horizontal axis than vertical axis. Therefore, the resultant force in lower swing phase loads led

to greater movement of the cup medial/laterally and higher separation of the cup with respect to the head.

The maximum load at the rim is affected by the same conditions that affected the separation. The maximum load at the rim differed for each conditions and higher translational mismatch level and lower swing phase load increased the maximum loading at the rim. Also, steeper cup inclination angle affected the load at the rim negatively. Moreover, it was indicated that there is a substantially higher load at the rim when the head is relocating to the concentric condition as the load is ramping up than when the head is separating. Although, the amplitude in load decrease after the second peak (separating time) is slightly shallower than ramping up (relocating), the magnitude of the load at the rim should potentially be slightly affected by it. Such substantially high load at the rim where the contact patch on the edge is small, could have a more dramatic effect on the contact mechanics of the bearing such as extreme deformation at the edge contact, wear and material damage.

#### **4.4.2 Validation**

The trend in the dynamic separation changes in the computational model, implies the overall behaviour of the explicit finite element of THR model under several parametric testing is plausible. The reliability of the model can be assured by comparison of *in vitro* and *in silico* output. The previous *in vitro* studies focused on the wear testing of the THR under only separation (Nevelos *et al.*, 2000, 2001; Williams *et al.*, 2003; Al-Hajjar *et al.*, 2013). *In vitro* testing on ceramic-on-ceramic (O'Dwyer Lancaster-Jones *et al.*, 2017) and metal-on-polyethylene (Appendix) THR were done in the recent studies to examine the effect of positioning and tissue laxity on the separation and wear of the bearings. The experimental data in this chapter

was extracted from Ali *et al* studies as the computational analyses were also carried out on the hard-on-soft bearings. In this comparison, the experimental and computational dynamic separation follow the same trend of changes with respect to the tested parameters. However, in some cases there is a disagreement in the dynamic separation level between the two cases.

The comparison of the experimental and computational dynamic separation and the load at the rim indicated a level of over/underestimation of the computational output. However, the difference between the results could be due to various factors. There is some additional mechanical displacement experimentally and damping in the loading system, associated with rocking of the cup holders in the mechanical fixtures and it is not known how this influences the dynamic response in the experimental system, and this may influence the measurement of the peak load on the cup, which occurs during a rapidly changing phase of the loading, these three factors may be expected to realise differences between the experimental and computational results and be important to explain the differences seen between the experimental and computational results.

Although the finite element model is designed to replicate the experimental set up, there are several assumptions that were necessary to make the model viable. Additionally, hardware tolerances and experimental set up cause variation in the results produced by practical experimentation. A combination of these factors could potentially be responsible for the difference in the results.

#### **4.4.2.1 *In vitro* versus *in silico* Assumptions**

**Angular movement:** As it was described in chapter 3, there are no angular movements of the hip applied to the FE model. On the other hand, EM13 simulator is designed to implement the angular movements on the hip namely

flexion/extension, internal/external rotation and abduction/adduction. Because of spherical geometry of the head, it is assumed that flexion/extension has minimal effect on the separation. However, the internal/external rotation and abduction/adduction alter the position of the cup with respect to the head during the gait cycle. In the testing that were carried out on the EM13 hip simulator (unpublished data), the dynamic separation varied when 2 axes (flexion/extension and internal/external rotation) and 3 axes (flexion/extension, internal/external rotation and abduction/adduction) of rotations were used. Although the degree of abduction/adduction is lower than the other axes of the rotations (+7/-4) based on ISO 14242-1:2012 for wear testing on hip simulators, however, the direction of the movement can possibly give the cup slightly higher contact zone and lower separation.

**Cup translation:** the cup can translate in all the directions in the experimental set up. However, the cup components are computationally constrained to translate in posterior-anterior and medial-lateral direction. This constraint was stated in chapter 3. The constraint in transverse plane may slightly affect the edge contact.

**Dashpot effect:** Before gait cycle implementation, a level of dashpot analysis was carried out to obtain the coefficient that gave a critically damped system on each of the conditions. However, the system could yet be slightly overdamped/underdamped as the dashpot analysis were carried out for certain amount of times due to long running time of the these analyses. If the system was not critically damped, the dynamic readings can be slightly affected. However, the factor should not affect the dynamic results majorly.

**Damping of the model:** The level of damping in the experimental system should be the same for all the conditions in experimental testing as the mechanical conditions

are the same. However, there is no study so far to understand and predict the level of damping *in vitro* or *in vivo* which makes it extremely challenging to assign a fixed damping condition for all the computational conditions.

**Axial spring:** The computational model contains only one spring which is the medial spring. The experimental EM13 set up consists of an axial spring on the cup holder as well as the medial spring. The function of the axial spring is to smooth out the axial load applied to the cup. Therefore, slightly different axial load (load magnitude or amplitude) is expected to be applied in experimental and computational set up which could affect the separation readings.

**Device geometry:** The computational model studied the design of the THR for one specific design specifications whereas the experimental components can have different dimensions such as tolerances and radial clearances. As the definition of edge loading is based on the value of the radial clearance, slightly different radial clearance can influence the separation and edge loading occurrence and also, it could make the direct comparison of the experimental and computational outputs challenging.

**Computational output intervals:** The separation data that is recorded at the head relocation to measure the load at the rim is presented in two data points and time at which 0.5mm separation occurred was calculated by assuming linear interpolation between those two data points. The difference between the two data points could be large especially in the conditions with higher dynamic separation. So, the linear interpolation may not be the best representative of data point in between.

#### 4.4.2.2 Experimental Variation

**Reliability of experimental data:** Three tests were carried out on each parameter *in vitro*. The results obtained had a wide variation in the maximum separation. The mean of these values was taken and compared to the values produced by the computational model. If the maximum dynamic separation produced by the computational model is compared to the range of the separation for each case, the computational cases that were underestimating the experimental separation are in a good agreement with *in vitro* output. Higher number of *in vitro* tests could likely improve the reliability of the results.

**Hip simulator station condition variations:** The axial load applied to each hip simulator station is different to the numerical input loading profile. This is due to machine hardware tolerances, particularly those of the motor. The axial load cell that measured the applied force recorded a difference between the numerical input load of the simulator and the actual applied load in different stations.

**Experimental set up:** the number of components used in the experimental set up, the geometry of them and the overall assembly can affect the dynamics of the experimental set up. On the other hand, the computational set up neglect the effect of these factors.

**Output noise:** As it was mentioned in previous chapter, there is a level of noise in the computational output. Moreover, the dynamic experimental testing also underwent the noise issue and particularly in this experimental studies, the level of noises is higher in the initial cycles which makes it challenging to export the exact value of the separation.

#### **4.4.3 Friction sensitivity analysis**

While friction in the bearing has been simulated computationally, experimentally, friction also occurs on other moving parts of the simulation machine, though the drive and loading systems, the extent to which these influence the dynamics of the experimental system is not known. The contact surfaces are lubricated during the experimental testing and the greatest resistance to the cup movement could be caused by the system friction than the contact bearings friction.

The friction coefficient has the most effect when higher swing phase load (300N) was applied as the normal force to the surface will be higher than the lower swing phase load. Although, friction decreased the maximum dynamic separation, however, the dynamic separation is still overestimated by the computational model. Moreover, as friction increased the running time of the analysis, the effect of friction is not convincing enough to implement friction in all the conditions.

#### **4.4.4 Summary of the key findings**

- Higher translational mismatch level, steeper cup inclination angle and lower swing phase load increased the maximum dynamic separation computationally.
- The computational output is in a broad agreement with *in vitro* studies and the computational model sensitivity to the parameters is in the same trend as *in vitro* studies.
- The difference between experimental and computational dynamic separation could be due to various reasons such as damping in the system, angular movements, variation in hip simulator station conditions and output noises.

- The maximum load at the rim is affected by the same conditions that affects the separation. If the separation is lower experimentally than the maximum load on the rim would also be expected to be lower experimentally.
- There is a substantially higher load at the rim when the head is repositioning to concentric condition than when it is separating from concentric condition.
- The friction decreased the maximum dynamic separation in the computational model on the chosen conditions. Although bearing friction decreased the computational dynamic separation, the effect of friction was not substantial enough compare to the result and the computational running time. Friction in other moving components in the experimental mechanical system may also reduce levels of separation seen experimentally.
- Experimentally, longer term tests cause greater deformation of the polyethylene cup and to date it is not known how this influences the dynamics and separation. However, the contact mechanics output could potentially produce valuable insight to the long term behaviour of the THR.

## Chapter 5 Parametric sweep contact mechanics analyses

### 5.1 Introduction

The replication of the *in vivo* environment in experimental and computational studies is challenging to model due to the combination of biomechanical and biological parameters that can affect the THR performance. However, in the literature, the experimental hip simulators studies were shown to correlate with the clinical studies by comparing the wear patches on the THR components (Nevelos *et al.*, 2000). Moreover, the higher level of dynamic separation is also proven to increase the wear rate of the THR *in vitro* (Al-Hajjar *et al.*, 2013) in ceramic-on-ceramic and metal-on-metal bearings. In *in vitro* studies, the direct correlation between adverse conditions and increased wear could not be obtained for CoP bearings (Williams *et al.*, 2003). Therefore, it is interesting to understand what could potentially trigger the occurrence of damage and wear in hard-on-soft bearings in different conditions.

It was concluded in chapter 4 that at a lower swing phase load, higher translational mismatch level and steeper inclination angle increase the level of dynamic separation in the model during the swing phase. The computational and experimental studies were shown to follow a similar trend of dynamic separation changes over the whole gait cycle due to the translational mismatch, rotational variation and swing phase loads.

To understand the potential damage, fatigue and wear of the contact surfaces, the contact mechanics of the head and the cup were investigated. Analysing the contact behaviour of the THR under various conditions provides an understanding of which factors result in an adverse contact behaviour and consequently, in which cases the risk of damage to the polyethylene cup is higher. Furthermore, the input factors and

separation correlation with parameters which describe the contact mechanics can be investigated.

In this chapter, contact pressure, stress and strain behaviour and the deformation under various translational mismatch level, cup inclination angle and swing phase load were studied. Firstly, for comparison purposes, the contact mechanics behaviour at the end of the swing phase load, when the maximum separation occurs, were analysed. Secondly, the stress and strain behaviour during the gait cycle loading was compared between the input conditions. The cases that caused a permanent material damage due to plastic deformation are presented and discussed. Finally, the correlation between the separation and the contact mechanics was studied. The outcome of analyses provides the severity of parameters effect on the material behaviour which could be the indication of the long term prediction when cyclic loading occur.

## **5.2 Methodology**

The output of the analyses that are presented in this chapter are the same analyses that were studied in chapter 4. The translational mismatch level of 0mm to 4mm, inclination angle of 45° and 65°, and swing phase load of 70N, 100N, 200N and 300N were studied. This chapter is made of three studies which focus on the effect of different parameters on the contact mechanics. These three studies are fixated on the input parameters, separation and bearing friction (Figure 5.1). Furthermore, the output measurements are split into two main categories:

1. Contact output: to study the contact location, distribution of pressure on the surface and potential wear zone by exporting contact pressure and contact area.

2. Material failure risk: to assess the relative material failure risk using stress failure components, namely von Mises stress and Principal stresses (compressive stress), and also by using plastic strain values.

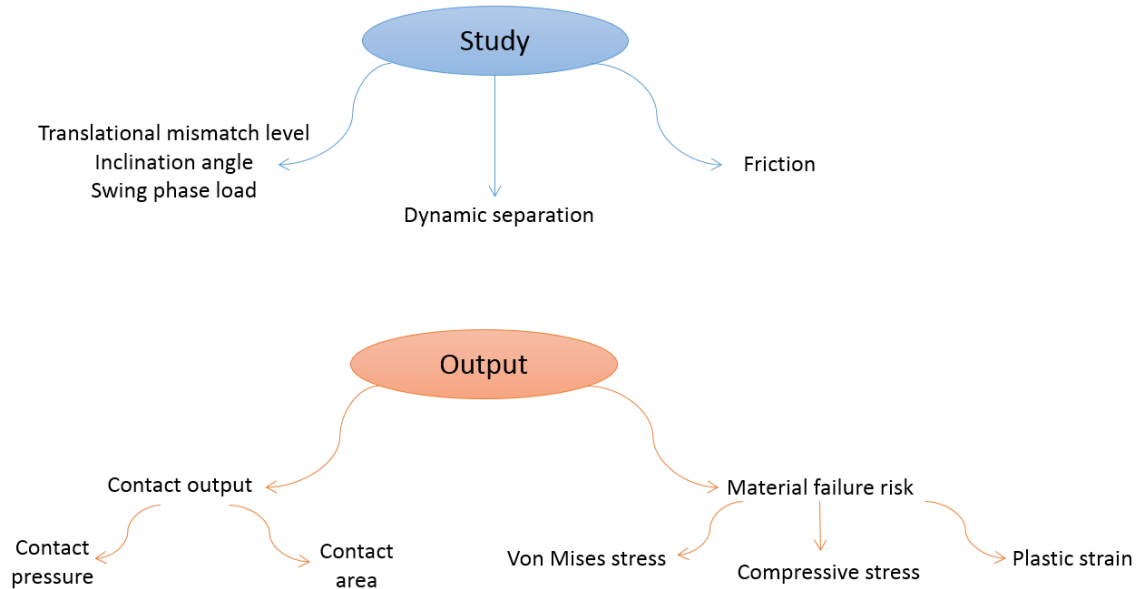


**Figure 5.1 The studies and outputs measurements of the chapter 5**

**Contact pressure distribution as contact indication:** To study the effect of dynamic separation on the contact mechanics of the model, the contact pressure of the nodes on the line of symmetry were recorded at the end of the swing phase load (the same time step that the medial-lateral separation in chapter 4 were recorded). The nodal contact pressure indicated the contact location when the maximum separation occurred. The contact pressure also indicated the level of pressure only on the surface of the cup.

As a baseline, the mismatch level was set to zero and the contact pressure distribution of the analysis was recorded to understand the contact pressure behaviour under standard conditions. As the pressure distribution is symmetrical on the inner surface of the cup, the surface nodes from the centre of the cup to the edge on the line of symmetry (where  $z = 0$ ) were recorded and the contact pressure of each node on the line were exported (see Figure 5.2). The same procedure was

repeated for all the analyses. The node set was equivalent for all the analyses. The behaviour of the contact pressure is compared between the standard conditions (0 mismatch) and corresponding adverse condition (various mismatches levels). The input swing phase loads of the compared cases are equal. As Figure 5.2 indicates, to represent the nodal contact pressure, the nodes are represented as an angle between the centres of the cup ( $0^\circ$ ) to the lateral edge where the contact occurs ( $96^\circ$ ). Moreover, the contact pressure behaviour throughout the gait cycle is presented to understand the overall contact behaviour.

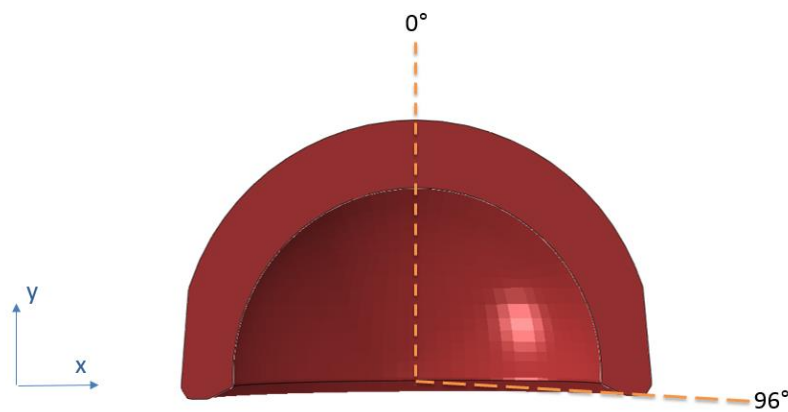


**Figure 5.2 The nodes on the symmetry line of the contact pressure with respect to the angle from the centre of the line to the lateral edge**

**Contact area:** As the contact area and the applied force are the main factors that potentially affect the stress and pressure behaviour, it is important to understand the contact area feedback from the loading and the geometry. The contact area throughout the gait cycle and at the swing phase load were recorded and presented.

**Stress and failure risk analysis:** It is important to study the stress behaviour throughout the gait cycle as the long-term behaviour of UHMWPE can be predicted by observing the stress behaviour on the cup. There is a large amount of literature precedent that analyse using a von Mises stresses (e.g. Plank *et al.*, 2005; Hua *et al.*, 2014). Von Mises stress is used as a representation of the total stress behaviour in

all of the directions. It is known as the maximum distortion energy theory of failure, as it accounts for hydrostatic conditions by including balanced stresses within the calculation. It is represented as:

$$\sigma_v^2 = \frac{1}{2} [(\sigma_{11} - \sigma_{22})^2 + (\sigma_{22} - \sigma_{33})^2 + (\sigma_{11} - \sigma_{33})^2 + 6(\sigma_{23}^2 + \sigma_{31}^2 + \sigma_{12}^2)]$$

Where  $\sigma_{11}$  is stress in x direction,  $\sigma_{22}$  is stress in y direction,  $\sigma_{33}$  is stress in z direction,  $\sigma_{23}$  is shear stress in yz plane,  $\sigma_{31}$  is shear in zx plane and  $\sigma_{12}$  is shear in xy plane. Von mises stress is mostly indication of the shear stress behaviour. If the von Mises stress on the cup exceeds the elasticity limit, it results in a permanent deformation of the cup. This failure mode is dependent on the yield point of UHMWPE and the position and stress level. If a small region on the cup is subject to some plastic deformation, it affects the material properties of the effected structure negatively by reducing the elastic modulus, making additional progressive failure more likely (Hertzberg and Manson, 1980). Such behaviour of plasticity can fatigue the cup especially during cyclic loading conditions such as walking. For this purpose, the maximum von Mises stress on the polyethylene cup was calculated.

For each analysis, the maximum von Mises stress at each step during the gait cycle loading was exported by using a python script (Appendix). Then, the maximum von Mises stress throughout the cycle was compared in all the cases.

**Stress components:** The contribution of the maximum principal stress on the stress behaviour was studied in standard and adverse condition cases as von Mises stress mostly account the shear stresses involved in the element. Principle stresses are used to describe phenomena such as the most tensile stress an object experiences (maximum) and the most compressive stress an object experiences (minimum). During the gait cycle, the cup liner is compressed against the head as the head and

the cup unit are fully fixed. Therefore, the compressive stress can potentially have an important role in the stress behaviour. As the previous output (von Mises stress data) indicates the crucial point during the gait cycle. The stress components i.e., maximum von Mises stress and compressive stress (minimum principal stress) at the same data point are compared to understand the principal and shear stress behaviour on the cup liner.

**Plastic Strain:** the maximum plastic strain on the cup was recorded for each case to understand in which analysis permanent material damage occurred. The plastic strain output is the maximum plastic strain equivalent to the Mises stress. As it was mentioned, the plastic deformation is a key indication to understand the long-term material behaviour.

**Separation related contact mechanics:** The aim of this set of analyses is to understand the correlation of the dynamic and contact mechanics behaviour of the THR. In the analyses up to this point, the effect of the parametric sweep is directly correlated to the contact mechanics output. In this section, the contact mechanics output are investigated based on the separation corresponded to the parametric sweep.

Finally, the effect of separation on the contact mechanics was separately investigated. The same method was used on the analyses that were carried out with 0.1 coefficient friction. The nodal contact pressure of the frictional analyses was compared to the frictionless analyses. Furthermore, the effect of friction on the stress components, contact area, and plastic strain is shown.

## **5.3 Results**

The output discussed in the methodology section is demonstrated and explained in this section. The results are presented in the same manner as it was discussed in the methodology.

### **5.3.1 Input parameters study**

#### **5.3.1.1 Contact output**

The contact pressure output is presented into two sections. In this section, the contact pressure behaviour throughout the gait cycle is first presented. Secondly, the variation in the contact pressure location and magnitude at the swing phase under all conditions is described.

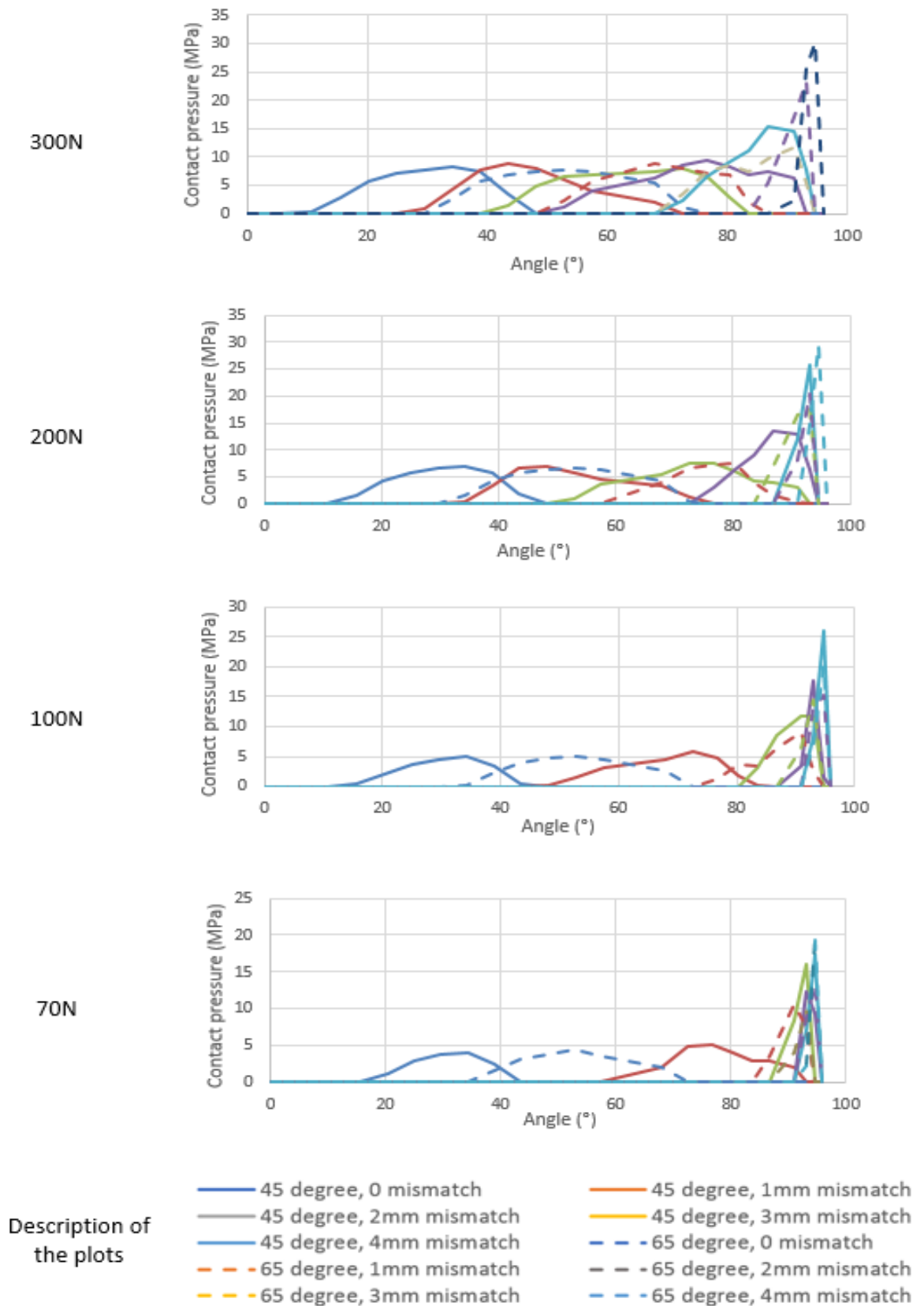
##### **5.3.1.1.1 Contact pressure behaviour under all condition**

Figure 5.3 represents the nodal contact pressure along the symmetry line in the 0mm to 4mm mismatch levels for various swing phase loads and inclination angles. As this figure shows, for all mismatch levels, the nodal pressure starts from zero from the centre to the lateral edge. The nodal pressure increased to the maximum value and dropped from the peak to zero pressure between the two ends. However, the distribution and magnitude of the pressure varied between the cases.

In standard conditions, the contact pressure was distributed between  $10^\circ$  to  $45^\circ$  of the nodal angle and the nodal pressure reached the peak pressure gradually. However, as the translational mismatch level increased, the nodal pressure distribution moved towards the lateral edge of the cup more to the point in which the contact is only at the lateral edge. Higher translational mismatch also affected the nodal pressure variation. As an example, under 300N swing phase load, nodal pressure in 4mm mismatch had a substantially higher peak than the rest of the translational mismatch levels (up to 16MPa) whereas the peak nodal pressure in 0

to 3mm cases varied between 8MPa to 9.8MPa in standard condition. Moreover, under steep cup inclination angle, the peak pressure of even substantially higher (23.5MPa and 30MPa for 3mm and 4mm, respectively) than the standard cup inclination angles under 300N swing phase load was observed. The nodal angle distribution of the cases experiencing higher peak values is lower than the cases that the pressure variation occurred gradually. Therefore, the maximum pressure produced under steep cup inclination angle was substantially higher than the maximum pressure under standard cup inclination angle.

In all the swing phase loads, higher translational mismatch level resulted in a closer contact pressure distribution to the lateral edge and also it resulted in a substantially higher peak pressure. However, the occurrence of edge contact depends on the conditions. The lower swing phase load increased the possibility of edge contact up to the point that in the analyses with 70N swing phase load, 3 out of 5 cases under standard cup inclination angle and 4 out of 5 cases under steep cup inclination angle underwent the edge contact with substantially higher peak than the peak pressure under standard conditions. Furthermore, the effect of steep cup inclination angle is mostly seen when the edge contact occurred. The steep cup inclination angle produced a higher pressure peak in the edge contact cases than the standard cup inclination angle.



**Figure 5.3** Nodal contact pressure along the line of the symmetry recorded at the end of the swing phase load. Each graph represent the nodal pressure for each swing phase load under standard and steep cup inclination angle. The description of the plots, which is the same for all graphs, represents the cup inclination angle and the translational mismatch level.

### **5.3.1.1.2 Contact pressure behaviour throughout gait cycle**

As an example of the contact pressure changes throughout the gait cycle, the contour plot of contact pressure throughout gait cycle under 0mm and 4mm translational mismatch level under 70N swing phase load are represented in Figure 5.4 and Figure 5.5 signify standard and steep cup inclination angle. Previous chapter also showed that the separation under 70N swing phase load were higher than any other swing phase loads. The contour plot of the contact pressure on the cup represent the pressure variation from minimum of 0Pa (blue) to the maximum value (red). The conditions with 0mm and 4mm translational mismatch were chosen for presentation as these two cases result in the minimum and maximum separation levels (demonstrated in the previous chapter).

It could be seen that under standard cup inclination angle (Figure 5.4), the maximum contact pressure throughout gait cycle followed the loading changes for both 0mm and 4mm translational mismatch condition. Although translational mismatch level increased the maximum contact pressure, the translational mismatch level produced the most difference in the contact pressure at the swing phase load where over four times higher contact pressure was produced in the condition with 4mm translational mismatch level than 0mm translational mismatch level. The contour plot of the contact pressure at the swing phase load also indicated the edge contact when translational mismatch level was applied.

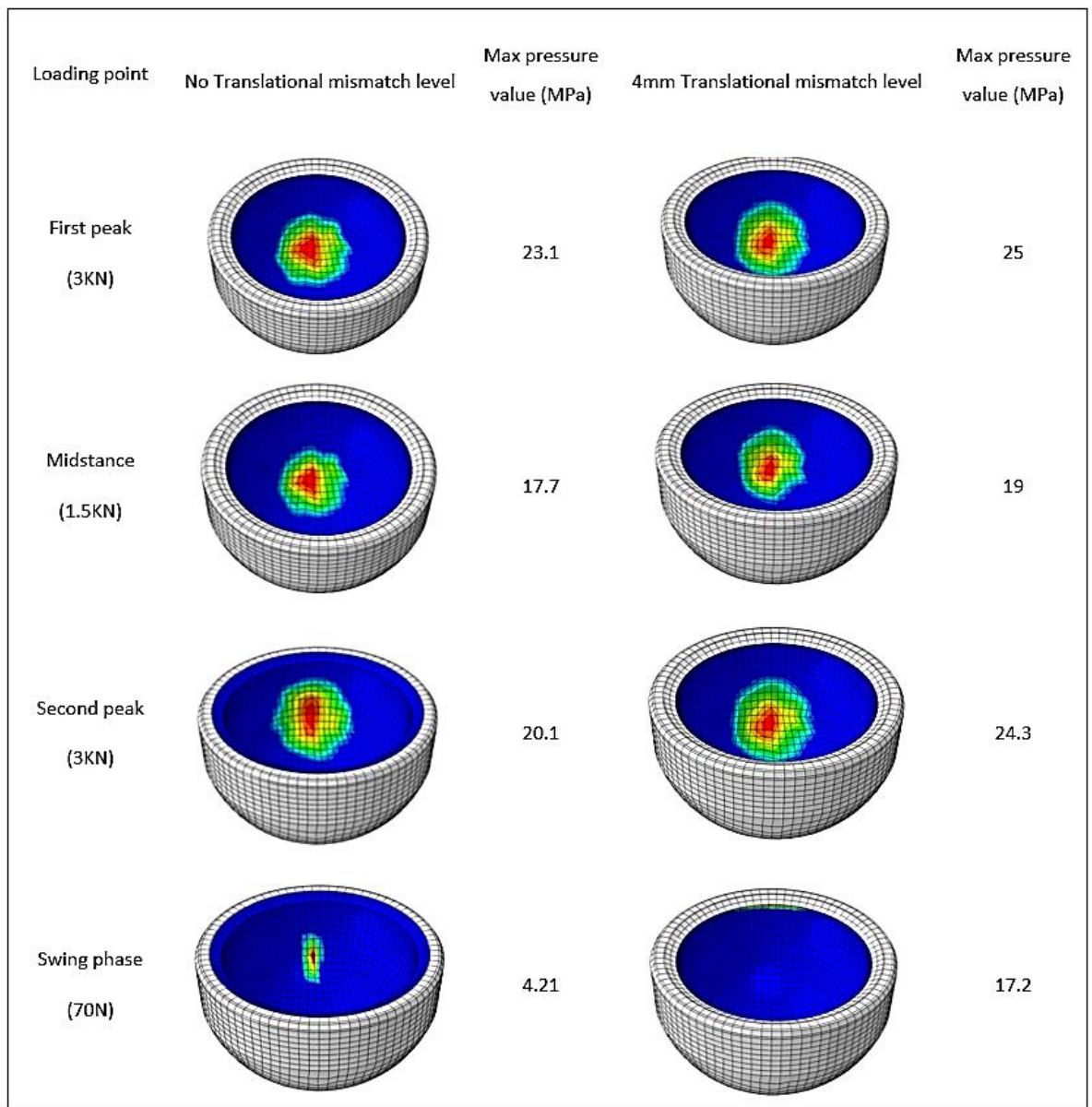


**Figure 5.4 Contact pressure contours and the maximum contact pressure on the liner inner surface throughout the gait cycle under 45° inclination angle, 70N swing phase load, translational mismatch level of 0 and 4mm**

The contact pressure contour plots under steep cup inclination angle produced a similar trend of contact pressure changes as the standard cup inclination angle. However, the predicted maximum contact pressure at the swing phase was over five times higher on the condition with translational mismatch level than the standard condition. The maximum contact pressure that is produced at the swing phase under 4mm translational mismatch level is only slightly less than the contact pressure that the cup undergoes at the peak load.

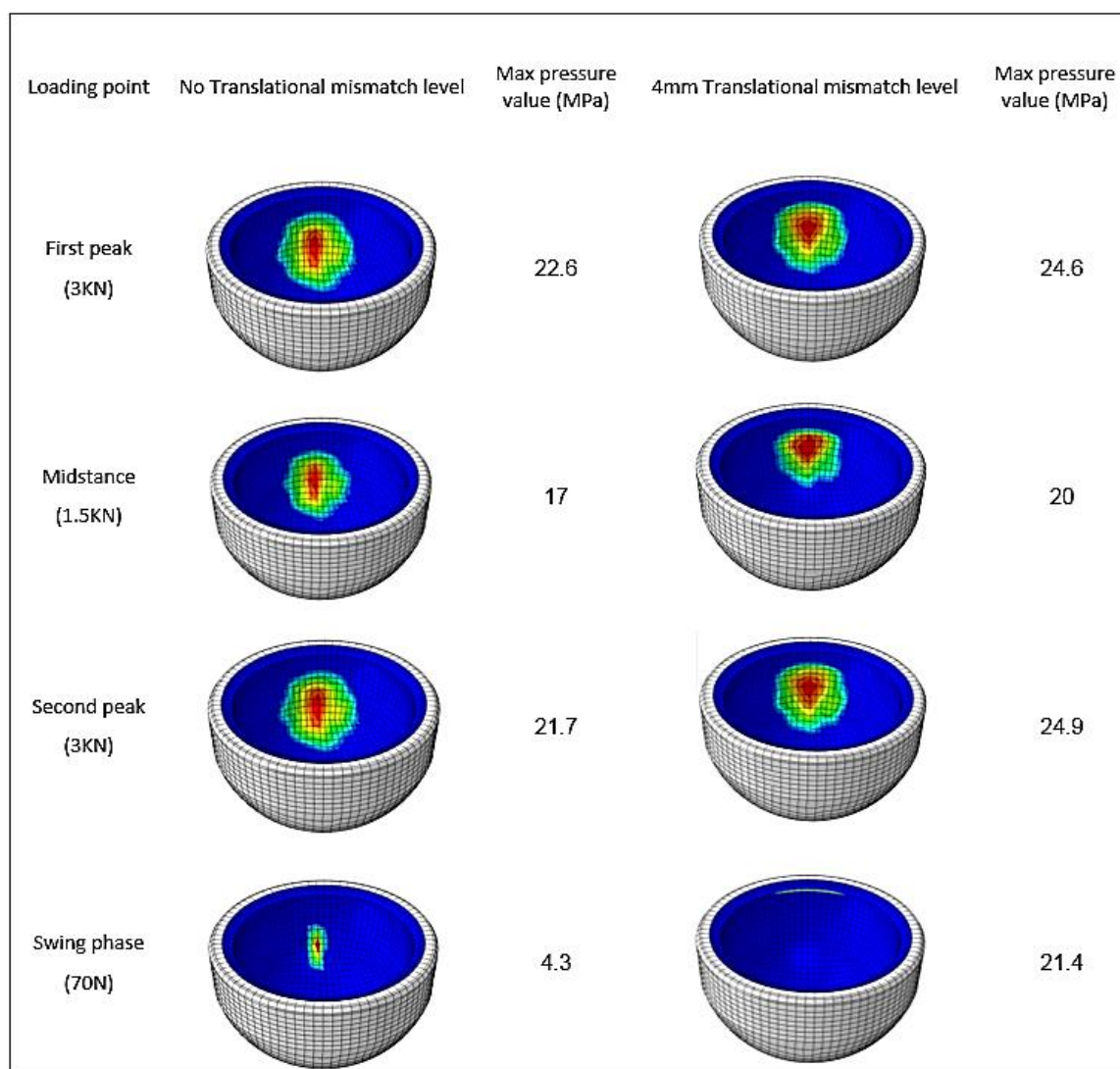


**Figure 5.5 Contact pressure contours and the maximum contact pressure on the liner inner surface throughout the gait cycle under 65° inclination angle, 70N swing phase load and translational mismatch level of 0 and 4mm.**

### 5.3.1.1.3 Contact area changes in input parameters

The difference in contact area between the peak and the low load was substantial. As Table 5.1 represents, the contact area at the peak load varied between 333 mm<sup>2</sup> to 354 mm<sup>2</sup> under standard cup inclination angle. Moreover, the peak contact area (that occurs at the peak load) in steep cup inclination angle was less than the peak contact area under standard cup inclination angle. The peak contact area was more affected by the cup inclination angle than the swing phase load as the peak contact area were generally similar in all swing phase loads. The contact area decreased in swing phase load substantially. In the most severe scenario, the contact area was

reduced to 45 mm<sup>2</sup> and 10 mm<sup>2</sup> at the swing phase under standard and steep cup inclination angle, respectively.

**Table 5.1 The comparison of contact area in the all analyses that were carried out at the peak (3KN) and minimum load (swing phase load) under standard and steep cup inclination angle.**

| Swing phase load (N) | Mismatch level (mm) | Contact area (mm <sup>2</sup> ) |       |       |      |
|----------------------|---------------------|---------------------------------|-------|-------|------|
|                      |                     | peak                            |       | swing |      |
|                      |                     | 45°                             | 65°   | 45°   | 65°  |
| 70                   | 0                   | 350.4                           | 285.9 | 72.1  | 34.7 |
| 70                   | 1                   | 344.7                           | 287.0 | 71.3  | 20.5 |
| 70                   | 2                   | 349.9                           | 277.1 | 40.9  | 16.8 |
| 70                   | 3                   | 345.2                           | 278.0 | 46.7  | 12.6 |
| 70                   | 4                   | 348.6                           | 266.5 | 45.0  | 9.7  |
| 100                  | 0                   | 350.4                           | 285.8 | 75.2  | 52.6 |
| 100                  | 1                   | 341.1                           | 285.3 | 78.9  | 40.8 |
| 100                  | 2                   | 349.9                           | 280.7 | 67.1  | 19.3 |
| 100                  | 3                   | 345.2                           | 277.8 | 51.9  | 13.4 |
| 100                  | 4                   | 333.8                           | 268.5 | 47.8  | 12.7 |
| 200                  | 0                   | 346.8                           | 285.9 | 96.3  | 83.2 |
| 200                  | 1                   | 344.7                           | 285.3 | 123.5 | 63.6 |
| 200                  | 2                   | 349.9                           | 282.1 | 108.1 | 29.7 |
| 200                  | 3                   | 345.2                           | 276.2 | 96.0  | 24.8 |
| 200                  | 4                   | 354.2                           | 266.9 | 77.1  | 17.1 |
| 300                  | 0                   | 350.4                           | 285.8 | 133.1 | 98.4 |
| 300                  | 1                   | 342.8                           | 287.0 | 132.1 | 80.7 |
| 300                  | 2                   | 349.9                           | 282.1 | 134.4 | 70.6 |
| 300                  | 3                   | 345.2                           | 276.2 | 127.5 | 34.9 |
| 300                  | 4                   | 354.2                           | 268.5 | 118.6 | 32.4 |

The contact area of the analyses at the end of the swing phase (when usually the adverse behaviour occurs) under standard and steep cup inclination angle is shown

in Figure 5.6. Generally, the contact area decreased as the translational mismatch level increased in all the conditions except 70N swing phase load and steep cup inclination angle where the contact area slightly increased between 2mm and 3mm translational mismatch level. In standard cup inclination angle the contact area varied between 135 mm<sup>2</sup> to 45 mm<sup>2</sup>. However, the contact area for all the cases dramatically decreases in steep cup inclination angle. The contact area variation under steep cup inclination angle is between 80 mm<sup>2</sup> to 10mm<sup>2</sup>.

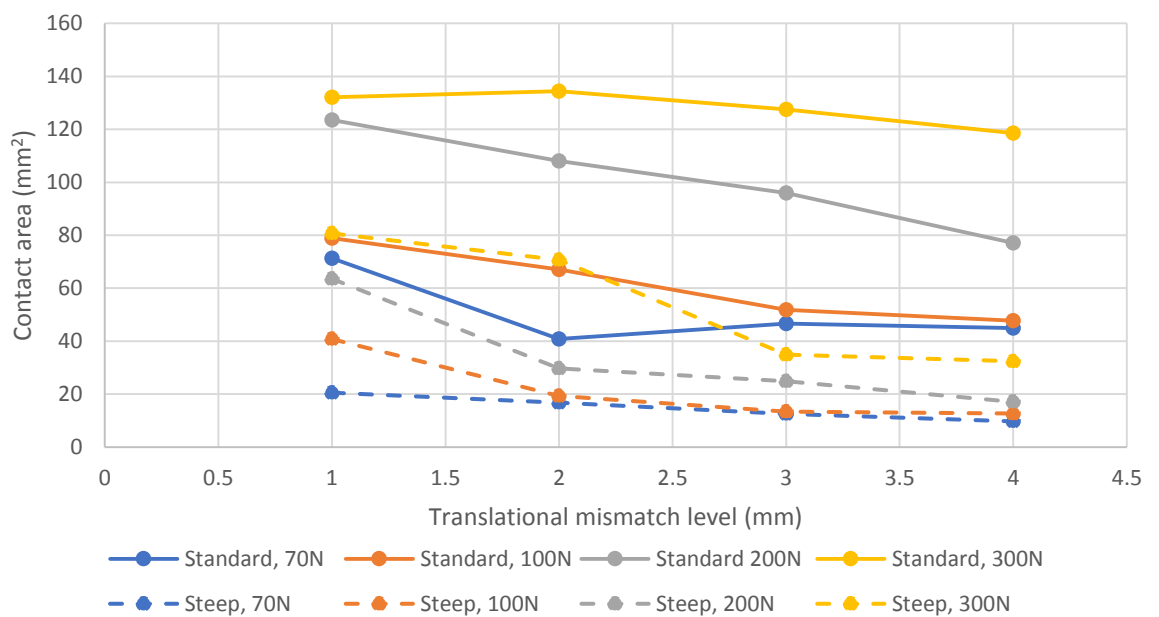


**Figure 5.6** The contact area at the end of the swing phase load for various translational mismatch level and swing phase loads. The contact area of the analyses under standard and steep cup inclination angle are plotted as 'standard' and 'steep', respectively

### 5.3.2 Material failure risk

#### 5.3.2.1 Von Mises stress throughout the gait cycle

Figure 5.7 represents the maximum stress behaviour during gait cycle in the concentric condition analyses (0 mismatch level) under 45° and 65° inclination angle and variation of swing phase loads. The overall stress behaviour follow the axial loading behaviour in all of the swing phase loads variations for all the cases. The largest difference between the cases occurred during the swing phase. Higher swing phase load resulted in a higher stress during the swing phase for both cup

inclination angles. Moreover, the steep cup inclination angle resulted in a lower stress value throughout the gait cycle in all swing phase loads.

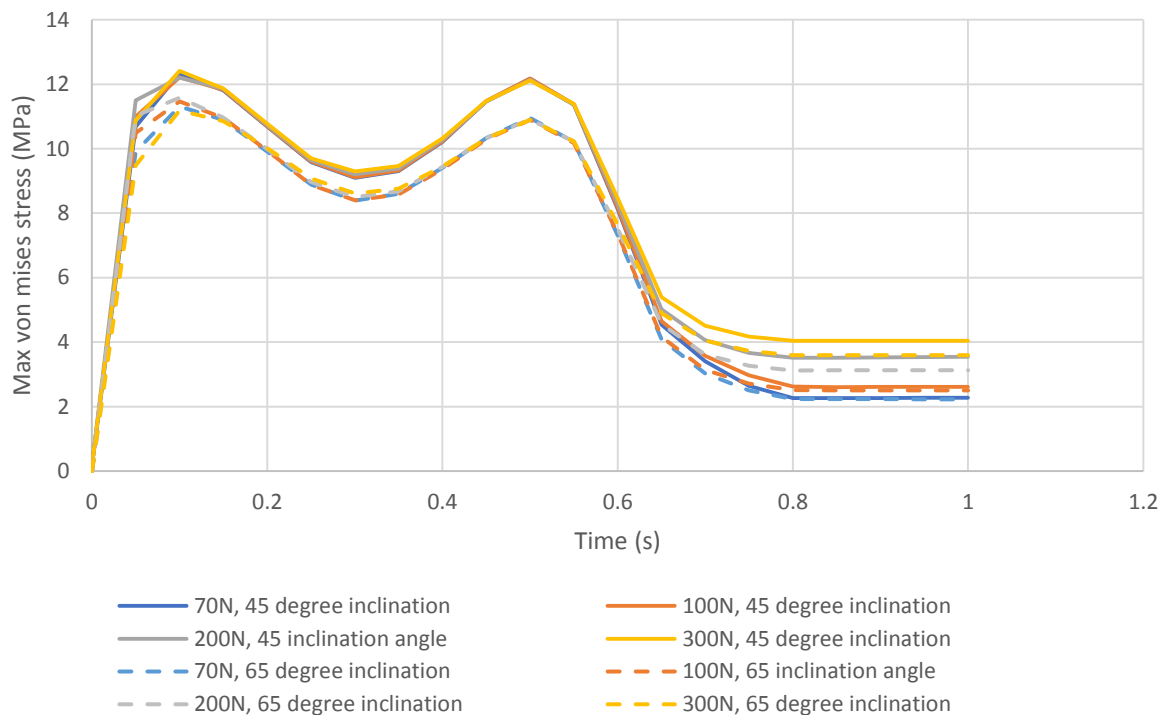


**Figure 5.7 Stress distribution of the analysis with 0 mismatch level under 45° inclination angle (solid lines) and 65° inclination angle (dotted lines) with swing phase load of 70N to 300N**

The ‘in cycle’ stress behaviour is observed to either follow the loading trend or produce a higher level of stress during swing phase load (adverse stress behaviour). However, as the swing phase load decreased the number of the conditions that produce adverse stress behaviour during swing phase increased in both standard and steep cup inclination angle (Figure 5.8). The cup underwent the adverse stress behaviour and the maximum stress value that is produced at the swing phase load decreased by decreasing the swing phase load. Since there is an axial loading (equivalent to the swing phase load of the analysis) during stabilisation step which occurs before gait cycle loading, the initial stress at the gait cycle is not zero.

When 300N swing phase load was applied, there is a similar stress behaviour in the analyses with 1mm, 2mm and 3mm mismatch level that followed the loading

changes under standard cup inclination angle. In the mentioned conditions translational mismatch level and the maximum stress was initiated and finished (at the swing phase load) at the value of 4.4MPa, 4MPa and 5.2MPa, respectively. Out of all of the cases that are demonstrated with 300N swing phase load and standard cup inclination angle, the analysis with 4mm mismatch level had a dissimilar behaviour. In this analysis, the stress behaviour was initiated with a substantially higher stress value of 10MPa. The stress behaviour during the stance phase was similar to the rest of the cases. However, during swing phase, the maximum stress initially decreased from 12.3MPa (the peak stress) to 6MPa then a moderate increase of maximum stress to 10MPa occurred. After the increase in the stress value during the swing phase load, the maximum stress becomes constant until the end of the swing phase load.

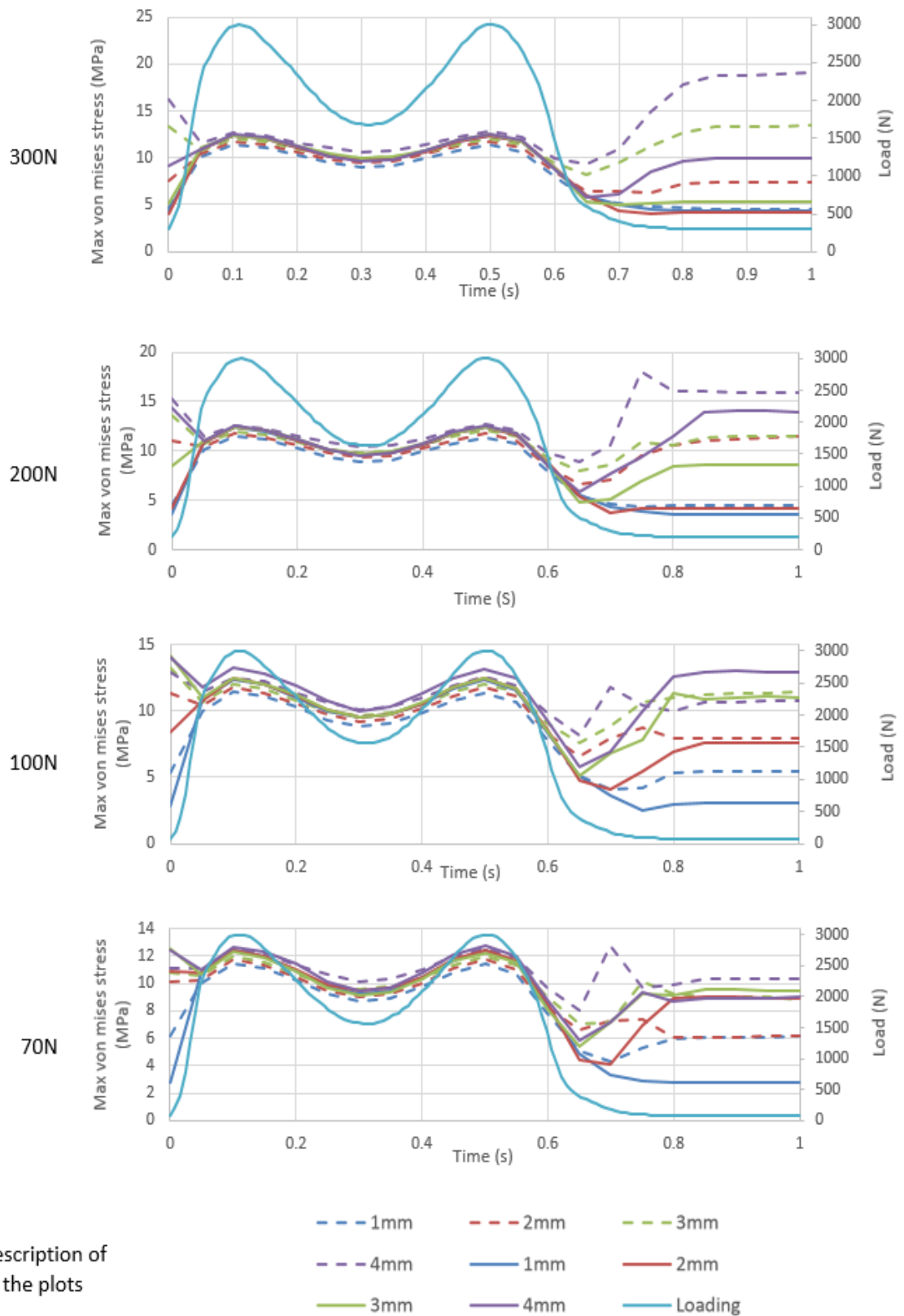


**Figure 5.8** The maximum von Mises stress throughout the gait cycle for all of the conditions. The dashed line plots represent steep cup inclination angle and the solid line plots represent standard cup inclination angle at different mismatch level

A similar trend of stress variation was seen in analyses under steep cup inclination angle for 300N swing phase load. However, the only condition that followed the

loading changes under steep cup inclination angle was the analysis with 1mm translational mismatch level. The rest of the analysis resulted in a higher stress level during swing phase load than expected. The conditions that resulted in a higher stress value during swing phase load also experienced higher stress value at the beginning of the cycle. Moreover, in all of the cases, steeper cup inclination angle produced higher stress at the swing phase load than the standard cup inclination angle.

The contour plot of the von Mises stress at the swing phase load under standard cup inclination angle is shown in Figure 5.9. The contour plot showed the stress distribution on the cross section area where the thickness of the cup is. In all the analyses, the same contour limit is used for a simpler comparison. In the same swing phase load, the stress distribution moved to the lateral edge of the cup by the increase in translational mismatch level. Moreover, higher swing phase load increased the stress value in the thickness of the cup.

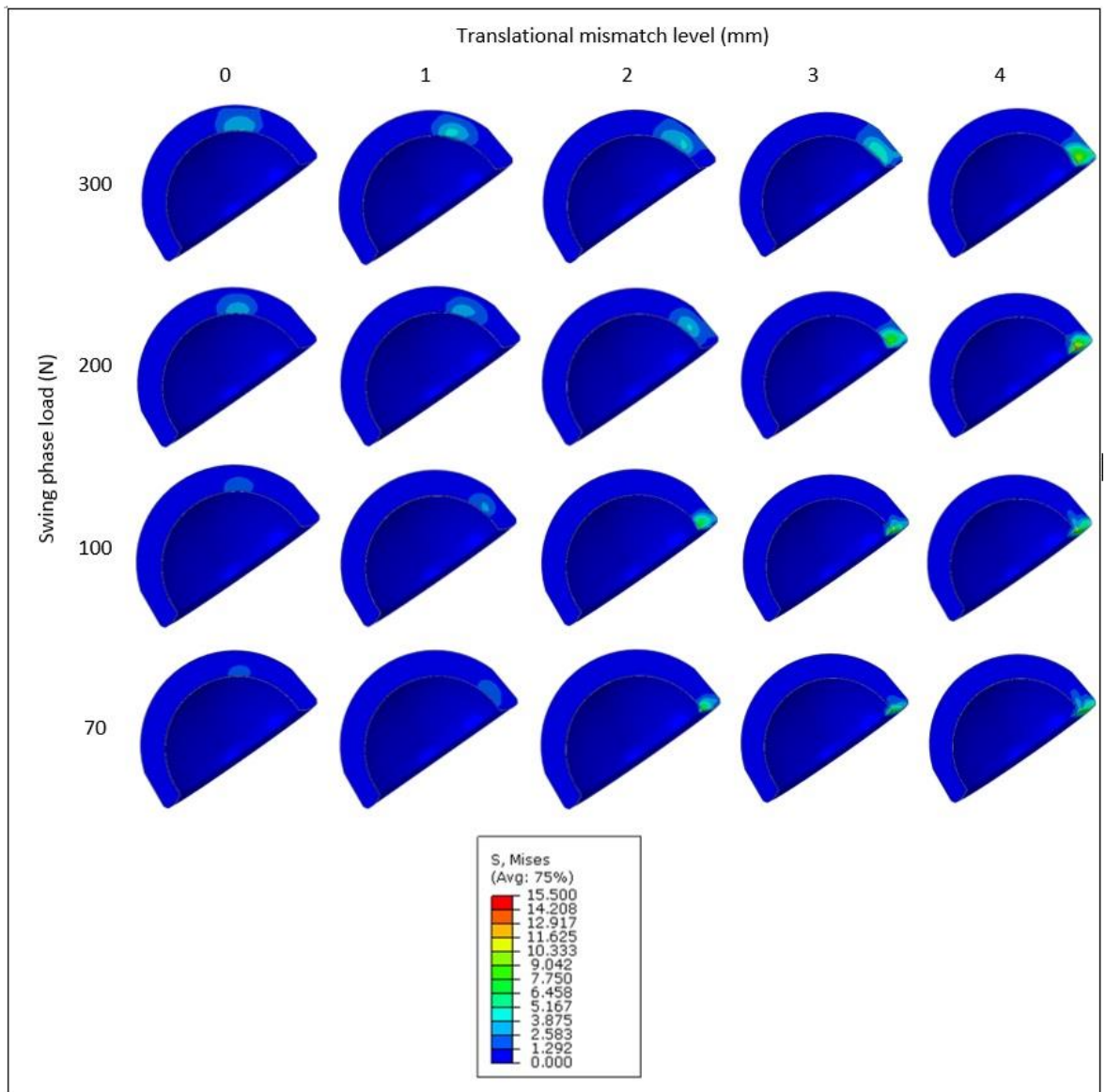


**Figure 5.9 The cross sectional contour of von Mises stress at the end of swing phase load under standard cup inclination angle for the analyses with swing phase load of 70N to 300N and translational mismatch level of 0mm to 4mm.**

Figure 5.10 represents the cross sectional contour of von Mises stress at the end of swing phase load under standard cup inclination angle. A similar trend can be seen in the steep cup inclination angle. Although, the stress distribution moved towards the edge by higher translational mismatch level, the stress distribution in standard condition is closer to the edge than the stress distribution in steep cup inclination angle which caused higher number of edge contact out of all the analyses. Furthermore, higher stress values were recorded for steeper cup inclination angle.

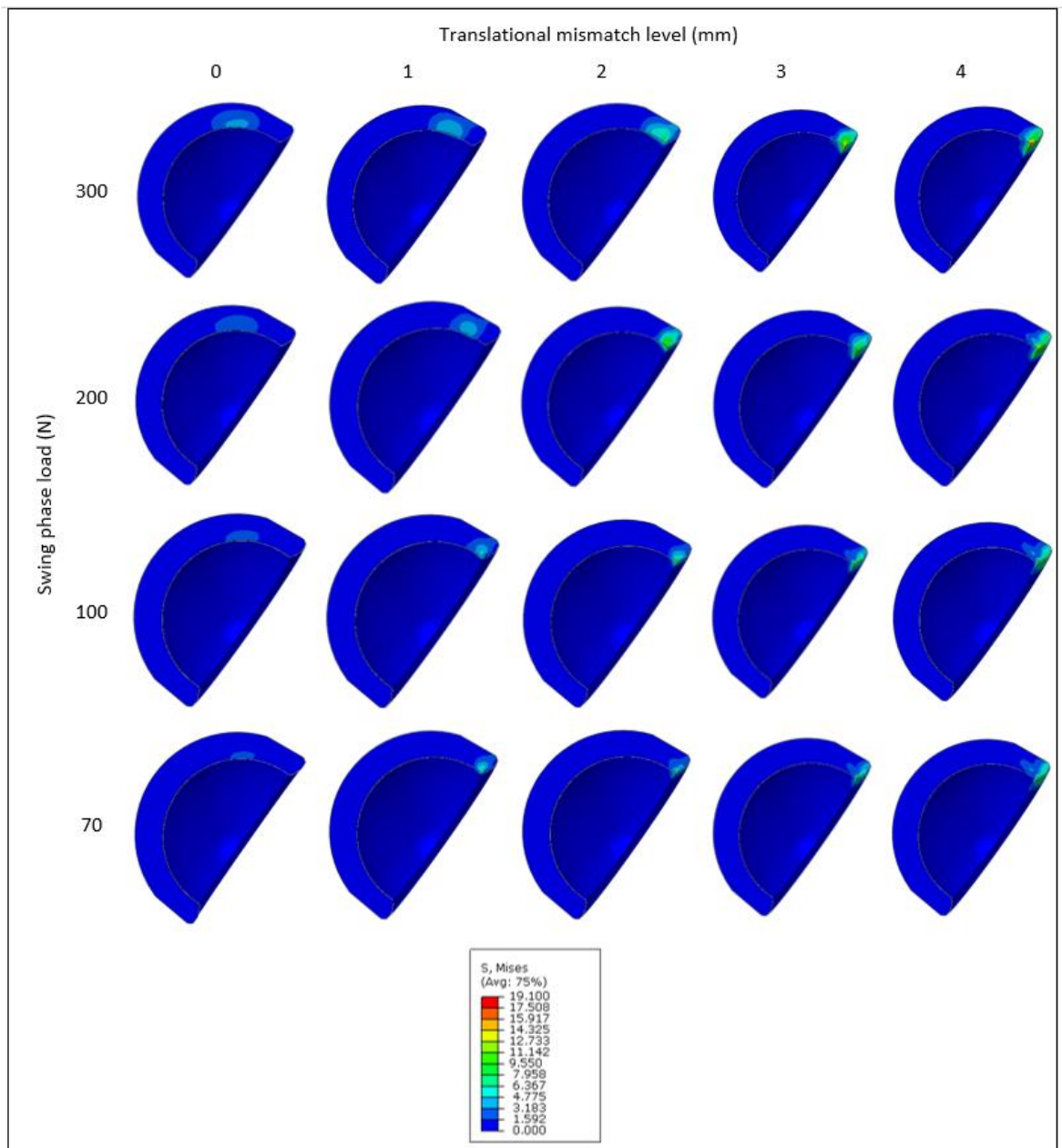


**Figure 5.10** The cross sectional contour of von Mises stress at the end of swing phase load under steep cup inclination angle for the analyses with swing phase load of 70N to 300N and translational mismatch level of 0mm to 4mm.

### 5.3.2.2 Maximum principal stress at swing phase load

Figure 5.11 shows the maximum compressive stress and the von Mises stress increased as the translational mismatch increases. Also, higher swing phase load resulted in higher stress values (both values) in a specific translational mismatch level condition. However, this trend could not be seen in the compressive stress of the conditions with 70N swing phase load. Furthermore, the maximum compressive stress at the swing phase load is substantially higher than the von Mises stress

values in most of the conditions. The only condition that the compressive stress is slightly higher than the von Mises stress is the one with 70N swing phase load and 4mm translational mismatch level.

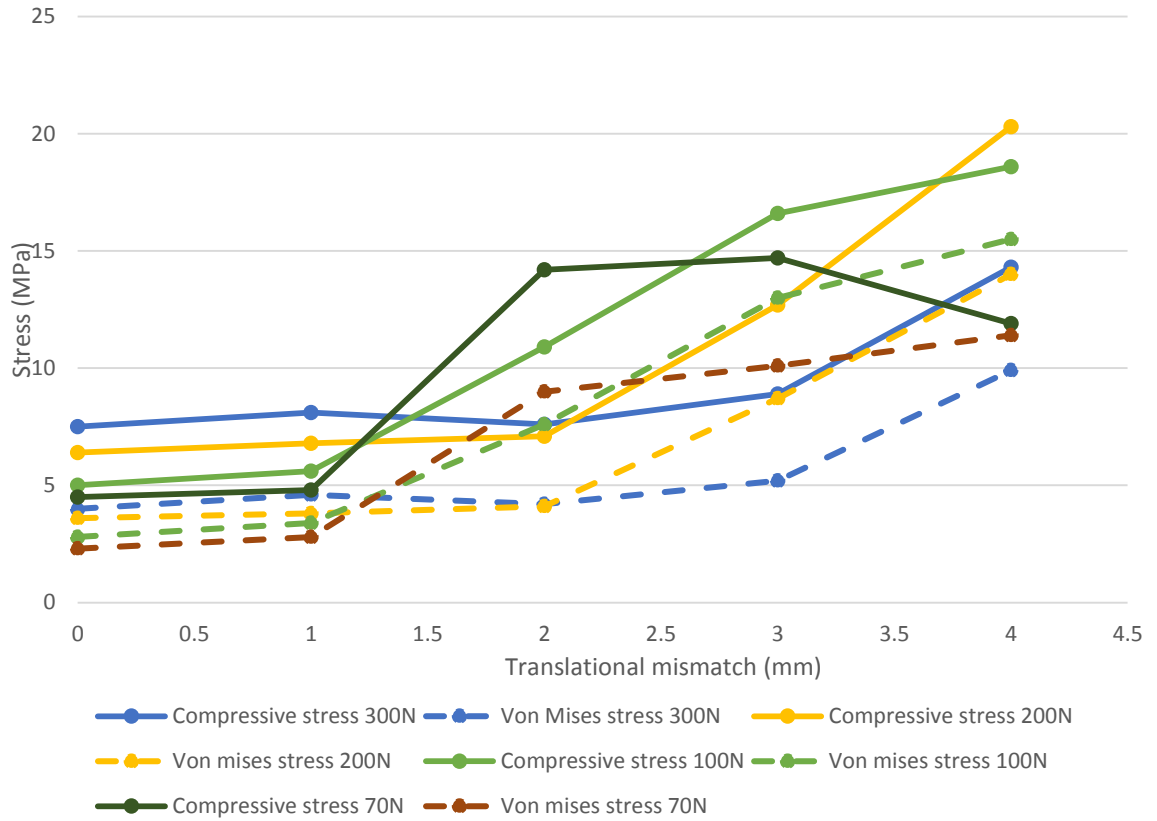


**Figure 5.11 Comparison of the maximum compressive stress and von Mises stress under standard cup inclination angle translational mismatch levels of 0mm to 4mm**

Figure 5.12 focuses on the compressive and von Mises stress of the analyses that were carried out under steep cup inclination angle. This figure agreed that the both stress types increased as the translational mismatch and swing phase load increased. The compressive stress that was produced was also notably higher than von Mises stress. The only condition that disagreed with the higher compressive stress than the von Mises stress outcome is the analysis with 100N swing phase load and 4mm translational mismatch level.

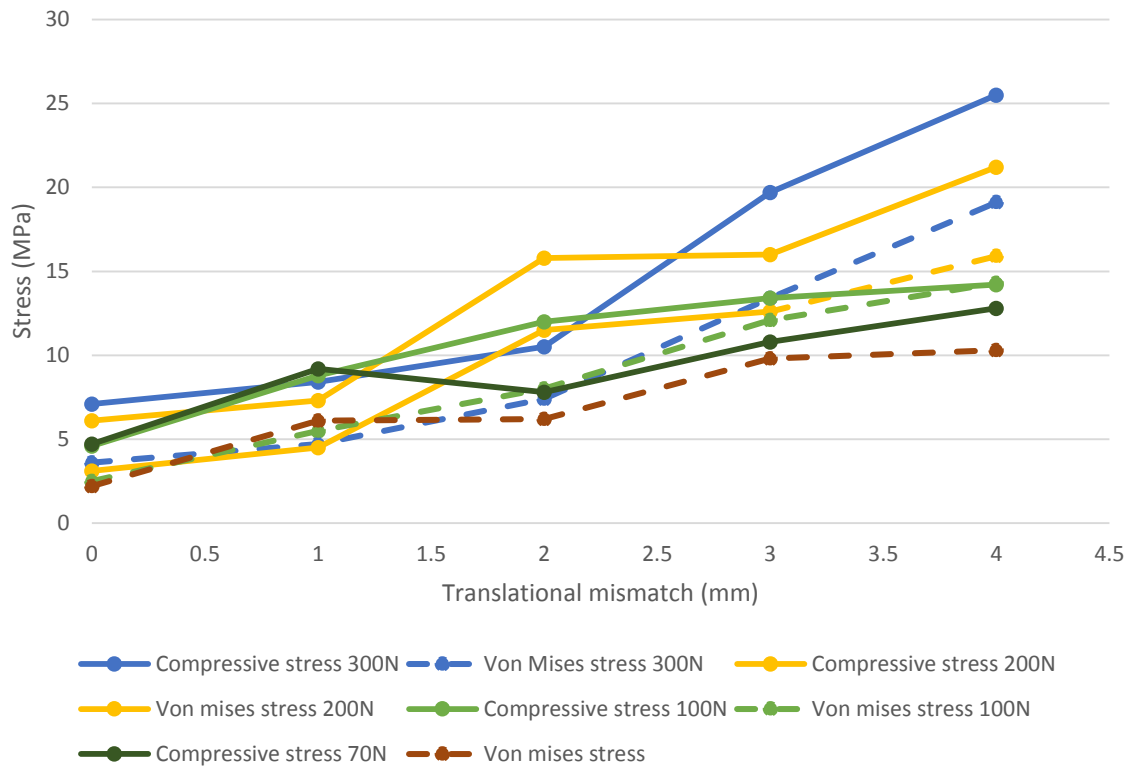


**Figure 5.12 Comparison of maximum compressive stress and von Mises stress under steep cup inclination angle and translational mismatch levels of 0mm to 4mm**

### 5.3.2.3 Plastic strain

No plastic strain was recorded when 300N swing phase load or 1mm mismatch level was applied (Figure 5.13). 200N swing phase load caused a plastic strain only when 4mm mismatch was applied. A level of plastic strain was recorded in 100N swing phase with 3mm and 4mm mismatch. The cases with most plastic strain occurrence is 70N swing phase load.

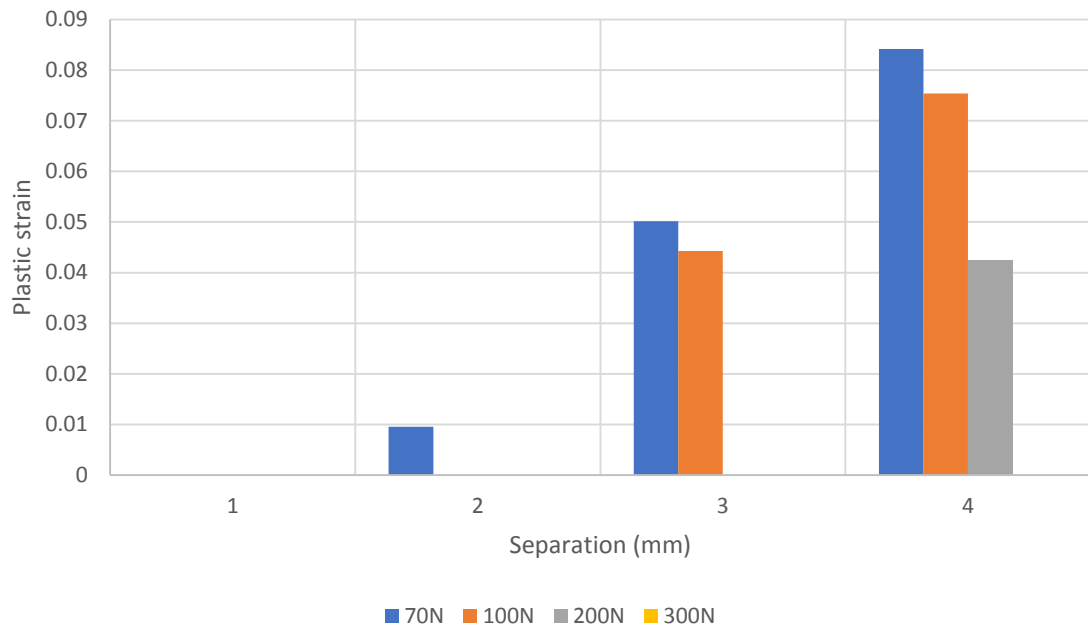


**Figure 5.13 Maximum plastic strain in the cases with various translational mismatch level and swing phase loads under 45° inclination angle**

Figure 5.14 demonstrates the plastic strain data exported under steep cup inclination angle. Once more, no plastic strain was recorded in 1mm mismatch level. In the cases with 3mm and 4mm mismatch level, occurrence of plastic strain was observed for all the swing phase loads and the only case that did not affect the plastic strain in 2mm mismatch level was 300N swing phase load. Therefore, the number of cases that the plastic strain occurred in, is higher in the cup inclination of 65° than 45°.

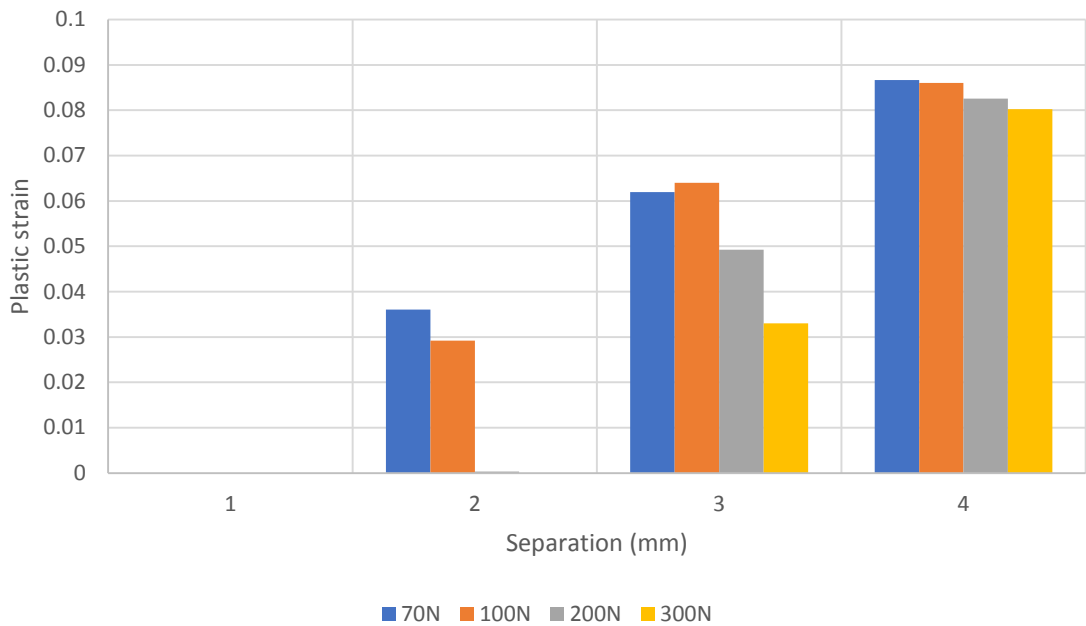


**Figure 5.14 Maximum plastic strain in the cases with 65° inclination angle and all of the swing phase loads and translational mismatch levels**

#### **5.3.2.4 Contact area as driven for stress behaviour**

Furthermore, it was shown in chapter 4 that there is a substantial load at the rim at the beginning of the stance phase. The high load at the rim was used as a reason for high wear rate when edge loading occurs. However, the stress behaviour indicated that the contact area increased substantially in the first 0.5s of the gait cycle which did not lead to high stress and potentially the most crucial damage zone (Figure 5.15). Although the load and contact area increased, the stress behaviour from the beginning of stance phase to the first peak load showed a decrease in the level of stress due to the substantial contact area increase. The contact area at 0.5s of the gait cycle was 320 mm<sup>2</sup> whereas the contact area at the beginning of the stance phase depended on the swing phase load (48mm<sup>2</sup> for 70N swing phase load to 125mm<sup>2</sup> for 300N swing phase load). Then, the contact areas changes between the 0.5s to the peak load is moderate and consequently, the stress increased moderately in the same time frame.

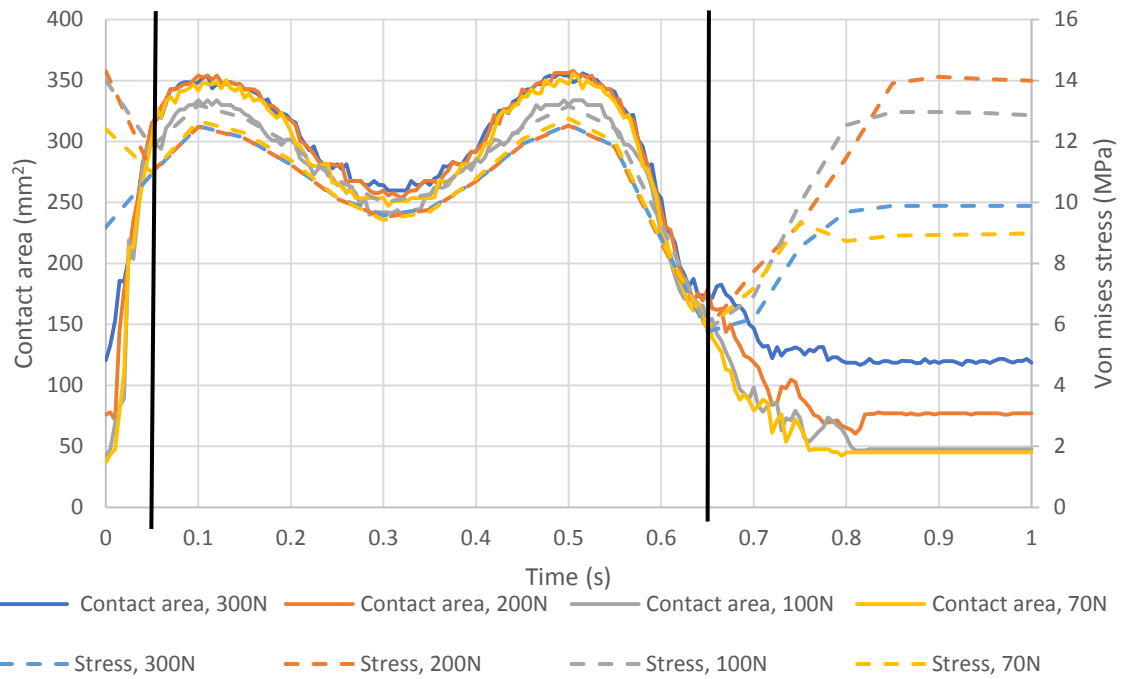


**Figure 5.15 Contact area and von Mises stress versus time in the analyses with 4mm translational mismatch level, various swing phase loads and standard cup inclination angle**

The corresponding contact area to the stress initialisation under steep cup inclination angle is shown by a black line in Figure 5.16. The value of corresponding contact area is less in steep cup inclination angle than the standard cup inclination angle. The variation of the contact area is between 55 mm<sup>2</sup> and 85 mm<sup>2</sup>. The point in which the adverse stress initiated from is similar in both standard and steep cup inclination angle (0.65s). The similar trend between the contact area and the stress behaviour was observed under standard cup inclination angle at the beginning of stance phase up to the first peak load. However, the changes of contact area in the first 0.5s of the gait cycle is greater in steep cup inclination angle than the standard cup inclination angle as the contact area at the beginning of stance phase was under 50 mm<sup>2</sup> for all swing phase loads.

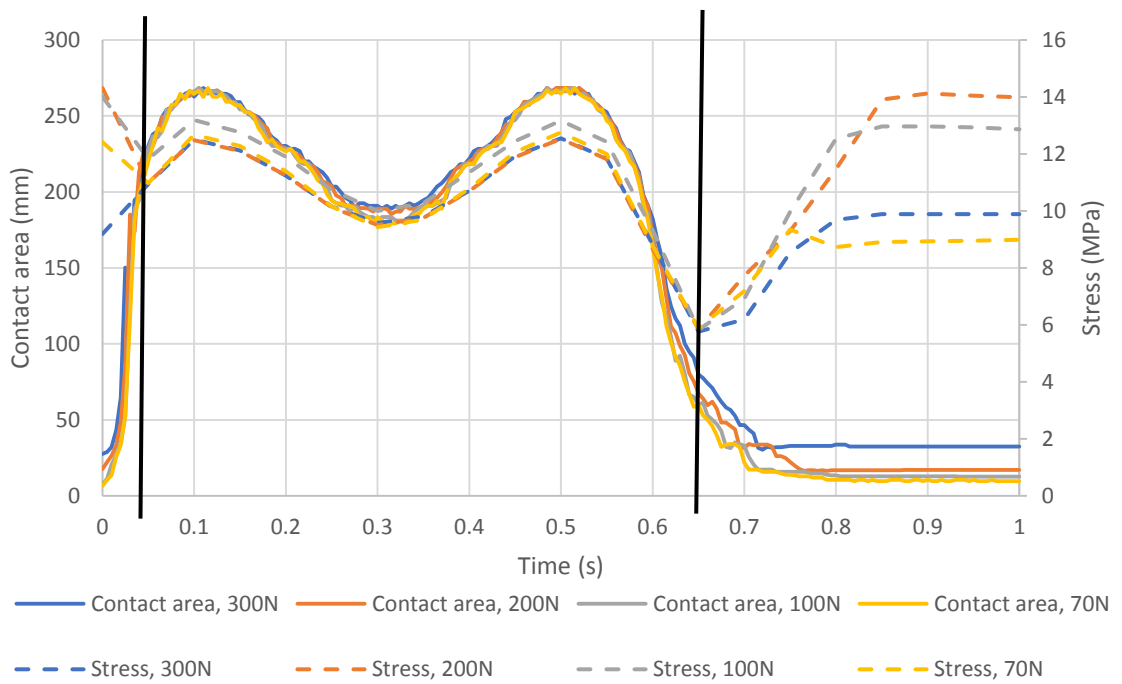


**Figure 5.16 Contact area and von Mises stress versus time in the analyses with 4mm translational mismatch level, various swing phase loads and steep cup inclination angle.**

### 5.3.3 Separation study

The relationship between the separation and the contact area resulted from the separation is shown in Figure 5.17. The contact area derived from the separation under 0.5mm varied especially in standard cup inclination angle. As it was defined in Chapter 4, the separation under 0.5mm doesn't result in edge loading. In both cup inclination angles, the contact area generally decreased as the separation increased (for over 0.5mm separations). However, the pattern of decreasing contact area (for separation higher than 0.5mm) can be clearly seen for the analyses under standard condition, and not in other conditions.

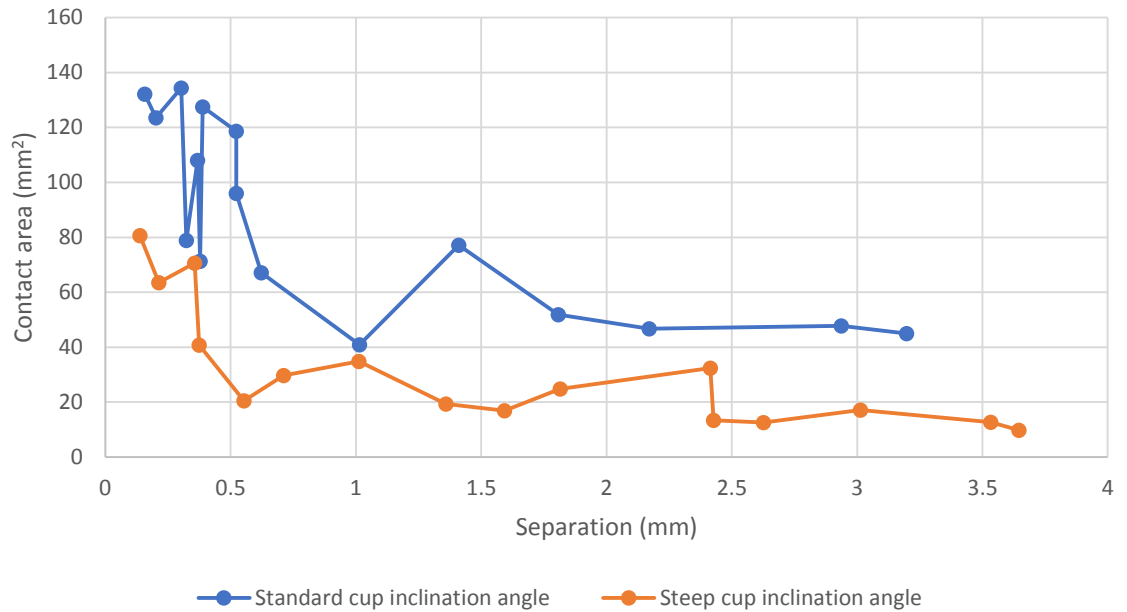


**Figure 5.17 Contact area at the maximum separation during the gait cycle under standard and steep cup inclination angle with all translational mismatch levels and swing phase loads.**

The other contact mechanics data such as contact pressure, compressive stress and von Mises stress cannot directly be compared to the separation value regardless of the condition taken as the swing phase load (Figure 5.18) and the translational mismatch level (consequently M/L force) affected these data. However, if the conditions are taken into consideration, higher translational mismatch level and higher swing phase load (in isolation) increased the maximum Von Mises stress, compressive stress and contact pressure. Moreover, it could be seen that the separation higher than 0.5mm also affect the mentioned parameters.

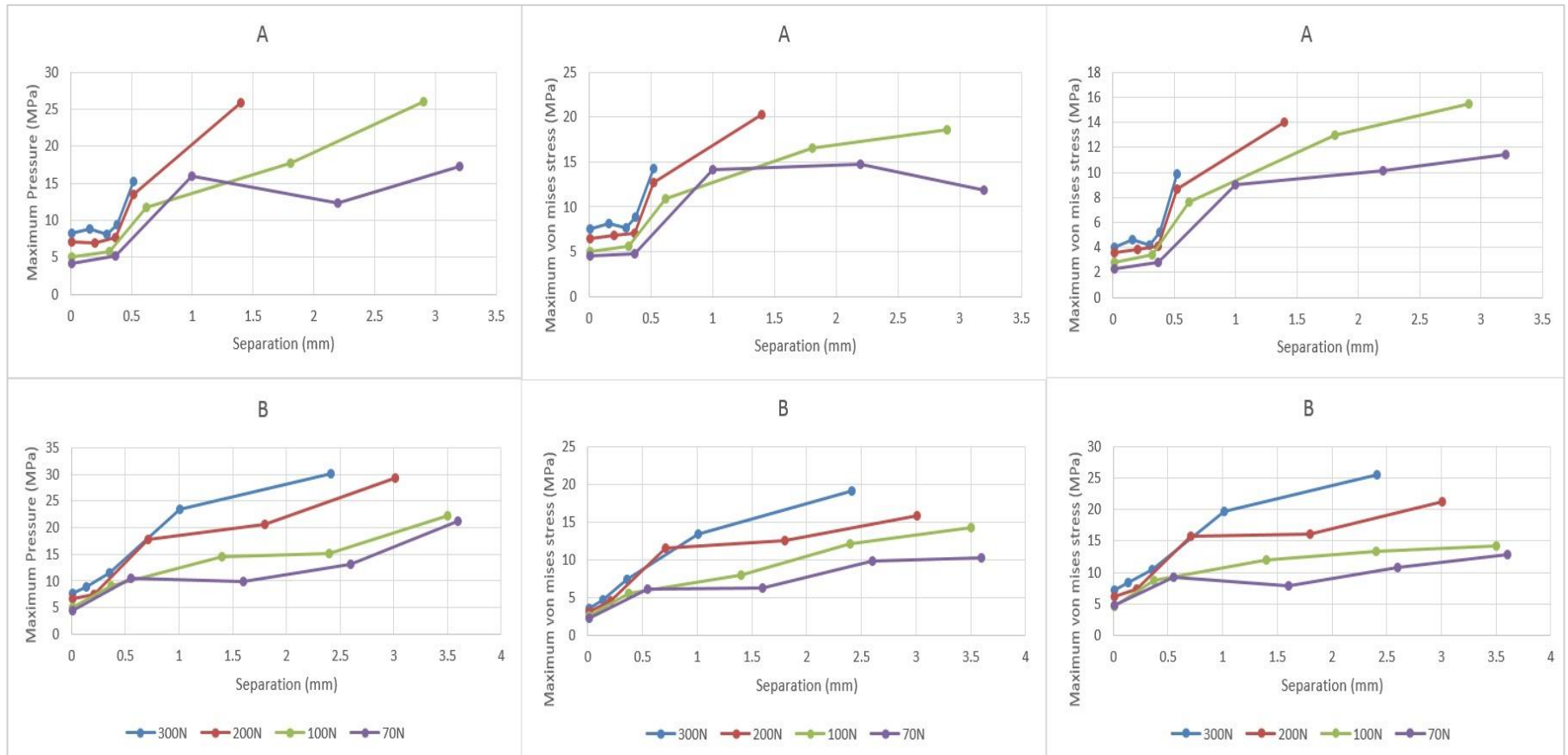


**Figure 5.18** The comparison of separation with von Mises stress, compressive stress and contact pressure. The analyses under standard cup inclination angle are presented as Plot A and the analyses under steep cup inclination angle is presented as Plot B

As Figure 5.19 represent, the plastic strain is initiated when the separation is higher than 0.6mm and 0.7mm in standard and steep cup inclination angle, respectively. The level of plastic strain increases as the separation level increases. In standard cup inclination angle, a linear relationship between separation and plastic was observed. However, the similar trend cannot be concluded in the analyses under steep cup inclination angle.

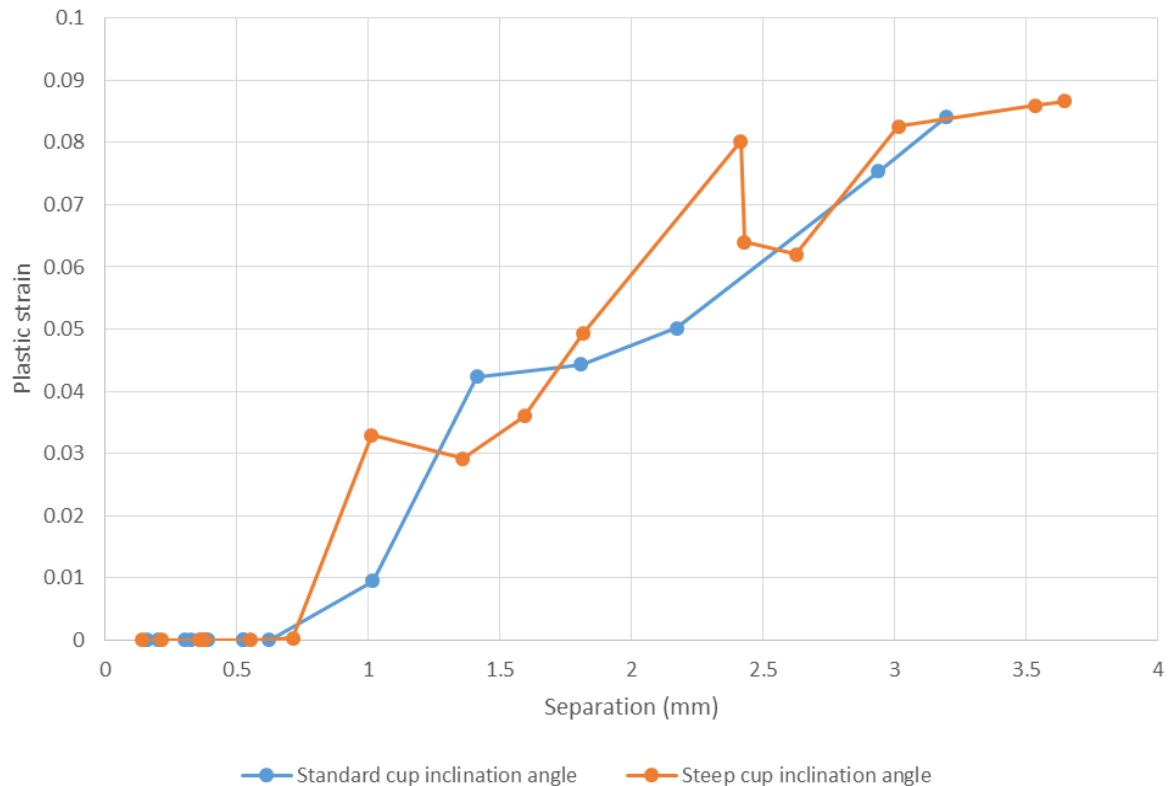
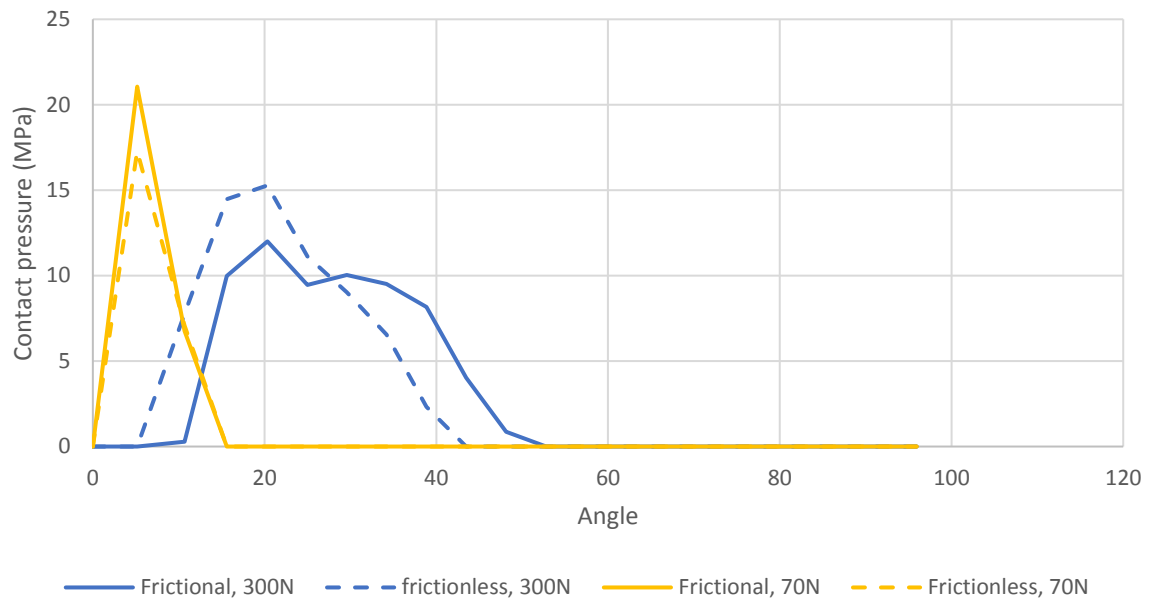


**Figure 5.19 The comparison of separation with plastic strain for both standard and steep cup inclination angles with all translational mismatch levels and swing phase loads.**

### 5.3.4 Friction

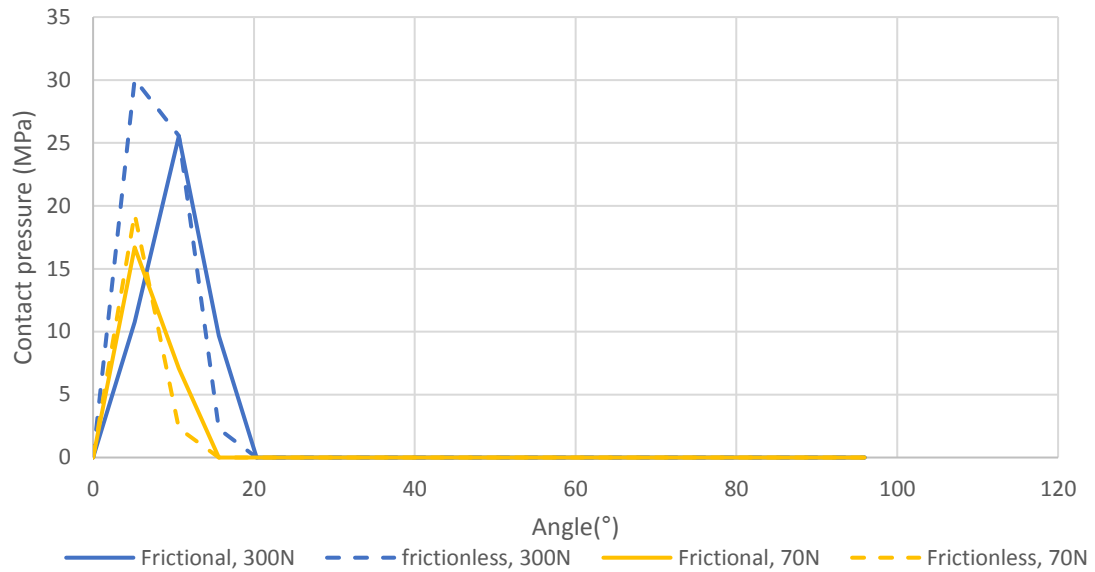
The effect of friction on contact mechanics was analysed. Figure 5.20 represents the nodal pressure along the line of symmetry with 0.1 coefficient of friction and no friction under steep cup inclination angle and various swing phase loads. The comparison of the two analyses only indicated a similar nodal pressure distribution position in 70N swing phase load and slightly different distribution in 300N swing phase load. However,

a difference in the peak nodal pressure was seen (4MPa difference). Moreover, the frictional analysis only increased the peak contact pressure in lower swing phase load (70N).



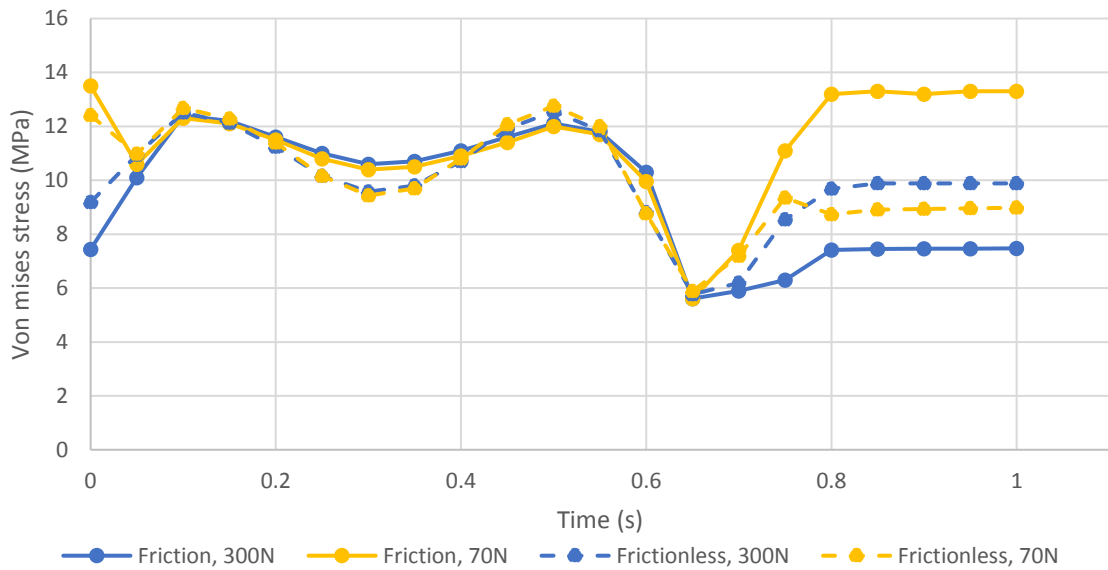
**Figure 5.20 Effect of friction on the contact pressure along symmetrical line under standard cup inclination angle, 300N and 70N swing phase load and 4mm translational mismatch level.**

The frictional analyses that were carried out under steep cup inclination angle resulted in the similar outcome in distribution (Figure 5.21). The correlation between the peak contact pressure and the swing phase load in the frictional and frictionless analyses was similar. In both swing phase loads, the friction between the contact surfaces decreased the peak contact pressure under steep cup inclination angle.



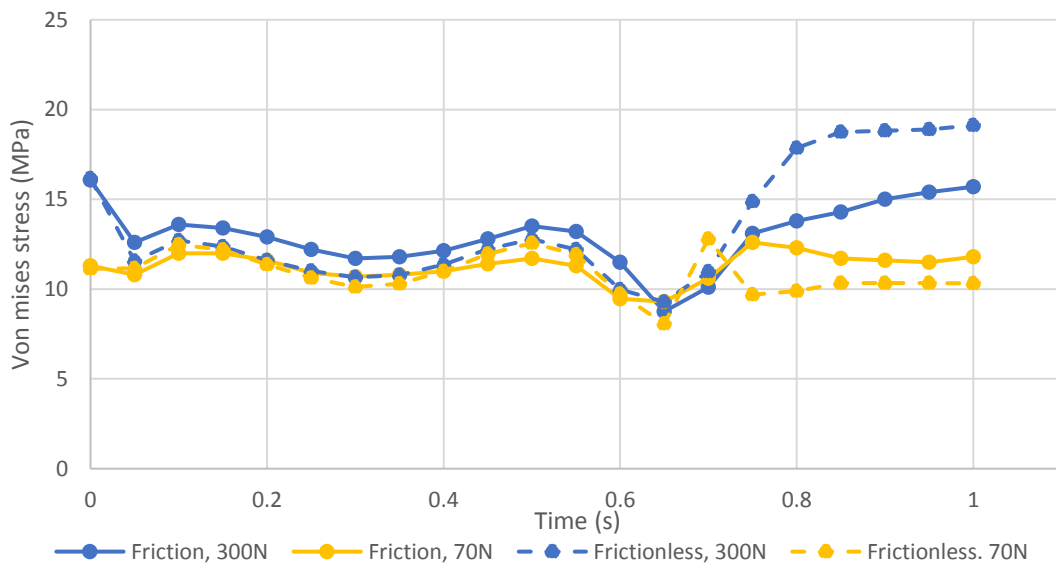
**Figure 5.21 Effect of friction on contact pressure along the symmetrical line under steep cup inclination angle, 300N and 70N swing phase load and 4mm translational mismatch level.**

Figure 5.22 represents the changes in the stress behaviour between the frictional and frictionless contact against the loading cycle in the analyses under standard cup inclination angle. Overall, the friction affected the stress changes during stance phase between two peaks for both conditions. However, the effect of friction on the stress during swing phase load was dependant on the swing phase load value. Lower stress value was found in the frictional analysis than the frictionless one whereas the lower swing phase load generated a higher stress during swing phase load than the frictionless analysis.



**Figure 5.22 Effect of friction on the analyses under standard cup inclination angle with the lowest (70N) and highest (300N) swing phase load. The figure represents the effect of friction on the von Mises stress during a gait cycle.**

The similar trend of the friction effect under standard condition was observed (Figure 5.23) in the analyses under steep cup inclination angle. Lower swing phase load negatively affected the stress values during the swing phase load under steep cup inclination angle.



**Figure 5.23 Effect of friction on the analyses under steep cup inclination angle with the lowest (70N) and highest (300N) swing phase load. The figure represents the effect of friction on the von Mises stress during a gait cycle.**

The friction had little effect on the compressive stress under steep cup inclination angle (Figure 5.24). However, conflicting results on the compressive stress was observed in different swing phase loads under standard cup inclination angle. Comparison of the frictional and frictionless analysis indicates that friction in low inclination angle resulted in a reduction in the compressive stress whereas higher swing phase load caused an increase in the compressive stress.

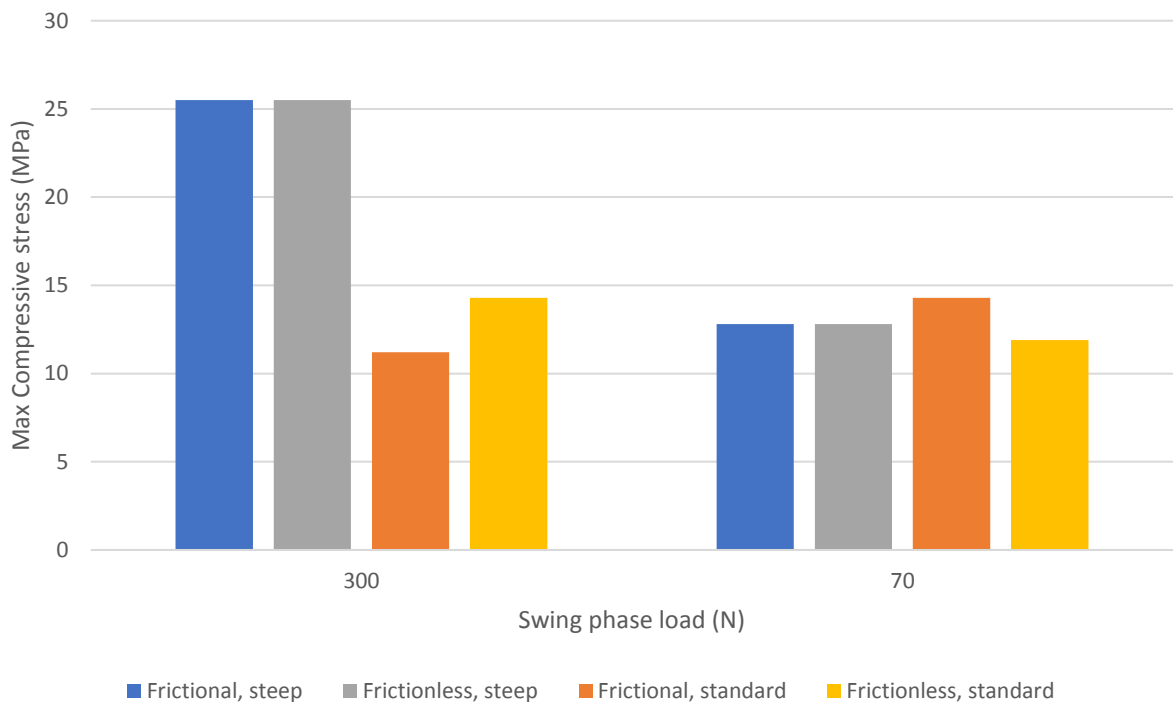


**Figure 5.24 The effect of friction on the compressive stress of the analyses. The friction coefficient of 0.1 was applied on the lowest (70N) and highest (300N) swing phase load and on the standard and steep cup inclination angle.**

Friction affected the contact area at the swing phase load and the magnitude of this effect depend on the cup inclination angle. As Figure 5.25 represents, friction decreased the contact area slightly in the steep cup inclination angle analyses. Although the friction effect on the contact area is not substantial, the reduction in contact area was more noticeable in standard cup inclination angle.

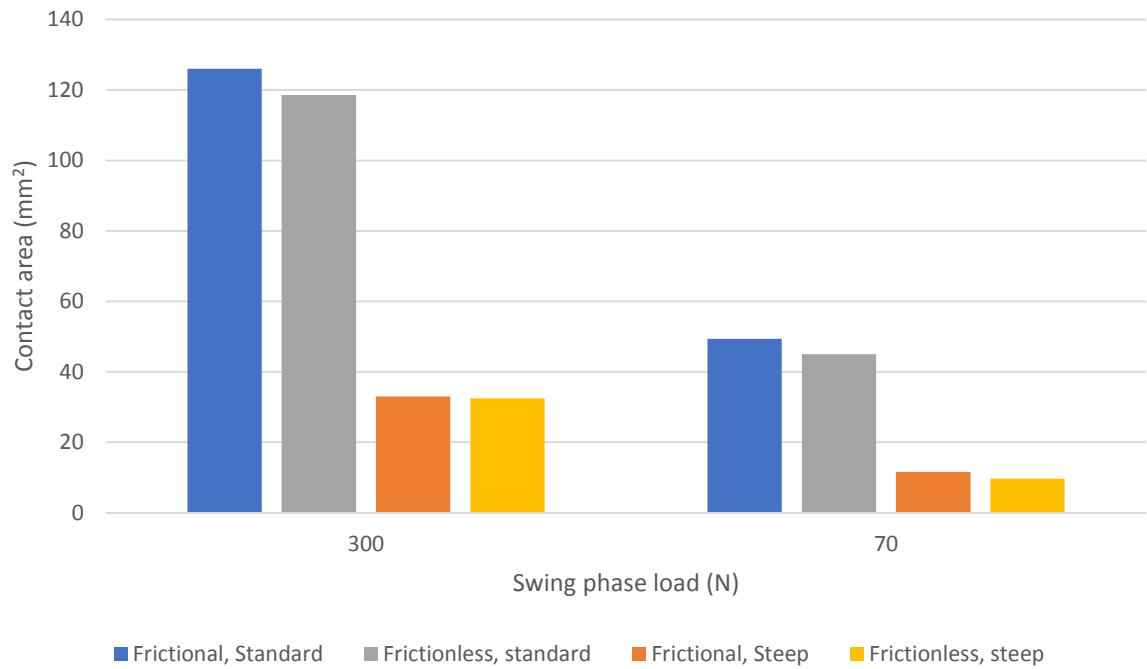


**Figure 5.25** The comparison of the contact area in the frictional and frictionless analyses. The friction coefficient of 0.1 was applied on the lowest (70N) and highest (300N) swing phase load and on the standard and steep cup inclination angle.

Although, friction slightly decreased the plastic strain of the conditions that were analysed, no substantial difference in plastic strain was observed for any of the cases (Figure 5.26).

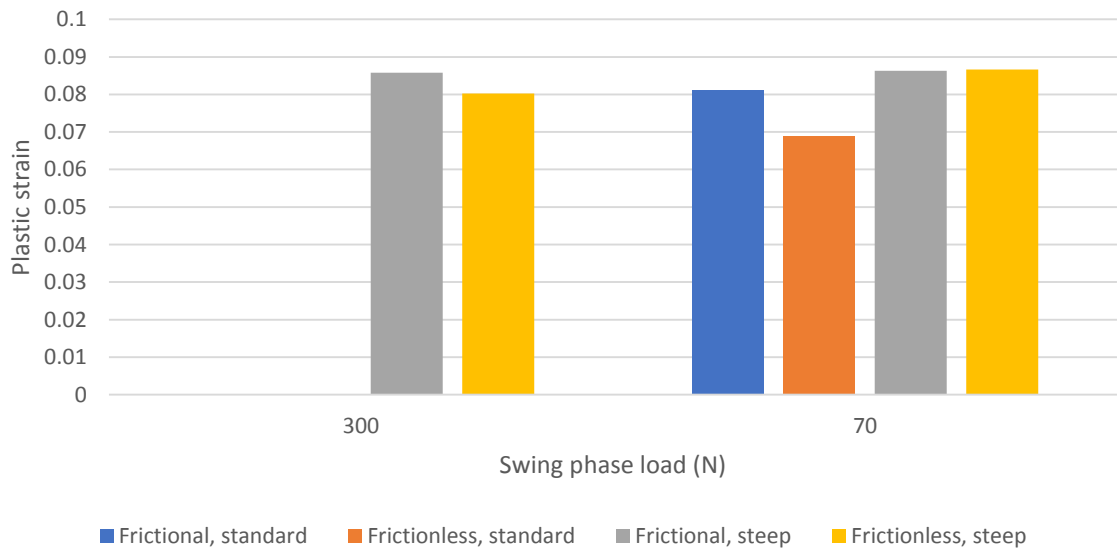


**Figure 5.26** The effect of friction on the plastic strain on the lowest (70N) and the highest (300N) swing phase load with 4mm translational mismatch level and on the standard and steep cup inclination angle.

## **5.4 Discussion**

Dynamic modelling of a THR under a load cycle provides a unique opportunity to predict and analyse the effect of various parameters describing the contact mechanics of the joint. These contact mechanics analyses produced a novel insight to understand the potential damage, fatigue and wear of the contact surfaces throughout the gait cycle under adverse conditions.

### **5.4.1 Contact behaviour due to the input parameters**

The pressure distribution in various mismatch levels indicated that the standard condition resulted in a concentric head and cup contact. The highest mismatch level caused the closest contact to the lateral edge in all the swing phase loads. Deviation from contact concentricity caused edge contact and therefore a substantially reduced contact area. The result of smaller contact area was a substantially higher localized contact pressure towards the edge. The highly localised pressure distribution, which could be an indication of the most damaged area, is observed more when the swing phase load is 70N, or 100N as compared to the 200N and 300N cases.

The comparison of the contact pressure behaviour in mismatch level variation for standard and steep cup inclination angle indicated that the edge contact pressure behaviour was observed in a greater number of cases when the cup inclination angle was steeper than standard cup inclination angle. The horizontal distance between the centre and the edge of the cup is less in the steep cup inclination angle cases than standard inclination angle cases due to lateral cup edge location. Consequently, the edge contact is more frequent in the cases with steeper cup inclination angle and the edge wear damage could potentially be higher for these cases.

## 5.4.2 Discussion of stress behaviour throughout gait cycle

Contact mechanics analysis within the gait cycle was also studied based on the level of stress that the cup undergoes. In the standard conditions, the stress variation followed the loading changes throughout the gait cycle. In the adverse conditions, edge loading and permanent deformation are multifactorial scenario occurrences and the effect of each input parameter is challenging to identify. Higher translational mismatch, steeper cup inclination angle and lower swing phase load all increased the separation level and occurrence of edge loading (Figure 5.27). A similar trend was observed in contact mechanics output.

| Standard cup inclination angle |                              |        |  |       |        |        |       |        |        |       |        |        |
|--------------------------------|------------------------------|--------|--|-------|--------|--------|-------|--------|--------|-------|--------|--------|
| Swing phase load               | Translational mismatch level |        |  |       |        |        |       |        |        |       |        |        |
|                                | 1mm                          |        |  | 2mm   |        |        | 3mm   |        |        | 4mm   |        |        |
| 300N                           |                              |        |  |       |        |        |       |        |        |       | Yellow |        |
| 200N                           |                              |        |  |       |        |        | Green | Yellow |        | Green | Yellow | Orange |
| 100N                           |                              |        |  | Green | Yellow |        | Green | Yellow | Orange | Green | Yellow | Orange |
| 70N                            |                              |        |  | Green | Yellow | Orange | Green | Yellow | Orange | Green | Yellow | Orange |
| Steep cup inclination angle    |                              |        |  |       |        |        |       |        |        |       |        |        |
| Swing phase load               | Translational mismatch level |        |  |       |        |        |       |        |        |       |        |        |
|                                | 1mm                          |        |  | 2mm   |        |        | 3mm   |        |        | 4mm   |        |        |
| 300N                           |                              |        |  |       | Yellow |        | Green | Yellow | Orange | Green | Yellow | Orange |
| 200N                           |                              |        |  | Green | Yellow |        | Green | Yellow | Orange | Green | Yellow | Orange |
| 100N                           |                              | Yellow |  | Green | Yellow | Orange | Green | Yellow | Orange | Green | Yellow | Orange |
| 70N                            | Green                        | Yellow |  | Green | Yellow | Orange | Green | Yellow | Orange | Green | Yellow | Orange |

**Figure 5.27** The correlation between the input parameters and edge loading, adverse stress behaviour and plastic strain occurrence. The green, yellow and orange cells represent the edge loading, adverse stress and plastic strain occurrence for various swing phase loads, respectively

The stress behaviour during the stance phase is dictated by the loading however the stress behaviour during the swing phase is affected by various factors. During swing phase, in some cases, the maximum stress initially decreases, increases and then becomes constant. There are two factors that contribute to such stress behaviour:

- 1) The resultant force that is influenced by both the swing phase load (axial load) and the translational mismatch level which affects the medial-lateral force (by varying the compression of the spring). As the axial load decreased to the swing phase load, the contact area moved towards the edge of the cup. However, the contact area is still in the 'safe support zone' to the point that the stress level is decreased to the minimum. This suggests that up to this point of the cycle changes in contact area are negligible, so the decrease in stress level corresponded to the decrease in axial loading. After this point of the cycle, the contact area started being in the 'crucial region' where the contact area became significantly smaller. Consequently, the stress raised again as the axial loading is constant. The lower swing phase load and the higher translational mismatch level drives the cup towards the lateral edge where the contact zone was significantly smaller.
- 2) The cup inclination angle plays an important role in the contact zone as the location of the lateral edge varied by the inclination angle. It was described that the travelling distance of the head to the lateral cup edge is less in steeper cup inclination angle (Chapter 4). Under steep cup inclination angle, the translational mismatch level of 3mm and 4mm caused permanent deformation regardless of the swing phase load. The permanent deformation for the same translational mismatch levels (3mm and 4mm) under standard cup inclination angle did not occur under higher swing phase load than 200N. In the standard cup inclination angle case the larger contact area associated with the 45° cup inclination angle reduced the severity of the contact mechanics, such as stress and permanent deformation, due to the location of the lateral edge and the resistance to the lateral movement.

Although a high load level was observed on the rim at the beginning of stance phase where the separation was greater than 0.5mm, no substantial contact output such as stress level was observed during this time duration. The stress level actually decreased initially as the contact area increased dramatically from the start of the stance phase to the first peak load. Therefore, most of the load is distributed in the higher contact area and the higher contact area potentially overcame the high load on the rim.

The initial and final stress behaviour of each cases in adverse conditions seemed to be similar. In fact, in some of the conditions with the 4mm mismatch level, the stress value is initiated in a substantially higher value that caused an unexpected stress variation as the axial load reached its first peak. In the extreme conditions, the initial stress value is higher than the stress generated at the peak load due to the changing contact area. As the load increased rapidly to the first peak, it could have a significant impact on the cup material behaviour due to the rapid sliding and the high stress values.

Dynamic modelling enabled the analysis of the time that the THR is under adverse loading conditions as a proportion of the total time for one cycle. The maximum von Mises stress throughout the gait cycle indicated that the area in which the adverse stress level occurred experienced this stress for over 35% of the gait cycle. Moreover, the severity of the adverse stress behaviour is affected by the level of input parameters. From a failure perspective, it could be concluded that under the cyclic loading, the conditions that show a higher severity of the adverse stress behaviour are likely to have a greater risk of earlier failure due to the large stress level within the zone.

### 5.4.3 Failure Prediction

There are a number of failure theories such as shear strain energy theory (von Mises) and maximum principal stress theory that are applicable for ductile or brittle materials. In FE packages, the input yield stress is based on the von Mises stress value. Therefore the von Mises stress failure criterion has been used as the failure prediction in many previous studies (Mak and Jin, 2002; Korhonen *et al.*, 2005; Hua *et al.*, 2014). If the von Mises stress in the model exceeds the yield stress, permanent deformation of the material occurs. When this is applied to THR, after the yield stress is reached the material deforms permanently and changes the shape of the edge of the cup. The von Mises stress reported by the model after the failure can be unreliable, as the properties of the deformed component have changed and Hooke's law no longer applies. Von Mises stress is predominantly driven by shear stresses, however it still considers the principal stress within the calculation. It was shown that the maximum compressive stress is substantially higher than the value of the von Mises stress in all the conditions which indicates the compressive stress dominated the stress behaviour. There may be an argument to consider other failure theories for this reason.

One of the main reasons for UHMWPE failure in THR is reported to be fatigue (Kurtz, 2004; Partridge, 2016). Fatigue damage is caused by repeated cyclic loading that is not fully considered in this study. However, some predictions can be made based on the overall stress behaviour. The higher plastic strain was observed more for the conditions with higher edge loading and due to the high concentrated stress in the edge area. Further cyclic loading is expected to weaken the material properties in this region and potentially cause a failure below the yield stress. With a single cycle the type and

severity of failure cannot be predicted. However, the model predicts a high stress from the centre of the cup to the lateral edge. Therefore, this is assumed to be the main area of the damage, and experimental data showed increased wear and deformation in this region. The worn and damaged area on the cup that is shown in Figure 5.28 is for the experimental testing under 70N swing phase load. Figure 5.28 indicated that the higher translational level and steeper cup inclination angle firstly increases the level of deformation and wear, and secondly affected the lateral edge of the cup. Although it is not possible to distinguish between the level of wear and deformation in the experimental study, higher translational mismatch and/or steeper cup inclination angles increases the stress on the edge which would be expected to cause more damage over time. The direct comparison of the experimental and computational damage for this specific swing phase load (70N) is a challenging task as the computational study shows higher separation level (Chapter 4) than the experimental study which can directly affect the stress concentration and consequently the predicted damaged area.

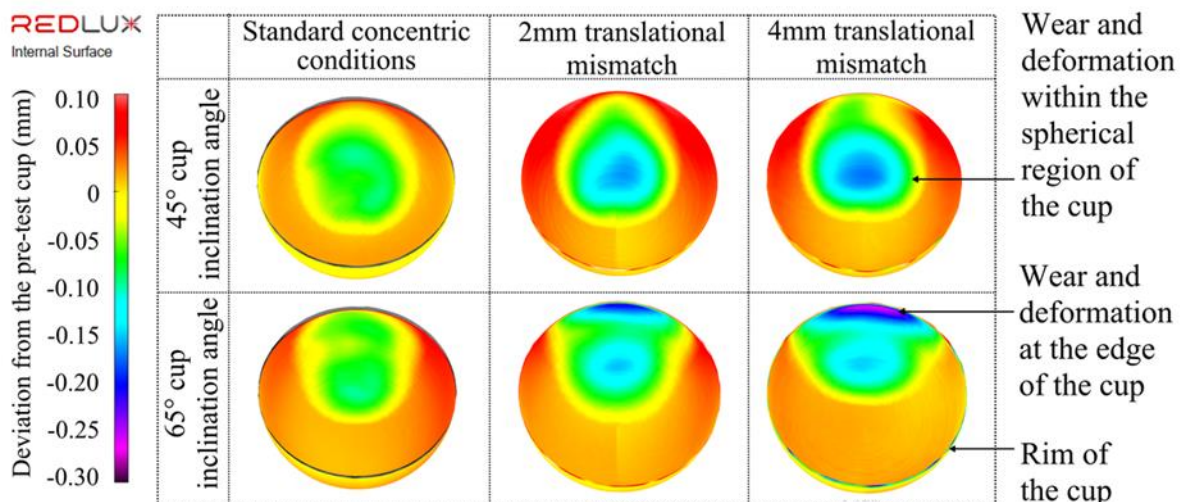


**Figure 5.28 The worn and deformed area of the UHMWPE cup under 0mm, 2mm and 4mm translational mismatch level, standard and steep cup inclination angle and 70N swing phase load. The worn area indicates the worn and deformation on the inner surface of the liner (Appendix)**

#### **5.4.4 The correlation between separation and contact mechanics**

The analyses all indicated higher level of separation resulted in higher stress, contact area and plastic strain values. This conclusion is supported by a previous study on the effect of dynamic separation on the contact mechanics of THR statically (Hua *et al.*, 2014). However, their static FE model studied a lower level of separation than this study. The correlation between the separation and contact mechanics was investigated and it was indicated that the contact area at the swing phase load decreased substantially when the separation level was higher than 0.5mm under standard cup inclination angle. However, the border of the separation level for higher contact area was slightly less (0.4mm) under steep cup inclination angle. A similar trend was seen between the separation level and the stress values. This indicated the dynamic separation that is required to noticeably affect the contact mechanics output is less in the steep cup inclination angle. The higher occurrence of plastic strain in the 65° cup inclination angle supported the conclusion that more cases are potentially damaged under comparable conditions.

#### **5.4.5 Friction effect**

The effect of friction was highest when the contact mechanics of standard cup inclination angle and lower swing phase load were observed. The stress level, contact pressure and plastic strain all increased when friction was added into the model. The high M/L load in 70N condition drove the contact area towards the edge of the cup, where the geometry of the edge under the standard cup inclination angle forms a locking mechanism (compared to the steeper cup inclination angle where the lateral movement is easier) and a resistance to the movement to the edge. Furthermore, the

resistance force formed by the friction affected the stress level on standard cup inclination angle with low swing phase load condition more than the other conditions tested. Friction did not play an important role in terms of the dynamic output of the model (separation). However, the contact mechanics of the model can be altered by the friction in the bearing surfaces.

#### **5.4.6 Model improvements**

It was shown in the previous chapter that the developed model is sensitive to the input parameters under dynamic conditions. The contact mechanics studies of the model also indicate that the variation in input parameters affects the contact behaviours, as hypothesised. However, this developed model could be improved for a more efficient and accurate contact output. As an example, no mesh sensitivity analysis was carried out when edge loading occurred as the mesh sensitivity was done under standard condition during the model development. Therefore, a change of the value of the contact mechanics output could be expected if this were implemented. However, the trend of the contact changes is not expected to change as the same meshing ratio was configured for all the conditions. Moreover, as presented in chapter 2, the output was not affected by the refinement when the same meshing ratio on both contact surfaces was created. Therefore, as the same meshing ratio is applied to the contact surfaces in all models, only slight changes in the magnitude of the outputs is expected.

In FE modelling, the material model plays a very important role in contact mechanics behaviour. In this study the material behaviour is assumed to be elastic-plastic and this material behaviour is used in the THR model previously (Hua *et al.*, 2014), however, this material model is mostly suitable for metals that have insubstantial plastic strains.

There are previous studies investigating the most suitable material for modelling UHMWPE and it was concluded that the hybrid material model can predict the UHMWPE behaviour more accurately than elastic-plastic model (Bergström, Rimnac and Kurtz, 2005). Furthermore, it was shown the hybrid material model can predict failure methods by using chain stretch theory, which studies the breakage of the polymer chains in the material. Therefore, if a hybrid material model is assigned to the UHMWPE, better predictions of the contact mechanics can be made. However, the effect of the hybrid material model on the running time and efficiency of the FEA should be examined.

## **5.5 Key points**

- As the experimental and computational simulations both propose an agreement in dynamic and contact mechanics outcomes, it could be concluded that the developed methodology could be a great tool to predict the device sensibility under various conditions.
- The contact mechanics behaviour is dependent on the following combination of parameters: geometric changes caused by changes in cup inclination angle; and the resultant force on the cup, which is affected by the swing phase load and the translational mismatch level.
- Higher translational mismatch level, lower swing phase load and steeper cup inclination angle resulted in a reduced contact area, higher adverse stress occurrence and higher permanent deformation on the edge of the cup.

- The THR is better to be implanted in the standard cup inclination angle as the indications of the damage were observed in the steep cup inclination angle conditions.

## **Chapter 6 Final discussion and future work**

This chapter focuses on the overall model development, the potential consequences and the limitations of the developed method. Furthermore, the possible application of this method in the future is described.

### **6.1 Model development**

The ultimate aim of this project was to develop a computational model to simultaneously compute the dynamic and contact mechanics of the THR under adverse conditions. The developed model can analyse dynamic contact mechanics patterns throughout the gait cycle, which would be impossible using current static modelling techniques. The immediate implication of this is the ability to study how the separation is driven dynamically by the effect of external factors. Additionally, the contact mechanics can be studied concurrently. This computational model can be used as a tool to complement experimental observations and provide data that is unavailable experimentally, such as the THR contact mechanics behaviour throughout one loading cycle, resulting in analysis through various load and contact conditions. With some additional development, this computational model could be modified to suit the applications within research, industry or as a preoperative tool.

The development of explicit THR models is challenging as it has not been explored until recently for use in preclinical testing. The integration of the dynamic and contact mechanics under adverse conditions can cause model instability as a result of edge loading. Therefore, it was important to first build a basic model and then gradually add sophistication such as loading profiles and detailed geometry.

The model was set to mimic a station of Leeds II hip simulator that has been used to examine THR wear characteristics under adverse conditions (Al-Hajjar *et al*, 2010). The development is fully described in Chapters 2 and 3. Not all the experimental aspects of this simulator are necessary to replicate the separation or the contact mechanics, so some assumptions and simplifications can be made to reduce the time of the analysis, increase the model reliability, and aid troubleshooting. The most crucial experimental component that was implemented into the computational model was the spring, which created the separation between the contact surfaces. The spring has a major effect on the outputs and oscillations in the model and one of the challenges was to ensure appropriate damping for specific cases, as each of the input factors and their interactions affected those damping conditions.

The next step of the development was the validation of the *in silico* dynamic outputs against the *in vitro* studies. The comparison demonstrated similar levels of separation and contact mechanics changes in both experimental studies and computational models. However, future modifications of this model could potentially provide a more reliable outcome compared to the experimental studies as will be discussed below. Furthermore, the validation of the dynamic data increases the reliability of the contact mechanics outputs as the contact mechanics related parameters cannot be measured directly from *in vitro* studies.

The advanced developments of the model could be dependent on the applications of it. The current model mimics the general THR behaviour of the *in vitro* loading, geometry and positioning of the stations of the hip simulators. Therefore, if the outcome of interest is the overall THR *in vitro* performance under numerous conditions, the computational model inputs can be based on the experimental set up. If the model is

used to study the effect of other factors on the THR performance, then the modifications can be done on the model that is already developed. In addition, if the model was used to study patient specific outputs, then the patient's data such as the bone anatomy, axial loading and tissue behaviour would also need to be implemented in the model for a more realistic output. It should be noted it is currently challenging to discover the patient's specific data as there are not many patient related data sets published due to the difficulty in measuring the patient's data.

Implementation of an anterior-posterior spring to mimic various hip tissues behaviour could be the next step to replicate a more *in vivo* representative situation in the computational model. The hip joint is supported well by iliofemoral, pubofemoral, and ischiofemoral ligaments and they are surrounded by rectus femoris muscles for better stability (Tortora and Nielsen, 2009). The anterior-posterior spring could be a useful tool to implement different soft-tissue scenarios.

## **6.2 Discussion of findings**

The dynamic behaviour and contact mechanics of the CoP THR under adverse conditions were analysed in Chapters 4 and 5. It was concluded from the analyses that a higher translational mismatch level, steeper cup inclination angle and lower swing phase load could all increase the dynamic separation. The same trend was seen in experimental studies (Ali *et al.*, 2016). However, the magnitude of the dynamic output was not always similar which could be due to the various reasons such as damping conditions, friction and angular movements. The computational model clearly distinguished the effect of each input on the model dynamically. Therefore, the model can be used to understand the effect of variety of parameters on the dynamic aspect of the model.

A similar trend to the separation was seen in stress behaviour on the cup. If the adverse conditions caused dynamic separation of more than 0.5mm in the standard cup inclination angle condition or 0.4mm in the steep cup inclination angle condition, then an adverse 'in cycle' stress behaviour was produced on the edge of the cup where the contact occurred. As the dynamic separation increased, high stress occurred on the edge and consequently the plastic strain increased.

Such contact behaviour could potentially be an indication of the long-term THR performance *in vitro* and *in vivo*. *In vitro* studies previously indicated that the increase in dynamic separation primarily affects the wear rate of the device (Al-Hajjar et al, 2013, Williams et al 2009). However, it is not experimentally possible to know if the damage, especially on the edge, is wear or other form of damage. As the *in silico* analyses suggest, plastic deformation occurred at the edge under edge loading conditions. Therefore, cyclic loading under these edge loading conditions could even produce a higher deformation and more substantial damage such as crack propagation that could potentially lead to fatigue of the cup in long term. The lack of lubrication and high contact friction in UHMWPE cups that was reported from the explants (Burger et al, 2007) increase the possibility of the greater damage in these high stress regions.

In the adverse conditions, edge loading and permanent deformation are multi scenario occurrences and the occurrence of them depends on the axial loading, M/L loading and the cup positioning. Although all the variation in the input parameters, translational mismatch level, cup inclination angle and swing phase load, affected the contact mechanics outputs, a safe zone of positioning could be suggested that does not activate any adverse behaviour. Translational mismatch of 1mm and 2mm rarely resulted in adverse behaviour under any swing phase load. The cup inclination angle of 45°

performed as a resistance to M/L movement and edge contact. Moreover, higher swing phase load than 200N reduced the number of cases in which adverse contact behaviour was observed.

### **6.3 Limitations**

The methodology presented in this study is the first step, further progress will allow a more thorough model to be developed. Therefore, assumptions were made with respect to the *in vitro* input during the development that could potentially lead to discrepancies between the two responses. As an example of the simplifications, neglecting the rotational movement of the device namely flexion/extension, abduction/adduction and internal/external rotation of the cup. The experiments that were carried out in house indicated that the dynamic separation can be affected by the rotational movement. However, the rotational movement i.e. abduction/adduction have no substantial impact on the magnitude of the separation.

Although the model was validated against *in vitro* data (Chapter 4), the current model possesses limitations. The initial limitation is the accuracy of the result as edge loading occurs. The mesh sensitivity analysis that were carried out on the model was done under standard axial loading with no dynamic separation during the initial model development. The mesh sensitivity analyses (Chapter 2) suggested that the equivalent meshing ratio on the contact surfaces results in convergence regardless of the element size. There is a possibility that the contact mechanics performance of the device could not be the most accurate and the magnitude of the contact outputs such as contact area, stress and consequently the plastic strain could be varied as the contact zone changes from standard condition contact zone. A refined mesh could produce more precise contact pressure distribution on the edge. However, the overall contact mechanics

behaviour is unlikely to be affected. As an example, the refined mesh analysis will produce the adverse stress behaviour that was observed during the swing phase load. However, the mesh refinement is expected to maintain the consistency in the stress values.

The contact output is affected by the material model that represents the material behaviour of the components. In this study the elastic-plastic material model that has been used previously (Lin et al, 2010; Hua et al, 2014) was used for the UHMWPE. UHMWPE has complex material properties that the loading and the environmental conditions can influence (Sobieraj and Rimnac, 2009). A study has been carried out to examine the most precise material models to represent UHMWPE behaviour including the prediction of failure and this has shown that the hybrid material model in combination with the chain stretch failure criteria that predicts the critical chain stretch in the amorphous polymer chains, could produce the most accurate UHMWPE behaviour computationally (Bergstrom et al, 2005). However, the effect of more complicated material models on the running time of the analysis would need to be examined.

#### **6.4 Possible applications and future work**

Despite the simplifications that were assumed in this model, the dynamics and contact mechanics outputs were proven to be sensitive to any input parameters that were implemented. Consequently, the developed model could potentially be used to estimate the overall THR behaviour under various conditions in several fields such as research, industry and preoperative planning. The potential applications of the model in the mentioned fields are discussed below.

**Research:** Many factors such as head size, soft tissue tension, material, cup version angle, design, clearance, medialized cup, stem subsidence, kinetic and kinematics can affect the separation. To test the potential factors that cause dynamic separation *in vitro*, the hip simulators need to be prepared and developed for each specific test that could potentially be very costly and time consuming. Therefore, a computational tool that produces an insight of THR behaviour due to the input parameters can help to:

1. Specify the severity of the effect of each factor (or the combination of factors) on the dynamics and contact mechanics of the THR.
2. Prioritize the *in vitro* testing of the factors based on their effects.

The developed model has the ability to study the effect of input variation on the THR in a shorter time and with less cost than *in vitro* testing. Therefore, this model could be used as a pre-testing *in vitro* device to focus on the most crucial factors that detrimentally affect the THR performance.

**Industry:** The model can be used as a preclinical testing tool to determine the device behaviour from different aspects such as the components behaviour, *in vivo* performance and implant design such under edge loading condition. The potential areas to focus on are as follows:

1. Material properties: If the focus is on ceramic-on-polyethylene, different polyethylene specifications that are varied during manufacturing within the same bearing and design can be tested to rationalize the most suitable material properties.
2. Bearing materials: this study focuses on the hard-on-soft bearing contacts especially ceramics-on-polyethylene bearings. However, hard-on-hard bearing contact performs differently because of the reduction in deformation of the bearings due to

higher Young's modulus of the materials. Various bearing materials can be tested in the model.

3. Implant design: Testing a new hip implant design could be very costly for the company. Hence, this computed model can be used to study the new implant design behaviour under adverse conditions. The potential implant criteria that could influence the THR behaviour are the factors that are mostly associated to the edge loading such as inner cup radius, radial clearance, head and liner size, coverage angle, rim radius and surface roughness.
4. Locking mechanism: The primary purpose of this model development was to determine the separation caused between the head and the cup. The next potential criteria could be to determine the effect of separation on the locking mechanism between the polyethylene cup and the metal shell. The Pinnacle acetabular cup consists of anti-rotational devices (ARDs) on the outer surfaces that fits in the barbs designed on the metal shell to prevent rotation of the cup. These ARD features could be examined although the features would increase the level of meshing complexity and require the definition of another interaction which could substantially increase the running time of the analysis and consequently, the cost of the analysis. Moreover, the effect of the cup supporting component features (metal shell) such as the metal shell edge thickness could be studied to understand if the shell specification can influence the occurrence and severity of edge loading. Furthermore, an optimum ratio of the shell and liner thickness could be studied to prevent severe edge loading.
5. Dislocation: In the worst case, subluxation of the head can cause spinning out of the cup which leads to impingement of the cup inner surface with the stem neck. This

event causes deformation of the cup edge surface and has an impact on the ARDs.

This worst case scenario could be tested on the bearing combination to evaluate the likelihood of failure.

**Preoperative planning:** This model could be a helpful preclinical tool to understand the effect patient specific factors as much as the components specifications. The model could be used to understand the behaviour of the THR based on positioning of it before implantation to the patient. As each patient has a specific hip and femur anatomy, the model can indicate in which surgical positioning, the dynamics and contact mechanics behaviour of the implant is less likely to be affected based on the patient's anatomy. Therefore, variation in components positioning such as inclination angle of the cup, version angle of the cup, head/stem ratio and contact bearing sizes could be examined before the device is implanted. Although the running time of this analyses are long for pre-operative planning, the method could be a helpful tool for the complicated hip replacement positioning.

## **6.5 Conclusion**

In conclusion, this model provides valuable information on the dynamic and contact mechanics of the THRs that could allow understanding the source of THR weaknesses under adverse conditions. The developed method is the first computational model which can predict the separation and interaction output as a result of input parameters. The developed model is fit for the desired application in this study while further improvements can be done based on the specific purposes. As coupling of the dynamics and contact mechanics of THRs is an innovative and novel approach to understand the THR performance in depth, this study effectively proves the concept of the method that was applied to the computational model. The model is a functional tool for research in

implant designs, implant types, surgical pre-operative positioning and patient specific implant performance. This is the most applicable method to analyse the hip implants in a clinical and experimental environment that is cost and time effective.

## Chapter 7 Bibliography

Abaqus 6.12 Documentation (2012). *Dassault Systèmes*. Available at :  
<http://abaqus.software.polimi.it/v6.12/index.html>

Abaqus 6.14 Documentation (2014). *Dassault Systèmes*. Available at :  
<http://abaqus.software.polimi.it/v6.14/index.html>

Affatato S., Leardini W., Zavalloni M. (2006) Hip Joint Simulators: State of the Art. In: Benazzo F., Falez F., Dietrich M. (eds) *Bioceramics and Alternative Bearings in Joint Arthroplasty*. Ceramics in Orthopaedics. Washington D.C.: Steinkopff.

Affatato, S., Spinelli, M., Zavalloni, M., Mazzega-Fabbro, C. and Viceconti, M. (2008) 'Tribology and total hip joint replacement: Current concepts in mechanical simulation', *Medical Engineering and Physics*, 30(10), pp. 1305–1317. doi: 10.1016/j.medengphy.2008.07.006.

Affatato, S., Torrecillas, R., Taddei, P., Rocchi, M., Fagnano, C., Ciapetti, G. and Toni, A. (2006) 'Advanced nanocomposite materials for orthopaedic applications. I. A long-term in vitro wear study of zirconia-toughened alumina', *Journal of Biomedical Materials Research Part B: Applied Biomaterials*, 78B(1), pp. 76–82. doi: 10.1002/jbm.b.30462.

Al-Hajjar, M., Fisher, J., Tipper, J. L., Williams, S. and Jennings, L. M. (2013) 'Wear of 36-mm BIOLOX (R) delta ceramic-on-ceramic bearing in total hip replacements under edge loading conditions', *Proceedings Of the Institution Of Mechanical Engineers Part H- Journal Of Engineering In Medicine*, 227(H5), pp. 535–542. doi: 10.1177/0954411912474613.

Al-Hajjar, M., Leslie, I. J., Tipper, J., Williams, S., Fisher, J. and Jennings, L. M. (2010)

'Effect of cup inclination angle during microseparation and rim loading on the wear of BIOLOX delta ceramic-on-ceramic total hip replacement', *Journal of Biomedical Materials Research - Part B Applied Biomaterials*, 95 B(2), pp. 263–268. doi: 10.1002/jbm.b.31708.

Ali, M., Al-Hajjar, M., Jennings, L. M. and Fisher, J. (2016) 'Variations in Component Positioning Leading to Dynamic Separation and Edge Loading Influences the Deformation and Wear of Metal-on-Polyethylene Hip Replacement Bearings', in *ORS*. Available at: [http://www.imbe.leeds.ac.uk/news/documents/ORS2017Web/Poster\\_1032\\_MA\\_OR2017.pdf](http://www.imbe.leeds.ac.uk/news/documents/ORS2017Web/Poster_1032_MA_OR2017.pdf).

Bachus, K. N., DeMarco, A. L., Judd, K. T., Horwitz, D. S. and Brodke, D. S. (2006) 'Measuring contact area, force, and pressure for bioengineering applications: using Fuji Film and TekScan systems.', *Medical Engineering & Physics*, 28(5), pp. 483–8. doi: 10.1016/j.medengphy.2005.07.022.

Baker R (2013) *Measuring walking: a handbook of clinical gait analysis*. London: Mac Keith Press.

Baldwin, M. A., Clary, C., Maletsky, L. P. and Rullkoetter, P. J. (2009) 'Verification of predicted specimen-specific natural and implanted patellofemoral kinematics during simulated deep knee bend', *Journal of Biomechanics*. Elsevier, 42(14), pp. 2341–2348. doi: 10.1016/j.jbiomech.2009.06.028.

Barbour, P. S. M., Stone, M. H. and Fisher, J. (1999) 'A hip joint simulator study using simplified loading and motion cycles generating physiological wear paths and rates', *Proceedings of the Institution of Mechanical Engineers, Part H: Journal of Engineering in Medicine*, 213(6), pp. 455–467. doi: 10.1243/0954411991535068.

Bargar, W. L., Bauer, A. and Börner, M. (1998) 'Primary and revision total hip replacement using the Robodoc system.', *Clinical Orthopaedics and Related Research*, (354), pp. 82–91.

Bartel, D. L., Burstein, a H., Toda, M. D. and Edwards, D. L. (1985) 'The effect of conformity and plastic thickness on contact stresses in metal-backed plastic implants.', *Journal of Biomechanical Engineering*, 107(3), pp. 193–9. doi: 10.1115/1.3138543.

Bergmann, G. *et al.* (2001) 'Hip forces and gait patterns from routine activities', *Journal of Biomechanics*, 34, pp. 859–871. doi: [http://dx.doi.org/10.1016/S0021-9290\(01\)00040-9](http://dx.doi.org/10.1016/S0021-9290(01)00040-9).

Bergström, J. S., Rimnac, C. M. and Kurtz, S. M. (2005) 'Molecular chain stretch is a multiaxial failure criterion for conventional and highly crosslinked UHMWPE', *Journal of Orthopaedic Research*, 23(2), pp. 367–375. doi: 10.1016/j.orthres.2004.08.014.

Besong, a a, Lee, R., Farrar, R. and Jin, Z. M. (2001) 'Contact mechanics of a novel metal-on-metal total hip replacement.', *Proceedings of the Institution of Mechanical Engineers. Part H, Journal of Engineering in Medicine*, 215(6), pp. 543–548. doi: 10.1243/0954411011536145.

Blumenfeld, T. J., Glaser, D. A., Bargar, W. L., Langston, G. D., Mahfouz, M. R. and Komistek, R. D. (2011) 'In Vivo Assessment of Total Hip Femoral Head Separation from the Acetabular Cup During 4 Common Daily Activities', *Orthopedics*, 34(6). doi: 10.3928/01477447-20110427-06.

Bono, J. V, Sanford, L. and Toussaint, J. T. (1994) 'Severe polyethylene wear in total hip arthroplasty', *The Journal of Arthroplasty*, 9, p. 119.

Boutin, P. (1972) 'Total arthroplasty of the hip by sintered aluminum prosthesis. Experimental study and 1st clinical applications.', *Revue de Chirurgie Orthopédique et Traumatologique*, 58, pp. 229–246.

Bracco, P., Bellare, A., Bistolfi, A., Affatato, S. (2017) ' Ultra-High Molecular Weight Polyethylene: Influence of the Chemical, Physical and Mechanical Properties on the Wear Behavior. A Review', *Materials*, 10(7), 791.

Bragdon, C. R., Jasty, M., Muratoglu, O. K., O'Connor, D. O. and Harris, W. H. (2003) 'Third-body wear of highly cross-linked polyethylene in a hip simulator.', *The Journal of Arthroplasty*, 18(5), pp. 553–61.

Brockett, C., Williams, S., Jin, Z., Isaac, G. and Fisher, J. (2006) 'Friction of Total Hip Replacements With Different Bearings and Loading Conditions', *Journal of Biomedical Materials Research Part B-Applied Biomaterials*, (81B), pp. 508–515. doi: 10.1002/jbmb.

Brown, S. S. and Clarke, I. C. (2006) 'A Review of Lubrication Conditions for Wear Simulation in Artificial Hip Replacements', *Tribology Transactions*, 49(1), pp. 72–78. doi: 10.1080/05698190500519223.

Buechel, F. F. and Pappas, M. J. (2012) *Principles of Human Joint Replacement; Design and clinical application*. Berlin: Springer.

Carter, D. R., Vasu, R. and Harris, W. H. (1982) 'Stress distributions in the acetabular region-II. Effects of cement thickness and metal backing of the total hip acetabular component', *Journal of Biomechanics*, 15(3), pp. 165–170. doi: 10.1016/0021-9290(82)90248-2.

Coombs, R., Gristina, A. and Hungerford, D. (1990) *Joint replacement: state of the art*. London: Butler & Tanner Ltd.

- Dandy, D. J. and Edwards, D. J. (2009) *Essential orthopaedics and trauma*. Edinburgh: Churchill Livingstone. doi: 10.1016/B978-0-443-06718-1.00005-2.
- Dattani, R. (2007) 'Femoral osteolysis following total hip replacement.', *Postgraduate medical journal*, 83(979), pp. 312–6. doi: 10.1136/pgmj.2006.053215.
- Delbert, P. (1919) 'Resultat eloigne d'un visage pour fracture transcervicale du femur.', *Bulletin Societe Chirurgie*, 45, p. 305.
- Dennis, D. A., Komistek, R. D., Northcut, E. J., Ochoa, J. A. and Ritchie, A. (2001) "'In vivo" determination of hip joint separation and the forces generated due to impact loading conditions', *Journal of Biomechanics*, 34(5), pp. 623–629. doi: 10.1016/S0021-9290(00)00239-6.
- Dorr, L. D. and Wan, Z. (1998) 'Causes of and treatment protocol for instability of total hip replacement.', *Clinical orthopaedics and related research*, (355), pp. 144–51. Available at: <http://www.ncbi.nlm.nih.gov/pubmed/9917599>.
- Dowson, D. (2001) 'New joints for the Millennium: Wear control in total replacement hip joints', *Proceedings of the Institution of Mechanical Engineers, Part H: Journal of Engineering in Medicine*, 215(4), pp. 335–358. doi: 10.1243/0954411011535939.
- Dowson, D., McNie, C. M. and Goldsmith, a J. (2000) 'Direct experimental evidence of lubrication in a metal-on-metal total hip replacement tested in a joint simulator', *Journal of Mechanical Engineering Science*, 214, pp. 75–86. doi: 10.1243/0954406001522822.
- Dowson, D. and Wright, V. (1973) 'Bio-tribology. Proceedings of the Conference on The Rheology of Lubrication', *The Institution of Mechanical Engineers and the British Society*

*of Rheology*, pp. 81–85.

El-Deen, M., Garcia-Finana, M. and Jin, Z. M. (2006) 'Effect of ultra-high molecular weight polyethylene thickness on contact mechanics in total knee replacement.', *Proceedings of the Institution of Mechanical Engineers. Part H, Journal of Engineering in Medicine*, 220(7), pp. 733–742.

Estupinan, J. A., Bartel, D. L. and Wright, T. M. (1998) 'Residual stresses in ultra-high molecular weight polyethylene loaded cyclically by a rigid moving indenter in nonconforming geometries', *Journal of Orthopaedic Research*, 16(1), pp. 80–88. doi: 10.1002/jor.1100160114.

Fisher, J. (2011) 'Bioengineering reasons for the failure of metal-on-metal hip prostheses', *Journal of Bone and Joint Surgery [Br]*, 93(8), pp. 1001–4. doi: 10.1302/0301-620X.93B8.

Fisher, J., Al Hajjar, M., Williams, S., Tipper, J., Ingham, E. and Jennings, L. (2012) '(v) Simulation and measurement of wear in metal-on-metal bearings in vitro—understanding the reasons for increased wear', *Orthopaedics and Trauma*. Elsevier Ltd, 26(4), pp. 253–258. doi: 10.1016/j.mporth.2012.05.005.

Fisher, J., Jin, Z., Tipper, J., Stone, M. and Ingham, E. (2006) 'Tribology of alternative bearings.', *Clinical orthopaedics and related research*, 453(453), pp. 25–34. doi: 10.1097/01.blo.0000238871.07604.49.

Galanis, N. I. and Manolagos, D. E. (2011) 'Design of a hip joint simulator according to the ISO 14242', *Proceedings of the World Congress on Engineering, III*, pp. 2–7.

Gao, Y., Jin, Z., Wang, L. and Wang, M. (2015) 'Finite element analysis of sliding distance

and contact mechanics of hip implant under dynamic walking conditions.’, *Proceedings of the Institution of Mechanical Engineers. Part H, Journal of engineering in medicine*, 229(6), pp. 469–474. doi: 10.1177/0954411915585380.

García-Rey, E. and García-Cimbrelo, E. (2010) ‘Polyethylene in total hip arthroplasty: half a century in the limelight’, *Journal of Orthopaedics and Traumatology*, 11(2), pp. 67–72. doi: 10.1007/s10195-010-0091-1.

Germain, M. A., Hatton, A., Williams, S., Matthews, J. B., Stone, M. H., Fisher, J. and Ingham, E. (2003) ‘Comparison of the cytotoxicity of clinically relevant cobalt-chromium and alumina ceramic wear particles in vitro’, *Biomaterials*, 24(3), pp. 469–479. doi: 10.1016/S0142-9612(02)00360-5.

Gluck, T. (1890) ‘Autoplastik-Transplantation: Implantation von Fremdkörpern.’, *Berl Klin Wschr* 19, 27, pp. 421–427.

Godest, A. C., Beaugonin, M., Haug, E., Taylor, M. and Gregson, P. J. (2002) ‘Simulation of a knee joint replacement during a gait cycle using explicit finite element analysis’, *Journal of Biomechanics*, 35(2), pp. 267–275. doi: 10.1016/S0021-9290(01)00179-8.

Granchi, D. *et al.* (2003) ‘Immunological changes in patients with primary osteoarthritis of the hip after total joint replacement.’, *Journal of Bone and Joint Surgery - Series B*, 85(5), pp. 758–764. doi: 10.1302/0301-620X.85B5.13729.

Hall, R. M., Bankes, M. J. K. and Blunn, G. (2001) ‘Biotribology for joint replacement’, *Current Orthopaedics*, 15(4), pp. 281–290. doi: 10.1054/cuor.2001.0197.

Halley, D., Glassman, A. and Crowninshield, R. D. (2004) ‘Recurrent dislocation after revision total hip replacement with a large prosthetic femoral head. A case report.’, *The*

*Journal of Bone and Joint Surgery. American volume*, 86–A(4), pp. 827–30. Available at: <http://www.ncbi.nlm.nih.gov/pubmed/15069152>.

Halloran, J. P., Petrella, A. J. and Rullkoetter, P. J. (2005) 'Explicit finite element modeling of total knee replacement mechanics', *Journal of Biomechanics*, 38(2), pp. 323–331. doi: 10.1016/j.jbiomech.2004.02.046.

Hanna, S. A., Somerville, L., McCalden, R. W., Naudie, D. D. and MacDonald, S. J. (2016) 'Highly cross-linked polyethylene decreases the rate of revision of total hip arthroplasty compared with conventional polyethylene at 13 years follow-up', *The Bone & Joint Journal*, 98–B(1), pp. 28–32. doi: 10.1302/0301-620X.98B1.36527.

Hashimoto, N., Ando, M., Yayama, T., Uchida, K., Kobayashi, S., Negoro, K. and Baba, H. (2005) 'Dynamic analysis of the resultant force acting on the hip joint during level walking', *Artificial Organs*, 29(5), pp. 387–392. doi: 10.1111/j.1525-1594.2005.29065.x.

Hatton, a, Nevelos, J. E., Matthews, J. B., Fisher, J. and Ingham, E. (2003) 'Effects of clinically relevant alumina ceramic wear particles on TNF-alpha production by human peripheral blood mononuclear phagocytes.', *Biomaterials*, 24(7), pp. 1193–204. doi: 10.1016/S0142-9612(02)00510-0.

Hertzberg, R. W. and Manson, J. A. (1980) *Fatigue of engineering plastics*. New York: Academic press.

Hua, X., Li, J., Wang, L., Jin, Z., Wilcox, R. and Fisher, J. (2014) 'Contact mechanics of modular metal-on-polyethylene total hip replacement under adverse edge loading conditions', *Journal of Biomechanics*. Elsevier, 47(13), pp. 3303–3309. doi: 10.1016/j.jbiomech.2014.08.015.

Hua, X., Wroblewski, B. M., Jin, Z. and Wang, L. (2012) 'The effect of cup inclination and wear on the contact mechanics and cement fixation for ultra high molecular weight polyethylene total hip replacements', *Medical Engineering and Physics*. Institute of Physics and Engineering in Medicine, 34(3), pp. 318–325. doi: 10.1016/j.medengphy.2011.07.026.

Ingham, E. and Fisher, J. (2000) 'Biological reactions to wear debris in total joint replacement', *Proceedings of the Institution of Mechanical Engineers, Part H: Journal of Engineering in Medicine*, 214(1), pp. 21–37. doi: 10.1243/0954411001535219.

Ingram, J. H., Stone, M., Fisher, J. and Ingham, E. (2004) 'The influence of molecular weight, crosslinking and counterface roughness on TNF-alpha production by macrophages in response to ultra high molecular weight polyethylene particles', *Biomaterials*, 25(17), pp. 3511–3522. doi: 10.1016/j.biomaterials.2003.10.054.

Iosa, M., Fusco, A., Marchetti, F., Morone, G., Caltagirone, C., Paolucci, S. and Peppe, A. (2013) 'The golden ratio of gait harmony: Repetitive proportions of repetitive gait phases', *BioMed Research International*, 2013. doi: 10.1155/2013/918642.

Isaac, G. H., Brockett, C., Breckon, A., van der Jagt, D., Williams, S., Hardaker, C., Fisher, J., Schepers, A. and Surgeon, O. (2009) 'ceramic-on-metal bearings in total hip replacement whole blood metal ion levels and analysis of retrieved components', *The Journal of Bone and Joint Surgery [Br]*, 91, pp. 1134–41. doi: 10.1302/0301-620X.91B9.

Jacobs, J., Shanbhag, A., TT, G., Black, J. and JO, G. (1994) 'Wear debris in total joint replacements', *The Journal of the American Academy of Orthopaedic Surgeons*, 2(2), pp. 212–220.

Jagatia, M. and Jin, Z. M. (2001) 'Elastohydrodynamic lubrication analysis of metal-on-

metal hip prostheses under steady state entraining motion', *Proceedings of the Institution of Mechanical Engineers, Part H: Journal of Engineering in Medicine*, 215(6), pp. 531–541. doi: 10.1243/0954411011536136.

Jalali-Vahid, D., Jagatia, M., Jin, Z. M. and Dowson, D. (2001) 'Prediction of lubricating film thickness in UHMWPE hip joint replacements', *Journal of Biomechanics*, 34, pp. 261–266. doi: 10.1016/S0021-9290(00)00181-0.

Jassim, S. S., Vanhegan, I. S. and Haddad, F. S. (2012) 'The epidemiology of total hip arthroplasty in England and Wales', *Seminars in Arthroplasty*. Elsevier, 23(4), pp. 197–199. doi: 10.1053/j.sart.2012.12.001.

Jennings, L. M., Al-Hajjar, M., Brockett, C. L., Williams, S., Tipper, J. L., Ingham, E. and Fisher, J. (2012) '(iv) Enhancing the safety and reliability of joint replacement implants', *Orthopaedics and Trauma*. Elsevier Ltd, 26(4), pp. 246–252. doi: 10.1016/j.mporth.2012.05.006.

Jin, Z. M., Dowson, D. and Fisher, J. (1994) 'A parametric analysis of the contact stress in ultra-high molecular weight polyethylene acetabular cups.', *Medical engineering & physics*, 16(5), pp. 398–405. doi: [http://dx.doi.org/10.1016/1350-4533\(90\)90006-T](http://dx.doi.org/10.1016/1350-4533(90)90006-T).

Jin, Z. M., Fisher, J. and Ingham, E. (2006) 'Biotribology: Material Design, Lubrication, and Wear in Artificial Hip Joints', in *Handbook of lubrication and tribology*. CRC Press.

Jin, Z. M., Heng, S. M., Ng, H. W. and Auger, D. D. (1999) 'An axisymmetric contact model of ultra high molecular weight polyethylene cups against metallic femoral heads for artificial hip joint replacements', *Proceedings of the Institution of Mechanical Engineers Part H-Journal of Engineering in Medicine*, 213(H4), pp. 317–327. doi: 10.1243/0954411991535158.

Jin, Z. M., Stone, M., Ingham, E. and Fisher, J. (2006) 'Biotribology', *Current Orthopaedics*, 20, pp. 32–40.

Johnson, K. I. (1985) *Contact mechanics*. Cambridge University Press.

Johnston, R. C. and Smidt, G. L. (1969) 'Measurement of hip-joint motion during walking', *Journal of Bone and Joint Surgery*, 6(6), pp. 1083–1094.

Kaddick, C. and Wimmer, M. A. (2001) 'Hip simulator wear testing according to the newly introduced standard ISO 14242', *Proceedings of the Institution of Mechanical Engineers, Part H: Journal of Engineering in Medicine*, 215(5), pp. 429–442. doi: 10.1016/j.jbiomech.2004.04.003.

Kayabasi, O. and Ekici, B. (2007) 'The effects of static, dynamic and fatigue behavior on three-dimensional shape optimization of hip prosthesis by finite element method', *Materials & Design*, 28(8), pp. 2269–2277. doi: 10.1016/j.matdes.2006.08.012.

Kennon Robert E. (2008) *Hip and knee surgery: a patient's guide to hip replacement, hip resurfacing, Knee replacement, & Knee Arthroscopy*. Middlebury, CT: Orthopaedic Surgery, P.C.

Knahr, K. (2011) 'Tribology in Total Hip Arthroplasty', in *Tribology in Total Hip Arthroplasty*. Heidelberg: Springer. doi: 10.1007/978-3-642-19429-0.

Komistek, R. D., Dennis, D. A., Ochoa, J. A., Haas, B. D. and Hammill, C. (2002) 'In vivo comparison of hip separation after metal-on-metal or metal-on-polyethylene total hip arthroplasty', *The Journal of bone and joint surgery. American Volume*, 84–A(10), pp. 1836–1841. doi: 327.

Komistek, R. D., Stiehl, J. B., Dennis, D. a, Paxson, R. D. and Soutas-Little, R. W. (1998)

'Mathematical model of the lower extremity joint reaction forces using Kane's method of dynamics.', *Journal of Biomechanics*, 31(2), pp. 185–9. doi: 10.1016/S0021-9290(97)00128-0.

Korhonen, R. K., Koistinen, A., Konttinen, Y. T., Santavirta, S. S. and Lappalainen, R. (2005) 'The effect of geometry and abduction angle on the stresses in cemented UHMWPE acetabular cups – finite element simulations and experimental tests', *BioMedical Engineering OnLine*, 4(1 @ 1475-925X), p. 32. doi: 10.1186/1475-925X-4-32 %U <http://dx.doi.org/10.1186/1475-925X-4-32>.

Kurtz, S. M. (2004) *The UHMWPE Handbook, The UHMWPE Handbook*. Academic Press. doi: 10.1016/B978-012429851-4/50003-6.

Kurtz, S. M., Edidin, A. A. and Bartel, D. L. (1997) 'Thickness on the Contact Stresses in Metal-Backed', *Bone*, 30(6).

Kurtz, S. M., Ochoa, J. A., White, C. V., Srivastav, S. and Cournoyer, J. (1998) 'Backside nonconformity and locking restraints affect liner/shell load transfer mechanisms and relative motion in modular acetabular components for total hip replacement', *Journal of Biomechanics*, 31(5), pp. 431–437. doi: 10.1016/S0021-9290(98)00030-X.

Kurtz, S. M. and Patel, J. D. (2016) *UHMWPE Biomaterials Handbook*. Amsterdam, The Netherlands: Elsevier.

Labek, G., Janda, W., Agreiter, M., Schuh, R. and Böhler, N. (2011) 'Organisation, data evaluation, interpretation and effect of arthroplasty register data on the outcome in terms of revision rate in total hip arthroplasty', *International Orthopaedics*, 35(2), pp. 157–163. doi: 10.1007/s00264-010-1131-4.

Leng, J., Al-Hajjar, M., Wilcox, R., Jones, A., Barton, D. and Fisher, J. (2017) 'Dynamic virtual simulation of the occurrence and severity of edge loading in hip replacements associated with variation in the rotational and translational surgical position', *Proceedings of the Institution of Mechanical Engineers, Part H: Journal of Engineering in Medicine*, 231(4), pp. 299–306. doi: 10.1177/0954411917693261.

Leslie, I., Williams, S., Brown, C., Isaac, G., Jin, Z., Ingham, E. and Fisher, J. (2008) 'Effect of bearing size on the long-term wear, wear debris, and ion levels of large diameter metal-on-metal hip replacements - An in vitro study', *Journal of Biomedical Materials Research - Part B Applied Biomaterials*, 87(1), pp. 163–172. doi: 10.1002/jbm.b.31087.

Lewinnek, B. Y. G. E., From, J. J., Tarr, M. and Compere, I. C. L. (1978) 'Dislocations after Total Arthroplasties', *Journal of Bone and Joint Surgery*, 60(2), pp. 217–220.

Liu, F., Leslie, I., Williams, S., Fisher, J. and Jin, Z. (2008) 'Development of computational wear simulation of metal-on-metal hip resurfacing replacements', *Journal of Biomechanics*, 41(3), pp. 686–694. doi: 10.1016/j.jbiomech.2007.09.020.

Liu, F., Udofia, I. J., Jin, Z. M., Hirt, F., Rieker, C., Roberts, P. and Grigoris, P. (2005) 'Comparison of Contact Mechanics between a Total Hip Replacement and a Hip Resurfacing with a Metal-On-Metal Articulation', *Proceedings of the Institution of Mechanical Engineers, Part C: Journal of Mechanical Engineering Science*, 219(7), pp. 727–732. doi: 10.1243/095440605X31490.

Liu, F., Williams, S., Jin, Z. and Fisher, J. (2013) 'Effect of head contact on the rim of the cup on the offset loading and torque in hip joint replacement', *Proceedings of the Institution of Mechanical Engineers, Part H: Journal of Engineering in Medicine*, 227(11), pp. 1147–1154. doi: 10.1177/0954411913496016.

Liu, H., Ellison, P. J., Xu, H. and Jin, Z. (2010) 'Coupling of dynamics and contact mechanics of artificial hip joints in a pendulum model', *Proceedings of the Institution of Mechanical Engineers, Part H: Journal of Engineering in Medicine*, 224(8), pp. 989–1003. doi: 10.1243/09544119JEIM687.

Lombardi, A. V, Mallory, T. H., Dennis, D. A., Komistek, R. D., Fada, R. A. and Northcut, E. J. (2000) 'An in vivo determination of total hip arthroplasty pistoning during activity', *The Journal of Arthroplasty*, 15(6), pp. 702–709. doi: 10.1054/arth.2000.6637.

Mak, M., Jin, Z., Fisher, J. and Stewart, T. D. (2011) 'Influence of Acetabular Cup Rim Design on the Contact Stress During Edge Loading in Ceramic-on-Ceramic Hip Prostheses', *Journal of Arthroplasty*. Elsevier Inc., 26(1), pp. 131–136. doi: 10.1016/j.arth.2009.10.019.

Mak, M. M. and Jin, Z. M. (2002) 'Analysis of contact mechanics in ceramic-on-ceramic hip joint replacements.', *Proceedings of the Institution of Mechanical Engineers. Part H, Journal of engineering in medicine*, 216(4), pp. 231–6. doi: 10.1243/095441102321032193.

Manaka, M., Clarke, I. C., Yamamoto, K., Shishido, T., Gustafson, A. and Imakiire, A. (2004) 'Stripe Wear Rates in Alumina THR—Comparison of Microseparation Simulator Study with Retrieved Implants', *Journal of Biomedical Materials Research*, 69, pp. 149–157. doi: 10.1002/jbm.b.20033.

Mattei, L., Di Puccio, F., Piccigallo, B. and Ciulli, E. (2011) 'Lubrication and wear modelling of artificial hip joints: A review', *Tribology International*. Elsevier, 44(5), pp. 532–549. doi: 10.1016/j.triboint.2010.06.010.

Maxian, T. A., Brown, T. D., Pedersen, D. R. and Callaghan, J. J. (1996) 'A sliding-distance-

coupled finite element formulation for polyethylene wear in total hip arthroplasty.', *Journal of Biomechanics*, 29(5), pp. 687–92. Available at: <http://www.ncbi.nlm.nih.gov/pubmed/8707799>.

Mccollum, D. and Gray, W. (1990) 'Dislocation After Total Hip Arthroplasty Causes and Prevention.', *Clinical Orthopaedics and Related Research*, 261, pp. 159–172.

McKee, G. K. and Watson-Farrar, J. (1966) 'Replacement of arthritic hips by the McKee-Farrar prosthesis.', *The Journal of Bone and Joint Surgery. British volume*, 48(2), pp. 245–259.

McKellop, H., Shen, F., Lu, B., Campbell, P. and Salovey, R. (1999) 'Development of an Extremely Wear-Resistant Ultra High Molecular Weight Polyethylene for Total Hip Replacements', *Joiirrial of Orthupaedic Research*, 17, pp. 157–167.

Meng, Q., Liu, F., Fisher, J. and Jin, Z. (2013) 'Contact mechanics and lubrication analyses of ceramic-on-metal total hip replacements', *Tribology International*. Elsevier, 63, pp. 51–60. doi: 10.1016/j.triboint.2012.02.012.

Miki, H., Sugano, N., Yonenobu, K., Tsuda, K., Hattori, M. and Suzuki, N. (2013) 'Detecting cause of dislocation after total hip arthroplasty by patient-specific four-dimensional motion analysis', *Clinical Biomechanics*. Elsevier Ltd, 28(2), pp. 182–186. doi: 10.1016/j.clinbiomech.2012.11.009.

*National Joint Registry* (2016). Available at: <http://www.njrcentre.org.uk/njrcentre/Portals/0/Documents/England/Reports/13th Annual Report/07950 NJR Annual Report 2016 ONLINE REPORT.pdf>.

Nevelos, J. E., Ingham, E., Doyle, C., Nevelos, A. B. and Fisher, J. (2001) 'Wear of HIPed

and non-HIPed alumina-alumina hip joints under standard and severe simulator testing conditions', *Biomaterials*, 22(16), pp. 2191–2197. doi: 10.1016/S0142-9612(00)00361-6.

Nevelos, J., Ingham, E., Doyle, C., Streicher, R., Nevelos, A., Walter, W. and Fisher, J. (2000) 'Microseparation of the centers of alumina-alumina artificial hip joints during simulator testing produces clinically relevant wear rates and patterns', *The Journal of Arthroplasty*, 15(6), pp. 7–795. doi: 10.1054/arth.2000.8100.

O'Dwyer Lancaster-Jones, O., Williams, S., Jennings, L. M., Thompson, J., Isaac, G. H., Fisher, J. and Al-Hajjar, M. (2017) 'An in vitro simulation model to assess the severity of edge loading and wear, due to variations in component positioning in hip joint replacements', *Journal of Biomedical Materials Research Part B: Applied Biomaterials*. doi: 10.1002/jbm.b.33991.

Oral, E., Christensen, S. D., Malhi, A. S., Wannomae, K. K. and Muratoglu, O. K. (2006) 'Wear Resistance and Mechanical Properties of Highly Cross-linked, Ultrahigh-Molecular Weight Polyethylene Doped With Vitamin E', *The Journal of Arthroplasty*, 21(4), pp. 580–591. doi: 10.1016/j.arth.2005.07.009.

Pare, P., Medley, J. B., Chan, F. W. and Young, S. K. (2003) 'On the role of the lambda parameter in simulator wear of metal-on-metal hip implants', *Tribology Series*, 41(Mc), pp. 281–290.

Parratte, S., Pagnano, M. W., Coleman-Wood, K., Kaufman, K. R. and Berry, D. J. (2009) 'The 2008 frank stinchfield award: Variation in postoperative pelvic tilt may confound the accuracy of hip navigation systems', *Clinical Orthopaedics and Related Research*, 467(1), pp. 43–49. doi: 10.1007/s11999-008-0521-z.

Partridge, S. (2016) *Wear and rim damage of UHMWPE acetabular cups in total hip replacement*. University of Leeds.

Parvizi, J., Kim, K.-I., Goldberg, G., Mallo, G. and Hozack, W. J. (2006) 'Recurrent instability after total hip arthroplasty: beware of subtle component malpositioning', *Clinical Orthopaedics and Related Research*®, 447(447), pp. 60–65. doi: 10.1097/01.blo.0000218749.37860.7c.

Paul, J. P. (1976) 'Force actions transmitted by joints in the human body.', *Proceedings of the Royal Society of London. Series B*, 192(1107), pp. 163–172. doi: 10.1098/rspb.1976.0004.

Peterson, M. (1980) *Clasification of wear process*. Edited by W. W. Peterson MB. New York: ASME.

Plank, G., Estok, D., Muratoglu, O., O'Connor, D., Burroughs, B. and Harris, W. (2005) 'Contact Stress Assessment of Conventional and Highly Crosslinked Ultra High Molecular Weight Polyethylene Acetabular Liners with Finite Element Analysis and Pressure Sensitive Film', *Journal of biomedical materials research. Part B, Applied biomaterials*, 80B, pp. 1–10. doi: 10.1002/jbmb.

Reeves, E. a, Barton, D. C., FitzPatrick, D. P. and Fisher, J. (1998) 'A two-dimensional model of cyclic strain accumulation in ultra-high molecular weight polyethylene knee replacements.', *Proceedings of the Institution of Mechanical Engineers. Part H, Journal of engineering in medicine*, 212(June 1997), pp. 189–198. doi: 10.1243/0954411981533971.

Reinders, J., Sonntag, R., Heisel, C., Reiner, T., Vot, L. and Kretzer, J. P. (2013) 'Wear Performance of Ceramic-On-Metal Hip Bearings', *PLoS ONE*, 8(8), pp. 1–7. doi:

10.1371/journal.pone.0073252.

Revell, P. A. (2008) *Joint replacement technology*. Cambridge, England: Woodhead Pub.

Ries, M. D. and Link, T. M. (2012) 'Monitoring and Risk of Progression of Osteolysis After Total Hip Arthroplasty', *The Journal of Bone & Joint Surgery*, 94–A, pp. 2097–105.

Saikko, V. (2005) 'A 12-station anatomic hip joint simulator.', *Proceedings of the Institution of Mechanical Engineers. Part H, Journal of engineering in medicine*, 219(6), pp. 437–48. doi: 10.1243/095441105X34419.

Sariali, E., Stewart, T., Jin, Z. and Fisher, J. (2012) 'Effect of cup abduction angle and head lateral microseparation on contact stresses in ceramic-on-ceramic total hip arthroplasty', *Journal of Biomechanics*. Elsevier, 45(2), pp. 390–393. doi: 10.1016/j.jbiomech.2011.10.033.

Schmalzried, T. P. (2009) 'The Importance of Proper Acetabular Component Positioning and the Challenges to Achieving It', *Operative Techniques in Orthopaedics*. Elsevier Inc., 19(3), pp. 132–136. doi: 10.1053/j.oto.2009.09.008.

Scholes, S. C. and Unsworth, A. (2006) 'The Effects of Proteins on the Friction and Lubrication of Artificial Joints', *Proceedings of the Institution of Mechanical Engineers, Part H: Journal of Engineering in Medicine*, 220(6), pp. 687–693. doi: 10.1243/09544119JEIM21.

Smith, S. L. and Unsworth, A. (2001) 'A five-station hip joint simulator', *Proceedings of the Institution of Mechanical Engineers, Part H: Journal of Engineering in Medicine*, 215(1), pp. 61–64. doi: 10.1243/0954411011533535.

Stewart, T. D., Tipper, J. L., Insley, G., Streicher, R. M., Ingham, E. and Fisher, J. (2003)

'Long-term wear of ceramic matrix composite materials for hip prostheses under severe swing phase microseparation', *Journal Of Biomedical Materials Research Part B- Applied Biomaterials*, 66B(2), pp. 567–573. doi: Doi 10.1002/Jbm.B.10035.

Tank, P. W. and Gest, T. R. (2008) *Lippincott Williams and Wilkins Atlas of Anatomy*. Lippincott Williams & Wilkins,US.

Taylor, S. J. G., Perry, J. S., Meswania, J. M., Donaldson, N., Walker, P. S. and Cannon, S. R. (1997) 'Telemetry of forces from proximal femoral replacements and relevance to fixation', *Journal of Biomechanics*, 30(3), pp. 225–234. doi: 10.1016/S0021-9290(96)00141-8.

Tortora, G. and Derrickson, B. (2009) *Principles of human anatomy*. Hoboken, NJ : John Wiley & Sons.

Walter, W. L., Insley, G. M., Walter, W. K. and Tuke, M. A. (2004) 'Edge loading in third generation alumina ceramic-on-ceramic bearings: Stripe wear', *Journal of Arthroplasty*, 19(4), pp. 402–413. doi: 10.1016/j.arth.2003.09.018.

Wang, A., Polineni, V. K., Stark, C. and Dumbleton, J. H. (1998) 'Effect of femoral head surface roughness on the wear of ultrahigh molecular weight polyethylene acetabular cups.', *The Journal of Arthroplasty*, 13(6), pp. 615–20. Available at: <http://www.ncbi.nlm.nih.gov/pubmed/9741435>.

Willert, H.-G. (2005) 'Metal-on-Metal Bearings and Hypersensitivity in Patients with Artificial Hip Joints A Clinical and Histomorphological Study', *The Journal of Bone and Joint Surgery (American)*, 87(1), p. 28. doi: 10.2106/JBJS.A.02039pp.

Williams, S., Al-Hajjar, M., Isaac, G. H. and Fisher, J. (2013) 'Comparison of ceramic-on-

metal and metal-on-metal hip prostheses under adverse conditions', *Journal of Biomedical Materials Research - Part B Applied Biomaterials*, 101 B(5), pp. 770–775. doi: 10.1002/jbm.b.32880.

Williams, S., Butterfield, M., Stewart, T., Ingham, E., Stone, M. and Fisher, J. (2003) 'Wear and deformation of ceramic-on-polyethylene total hip replacements with joint laxity and swing phase microseparation.', *Proceedings of the Institution of Mechanical Engineers. Part H, Journal of Engineering in Medicine*, 217(2), pp. 147–153. doi: 10.1243/09544110360579367.

Williams, S., Leslie, I., Isaac, G., Jin, Z., Ingham, E. and Fisher, J. (2008) 'Tribology and Wear of Metal-on-Metal Hip Prostheses: Influence of Cup Angle and Head Position', *The Journal of Bone and Joint Surgery-American Volume*, 90(Suppl 3), pp. 111–117. doi: 10.2106/JBJS.H.00485.

Williams, S., Schepers, A., Isaac, G., Hardaker, C., Ingham, E., van der Jagt, D., Breckon, A. and Fisher, J. (2007) 'The 2007 Otto Aufranc Award. Ceramic-on-metal hip arthroplasties: a comparative in vitro and in vivo study.', *Clinical Orthopaedics and Related Research*, 465(465), pp. 23–32. doi: 10.1097/BLO.0b013e31814da946.

Wright, T. and Goodman, S. (1995) 'Implant wear: the future of total joint replacement. Rosemont', in *USA: AAOS*.

## Chapter 8 Appendix

### 8.1 Experimental studies

The experimental studies that were shown for validation purposes are not published. These experimental biomechanical studies were done on electromechanical hip simulator (EM13) by Murat Ali and the dynamic separation output and load at the rim is presented in this section.

The biomechanical testing were done based on the loading and the angular displacement that was obtained from ISO 14242-1:2014. The bearing surfaces was lubricated with New-born calf serum. The following conditions were tested in the biomechanical testing:

- Translational mismatch of 1mm, 2mm, 3mm and 4mm.
- Swing phase load of 70N, 100N, 200N and 300N
- Cup inclination angle of 45° and 65° (clinically)

The dynamic output of the testing is shown below:

### 8.1.1 Dynamic separation

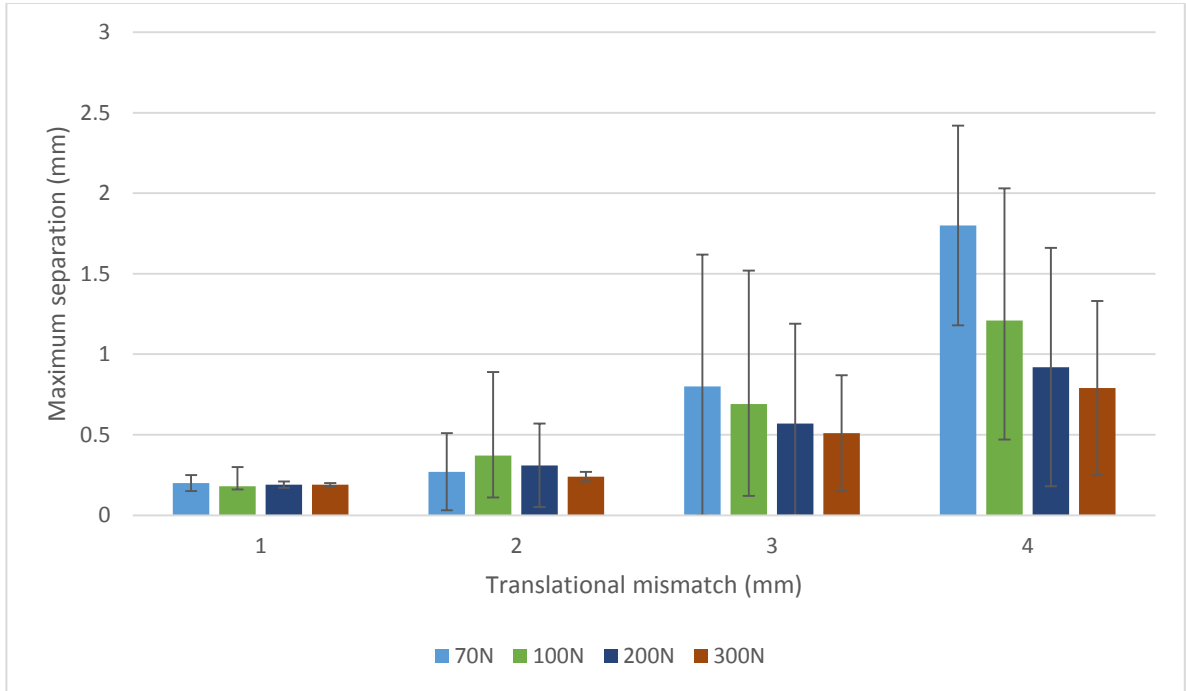


**Figure 8.1 Experimental maximum separation versus swing phase load and translational mismatch level under 45° inclination angle.**

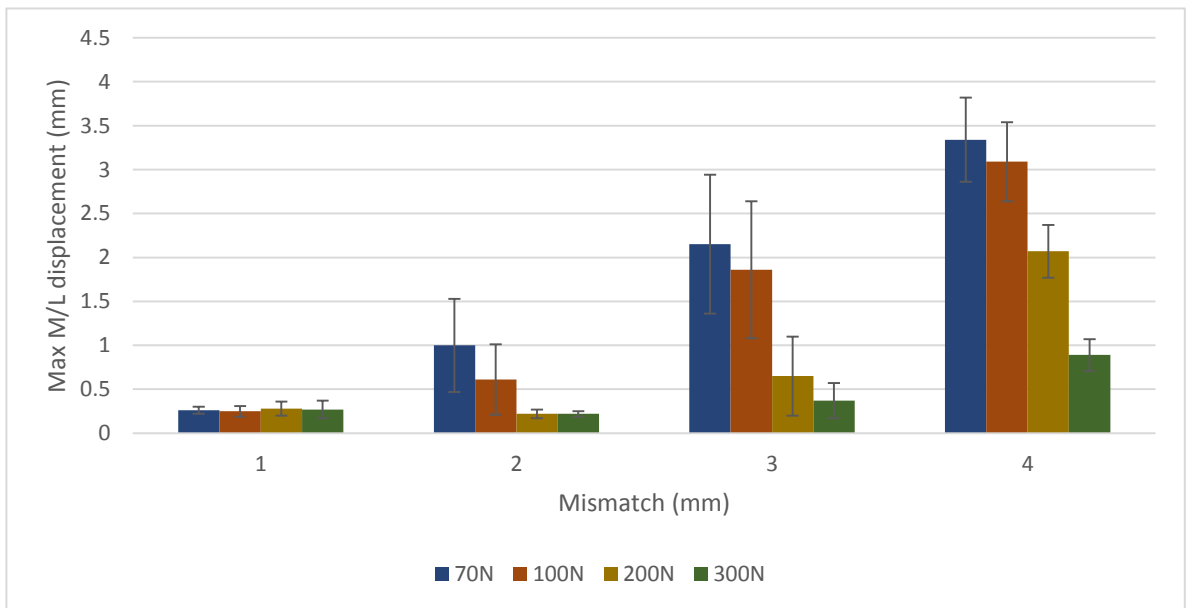


**Figure 8.2 Experimental maximum separation versus swing phase load and translational mismatch level under 65° inclination angle.**

### 8.1.2 Load at the rim

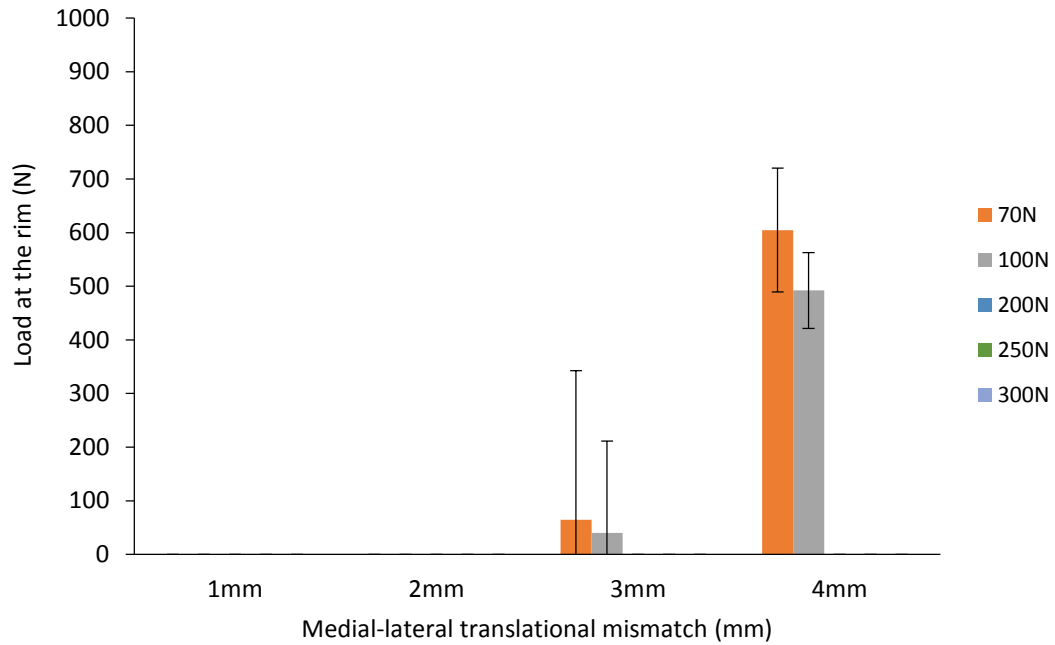


**Figure 8.3** The load at the rim with various translational mismatch level and swing phase loads under 45° cup inclination angle

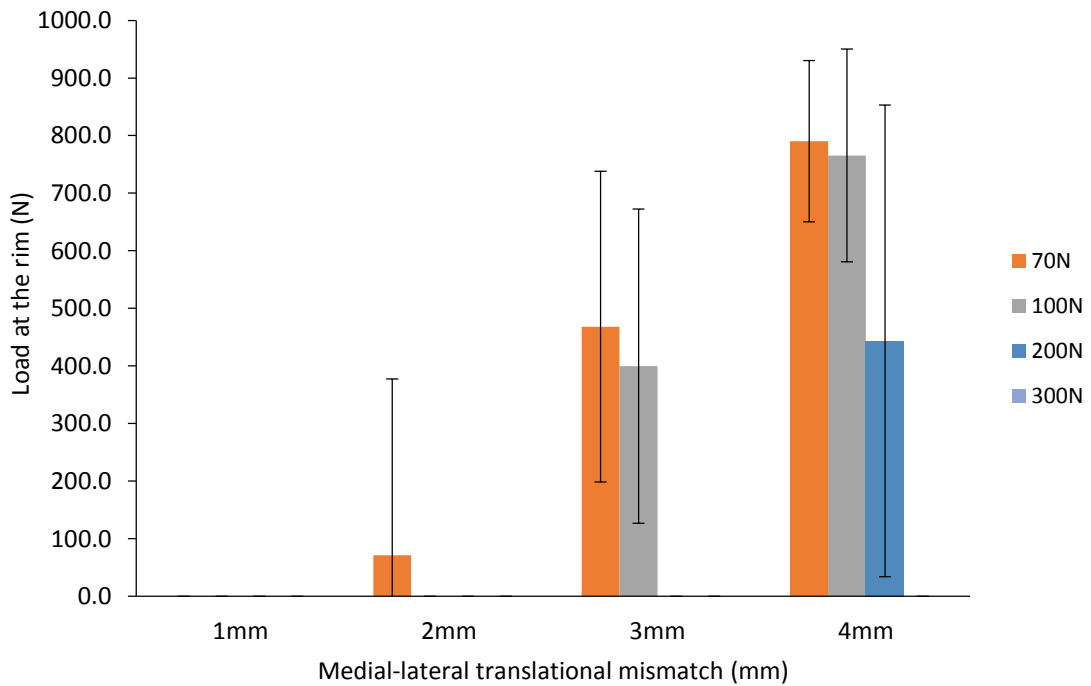


**Figure 8.4** The load at the rim with various translational mismatch level and swing phase loads under 65° cup inclination angle

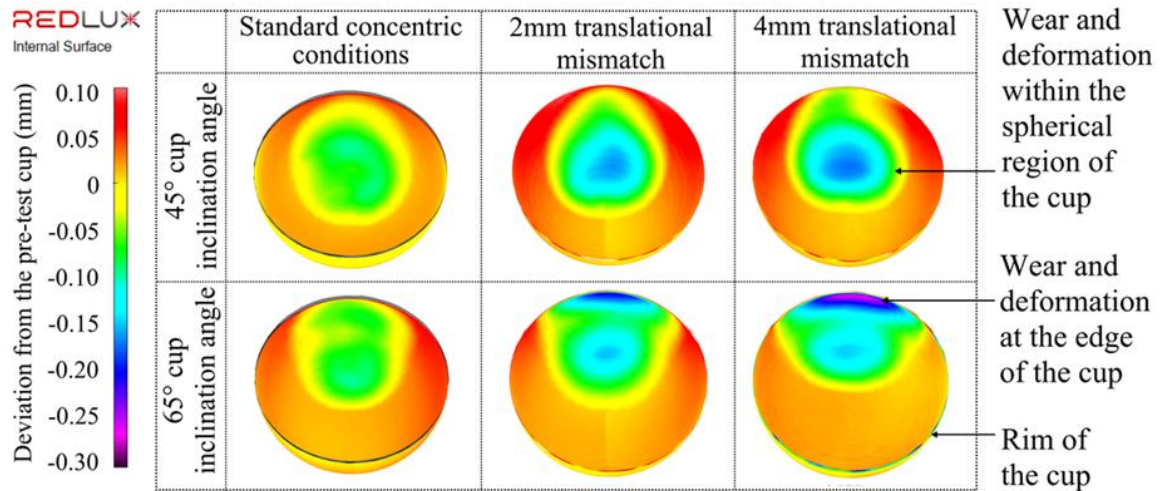


**Figure 8.5** The location of the in vitro wear and deformation under concentric conditions, 2mm and 4mm translational mismatch level, standard and steep cup inclination angle and 70N swing phase load carried out by Murat Ali (partially shown in Ali *et al*, 2016)

## 8.2 Python script for output processing

```

from abaqus import *
from abaqusConstants import *
from caeModules import *
from odbAccess import *

resultlocation = 'G:/Chapter 4 and 5/Results/65 degree/Final/'

hiplist = ['hundredonea', 'hundredtwoa', 'hundredthree', 'hundredfour', 'hundredfivea-1', 'hundredsix', 'hundredsevena', 'hundredeighta', 'hundredninea', 'hundredtenb', 'hundredeleven', 'hundredtwelve', 'hundredthirteenb', 'hundredforteen', 'hundredfifteen', 'hundredsixteen']

stepslist = ['Cycle 1']

def extracttab():
    for hhh in hiplist:
        # define Hip
        Hip = hhh
        # open output database
        o1 = session.openOdb(name=resultlocation+Hip+'.odb')
        session.viewports['Viewport: 1'].setValues(displayedObject=o1)

        # set number format for output
        nf = NumberFormat(numDigits=6, precision=0, format=AUTOMATIC)

```

```

# change viewer to poly
leaf = dgo.LeafFromPartInstance(partInstanceName=('POLY', ))
session.viewports['Viewport:
1'].odbDisplay.displayGroup.replace(leaf=leaf)
for sss in stepslist:

    # get end (index is always -1) frame number for step
    # try except continue means move on if no endframe exists (i.e.
that step aborted)
    try:
        endframe=o1.steps[sss].frames[-1]
    except:
        continue
    ### CPRESS
    session.fieldReportOptions.setValues(sort=DESCENDING)
    session.writeFieldReport(fileName='CC'+Hip+sss+'.rpt',
append=OFF,
        sortItem='CPRESS', odb=o1, step=0, frame=endframe,
        outputPosition=NODAL,          variable= (('CPRESS',
ELEMENT_NODAL), ))

    ### LE
    session.fieldReportOptions.setValues(sort=DESCENDING)
    session.writeFieldReport(fileName='LE'+Hip+sss+'.rpt',
append=OFF,
        sortItem='LE.Max. Principal', odb=o1, step=0,
frame=endframe,
        outputPosition=NODAL,          variable= (('LE',
INTEGRATION_POINT), ))

    ### PE
    session.fieldReportOptions.setValues(sort=DESCENDING)
    session.writeFieldReport(fileName='PE'+Hip+sss+'.rpt',
append=OFF,

```

```

frame=endframe,          sortItem='PE.Max. Principal', odb=o1, step=0,
                           outputPosition=NODAL,          variable= (('PE',
INTEGRATION_POINT), ))
                           ### S
                           session.fieldReportOptions.setValues(sort=DESCENDING)
                           session.writeFieldReport(fileName='S'+Hip+sss+'.rpt',
append=OFF,
                           sortItem='S.Mises', odb=o1, step=0, frame=endframe,
                           outputPosition=NODAL,          variable= (('S',
INTEGRATION_POINT), ))
# now extract desired lines from rpt files
# and record to text files
for hhh in hiplist:
    for sss in stepslist:
        reqline = 20
        reqlineL = 23

        # end of step
        fileName='CC'+hhh+sss+'.rpt'
        # get line 20
        try:
            with open(fileName) as f1:
                i = 0
                for line in f1:
                    if i == reqline-1:
                        break
                    i += 1
            # record to file
            with open("CResultop.txt", mode='a') as file:
                file.write(line)
        # if no data for step, record that it aborted
        except:
            with open("CResultop.txt", mode='a') as file:

```

```

        file.write('Aborts \n')
# end of step
fileName='LE'+hhh+sss+'.rpt'
# get line 23
try:
    with open(fileName) as f1:
        i = 0
        for line in f1:
            if i == reqlineL-1:
                break
            i += 1
        # record to file
        with open("LEResultop.txt", mode='a') as file:
            file.write(line)
# if no data for step, record that it aborted
except:
    with open("LEResultop.txt", mode='a') as file:
        file.write('Aborts \n')

# end of step
fileName='PE'+hhh+sss+'.rpt'
# get line 23
try:
    with open(fileName) as f1:
        i = 0
        for line in f1:
            if i == reqlineL-1:
                break
            i += 1
        # record to file
        with open("PEResultop.txt", mode='a') as file:
            file.write(line)
# if no data for step, record that it aborted

```

```

except:
    with open("PEResultop.txt", mode='a') as file:
        file.write('Aborts \n')
#end of step
fileName='S'+hhh+sss+'.rpt'
# get line 23
try:
    with open(fileName) as f1:
        i = 0
        for line in f1:
            if i == reqlineL-1:
                break
            i += 1
        # record to file
        with open("SResultop.txt", mode='a') as file:
            file.write(line)
# if no data for step, record that it aborted
except:
    with open("SResultop.txt", mode='a') as file:
        file.write('Aborts \n')

f1.close()
file.close()
def getstrains():
    stepofint = 'Cycle 1'
    # do this for steps of interest
    # define list of maxU nodes found using previous function...
    maxulist = [25, 474, 24, 23,473]
    for Hip, MaxUnode in zip(hiplist,maxulist):

        # opens odb
        odb=openOdb(path='G:/Chapter 4 and 5/Results/65
degree/Final/'+Hip+'.odb')
        # permanantly adds a node set

```

```

#odb.rootAssembly.NodeSetFromNodeLabels(name='Nodes1',
nodeLabels= (('POLY',(MaxUnode, )),))
# get nodal displacements at end of named step
displacement = odb.steps[stepofint].frames[-1].fieldOutputs['CPRESS']
# get for the specific set of nodes
interestingnodes = odb.rootAssembly.nodeSets['Nodes1']
Displacement = displacement.getSubset(region=interestingnodes)
dispValues = Displacement.values
# define oc to reduce code length
oc = odb.rootAssembly.instances['POLY'].nodes
outputFile=open(Hip+'output.m','w')
outputFile.write('Nodes = [')
for u in dispValues:
    outputFile.write('%d,' % (u.nodeLabel))
outputFile.write('; \n')
outputFile.write('basex = [')
for u in dispValues:
    outputFile.write('%F,' % (oc[u.nodeLabel-1].coordinates[0]))
outputFile.write('; \n')
outputFile.write('basey = [')
for u in dispValues:
    outputFile.write('%F,' % (oc[u.nodeLabel-1].coordinates[1]))
outputFile.write('; \n')
outputFile.write('basez = [')
for u in dispValues:
    outputFile.write('%F,' % (oc[u.nodeLabel-1].coordinates[2]))
outputFile.write('; \n')
outputFile.close()
#outputFile.close()

# call functions
#extracttab()
#getstrains()

```